Materials perspectives on achieving pyrochlore-based quantum spin liquid ground states

Inauguraldissertation

zur

Erlangung der Würde eines Doktors der Philosophie
vorgelegt der
Philosophisch-Naturwissenschaftlichen Fakultät der
Universität Basel

von

Victor Porée

Genehmigt von der Philosophisch-Naturwissenschaftlichen Fakultät
auf Antrag von:

Prof. Dr. Michel Kenzelmann
Prof. Dr. Daniel Loss
Prof. Dr. Kemp Plumb

Basel, 15.11.2022

Prof. Dr. Marcel Mayor
The Dean of Faculty

Abstract

Exotic magnetic systems often stem from frustration caused by competing interactions. The epitome of magnetically frustrated system is incarnated by the quantum spin liquids. These systems are expected to evade magnetic ordering or freezing down to absolute zero Temperature. Magnetic correlations are expected to be strong and can lead to quantum entanglement over large scales as well as the emergence of exotic excitations. Stabilizing such a phase in a rare-earth pyrochlore oxide yields a so-called quantum spin ice resulting from the coherent superposition of 'two-in-two-out' spin ice configurations, reminiscent of the arrangement of hydrogen atoms in water ice.

In some rare-earth pyrochlore oxides, magnetic rare earth ions experience a strong uniaxial anisotropy as well as frustrated ferromagnetic interactions, two of the main ingredients stabilizing a spin ice state. In particular, $Ho_2Ti_2O_7$ and $Dy_2Ti_2O_7$ have been thoroughly studied and are now two well established examples of classical spin ices. Owing to a reduced dipolar interaction, similar materials hosting smaller magnetic moments are thought to be ideal systems to search for quantum spin ices states. Such a state is favored by an Hamiltonian composed of a leading but not exceedingly large Ising term, forming the 'ice' state, accompanied by smaller but non-negligible transverse terms allowing quantum fluctuations to tunnel through equivalent spin ice configurations. Additionally, other properties such as multipolar degrees of freedom, structural disorder or low-lying crystal-electric field levels are expected to have significant contributions to the magnetic ground state.

Cerium-based pyrochlores are promising quantum spin liquids candidates, which received little attention until recently due to their demanding synthesis. Using thermodynamic measurements together with a detailed structural and crystal-electric field analysis, we show that both $Ce_2Sn_2O_7$ and $Ce_2Hf_2O_7$ display magnetic moments with an Ising character and no sign of spin ordering or freezing despite signs of magnetic correlations at low temperatures. Through various neutron experiments, we demonstrate that the compounds form a peculiar octupolar quantum spin ice state, where dominant octupolar correlations conspire to form a coherent 'ice-like' phase from which fractional excitations emerge. High resolution neutron backscattering spectroscopy shows convincing agreement with the theoretical predictions of the quantum electrodynamics emerging from a quantum spin ice phase.

Disorder is known to have a significant influence on spin liquids, typically leading to spin freezing or ordering. In particular, pyrochlore oxides containing non-Kramers rare earths are very sensitive to structural disorder, a specificity that was theoretically proposed as a way to stabilize a quantum spin liquid phase. We hereby present the study of three cases where structural disorder plays a prominent role in the low temperature magnetic properties. We start with the case of $Tb_2Hf_2O_7$, a strongly disordered yet very promising spin liquid candidate with a puzzling low temperature correlated state. A detailed structural analysis, coupled with a point charge model, yields a qualitative understanding of the single-ion properties of this compound and provides new insights

into the mechanisms behind its low temperature behavior. We then perform a comparative structural study of two praseodymium-based compounds, $Pr_2Hf_2O_7$ and $Pr_2Zr_2O_7$, which display distinct magnetic ground states in spite of their structural and chemical proximity. Finally, we show how the control over the structural disorder via chemical substitution allows the tuning of the magnetic behavior of spin ice state observed in $Ho_2Ti_2O_7$.

Contents

Introduction

Preamble

$\mathcal{O}$UR universe is a great source of inspiration for many, and despite tremendous progress in understanding it, numerous questions remain unanswered. Many of these interrogations circle around the fine-tuning of the universe [1, 2]. Indeed, as far as the human understanding goes, nature abounds of parameters, whose values science is so far not enable to explain [3]. The speed of light, the Planck constant, the Boltzmann constant or the gravitational constant are prime examples [4]. Some of these parameters are directly responsible for the development of the universe as we know it, and slight variations, even affecting the 4th decimal (or in the incredible case of the cosmological constant the 122nd decimal [5]) would lead to a drastically different universe or even no universe at all [6].

The fine-structure constant α [7] is one of these parameters, which continually shapes our universe [8]. It has several physical interpretations due to its universality across electromagnetic phenomena. For instance, quantum electrodynamics defines α as the interaction strength between electrons and photons. Its value is not predicted by theory. It is thus among the few empirical quantities in the Standard Model [9]. Experiments attribute it a value often approximated to 1/137, independently of the unit system used. The fine-structure constant governs electrodynamics, from the charge of the electron to the electronic configuration of atoms and of course the photoelectric effect. Naturally, the investigation of materials hosting emergent quantum electrodynamics (eQEM) attracted a lot of attention, owing to the possibility to study systems with a different subset of fine-tuned parameters. Quantum spin ices (QSI) are topological magnets whose fractionalized deconfined excitations find analogy in the 'standard model'. Indeed, QSIs are expected to host emergent gauge fields, with their own photon, electric and magnetic charges [10, 11], all surging from highly correlated yet disordered frustrated magnetic moments [12, 13, 14]. Consequently, this exotic eQED opens up a route to study and/or tune an emergent fine-structure constant [15, 16, 17], which strength may differs from normal QED, perhaps bringing answers to its long-lasting enigma.

However, after a few decades of research, no QSI system as been unambiguously recognized, mainly due to the absence of smoking-gun experiments. Luckily, the field benefits from a strong activity from both the theoretical and experimental sides. The difficult synthesis of some possibly interesting compounds is also an issue in the community and limits the range of accessible compositions and/or the set of techniques one can use to fully characterize some materials. Nevertheless, a few candidate compounds have been identified and are subject to detailed investigations [18]. The mechanisms allowing to stabilize QSI states are still subject to discussions since many effects can contribute to the Hamiltonian [14] of a given real system . For instance, multipolar interactions [19], magnetic defects or low lying crystal-electric field levels [20] are often used as arguments in order to explain the emergence of a possible QSI state. These well understood pro-

cesses compete with ubiquitous additional effects such as non-magnetic defects, further neighbor interactions or microscopic strain, rendering an exhaustive understanding often inaccessible in real systems. On the other hand, these initially unwanted additional contributions might be used at our advantage as driving mechanism to increase quantum fluctuations and promote new highly correlated electron systems [21, 22]. Going further, new QSI/QSL materials could be tailor made to satisfy new demands in spintronics, quantum memory devices or quantum computing [23, 24] by tuning quantum fluctuations through the control of non-magnetic defects, for instance.

This present work aims at opening new horizons in the search for QSI materials via various approaches. We start by studying the case of cerium-based pyrochlore oxides, newcomers in the domain of frustrated magnetism although already known in other areas of research. The trivalent cerium ion in these materials is found to host a ground state with correlated multipolar degrees of freedom. Using neutron scattering techniques, combined with bulk properties measurements, we provide a detailed understanding of the nature and energy scales governing correlations in $Ce_2Sn_2O_7$ and $Ce_2Hf_2O_7$.

We then investigate the highly disordered, yet highly correlated $Tb_2Hf_2O_7$ compound [25]. We carry out a comprehensive study of the disorder in the system through the analysis of structural diffuse scattering. We use our results to gain further insight in the intriguing magnetic ground state arising in this compound, featuring both dynamical and frozen magnetic correlations, while evading long-range order.

We also attempt to explain the difference in experimental observations between two praseodymium compounds, $Pr_2Zr_2O_7$ and $Pr_2Hf_2O_7$. Although iso-structural and chemically close, the two compounds exhibit a few discrepancies, especially in their spin dynamics, measured via inelastic neutron scattering, and the proposed type of magnetic ground state [26, 27, 28]. We show that this difference could be linked to the presence of structural disorder in the zirconate compound, which appears to be absent in its hafnium counterpart.

Finally, we explore the possible tunability of quantum fluctuations in QSI materials. The introduction of non-magnetic disorder in a canonical spin ice brings about transverse fields in the Hamiltonian, enhancing quantum fluctuations and entanglement in an otherwise classical system governed by entropy [21].

Before delving into the study of these fascinating materials, we shall introduce some basic concepts necessary to the understanding of these exotic states of matter that are QSI. We will also describe the various experimental techniques used throughout this work to synthesize and characterize our samples.

Chapter 1

General concepts

1.1 Overview of magnetism

Magnetism is a phenomenon observed and used for many centuries as a precious tool, from navigation devices in the middle ages to information storage nowadays. The connection between magnetism and electricity was established in the 19th century and turned out to be a fruitful source of inspirations, investigations and technological developments since then. Although it is easily generated by an electrical current, a magnetic field can also have a microscopic origin, the so-called *magnetic moments* which add up and provide the force one can observe with regular permanent magnets.

1.1.1 Magnetic moments

The magnetic moment is an essential quantity in magnetism. It has two distinct origins, namely the *angular* and *spin* momenta of electrons in an atom [29, 30]. The nucleus of an atom also possesses a magnetic moment of spin but is often neglected due to its relatively low value (due to its large mass), although its consideration is sometimes of great interest. The angular magnetic moment arises from the movement of an electron around its nucleus which can be assimilated to a circuit containing only one electron (see figure 1.1a). Its value can be calculated using the expression:

$$\boldsymbol{\mu}_l = -\frac{e}{2m_e}\mathbf{l} = \gamma \cdot \mathbf{l} \tag{1.1}$$

with m_e the electron mass, e its charge, γ the gyromagnetic ratio and $\mathbf{l}$ the angular momentum of the electron. Taking into account the quantization of the angular momentum, introducing the Bohr magneton μ_B together with the g-factor (equal to 1 in this case) and summing the contribution from all the electrons of a given atom, one can then express the angular magnetic moment as function of the total orbital momentum operator $\hat{L}$:

$$\boldsymbol{\mu}_l = -g \cdot \mu_B \frac{\hat{L}}{\hbar} \tag{1.2}$$

As a consequence of relativistic quantum mechanics, fermions like electrons have an intrinsic *spin* angular moment leading to the existence of a magnetic moment of spin (see figure 1.1b). It can be expressed in a very similar manner with respect to the orbital one, knowing:
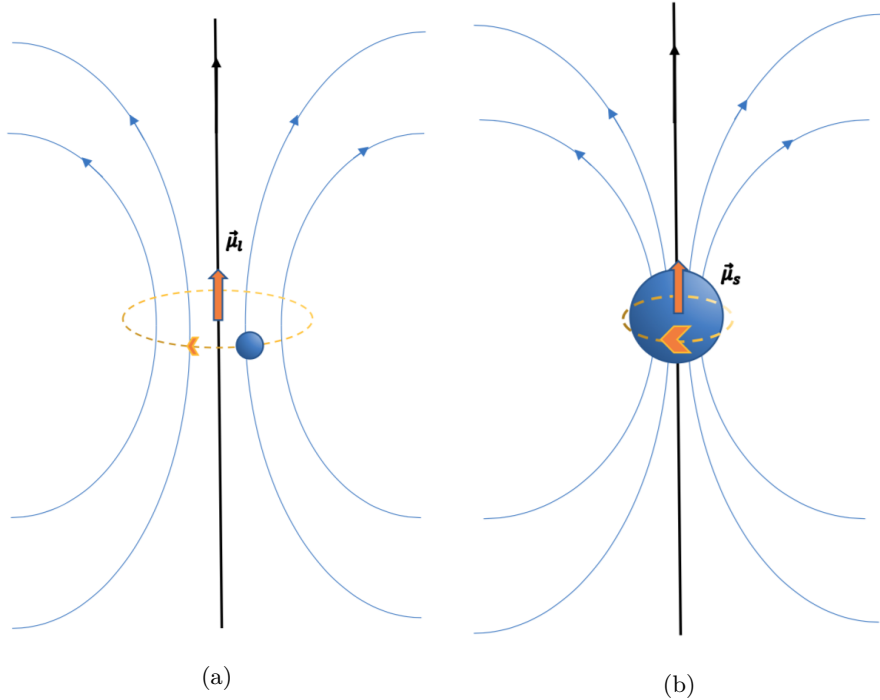
Figure 1.1: (a) Angular magnetic moment. (b) Spin magnetic moment.

$$\boldsymbol{\mu}_s = -\frac{e\hat{S}}{m_e} = -g_s \cdot \mu_B \frac{\hat{S}}{\hbar} = -\frac{g_s \mu_B \boldsymbol{\sigma}}{2} \tag{1.3}$$

with $\hat{S}$ the total spin momentum operator, g_s the g-factor (approximately 2 in the case of the electron spin) and $\boldsymbol{\sigma}$ a Pauli matrix.

Taking into consideration both the angular and spin magnetic moments, one can define the total angular momentum operator $\hat{J} = |\hat{L} - \hat{S}|$ or $\hat{L} + \hat{S}$, for less than half or more than half field orbitals respectively. This is called the Russell-Saunders coupling (or intermediate-coupling as opposed to the jj(strong)-coupling). From this consideration arises the expression for the total magnetic moment:

$$\boldsymbol{\mu}_{Tot} = -g_l \frac{\mu_B \hat{J}}{\hbar} \tag{1.4}$$

hereby introducing the Landé g-factor. For an atom in its ground state, the values of $\hat{L}$, $\hat{S}$ and $\hat{J}$ are deduced applying the Hund's rules. These quantities are also useful to determine the energy levels of a given atom (more on that in section 1.1.2). Of course the angular and spin magnetic moments also interact together through the so-called spin-orbit coupling, leading to a splitting of the electronic energy levels called fine structure levels. In the case of a large nuclear magnetic moment, interactions between the nucleus and the electrons can further split the energy levels leading to the hyperfine structure. Although the total magnetic moment would be in general the quantity of interest when dealing with magnetic moments in matter, one has to be careful when employing it. Indeed, it has been empirically observed that, in some cases, the magnetic moment of spin is the right one to use. This is due to crystal-electric field effects (discussed later, see 1.1.2). In a crystal, charge distribution on lattice sites generates an electrical

potential interacting with atomic orbitals. In the case of rare-earths, the $4f$ shell is localized deep inside the atom, mostly protected from the crystal field. This is not the case for $3d$ transition metals where partially filled orbitals are prone to interact with the crystal field, which becomes prominent with respect to the spin-orbit coupling. In this case, Hund's third rule is not strictly correct and systems are subject to orbital quenching, meaning that the ground will have a total orbital angular momentum of zero and a total angular momentum purely coming from the spins contributions.

1.1.2 Crystal electric field in $4f$ rare-earth elements

When dealing with magnetism in condensed matter, magnetic ions usually cannot be considered as isolated. Surrounding ions will impact its electronic state by introducing electrostatic potentials and one must take this effect into account in order to predict or understand the magnetic behavior of a given magnetic ion in a specific crystallographic environment. This perturbation of an ion electronic state is called *crystalline electronic field* (CEF) and has measurable effects in various physical properties such as specific heat or magnetic susceptibility, which are referred to as *crystal-field phenomena* [31]. A more general theory named *ligand field theory* emerged over the years, also taking into account covalent bonds between the central magnetic ion and its surrounding ligands [32].
The first consideration is the nature of the magnetic ion. In $3d$ transition metals, where partially filled d orbitals are directly exposed to the neighboring electrostatic potentials, the CEF has a stronger effect than the spin-orbit coupling and, in some cases, even stronger than the intra-atomic electron-electron interaction. In rare-earths, the magnetism stems from unpaired electrons in the $4f$ shell which is somewhat shielded by the bigger $5s$ and $5p$ orbitals. This relegates the CEF as a perturbation with respect to the intra-atomic electron-electron (ee) and spin-orbit (SO) interactions [33]:

$$\mathcal{H}_{ee} > \mathcal{H}_{SO} > \mathcal{H}_{CEF} \tag{1.5}$$

For weakly interacting Ln^{3+} cations in an insulator, the single-ion approximation can be used. Orbitals are filled following the Hund's rules, thus minimizing electron-electron repulsion, $\mathcal{H}_{ee}$. The SO interaction $\mathcal{H}_{SO}$, coupling the total orbital and spin momenta, only commutes with the total angular momentum, rendering the global Hamiltonian diagonal in $\hat{J}$. The obtained energy levels are called the J-multiplets and are usually denoted by the spectroscopic notation $^{(2S+1)}L_J$. These levels are 2J+1 degenerate in terms of the magnetic quantum number m_J [34]. Degeneracy is then partially lifted by the CEF, reaching the final distribution of electronic levels (in absence of Zeeman splitting). The remaining degeneracy of the energy levels depends on two things: the symmetry describing the environment around the central magnetic ion, and its number of electrons. Indeed, in the case of an odd number of electrons, the Kramers theorem implies that each CEF level remains doubly degenerate, in which case one speaks of Kramers ions [35]. For non-Kramers ions, having an even number of electrons, the degeneracy of a level solely relies on the symmetry of the CEF.
Two different formalisms were developed to describe the crystal-field Hamiltonian depending on whether or not the excited J-multiplets need to be included in the diagonalization (Wybourne [36] or Stevens [37] formalism respectively). Despite small differences in the notations and multiplets treatment, both Hamiltonians have the same form:

$$\mathcal{H}_{CEF} = \sum_{n,m} B_m^n \mathcal{O}_m^n \tag{1.6}$$

where $\mathcal{O}_m^n$ are components of spherical tensor operators and B_m^n are the crystal-field parameters to be determined from experiments [38, 39]. There are 27 independent CEF
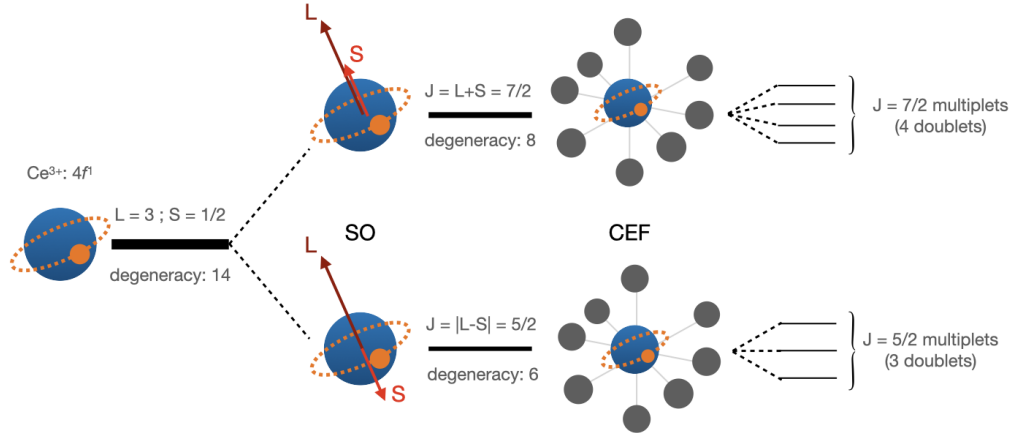
Figure 1.2: Splitting of the Ce^{3+} energy levels due to spin-orbit coupling and crystal-electric field (of D_{3d} symmetry in this case, as found in rare earth pyrochlore oxides).

parameters, some of them being complex. Thankfully, this number can be lowered based on symmetry arguments, forcing some to be zero and implying relationships between others.

The crystal-field parameters are related to the investigated ion and to the distribution of charges surrounding it. B_m^n values can thus be calculated using a point-charge model, providing a very rough approximation. The CEF Hamiltonian can then be written and diagonalized, giving estimated transition energies and associated intensities. By varying the CEF parameters, one can then fit the calculated energies and intensities to the experimental values [31], obtained via inelastic neutron scattering for instance (see 2.5.6). Once the fit has reached a satisfactory agreement, the CEF parameters are fixed and the final $\mathcal{H}_{CEF}$ is used to determine the energy levels (eigenvalues) and associated wavefunctions (eigenvectors), which can then be used to compute other quantities such as magnetic susceptibility, magnetization or contributions to the specific heat. Another useful piece of information is the anisotropy experienced by the magnetic moment due to its surrounding electronic environment. This is encapsulated in the concept of g-tensor, describing the direction(s) in which the moment is more likely to point. The g-tensor is evaluated by looking at the expectation values from the Zeeman coupling of a small magnetic field projected onto a subspace formed by the previously computed ground-state doublet (or in some cases on the subspace formed by the ground state and first excited singlets).

1.1.3 Multipoles in $4f$ rare-earth elements

Magnetic moments in ions are often considered as dipolar objects, akin to classical magnets we experience in the day to day life where we observe two poles creating a magnetic field around them. This approximation is usually a reasonable assumption and turned out to be correct in many cases, allowing to describe magnetic structures in term of long-range ordered dipolar magnetic moments.

Microscopically, the magnetism stems from the unpaired electrons density of probability, as these same electrons are responsible for the magnetism. This density of probability is described by the radial and angular wavefunctions, the second one being described in terms of spherical harmonics. The evaluation of these wavefunctions is paramount within the quantum mechanical treatment of atomic orbitals [39, 40] and is typically

expressed using the orbital angular momentum. Similarly, the magnetism produced by the open-shell electrons is described by magnetization operators composed of multipole operators. These multipoles are themselves made of total angular momentum operators and characterized by their type and rank. Operators which are odd under time reversal symmetry are denoted as magnetic multipoles, whereas the even ones are called electric multipoles. For instance, there are three magnetic dipolar (rank 1), five electric quadrupolar (rank 2) and seven magnetic octupolar (rank 3) operators [39, 41]. These operators can be defined as follows:

Magnetic dipoles :

$$J_x, \ J_y, \ J_z \tag{1.7}$$

Electric quadrupoles :

$$
\begin{aligned}
\hat{\mathcal{O}}_2^0 \ &= \ 3J_z^2 - J(J+1), \\
\hat{\mathcal{O}}_2^2 \ = \ J_x^2 - J_y^2, \ \hat{\mathcal{O}}_2^{-2} \ &= \ (J_xJ_y + J_yJ_x)/2, \\
\hat{\mathcal{O}}_2^{-1} \ = \ (J_yJ_z + J_zJ_y)/2, \ \hat{\mathcal{O}}_2^1 \ &= \ (J_zJ_x + J_xJ_z)/2
\end{aligned} \tag{1.8}
$$

Magnetic octupoles :

$$
\begin{aligned}
\hat{\mathcal{O}}_3^0 \ &= \ J_z + 5J_z^3 - 3J_z(J_x^2 + J_y^2 + J_z^2), \\
\hat{\mathcal{O}}_3^3 \ = \ (J_+^3 + J_-^3)/2, \ \hat{\mathcal{O}}_3^{-3} \ &= \ i(J_-^3 - J_+^3)/2, \\
\hat{\mathcal{O}}_3^2 \ &= \ (J_-^2(-I + J_z) + J_+^2(I + J_z))/2, \\
\hat{\mathcal{O}}_3^{-2} \ &= \ i(-J_-^2(-I + J_z) + J_+^2(I + J_z))/2, \\
\hat{\mathcal{O}}_3^1 \ = \ (5(-J_- + J_+)J_z + 5(J_- + J_+)J_z^2 &- (J_- + J_+)(-2 + J^2I))/2, \\
\hat{\mathcal{O}}_3^{-1} \ = \ i(5(-J_- + J_+)J_z + 5(J_- + J_+)J_z^2 &+ (J_- - J_+)(-2 + J^2I))/2,
\end{aligned} \tag{1.9}
$$

Typically, a largely dominant contribution to the magnetism comes from rank 1 multipoles i.e. magnetic dipoles, leading to the often used *dipole approximation* where further multipolar contributions are neglected. However this approximation is not always strictly applicable, particularly in the case of *f*-electron physics. For instance, non negligible octupolar components can be detected in NMR, muon experiments and, most interestingly in our case, in neutron scattering experiments (see section 2.5.7).
A fruitful playground to study the physics of multipoles is the actinide family [42]. Indeed, multipoles are thought to play an essential role in several actinide superconductors or oxides [42, 43, 44] and have been shown to form an intriguing hidden order in URu_2Si_2 [43, 45]. But the relevance of multipoles in not limited to the heaviest elements. A prominent example is CeB_6 where field-induced octupoles form a hidden order [41, 45]. Other rare-earth compounds have also displayed multipolar behaviors [45, 46] and few examples of even lighter magnetic elements can also be found [47].
The study of spin liquids has found a new interest in multipolar interactions as well, particularly in the case of non-Kramers pyrochlores where quadrupolar interactions are expected to be at play. Indeed, a small deviation from the ideal CEF environment can split the ground state doublet and induce sizable quadrupolar moments in these systems. This can be predicted based on CEF considerations, and although electric quadrupoles cannot be directly observed via neutron scattering, their presence and possible collective behavior can have a significant impact [27, 48]. Quadrupolar degrees of

freedom can more readily be studied using optical probes, but the typical temperatures accessible in such experiments are not low enough to be in the correlated phase of some QSI candidates. Owing to their 'electric' nature, quadrupoles can couple to electric fields, such as the the one generated by the surrounding charges in a crystal. This can cause a significant degree of magnetoelastic coupling, with for instance hybridization between low-lying CEF levels and phonons [48, 49].

Magnetic octupoles (rank 3) can be found in some pyrochlores hosting Kramers rare-earth ions, such as Ce^{3+} and Nd^{3+}. For instance, depending on the details of the CEF scheme, the magnetic ground state doublet of Ce^{3+} can happen to be a mix of $J^z = \pm 3/2$ states, yielding a ground-state of mixed 'dipolar-octupolar' character [50, 51]. In this particular case, on each rare-earth site i, a pseudo-spin $1/2$ operator $\hat{\tau}_i = (\tau_i^x, \tau_i^y, \tau_i^z)$ applied to the subspace formed by the ground state doublet, has its τ_i^x and τ_i^z components transforming like magnetic dipoles, whereas the τ_i^y component transforms like a magnetic octupole. The precise magnitude of the dipolar and octupolar moments depends on the composition of the ground state wavefunction which can be influenced by magnetic interactions and collective behavior, as well shall see later on in the case of $Ce_2Sn_2O_7$ and $Ce_2Hf_2O_7$.

As an example, let us take the case of the $J = 5/2$ ground state multiplet of Ce^{3+} on the pyrochlore lattice. Assuming a ground state composed of $J_z = \pm 3/2$ states, the Kramers doublet can be written in the $J_z = -J, ...J$ subspace as:

$$
\begin{aligned}
|\uparrow\rangle &= (0, b, 0, 0, a, 0) \\
|\downarrow\rangle &= (0, -a^*, 0, 0, b^*, 0)
\end{aligned}
\tag{1.10}
$$

with a and b respecting the normalization condition. Setting a to 1 and b to 0 for simplicity, one can easily apply the aforementioned multipolar operators. Expressing the result of the non zero operators in terms of the pseudo-spin components shows the mixed dipolar-octupolar of the ground state's magnetic moment:

$$
\begin{aligned}
\hat{J}_z &= 3\tau_z \\
\hat{\mathcal{O}}_3^0 &= -42\tau_z \\
\hat{\mathcal{O}}_3^3 &= -24\tau_x \\
\hat{\mathcal{O}}_3^{-3} &= -24\tau_y
\end{aligned}
\tag{1.11}
$$

1.1.4 Exchange interactions in insulators

Magnetic interactions are of two kinds: of dipolar origin and of exchange origin [30]. The magnetic dipole interaction strikes as the most evident as it is responsible for the behavior of two magnets placed in close proximity. Considering the magnetic dipole moments, $\boldsymbol{\mu}_1$ and $\boldsymbol{\mu}_2$, separated by a distance r, one can calculate the energy of interaction:

$$
\mathcal{E} = \frac{\mu_0}{4\pi r^3} \left[\boldsymbol{\mu}_1 \cdot \boldsymbol{\mu}_1 - \frac{3}{r^2}(\boldsymbol{\mu}_1 \cdot \boldsymbol{r})(\boldsymbol{\mu}_2 \cdot \boldsymbol{r}) \right]
\tag{1.12}
$$

However, considering individual magnetic moments, from magnetic ions for instance, this interaction is rather weak and cannot explain the magnetic ordering in most materials.

In magnetic insulators, the exchange interaction is typically the main interaction between the magnetic moments. In the most general setting, the exchange interaction

is written as a tensor, whose components size and sign dictate how two magnetic moments will align with one another. Now considering many moments and their respective interactions, a long-range magnetic order is prone to stabilize at temperatures close to the magnitude of the dominant exchange interaction in the system. A magnetic phase transition from paramagnetic to long-range order signifies that the magnetic structure (i.e. how the magnetic moments are arranged) goes from random and uncorrelated to a structure that is periodic and can be matched commensurably (or sometimes incommensurably) to the underlying crystallographic structure. A magnetic phase transition can be evidenced via a change of slope in magnetic susceptibility measurements, a sharp peak in heat capacity or the appearance of new Bragg reflections in neutron diffraction patterns.

Upon further cooling, other magnetic transitions (sometimes metamagnetic) can occur as weaker exchange interactions start to have non negligible strengths, requiring a rearrangement of the moments. The application of an external magnetic field or pressure can also modify the hierarchy of interactions, sometimes leading to new and interesting magnetic phases or to extremely rich magnetic phase diagrams. In materials with a strong coupling between the underlying lattice and the magnetism, a magnetic phase transition can be accompanied by a structural phase transition, very often towards a structure of lower symmetry.

Interactions of exchange origin can be classified in direct (i.e., involving an actual electronic cloud overlap between the two concerned atoms) and indirect (with a mediator that transmits the interaction). In view of the present work, the following discussion will be focused on the case of insulators, as exchange interactions represent such a large subject. Even after this restriction, one can find several mechanisms taking place in insulators, causing very interesting spin configurations.

Interactions between spins are usually described exchange Hamiltonian composed of two spins $\mathbf{S}_i$ and $\mathbf{S}_j$, interacting through the exchange integral $\mathcal{J}$:

$$\mathcal{H} = -\mathcal{J}\boldsymbol{S}_i \cdot \boldsymbol{S}_j \tag{1.13}$$

In the simplest case where spins have an Ising character (i.e. have only two possible states: up or down), the modulus of $\mathcal{J}$ shows the strength of the interaction between the two spins, and its sign, their relative orientation: a positive value results in a parallel order, also called ferromagnetic, whereas a negative one will display antiparallel spins, antiferromagnetic order. In a more general formalism, one speaks of Heisenberg Hamiltonian where the spins are described by the three Pauli matrices and the exchange interaction becomes a tensor.

The simplest exchange is called the direct exchange and is a direct result of the orbital overlap between two magnetic atoms. In this case, exchange integral is the fruit of the Coulomb repulsion between the electrons together with the Pauli exclusion principle [29]. Another exchange interaction is the superexchange. It can be described as the virtual hopping of electrons via the intermediate p-orbitals, gaining kinetic energy with respect to the Coulomb repulsion [52, 53]. It is hence classified as indirect exchange interaction. In spite of the complexity of the calculations in many electrons systems, the expected signs of the couplings in $3d$ metals were rationalized by J.B. Goodenough and J. Kanamori as a set of rules taking into account the occupation and the relative orientation of orbitals [29, 54].

In some cases, materials with low symmetry display asymmetric couplings. This phenomenon is called the Dzyaloshinski-Moriya interaction [55] and tends to align two spins perpendicularly:

$$\mathcal{H} = -\mathcal{D} \cdot (\boldsymbol{S}_i \times \boldsymbol{S}_j) \tag{1.14}$$

where $\mathcal{D}$ is a vector lying along a high-symmetry axis and is non zero only if there is no inversion center between the two spins. This coupling is typically much weaker than the superexchange.

Finally, the presence of higher rank multipoles introduces additional contributions to the interactions Hamiltonian and, in some cases, have been shown to play a substantial role. One can generally describe magnetic multipolar interactions as [39, 56]:

$$\mathcal{H}_{MMI} = \sum_{ll'mm'} \mathcal{J}_{ll'}^{mm'} \hat{\mathcal{O}}_l^m \hat{\mathcal{O}}_{l'}^{m'} \tag{1.15}$$

where l runs over the rank of the multipoles and m from $-l$ to l. $\mathcal{J}$ represents the strength of the interaction between the two corresponding $\hat{\mathcal{O}}$ multipolar operators. The number of allowed combinations is limited based on symmetry arguments, considering both bond symmetry and operator parity, as odd (even) operators can only couple with other odd (even) ones[39]. Note that assuming a purely dipolar magnetic moment stemming from electronic spin, one comes back to an equation similar to 1.13.

1.1.5   Magnetic frustration in insulators

In magnetic insulators, a spin can interact with neighboring spins via different exchange pathways. In many instances, it results in magnetic comfigurations, short- or long-ranged, which are more complex than a parallel or antiparallel arrangement. Non-collinear arrangements are often the result of the competition between different exchange interactions or to the presence of geometrical frustration [29, 30]

A simple illustration of geometrical magnetic frustration is to put spins at the three corners of a triangular lattice, posing the condition that they are all antiferromagnetically coupled (see figure 1.3). It is obvious that there is no configuration where spins can be antiparallel to one another. Thus, the spins will re-order themselves to minimize the energy of the system, in this case forming a 120° order. Geometrical frustration can be met in several types of lattices, such as the triangular, kagome and pyrochlore, among others. Interestingly, a ferromagnetic interaction leads to frustration in the pyrochlore structure whereas an antiferromagnetic exchange stabilizes long-range order [57]. In pyrochlores, and in other cases, the anisotropy experienced by the magnetic moments also plays a role as it can restrict them to point in particular directions or lie in specific planes.
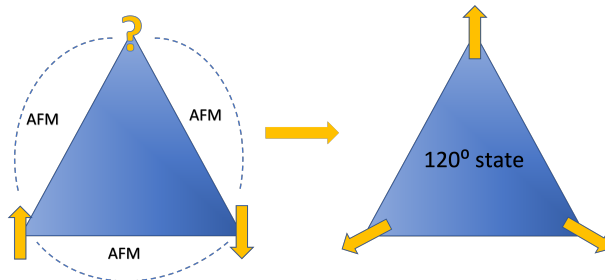

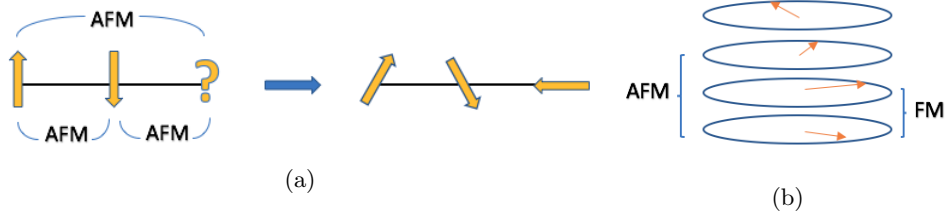Figure 1.3: Geometric frustration on a triangular lattice.

Figure 1.4: (a) Nearest neighbor and next-nearest neighbor competition. (b) Example of helimagnetic configuration, particular case of frustration due to NN and NNN interactions.

As mentioned just above, another source of frustration is the competition between several exchange interactions. Frustration can arise from a magnetic moment's interaction with its nearest (NN) and next-nearest neighbors (NNN) [30]. As an example, setting up a one dimensional chain of spins coupled antiferromagnetically, frustration can appear if NN and NNN couplings are of the same order, like in figure 1.4, where one can observe spiral arrangements. This mechanism is very relevant in many cases such as spin chains, spin ladders but also in more complex 2D and 3D systems, where frustration can involve even further neighbors.

Typical consequences of magnetic frustration are the stabilization of complex magnetic structures, often accompanied by rich phase diagrams as a function of temperature, applied magnetic field and pressure. For instance, the competition between the Dzyaloshinski-Moriya interaction and other couplings can lead to a variety of magnetic Skyrmions phases and other kinds of spin textures. Magnetic frustration can also delay the onset of the long-range order. Due to the competition between the interactions, the system does not pick up an ordered state even at temperatures below that of the dominant interaction(s). One can then estimate the degree of frustration by looking at the absolute ratio between the Curie-Weiss temperature and the actual ordering temperature, known as the frustration parameter. The higher the ratio, the more frustrated is the system. In some extreme cases, the frustration is so strong that no long-range order is expected to stabilize down to 0 K. Instead, the system remains disordered but is subject to short-range correlations owing to the presence of magnetic interactions, justifying the title of cooperative paramagnet introduced by Villain [58]. The next section treats of states called 'spin liquids', similar to cooperative paramagnet with the absence of magnetic long-range order but with the domination of short-range correlations and the development of emergent phenomena.

1.2 From spin liquids to quantum spin ices

1.2.1 Spin liquids

The study of magnetic frustration (1.1.5) began with the study of Ising antiferromagnets in systems hosting triangular motifs. Back in the 1950's, Wannier showed that this problem actually holds a large degeneracy due to the many ground state possibilities reaching the same energy [59]. Such degeneracy leads to an interesting phenomenon where the ground state retains some entropy, proportional to the number of spins involved. Due to the degeneracy, the spins can keep fluctuating at low temperatures, spanning the allowed micro-states. Owing to their anisotropy, the spins cannot adopt any direction they want and in some cases a cooperative behavior emerges. The pres-

ence of correlations and the absence of long range magnetic order gave it its name of cooperative paramagnet [58] or spin liquid, by analogy with the liquid phase of matter with which it shares similarities.

Naturally, the fluctuations of the spin configuration cannot happen completely on their own and necessitate a fluctuation mechanism. One can separate two types of spin liquids: classical and quantum [60]. On one hand, classical spin liquids rely on the thermal fluctuations to overcome the energy barrier between two spin configurations. Obviously, if the temperature gets so low that thermal fluctuations do not provide enough energy to maintain the fluctuations, the system will loose its dynamics and pick up a single ground state by either ordering or freezing. On the other hand, when spins are close to minimum value of $\frac{1}{2}$, quantum zero point fluctuations (coming from the quantum mechanical uncertainty principle) can be large enough to provide a way for the spins to tunnel between the various configurations, and this down to 0 K. A significant difference is that quantum fluctuations can be coherent. In the case of strong and coherent quantum fluctuations, spins are highly entangled.

This idea of short range entanglement was put forward by Anderson in his Resonating Valence-Bond theory in order to explain superconductivity at the time [61]. This state can be described as valence bonds (singlets) formed by neighboring spins [62]. The RVB state differs from a Valence Bond Solid (VBS) in that it is a macroscopic superposition state of many VBS configurations (see figure 1.5), thus preserving the underlying lattice symmetry. This proposal was very fruitful in the realm of frustrated magnetism and motivated a strong interest in finding materials realizing exotic magnetic phases such as the RVB state. Modern definitions of a quantum spin liquids differ in the scale of the entanglement. The RVB state assumes the formation of singlets between neighboring spins, thus the entanglement happens on a short range. In QSLs, the entanglement is expected to cover different length scales, both short and long, giving rise to exotic physics.
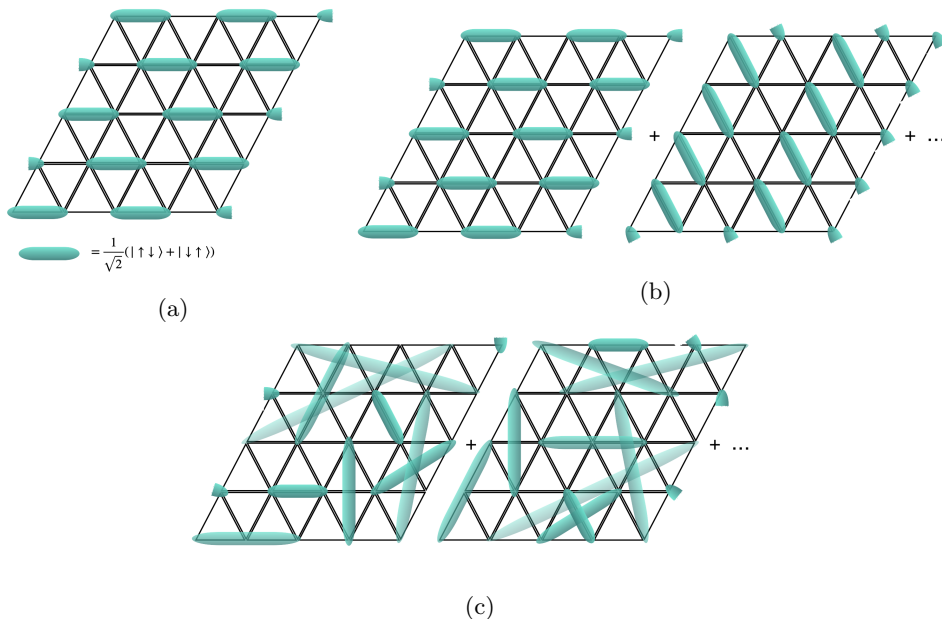
Figure 1.5: Scheme of a Valence Bond Solid (**a**), short range Resonating Valence-Bond (**b**) and long range Resonating Valence-Bond (**c**).

There exist many types of QSLs, however one common feature is that they support exotic excitations. [60]. A prominent example is known as spinons, neutral quasi-particle of spin 1/2. They are considered as fractional excitations, carrying a non-integer quantum number and no charge, differing from typical electron-like of magnon-like excitations. Although one dimensional systems are not strictly considered as quantum spin liquids, they offer a robust theoretical framework to understand spinon excitations. For instance, spin 1/2 antiferromagnetic Heisenberg chains indeed displays spinon excitations pictured as domain walls able to propagate within the chain. Such excitations can be created by flipping a spin, creating two spinons. This can be observed in neutron scattering experiments. The obtained spectra will display a broad continuum of gapless excitations reflecting the conservation of energy-momentum transferred from the neutron to the spinon pair (see Fig. 1.6a), as seen experimentally in the spin 1/2 antiferromagnets $KCuF_3$ [63, 64] or $CuSO_4 \cdot 5D_2O$ [65]. Haldane demonstrated [66] that these excitations become gapped for integer spins and are expected to appear as magnons i.e. sharp excitations, although continua of excitations have also been observed experimentally [67, 68]. The study of the distinct topological properties of both types of spin chains thus uncovered the presence of very different excitations. Similar differences can be found in two- and three-dimensional systems depending on the details of the underlying magnetic lattice and magnetic correlations, also resulting in quasi-particle excitations obeying different statistics. As a result, the observation and detailed analysis of excitations emanating from a QSL candidate constitute one of the main tools to identify and understand their exact magnetic ground state.

As mentioned earlier, two-dimensional materials have played a significant role in the quest for quantum spin liquids. Triangular and kagome structures provide natural geometrical frustration and motivated the investigation of many systems such as $YbMgGaO_4$ [69] or Herbertsmithite and some of its related compounds [70]. Inelastic Neutron Scattering performed on some of these compounds found evidence for continua of excitations (see Fig. 1.6b). However, the presence of structural disorder significantly complicates the modeling and interpretation of the data. More recently, the advent of the Kitaev model [71] strongly boosted the investigation of two-dimensional QSL candidates. Indeed, this model is particularly attractive owing to its exact solvability, the exotic magnetic ground states it stabilizes as well as the peculiar fractional excitations emerging from it. In this case, the QSL phase relies on strong frustration on each spin site of a two-dimensional honeycomb lattice, mediated through anisotropic Ising-like interactions (Fig. 1.6c). A few material candidates have already been investigated, yielding promising results [72, 73, 74, 75].

Last but not least, three dimensional materials have also been scrutinized in order to find experimental realizations of quantum spin liquid states. So far, the main candidates display hyperkagome or pyrochlore structures. The latter being renown to stabilize particular types of spin liquid named spin ices.

1.2.2 Dipolar spin ices

Pyrochlore oxides (1.3) turned out to be fruitful materials to study the physics of spin liquids in 3D systems. Namely, two compounds have been subject to intense studies: $Ho_2Ti_2O_7$ and $Dy_2Ti_2O_7$. The rare-earth ions in this family of compounds display a strong Ising character, due to the crystal-electric field formed by the oxygen environment surrounding them, forcing their magnetic moments to point either toward or away from the center of their tetrahedra. To a good approximation, a rather simple
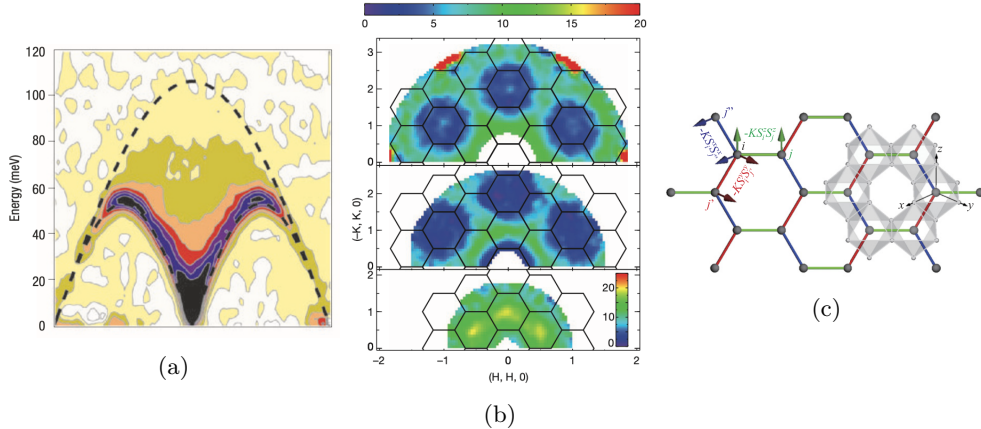
Figure 1.6: (a) Spinon continuum observed via INS in $KCuF_3$, from [64]. The x-axis goes from 0 to 1 in reciprocal lattice units along the chain direction. (b) Continuum of excitations measured on $ZnCu_3(OD)_6Cl_2$ using INS, from [76]. The cuts were taken at constant energies transfers of 6 meV, 2 meV and 0.75 meV from top to bottom. (c) Schematic drawing of the Kitaev model on the honeycomb lattice [77].

Hamiltonian can be used to describe the spin ice state:

$$\mathcal{H}_{SI} = -\sum_{ij} \mathcal{J}^{zz} \mathcal{S}_i^z \mathcal{S}_j^z \tag{1.16}$$

with $\mathcal{S}_i^z$ the local Ising component of the pseudo-spin on site i and $\mathcal{J}^{zz}$ the coupling between the Ising moments [57]. Surprisingly, ferromagnetic NN interactions lead to frustration in this instance. This is due to the Ising anisotropy experienced by the magnetic moment and to the cubic symmetry of the underlying lattice, conspiring to force the moments to point along their local $\langle 111 \rangle$ directions. As a result, an antiferromagnetic coupling is not frustrated and stabilize an 'all-in-all-out' configuration, whereas a ferromagnetic coupling yields a state where two of the four magnetic moments sitting on a given tetrahedra would point inward and the two others would point outward [57]. This is reminiscent to the configuration of water molecules in water ice [78], which led to the so-called '2-in-2-out' ice rule in pyrochlore spin ices. This is not the only resemblance between water ice and the spin ice state as they both have a highly degenerate ground state due to large number of energetically equivalent '2-in-2-out' configurations, which the system can explore via thermal fluctuations. Pauling showed that this can be observed in heat capacity measurements of water ice, showing up as a lack of recovered entropy compared to what is expected for a 2-levels system [79]. This residual entropy was also observed in spin ices [80] (see figure 1.7a), making heat capacity one of the go-to techniques to study spin ice systems. Another distinctive characteristic of dipolar spin ices is the presence of very sharp and anisotropic features named 'pinch-points' in neutron diffraction experiments [81], as shown in figure 1.7b.The pinch-points arise from the long-range interaction between the large magnetic moments, via the dipolar interaction.

Similarly to classical electrodynamics, one can define a (lattice) gauge field to describe the spin ice state. The use of gauge fields has found great applications in condensed matter physics as the mapping of a discrete system to a continuous one allows the use of probability distributions and application of standard field theory techniques. For the spin ice state, this is done by replacing the magnetic moments by the vector field
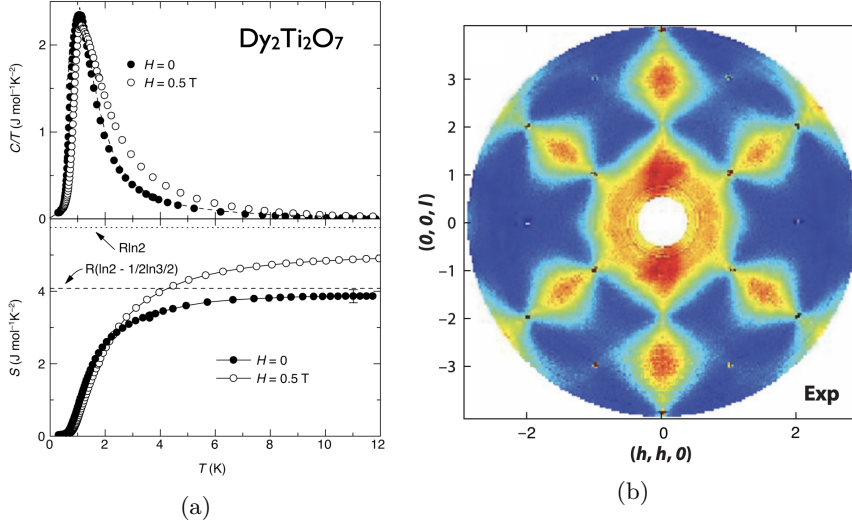
Figure 1.7: (a) Specific heat and associated recovered entropy in $Dy_2Ti_2O_7$, from [80]. (b) Experimental spin-flip scattering map at zero energy transfer, showing pinch-points collected on $Ho_2Ti_2O_7$, from [81].

$\mathbf{S}(\mathbf{x})$ (similar to a magnetic field) they generate. Constraining the $\mathbf{S}(\mathbf{x})$ to be divergence free (as in classical electrodynamics, $\nabla \cdot \mathbf{B} = 0$) means that on can express the vector field as $\mathbf{S}(\mathbf{x}) = \nabla \times \mathbf{A}$, with $\mathbf{A}$ the gauge field. The manyfold of degenerate ice-rule states can then be pictured as the vacuum of this gauge field, with magnetic degrees of freedom experiencing dipolar-like correlations. Breaking the ice-rule on a tetrahedron, by flipping a single spin/magnetic moment generates two opposite magnetic charges at the centers of the tetrahedra sharing the flipped spin [82, 83]. The obtained charges are equivalent to *magnetic monopoles* and can propagate by flipping other spins, jumping from a tetrahedron to another (see figure 1.8 [83]). These monopoles play the role of sources and sinks of the vector field $\mathbf{S}$, interacting through a Coulombic interaction owing to the dipolar correlation of the underlying spin ice state.

The study of equilibrium or out-of-equilibrium dynamics provides insight into frequency and momentum dependence of the spin correlations in real materials. It is mostly related to spin flip processes and can be described in terms of the magnetic monopole creation, annihilation and motion [84]. This part is not understood as well as the thermodynamic and static properties of spin ices although progress were made over the last few years. Several methods are used to explore the spin ice dynamics. The most common are zero-field-cooled/field-cooled experiments, ac-susceptibility, relaxation of magnetization or neutron spin echo. At high temperatures, spin flip are thermally activated, with a rather rapid relaxation time, increasing upon cooling [85]. Cooling further, the relaxation reaches a temperature independent plateau where spin dynamics appears to rely on quantum tunneling [86]. At even lower temperatures (typically sub-kelvin), the relaxation time increases exponentially due to the very low density of magnetic monopoles, showing that the system enters a kind of frozen state [86, 87, 88], making the measurement extremely long and practically impossible. To circumvent this problem, the density of monopoles can be increased by using a non-equilibrium method called magnetothermal avalanche quench (AQ), opening new opportunities to study the dynamics of spin ices at very low temperatures [89].
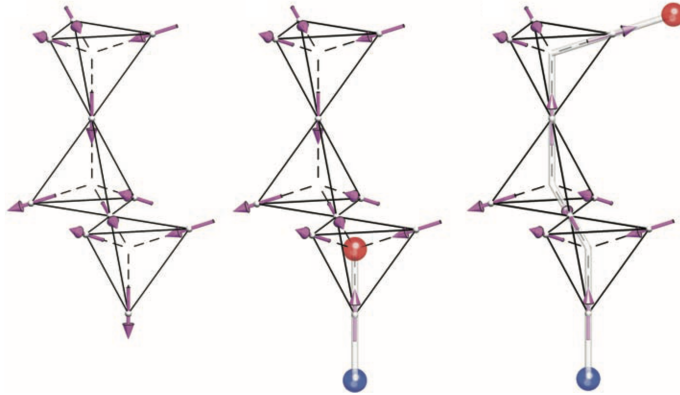
Figure 1.8: Scheme of the creation and propagation of magnetic monopoles in spin ices, from [81].

1.2.3   Quantum spin ices

As suggested by their name, quantum spin ices are the quantum analog of the dipolar/canonical spin ices. Here, the magnetic moments are not as Ising as in the classical case and small but non negligible planar pseudo-spin components act as transverse terms in addition to the *classical* spin ice part (1.16). In its simplest shape, the Hamiltonian can be written as an XXZ Heisenberg system [12, 90, 91]:

$$\mathcal{H}_{QSI} = \sum_{ij} \mathcal{J}^{zz} \mathcal{S}_i^z \mathcal{S}_j^z - \frac{\mathcal{J}_\perp}{2} (\mathcal{S}_i^+ \mathcal{S}_j^- + \mathcal{S}_i^- \mathcal{S}_j^+) \qquad (1.17)$$

where $\mathcal{S}$ are pseudo-spin operators and where the transverse exchange $\mathcal{J}_\perp$ is smaller than $\mathcal{J}^{zz}$. This $\mathcal{J}^{zz}$ should be positive so as to enforce the spin ice ground state but not exceedingly big to keep the magnitude of quantum fluctuations relevant. A key difference between classical and quantum spin ices is that the former is governed by entanglement as opposed to entropy [91]. This is due to the quantum nature of the fluctuations and means that the ground state is a superposition of spin ice states, which is different from a state exploring spin ice configurations through fluctuations. Actually, the introduction of the transverse terms effectively lifts the degeneracy observed in the case of a classical spin ice. However, their perturbative and quantum nature maintains a superposition of ice states while leading to a topological order [12, 90, 91].

An interesting property of the topological order stabilized in a QSI state is found in the novel excitations it supports. As introduced for the dipolar/classical spin ices, a gauge field approximation is often used to describe QSIs [12]. Although it might not provide the ground state wavefunction, it provides a remarkable tool to understand the excitations of the system. Depending on the exact details of the Hamiltonian considered, the system can be identified with different gauge fields symmetries. In many cases, the U(1) gauge theory, used in quantum electrodynamics, is found to be relevant. As a result, the dynamics of QSIs are seen as emergent quantum electrodynamics. In analogy with 'normal' quantum electrodynamics, QSIs support three different excitations (Fig. 1.9a). The highest in energy is reminiscent of the magnetic monopole excitations in dipolar spin ices. It corresponds to sources and sinks of an emergent electric field due to excitations out of the '2-in-2-out' manifold, and is referred to as a *spinon* [64] (similar to spinons in one dimensional systems mentioned previously). Spinons are fractional excitations created/annihilated by pairs and therefore take the shape of a gapped continuum of
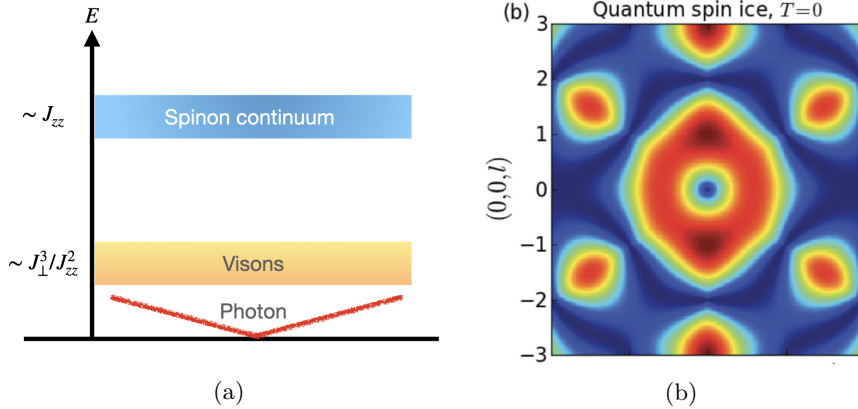
Figure 1.9: (**a**) Scheme of the excitations expected in a quantum spin ice. (**b**) Calculated equal-time magnetic structure factor for a quantum spin ice [10], expected to reflect the emergent photon.

excitations, sometimes observable in INS experiments, centered around the energy scale of the dominant exchange interaction. The next excitation lies lower in energy as it involves the transverse terms of the Hamiltonian while it preserves the spin ice manifold. It can been seen as the flipping of all the spins on an hexagonal plaquette (shortest loop one can built on the pyrochlore lattice). These are equivalent to sources and sinks of an emergent magnetic field and are thus referred to as *magnetic monopoles* (or visons). These visons have not been experimentally confirmed via neutron scattering so far. Last but not least, the long-distance quantum fluctuations of the spin ice manifold supports the emergence of a gapless *artificial* photon. These last excitations are more difficult to picture as they directly come from the coherent nature of the spin fluctuations, leading to the appearance of a particle similar to the photon in quantum electrodynamics but behaving somehow differently (having a different fine-structure constant for instance). It can, in principle, be observed in neutron experiments through the equal-time dynamical structure factor, differing from the dipolar spin ice by the suppression/smoothing of the pinch points at $T = 0 \ K$, expressing the passage from short- to long-distance quantum correlations (Fig. 1.9b), and detachment from dipolar correlations [10, 11]. These excitations are expected to be deconfined as they can easily propagate through the constant rearrangement of the underlying spin ice background. The terminology sometimes mixes up terms but a clear distinction between the excitations and associated names can be found in [13].

The identification of the aforementioned excitations is a difficult task, and so far the absence of smoking-gun experiments is limiting their identification but a few good candidates were investigated. Candidate materials are typically based on rare-earth ions and materials such as $Er_2Ti_2O_7$ [92] and $Yb_2Ti_2O_7$ [93], or in the praseodymium-based $Pr_2Hf_2O_7$ [94] seem to be well described by a QSI Hamiltonian.Yet, several other mechanisms can also favor a quantum spin ice state. For instance, the ground state of the rare-earth ion can allow for multipolar pseudo-spin components, acting as transverse terms in the Hamiltonian, as proposed in $Nd_2Zr_2O_7$ [95] and $Pr_2Zr_2O_7$ [26, 27, 96, 97]. Interestingly, the ground state doublet of non-Kramers rare-earth pyrochlores is very sensitive to disorder. For instance, non-magnetic disorder could significantly affect the interaction Hamiltonian, introducing transverse fields h_i, coupled to planar components of the pseudo-spins, $\mathcal{S}_i^x$. One speaks in the instance of disorder-induced quantum spin

liquid [21, 22], which can be written as the random transverse field Ising model:

$$\mathcal{H}_{RTFIM} = \sum_{ij} \mathcal{J}^{zz} \mathcal{S}_i^z \mathcal{S}_j^z - \sum_i h_i \mathcal{S}_i^x \qquad (1.18)$$

Another compound worth mentioning is $Tb_2Ti_2O_7$. Although its exact ground state is still under debate, the existence of a low lying crystal-electric field level was proposed to introduce a non negligible mixing with the ground state, possibly promoting a quantum spin ice phase [20].

1.3 Pyrochlore oxides and frustrated magnetism

The pyrochlore family owes its denomination to the homonymous and iso-structural material $(Na,Ca)_2Nb_2O_6(OH,F)$ [98]. This mineral was named pyrochlore ('green fire') due to its green tint upon ignition. The pyrochlore family regroups numerous materials, pushing for the restriction of this section to the pyrochlore oxides. Often referred to using the formulation $A_2B_2O_7$ (or $A_2B_2O_6O'$), pyrochlore oxides are usually described using the $Fd\bar{3}m$ (227) space group symmetry, with its origin at the inversion center (general multiplicity of 192). The A ion is placed at the $16d$ site, the B ion at the $16c$ site, O and O' at the $48f$ and $8b$ respectively. In such a geometry, the only adjustable structural parameter is the x coordinate of the $48f$ oxygen, that determines the environment around the A and B ions. This parameter also renders a simple and unique description of the structure impossible. For the studies of magnetic pyrochlores, it is important to notice that there are two interpenetrating networks of corner sharing tetrahedra formed by either A and B, one of which being magnetic (See figure 1.10a) [18, 99], although cases where both sublattices are occupied by different magnetic ions exist. One can also observe the stacking of layers, formed either by the $16c$ or $16d$ sites, along the [111] crystallographic direction. This highlights the presence of alternating kagome and triangular planar layers (1.10b). The materials investigated in this work are all following a similar constitution, with a magnetic trivalent rare-earth cation occupying the A site and a non-magnetic tetravalent ion on the B site. As it is the case in this work, the CEF splitting of rare-earth ions occupying the A site is sometimes favorable for spin ice physics, allowing for anisotropic magnetic moments and multipolar degrees of freedom. The network of corner sharing tetrahedra provides a very high degree of geometrical frustration, with the exchange interaction being mediated by the surrounding oxygen ions. Together with the Ising character of the magnetic moments induced by the CEF, they are at the origin of the ice-rule found in spin ices.

The attractiveness of the pyrochlore oxide structure is also justified by its chemical flexibility. Several combinations of A and B atoms can be stabilized without compromising the structural order. This property allowed to study various magnetic ground states by changing the magnetic and/or non-magnetic cations. One can then 'play' with the anisotropy, the exchange interactions, the size of the magnetic moment, etc. However, even a slight deviation from the ideal structure (random or correlated structural disorder) is enough to dramatically affect the magnetic ground state, which often relies on an extremely fine balance between several mechanisms [100].

There exist various types of disorder in the pyrochlore structure. A typical one is the cation site mixing where some A and B cations swap position [99, 101]. This can happen when cations have a similar size. Stuffing can also be present [102], in which case, one of the two cations is in excess with respect to the other one. Disorder linked to different oxidation states is possible, in which case the oxygen stoichiometry might differ from the perfect one [103]. Several elements can occupy the A or the B site as well, leading
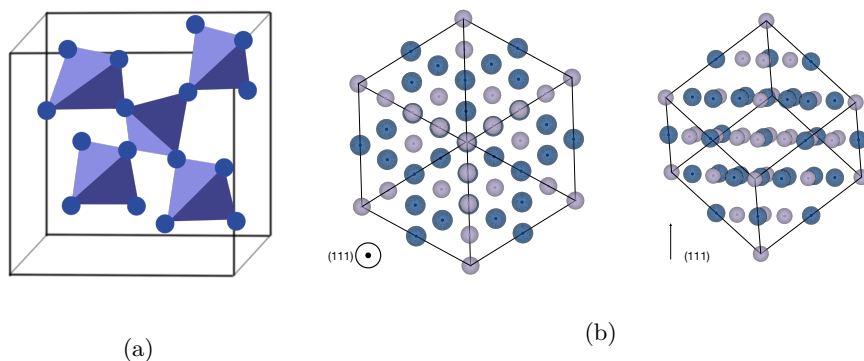
Figure 1.10: (a) Drawing of the network of corner sharing tetrahedra in the pyrochlore structure. Only one type of atom is shown here for visibility sake. (b) Stacking of the A and B ions with respect to the (111) crystallographic direction.

to some interesting phases such as the 'charge ice' [104]. One last kind of disorder we will mention here concerns oxygen disorder. In most pyrochlores, if the cations are well ordered, some oxygen anions might still depart from their ideal crystallographic sites (typically the $48f$) and migrate to another one (the most favorable one usually being the $8a$) [101, 103, 105], which can be interpreted as a sub-lattice transition from the pyrochlore structure to one known as the fluorite structure.

Chapter 2

Experimental Techniques

Preamble

*T*HROUGH this chapter we will, in a brief and general manner, present the various techniques and principles used during this work, going from the synthesis methods to the various macro- and microscopic probes employed and associated analytic tools.

2.1 Solid state synthesis

The solid state synthesis is a commonly used method in material science to prepare (poly-)crystalline samples [106]. It first consists in weighting and mixing of initial chemicals (also called precursors) in the required amount based on the stoichiometry of the desired final products as well as on the different chemical reactions expected to happen during the synthesis. In some cases preheating the precursors can be beneficial in order to get rid of moisture and volatiles molecules.

In a second step, the prepared mixture is subject to a heat treatment. This is the central part of the synthesis which required precise and/or high temperatures, typically ranging from 500° to 2000°. This thermal treatment can be composed a several steps and last between a few hours and a few weeks. Artificial atmospheres can be needed to obtain neutral, reducing or oxidizing conditions. The cooling is also a crucial stage of the thermal treatment, especially when trying to recover single crystals. The whole process may necessitate several iterations with intermediate grinding before obtention of the ideal final product.

2.2 Optical floating zone growth

The optical floating zone technique is a widely spread method to grow single crystals of various materials such as metals and oxides. This techniques has significantly evolved since its creation in the early 1950s, with ever increasing power and sample size [107]. The building blocks of this technique are halogen or xenon lamps and high quality ellipsoidal mirrors. The aim is to focus as much light as possible in a rather small volume (the central focal point of the mirrors), where the temperature will evidently become very high, proportional to the input power of the lamps. Prior to ramping up the power, two ceramic rods of the starting compound(s) are prepared by sintering pressed powder. These rods are vertically mounted in the growth chamber, one on top

of the other, with their tips close to the mirrors focal point. The top and bottom rods are denoted as the feed and seed respectively. The set-up can be seen in 2.1.

The growth starts by melting the tips of the rods in order to connect them and create a liquid interface called the *floating zone*. Once this stage reached and stabilized, the rods are rotated and the *floating zone* is moved along the feed rod (either by moving the mirrors up or pulling both rods down). The rotation rates, rotation directions and speed of growth (vertical translation) are experimentally determined and optimized for each growth. These parameters are crucial as they impact the convection of the liquid in the *floating zone*, which influences the homogeneity of the mix, the shape of the crystallization front as well as the defects creation. While the zone goes up along the feed rod, the liquid at the bottom of the zone, i.e. on the seed rod side, cools down and crystallizes; the nucleation can now start. At first, several small crystallites will be created. If the growth conditions are stable enough, one crystallite will eventually prevail and give rise to a cylindrical-like single crystal.
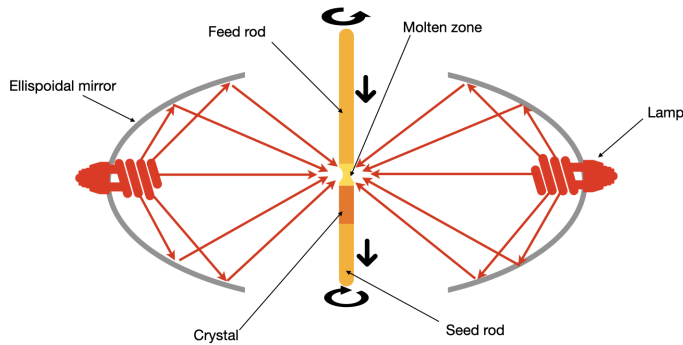
Figure 2.1: Sketch of an optical floating zone growth set-up.

2.3 Magnetometry

The magnetization $\mathbf{M}$ of a sample corresponds to its total magnetic moment per unit of volume i.e. the sum of all the individual magnetic moment from all the magnetic atoms in a given unitary volume. It is usually considered to be a homogeneous vectorial quantity inside a solid. For linear, isotropic and homogeneous (LIH) media, the magnetization $\mathbf{M}$ can be related to the local ($\mathbf{H}_{loc}$) or the external ($\mathbf{H}_{ext}$) magnetic field via the magnetic susceptibility tensors :

$$\boldsymbol{M} = \chi \boldsymbol{H}_{loc} = \chi_{ext} \boldsymbol{H}_{ext} \tag{2.1}$$

with $1/\chi = 1/\chi_{ext} - \mathbf{N}$, where $\mathbf{N}$ is the demagnetizing tensors. For the sake of simplicity, let us assume that the susceptibility is small, the magnetic field weak and all crystallographic direction are equivalent. In this case, one can neglect the demagnetizing tensor and write down the simple expression :

$$\boldsymbol{M} = \chi \boldsymbol{H} \Leftrightarrow \chi = \frac{\|\boldsymbol{M}\|}{\|\boldsymbol{H}\|} \tag{2.2}$$

where the magnetic susceptibility is presently a scalar [29, 30]. The susceptibility can thus be seen as the response of the media to the applied magnetic field, which becomes more complicated when dealing with strong magnetic fields and/or magnetic transitions.

DC-magnetometry refers to measurements where the applied magnetic field is constant while the magnetization is probed. This type of data is typically shown with the magnitude of the sample's magnetization as a function of applied magnetic field (at fixed temperature) or as a function of temperature (at fixed applied magnetic field). Such measurements are valuable tools to investigate magnetic properties, giving access to quantities such as the Curie-Weiss temperature related to the type and strength of the magnetic interaction inside the sample, the Néel temperature indicating a magnetic phase transition, hysteresis loops and anisotropic behaviors.

In addition to a constant magnetic field, an alternating magnetic field can be applied onto the sample (ac-magnetometry), effectively inducing time-dependent magnetic moments in the system and allowing one to separate the real and imaginary parts of the magnetic susceptibility. AC-susceptibility provides useful information about the dynamics of the system, such as magnetic domain wall motion, energy dissipation or freezing [29].

For most devices, the detection principle is based on the Faraday induction law. While the temperature is changed and/or a magnetic field(s) is applied, the sample is driven inside detecting coils, generating an induced fluctuating current in the coil. This current produces variations of the voltage which are proportional to the magnetization of the sample.

2.4 Specific heat

A specific heat measurement demonstrates the capacity of a system to absorb heat. Thermodynamically, it is defined as :

$$C_p = \left(\frac{\partial E}{\partial T}\right)_p = T\left(\frac{\partial S}{\partial T}\right)_p \tag{2.3}$$

This quantity incorporates several well documented contributions from phonons, crystal-electric field levels, hyperfine coupling or magnetic correlations. It is also highly sensitive to phase transitions showing up as sharp features and enables one to determine the order of the transitions.

The existence of several methods and the commercialization of equipment allowing to easily perform such experiments make it one of the most widespread techniques to characterize samples at low temperature. A common way of measuring the specific heat is called the relaxation method and consists of sending a heat pulse to the sample, which is connected to a 'thermal bath' having a constant temperature, and measuring the time required by the sample to relax to the 'bath' temperature. The temperature relaxation follows an exponential law, with its relaxation rate proportional to the specific heat [108] :

$$\Delta T = \Delta T_{max} e^{(-\tau/t)} \quad ; \quad \Delta T_{max} = \frac{P}{K_{eff}} \quad ; \quad \tau = \frac{C_p}{K_{eff}} \tag{2.4}$$

with P the power supplied to heat up the sample and K_{eff} the effective thermal conductance. Such measurements have high accuracy, with samples of only a few milligrams but suffer from long relaxation times at low temperature and becomes experimentally challenging below about 300 mK.

2.5 Neutron scattering

2.5.1 The neutron

Discovered in 1932 by James Chadwick [109], the neutron is an electrically neutral particle of mass close to the proton one ($m_n = 1.0013(...)m_p \approx 935.565 MeV/c^2$). It is unstable against β decay with a mean lifetime of about 880 seconds. Consequently, it is normally only found in atomic nuclei. Within the standard model, the neutron belongs to the baryon's family. It is made up of three quarks (one up and two down), conferring it its neutrality and a yet to be experimental observed electric dipole moment. The neutron possesses a spin $\frac{1}{2}$, which means it has a magnetic moment. As we shall see, the electric neutrality and magnetic moment of the neutron make it a very powerful tool for scattering.

2.5.2 Neutron sources

For material science purposes, one can mention two main sources of neutrons:

- **Nuclear reactors :**
  Nuclear reactors take advantage from the nuclear chain reaction, driven by the fission of so-called nuclear fuels. The chain reaction produces a substantial and continuous amount of neutrons that are then moderated and directed towards different instruments in order to further refine their energy and spatial distribution before hitting a sample.

- **Spallation sources :**
  In such facilities, protons are produced and accelerated towards a target. Entering the target, the proton will collide with a nucleus and transfer some of its energy to some nucleons inside this nucleus. These nucleons will then collide with other nucleons inside the nucleus and with other nuclei. These processes are called intra- and inter-nuclear cascades respectively. Due to their charge, the protons will be stopped within the target, but neutrons can be extracted and used. Spallation sources typically provide a pulsed flux of neutrons, although continuous sources can also use spallation principles (such as the SINQ at the Paul Scherrer Institut).

One can point out the fact that those sources require a very different amount of energy to produce neutrons. Indeed, in the case of reactors, fission requires an energy of a few meV whereas spallation sources need way higher energy (in the order of MeV).

2.5.3 Neutron diffraction

Employing the matter wave theory [110], neutrons can be described as waves. If the associated wavelength is on the same order than the distances separating crystallographic planes of a crystal (or periodic structure), the neutrons, interacting with the atomic nuclei through the *Nuclear Interaction*, will be subject to interference phenomena. Constructive interferences arise when the Bragg's equation is satisfied :

$$n\lambda = 2d_{hkl} \cdot sin(\theta) \tag{2.5}$$

where n is the order of the reflexion, λ the neutron's wavelength, d_{hkl} the inter-planar distance between two successive crystallographic planes denoted by the Miller indices

(h, k, l) and 2θ the angle between incident and diffracted neutron wavevector. The spatial distribution of the Bragg peaks and their intensities are linked to the actual structure of the crystal together with its composition through the concept reciprocal space. Hence, the intensities of the Bragg reflections are proportional to the squared spatial Fourier transform of the neutron nuclear scattering cross section distribution in real space:

$$I(\mathbf{Q}) \propto \sum_n e^{i\mathbf{Q}\mathbf{r}_n} \sum_j \bar{b}_j e^{i\mathbf{Q}\cdot\mathbf{r}_j} \tag{2.6}$$

which can be split into the two terms. The first one is the lattice sum, dictating the spatial distribution of the Bragg reflections as well as systematic extinctions related to the space group symmetry:

$$\sum_n e^{i\mathbf{Q}\mathbf{r}_n} \tag{2.7}$$

running on n unit cells of origin located at $\mathbf{r}_n$. The second term is the nuclear structure factor governing the amplitude of the reflections:

$$F_N(\mathbf{Q}) = \sum_j \bar{b}_j e^{i\mathbf{Q}\cdot\mathbf{r}_j} e^{-W_j} \tag{2.8}$$

with the j atoms of the unit cell, of coherent scattering length $\bar{b}_j$ sitting at position $\mathbf{r}_j$. The Debye-Waller term e^{-W_j} takes into account thermal displacements around the average $\mathbf{r}_j$ positions and typically leads to a decrease of the Bragg peak intensities at high $\mathbf{Q}$. Owing to the erratic dependence of the neutron scattering cross section with the atomic number, neutron diffraction is quite useful to obtain information complementary to the one obtained from x-ray diffraction (see later) about the chemical structure of a compound.

Another virtue of neutron diffraction is its ability to probe magnetism. Due to its spin, the neutron possesses a magnetic moment which can interact with the local magnetic field inside the sample through the dipolar interaction, giving rise to magnetic reflections similar to nuclear Bragg peaks. The mathematical description of this scattering process is similar to the previous case of scattering from nuclei but differs in two notable ways. First, the neutrons are only sensitive to the magnetization components that are perpendicular to the scattering vector $\mathbf{Q}$. This is due to the divergence free condition of an electron's magnetic field ($\nabla \cdot \mathbf{B}_e(\mathbf{r}) = 0$), with which the neutron's magnetic moment ($-\gamma\boldsymbol{\mu}_N$) interacts via a magnetic pseudo-potential $V_m(\mathbf{r}) = -\gamma\boldsymbol{\mu}_N\mathbf{B}_e(\mathbf{r})$. Second, the nuclear structure factor in now replace by the magnetic structure factor, which is the Fourier transform of the magnetization of discrete objects as :

$$\mathbf{M}(\mathbf{Q}) = \sum_j \mathbf{m}_j f_j(Q) e^{i\mathbf{Q}\cdot\mathbf{r}_j} \tag{2.9}$$

where $\mathbf{m}_j$ is the magnetic moment of the atom located at $\mathbf{r}_j$. The f_j term is the magnetic form factor i.e. the Fourier transform of the unpaired electrons spatial density (which are responsible for the magnetism), effectively taking into account the spread of the magnetic moment $\mathbf{m}_j$ around the atom at sitting at $\mathbf{r}_j$. One notable implication of this magnetic form factor is the rapid damping of the magnetic peaks intensity as a function of the scattering vector $\mathbf{Q}$ within the dipole approximation [111, 112] (more on that in section 2.5.7).

Thanks to its neutrality, the neutron is able to penetrate relatively deep inside the samples. However, neutron scattering events are somewhat rare. This is due to the

tiny volume occupied by the scattering centers (atomic nuclei), much smaller that the spacial extension of their electronic clouds. Another reason is the very short range of the Nuclear Interaction compared with the Electrostatic interaction. All together this leads to long acquisition times and a poorer resolution compared to x-ray diffraction, but the possibility to probe larger samples.

2.5.4 Quantum mechanical treatment

The scattering of neutrons from matter is rigorously captured by the concept of double differential cross section. This quantity defines the probability of a neutron, having a given incoming energy, to be scattered by a sample in a given solid angle Ω and with a given outgoing energy E_f. It is expressed as :

$$\frac{\mathrm{d}^2\sigma}{\mathrm{d}\Omega\mathrm{d}E_f} = \frac{k_f}{k_i}\frac{1}{2\pi\hbar}\sum_{j,j'} b_j b_{j'} \int dt \left\langle e^{-i\mathbf{Q}\mathbf{R}_{j'}(0)} e^{i\mathbf{Q}\mathbf{R}_j(t)} \right\rangle e^{-i\omega t} \tag{2.10}$$

with b_j the scattering length of the atom located at $\mathbf{R}_j$ ($\mathbf{R}_j(t)$ being the time-dependent Heisenberg operator) and k_f (k_i) the norm of the outgoing (incoming) neutron wavevector [111]. Here, the bracket notation denotes the thermal averaging over all initial and final states of the system [111, 112]. Focusing on the coherent processes and replacing the scattering lengths by their expected values (thus using the associated coherent cross section), one can rewrite the previous equation as :

$$\left(\frac{\mathrm{d}^2\sigma}{\mathrm{d}\Omega\mathrm{d}E_f}\right)_{coh} = \frac{\sigma_{coh}}{4\pi}\frac{k_f}{k_i} N S(\mathbf{Q},\omega) \tag{2.11}$$

which introduces the coherent scattering function, also called dynamical structure factor $S(\mathbf{Q},\omega)$, defined as :

$$S(\mathbf{Q},\omega) = \frac{1}{2\pi\hbar N} \int dt \sum_{j,j'} \left\langle e^{-i\mathbf{Q}\mathbf{R}_{j'}(0)} e^{-i\mathbf{Q}\mathbf{R}_j(t)} \right\rangle e^{-i\omega t} \tag{2.12}$$

This is the measured quantity during an inelastic neutron spectroscopy experiment. This object contains information about coherent collective processes occurring in the system, such as phonons or other dynamical phenomena involving nuclei [111]. On the other hand, diffraction experiments give access to the differential cross section :

$$\left(\frac{\mathrm{d}\sigma}{\mathrm{d}\Omega}\right)_{coh} = \frac{\sigma_{coh}}{4\pi} N I(\mathbf{Q},0) \tag{2.13}$$

with $I(\mathbf{Q},0)$ the temporal Fourier transform of the dynamical structure factor at $t = 0$, and assuming no energy transfer ($k_i = k_f$, also called the *static approximation*). Similarly, one can express the magnetic scattering of neutrons by [111, 112] :

$$\frac{\mathrm{d}^2\sigma}{\mathrm{d}\Omega\mathrm{d}E_f} = \left(\frac{\gamma r_0}{2\mu_B}\right)^2 \frac{k_f}{k_i} \sum_{\alpha,\beta} \left(\delta_{\alpha\beta} - \frac{Q_\alpha Q_\beta}{\mathbf{Q^2}}\right) \sum_{\lambda_f,\lambda_i} p_{\lambda_i} \left\langle \lambda_i \left| \hat{\mathbf{M}}_\alpha^* \right| \lambda_f \right\rangle \left\langle \lambda_f \left| \hat{\mathbf{M}}_\beta \right| \lambda_i \right\rangle$$

$$\delta(\hbar\omega + E_{\lambda_i} - E_{\lambda_f})$$

$$= \left(\frac{\gamma r_0}{2\mu_B}\right)^2 \frac{k_f}{k_i} S(\mathbf{Q},\omega) \tag{2.14}$$
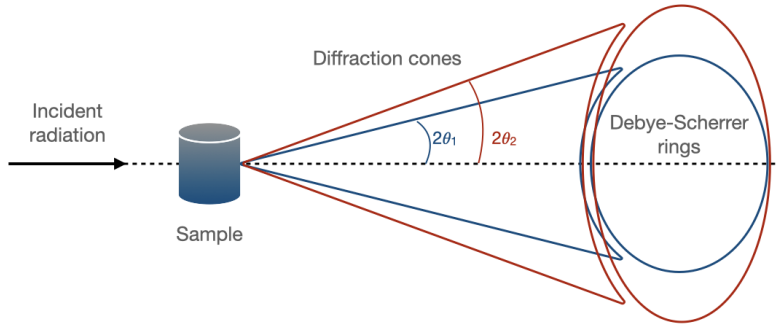
Figure 2.2: Diffraction cones and Debye-Scherrer rings in Debye-Scherrer geometry powder diffraction experiments.

with γ the gyromagnetic ratio (=-1.91), r_0 a constant acting as some kind of magnetic scattering length (interestingly leading to a scattering cross section of a similar size with respect to nuclear ones, producing signals of similar magnitude) and μ_B the Bohr magneton. The indices α and β run over the Cartesian coordinates axis, whereas λ_i and λ_f run over the initial and final states of the scattering system, with p_{λ_i} the thermal population of state λ_i. $\hat{\mathbf{M}}_\alpha$ is the component α of the magnetization operator (see section 2.5.7) and $\hat{\mathbf{M}}_\alpha^*$ its complex conjugate. The term between parentheses in the summation insures that only the components of the magnetic interaction operator perpendicular to the momentum transfer contributes to the intensity. Finally, S($\mathbf{Q}$,ω) is the magnetic dynamical structure factor (also called response function or spin-spin correlation function in some cases), and is obtained in a similar way to the dynamical structure factor introduced previously.

Neutron powder diffraction

For many compounds, single crystals are rather hard or even impossible to grow. In such situation, polycrystalline powder samples are an alternative of choice. Powder samples are composed of numerous but tiny crystallites, randomly orientated. Crystallites with planes (hkl) at an angle θ given by the Bragg's law relative to an incoming beam produce diffraction peaks. Due to the randomness of their orientations and the geometry of the set-up, the signal is diffracted with the shape of a cone called Debye-Scherrer cone. Intercepted by a screen, the diffractogram is composed of so-called Debye-Scherrer rings (figure 2.2). Thanks to the geometry of the experiment, the only degree of freedom is θ which makes powder diffraction a simple and efficient tool to investigate crystal structures.

The Rietveld Method

In 1969, H.M. Rietveld introduced a method to solve crystal structures using powder diffraction data [113]. The main feature of the Rietveld Method is that the integrated intensities of a powder diffraction pattern (and not only the reflection positions) can be extracted and used for the determination of the atomic coordinates. A key ingredient is the description of the profile and its evolution with the scattering angle, necessary for extracting reliable values of the integrated intensities. The idea is the following: in diffraction experiments, measured patterns are often given as a set of angular positions with the corresponding intensities and standard deviations measured $\{\mathrm{T}_i, \mathrm{y}_i, \sigma_i\}_{i=1\ldots n}$.

A profile can be modeled using the calculated counts y_{ci} at the i-th step by summing the contribution from neighboring Bragg reflections plus the background as :

$$y_{c,i} = \sum_{\phi} S_\phi \sum_{\mathbf{h}} I_{\phi,\mathbf{h}} \Omega(T_i - T_{\phi,\mathbf{h}}) + b_i \tag{2.15}$$

ϕ and $\mathbf{h}$ denote the phase and the Bragg reflection respectively. Ω is a reflection profile function that models both instrumental and sample effects, S_ϕ is the scale factor of the phase ϕ and b_i the background at this position. $I_{\phi,\mathbf{h}}$ is the integrated intensity for the phase ϕ and for the Bragg reflections $\mathbf{h}$. It is generally given by the formula:

$$I_{\phi,\mathbf{h}} = \{LAPCF^2\}_{\phi,\mathbf{h}} \tag{2.16}$$

where $L_{\mathbf{h}}$ contains the Lorentz, polarization and multiplicity factors, $A_{\mathbf{h}}$ is the absorption correction, $P_{\mathbf{h}}$ is the preferred orientation function, $C_{\mathbf{h}}$ includes special corrections (non linearity, efficiencies, special absorption corrections, extinction, etc) and $F_{\mathbf{h}}$ is the so-called structure factor. The next step consists in minimizing the weighted squared difference between the observed and calculated patterns. The minimized function is :

$$\chi^2 = \sum_{i=1}^{n} w_i \{y_i - y_{c,i}(\alpha)\}^2 \tag{2.17}$$

where α is the parameter vector containing the parameter to adjust and w_i the inverse of the variance of the intensity observed at position i.

Total scattering and neutron pair distribution function

Total scattering englobes all scattering processes happening between an incident radiation and the probed system. This includes coherent or incoherent as well as static or dynamic processes [114]. The pair distribution function (PDF) is the most widespread method making use of total scattering. It originated in 1927, when the relationship between the real-space atomic pair density and the total scattering in reciprocal space was pointed out [115]. It only experienced a significant growth over the last decades, owing to improved instrumentation and increased computational powder. The PDF is the sine-Fourier transform of the total scattering and provides information about the probability of finding an atom at a given distance from another atom. The PDF analysis allows one to go beyond the determination of the average structure by providing information about short-range correlations (local distortions, chemical short-range order...). This method finds many applications in the fields of amorphous/nano materials as well as disordered crystalline systems. The PDF function $G(r)$ is mathematically defined as :

$$G(r) = \frac{2}{\pi} \int_{Q_{min}}^{Q_{max}} Q[S(Q) - 1]sin(Qr)dQ \tag{2.18}$$

with Q the momentum transfer going from Q_{min} to Q_{max} and $S(Q)$ the total scattering structure factor. However, the produced data typically need further treatment to account for limited Q range, finite Q resolution as well as finite measurement times [116]. There exists several approaches to model PDF data. A first one is to use small-box modeling, where one performs a least squares refinement of an average structure containing up to a few hundred atoms (PDFgui [117] is an example of such modeling software). Going one step further, big-box modeling can be implemented where a few thousand atoms are subject to Reverse Monte Carlo simulation, optimizing several types of data at the same time (for instance RMCProfile [118]). It can sometimes be preferable to

(a)

(b)
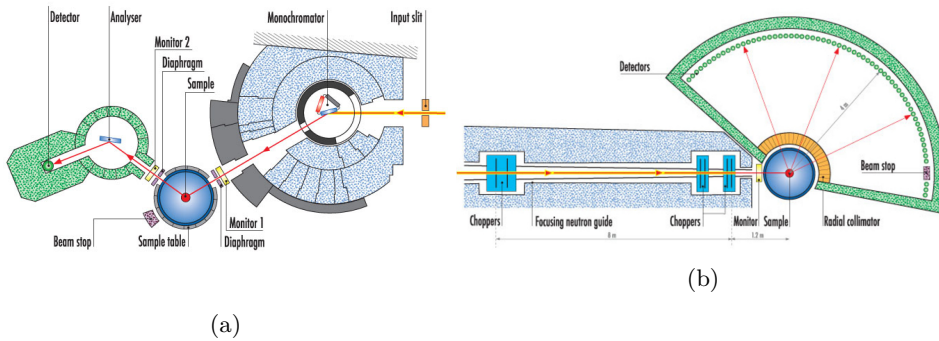
Figure 2.3: (a) Scheme of triple-axis spectrometer and (b) of a neutron time-of-flight spectrometer taken from the IN8 [122] and IN5 [123] webpages respectively.

refine parameters of a higher level (not individual atomic positions), leading to the use of multi-level or complex modeling as well as *ab initio* or force-field based methods.

2.5.5 Inelastic neutron scattering

Inelastic neutron scattering (INS) grants access to information about static as well as dynamic properties of a system. It allows one to measure a quantity called the (magnetic) dynamical structure factor $S(\mathbf{Q}, \omega)$ (defined in section 2.5.4), which describes where atoms/magnetic moments sit and/or how they move. For instance, many-body effects, such as phonons (collective displacement excitations) or magnons (collective magnetic excitations), show up in INS experiments, which can then be modeled owing to the regular arrangements of atoms in crystals. This is qualified as *oscillatory dynamics*. There are several techniques to explore the four-dimensional space formed by $\{\mathbf{Q}, \omega\}$. A first one is triple-axis spectroscopy (TAS) [119], where rotations around three different axis (around a monochromator to select incident energy, around the sample to select a given Q-point and around an analyzer to select final energy, shown in 2.3a) allows to measure points in the $\{\mathbf{Q}, \omega\}$ space. Newly developed multiplexing techniques now allow to measure several points at once using several analyzers covering a given Q-range and multiple final energies [120].

Alternatively, one can use the fact that the neutron energy is related to its speed to discriminate between incident/outgoing energies based on time consideration (see 2.3b). This is called Time-of-flight (TOF) spectroscopy [121]. This typically relies on pulsed neutron beams, and uses detectors covering a large angular range, making it possible to measure a whole slice of $\{\mathbf{Q}, \omega\}$ at once. The two previous techniques are usually exploring the excitations in the meV range.

To explore quasi-elastic processes happening on a μeV scale, the use of higher resolution techniques is required. This is the realm of backscattering [124] and spin-echo [125] spectroscopy. The first makes use of the increase resolution of monochromator and analyzers in backscattering conditions, i.e. for $\theta = \pi/2$. This can be seen from the simplified energy resolution equation:

$$\frac{\Delta E}{E} = \Delta\theta cot\theta \tag{2.19}$$

Due to the required geometry, the 'analyzed' beam has to pass very close tor even through the sample before being detected. Luckily neutron scattering cross sections
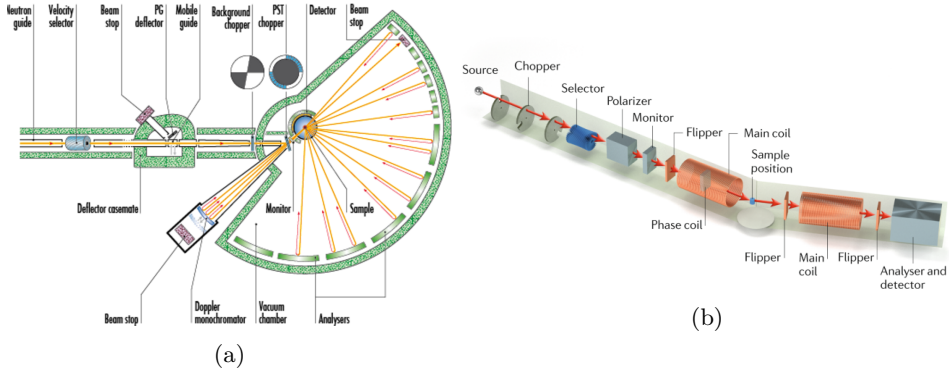
Figure 2.4: (a) Scheme of the IN16b backscattering spectrometer [126] and (b) of a spin echo spectrometer, taken from [127].

make multiple scattering event rare, whereas the neutron absorption cross section can have dramatic effects. Additionally, the incoming beam has to be pulsed in order to differentiate between scattered and analyzed neutrons and neutrons directly scattered by the sample towards the detector, based on time-of-flight considerations. From Fig. 2.4a, one can see that several analyzers can be arranged around the sample, allowing to access the energy transfer at different $\mathbf{Q}$. The analyzers operating at fixed energy, the different energy transfers are accessed by varying the incident energy. To do so, a Doppler effect can be induced by periodically driving the monochromator back and forth to change the energy of a previously monochromatized neutron beam or alternatively, the time-of-flight method can again be used.

The spin echo spectroscopy relies on the Larmor precession of the neutron spin around a magnetic field and polarization analysis to capture the tiniest energy exchanges between the sample and the neutrons. A oversimplified explanation of the principle could be as follows. On its path, a fully polarized neutron beam enters a coil, the neutrons spins process around the magnetic field generated inside the coil before exiting it and scattering with the sample. The neutrons then enter a second coil of the exact same length as the first one but producing the opposite magnetic field, around which the neutrons spins will again experience a Larmor precession, although in opposite direction. The neutrons spins are then analyzed before being detected meaning that only the neutrons having the same polarization as the initial beam will be counted. If neutrons scatter elastically with the sample, then their speed through both coils have been the same and the two precessions experienced cancel out resulting in neutrons having the exact same polarization as the initial one. Now if some neutrons exchanged energy with the sample, i.e. scatter inelastically, their speeds in the two coils are different, the precessions experienced do not cancel out anymore and these neutrons will be rejected by the polarization analyzer. The detected beam will thus be of lower intensity and said to be depolarized. Due to the high frequency of the Larmor precession, this technique is very sensitive and allows to measured very small energy transfers. Real instruments rely on more complicated set-ups involving spin flippers and spin rotators due to practical and instrumental considerations (Fig. 2.4b).

2.5.6 Inelastic neutron spectroscopy and crystal-electric field

When magnetically interacting with magnetic ions, neutrons are able to exchange energy. Through this energy exchange, the neutrons can induce transitions between

(partially) occupied crystal-electric field levels to (partially) unoccupied ones [112]. The obtained neutron spectrum can thus be described by the magnetic dynamical structure factor S($\mathbf{Q}$,ω), which can be expressed as :

$$S(\mathbf{Q}, \omega) \propto \sum_i p_i \sum_f |\langle \Gamma_f | \hat{\mathbf{M}}_\perp(\mathbf{Q}) | \Gamma_i \rangle|^2 \delta(\hbar\omega + E_{\lambda_i} - E_{\lambda_f}) \tag{2.20}$$

with E_i and E_f the energies of the initial state Γ_i (with thermal probability distribution p_i) and final state Γ_f, respectively. $\mathbf{M}_\perp(\mathbf{Q})$ is the magnetization vector (or more precisely the magnetic interaction operator) perpendicular to the momentum transfer $\mathbf{Q}$. The dipolar approximation (see section 2.5.7) is typically correct and allows one to write :

$$\hat{\mathbf{M}}_\perp(\mathbf{Q}) = f(Q) g_J \hat{J}_\perp \tag{2.21}$$

where $\mathbf{J}_\perp$ is the total angular momentum perpendicular to $\mathbf{Q}$, g_J is the landé g factor and $f(Q)$ the dipolar form factor. From the above equations and the absence of momentum-energy relation, one expects the CEF transitions to be dispersion-less and their intensity to follow a dipolar magnetic form factor i.e. to decrease with increasing momentum transfer. Due to sample and/or time restrictions, CEF measurements are often performed on powder samples yielding S(Q,ω) maps where the CEF levels appear as excitations of constant energy with high intensity at low Q. This momentum dependence also allows to distinguish between CEF excitations and phonons, the latter following a different form factor with high intensity at high momentum transfer. However, CEF measurements on single-crystals provides more information and is sometimes required to study complex mechanisms such as spin-lattice coupling where hybridization of CEF levels and phonons can happen.

2.5.7 Neutron scattering from multipoles

As introduced earlier, neutrons can interact with the magnetic moments produced by electrons via a magnetic pseudo-potential $\hat{V}_m(\mathbf{r}) = -\gamma\mu_N\hat{\sigma}B_e(\mathbf{r})$, where $\mathbf{B}_e(\mathbf{r})$ is the magnetic field produced by the an electron and using operator noations. This magnetic field has two origins: the spin of electrons and their orbital angular momentum which are given by the $\hat{S}$ and $\hat{L}$ operators within the Russell-Saunders coupling scheme [112]. First, one can express this potential with the spin and momentum operators of the electrons and write the magnetic dynamical structure factor $S(\mathbf{Q}, \omega)$ as a function of a magnetic interaction operators $\hat{\mathbf{M}}_\perp$ defined as:

$$\hat{\mathbf{M}}_\perp = \frac{1}{\mathbf{Q^2}} \sum_i exp(i\mathbf{Qr})(\mathbf{Q} \times \hat{S}_i \times \mathbf{Q} - \frac{i}{\hbar}\mathbf{Q} \times \hat{p}_i) \tag{2.22}$$

In order to exactly express this operator in terms of quantum numbers, it can be convenient to work with the magnetization operator $\hat{\mathbf{M}}$, related to $\hat{\mathbf{M}}_\perp$ through:

$$\hat{\mathbf{M}}_\perp = \mathbf{Q} \times \hat{\mathbf{M}} \times \mathbf{Q} \tag{2.23}$$

This magnetization operator evaluates the spin contribution to the magnetization (which is sometimes enough on its own) but more importantly evaluates the orbital contribution. The former has to take into account the shape and extend of the orbitals. The development of the magnetization operator is rather heavy [112], but it can be shown that its components are given by:

$$
\hat{M}^x_{m,m'} = \sum_{p=1,3,5,7,\ldots} \sum_{q=-p,..,p} \sqrt{4\pi}\, \frac{Z_p}{p}\, (-1)^{J-m'}\, \frac{\begin{pmatrix} p & J & J \\ -q & m' & -m \end{pmatrix}}{\begin{pmatrix} p & J & J \\ 0 & J & -J \end{pmatrix}}
$$
$$
\times \frac{Y_{p-1,q+1}(\mathbf{Q})\sqrt{(p-q)(p-q-1)} - Y_{p-1,q-1}(\mathbf{Q})\sqrt{(p+q)(p+q-1)}}{2}
$$

$$
\hat{M}^y_{m,m'} = \sum_{p=1,3,5,7,\ldots} \sum_{q=-p,..,p} -i\,\sqrt{4\pi}\, \frac{Z_p}{p}\, (-1)^{J-m'}\, \frac{\begin{pmatrix} p & J & J \\ -q & m' & -m \end{pmatrix}}{\begin{pmatrix} p & J & J \\ 0 & J & -J \end{pmatrix}}
$$
$$
\times \frac{\left(Y_{p-1,q+1}(\mathbf{Q})\sqrt{(p-q)(p-q-1)} + Y_{p-1,q-1}(\mathbf{Q})\sqrt{(p+q)(p+q-1)}\right)}{2}
$$

$$
\hat{M}^z_{m,m'} = \sum_{p=1,3,5,7,\ldots} \sum_{q=-p,..,p} \sqrt{4\pi}\, \frac{Z_p}{p}\, (-1)^{J-m'}\, \frac{\begin{pmatrix} p & J & J \\ -q & m' & -m \end{pmatrix}}{\begin{pmatrix} p & J & J \\ 0 & J & -J \end{pmatrix}}
$$
$$
\times Y_{p-1,q}(\mathbf{Q})\sqrt{(p-q)(p+q)}
$$

where J is the total angular momentum and m/m' run on the corresponding $2J+1$ values (two are needed as the $\hat{M}$ above operate on the $2J+1$ space). p runs over the odd integer and corresponds to the rank of the multipoles considered in the calculations (1 being for a dipole, 3 the octupole, etc.). Even integer lead to zero, illustrating the fact that neutrons are not sensitive to quadrupoles (rank 2) for instance. The Z_p are given in tables using c_p coefficients and $\langle j_p \rangle$ radial functions :

$$
Z_p = c_{p,1}\,\langle j_{p-1}\rangle \;+\; c_{p,2}\,\langle j_{p+1}\rangle
$$

with

$$
\langle j_p \rangle = \int_0^\infty dr\; j_p(Q\,r) r^2 f(r)^2
$$

where $f(r)$ is the radial part of the electrons wavefunction.

The quantities $\begin{pmatrix} p & J & J \\ -q & m' & -m \end{pmatrix}$ are 3j symbols related to Clebsch-Gordan coefficients and the $Y_{l,m}$ are the Laplace spherical harmonics made up of the associated Legendre polynomials.

At the lowest order in the above expansion (p = 1), one finds himself within so called 'dipole approximation'. In this case, the magnetization operator $\hat{\mathbf{M}}$ simplifies tremendously and can be expressed as :

$$
\hat{\mathbf{M}}(\mathbf{Q}) = f(Q)g_J\hat{J} \tag{2.24}
$$

where g_J is the Landé g-factor and $f(Q)$ is the previously mentioned magnetic form factor obtained by evaluating the Z_p function for p = 1. The magnetic form factor thus corresponds to the Fourier transform of the density of unpaired electrons assuming the electrons evolved are in dipolar-like orbitals. A direct consequence of the magnetic form factor is the momentum transfer dependence of magnetic signals which are quickly dumped as $\mathbf{Q}$ increases. This is readily seen through neutron scattering measurements. Interestingly, the dipole approximation is sometimes inappropriate, requiring further

terms in the magnetization operator's expansion. For instance, magnetic octupoles give a very different contribution in neutron experiments. This stems from the octupolar form factor, which is broader and peaked at higher momentum transfer compared to the dipolar one.

2.6 X-ray techniques

2.6.1 The X-rays

X-rays belong to the electromagnetic spectrum and is thus qualified as light. it corresponds to photons of wavelengths ranging from approximatively 10 pm to 10 nm. This radiation was discovered back in 1895 by a german scientist named W. C. Röntgen and nowadays finds a multitude of applications in medicine, security, imaging and research. The x-rays interact with matter under several processes, of which the most commonly used for material science are the Thomson scattering (responsible for diffraction) and photo-absorption/emission (used in most x-ray spectroscopy techniques).

2.6.2 X-ray sources

We will restrict ourselves to sources commonly used for material science and neglect other natural sources, such as stars and other cosmic objects.

- **X-ray tubes radiation :**
  The traditional sources of X-ray in laboratories are the X-ray tubes. The working principle is to produce and accelerate electrons towards a metallic anode (see 2.5a). The spectrum of the generated radiation is composed of two parts (figure 2.7b). The first is known as *Bremsstrahlung*. It covers a large energy range and is due to the significant deceleration of the electrons when entering the anode. The second takes the shape of rather sharp emission peaks, with energies corresponding to the K_α and K_β edges (figure 2.5b) of the metal from which the anode is made of. This mechanism is well understood and can be sketched as follow. Incoming electrons will kick out some electrons occupying the orbitals of the atoms making up the anode. When the ejected electron belong to the innermost electronic shell, the hole created can be filled by an electron of another shell, emitting a photon of energy corresponding to the energy difference between the two shells. Once generated by the anode, the X-rays are focused towards the samples and then detected. These instruments generally work in a reflective geometry, also called Bragg-Brentano (Fig. 2.7a), due to the high absorption x-rays by heavy elements. A filter is also used to suppress the K_β line, allowing one to use the K_α lines to perform the diffraction experiments (figure 2.7b).

- **Synchrotron radiation :**
  First considered as an unwanted parasitic radiation in colliders, the synchrotron light is one of the most fruitful tools used by scientists all around the globe and in many fields of science. Synchrotron radiation is nowadays produced in two main types of instruments: synchrotron facilities and Free Electron Lasers (see figure 2.6). In both cases, the idea is to force electrons traveling at a velocity close to light speed onto a curved path (either circular or oscillating). Subject to such conditions, the electrons emit a very powerful radiation covering a large range of wavelength including UV and X-rays. This radiation is subsequently tailored to reach impressive brilliance and coherence, which are crucial for challenging experiments.
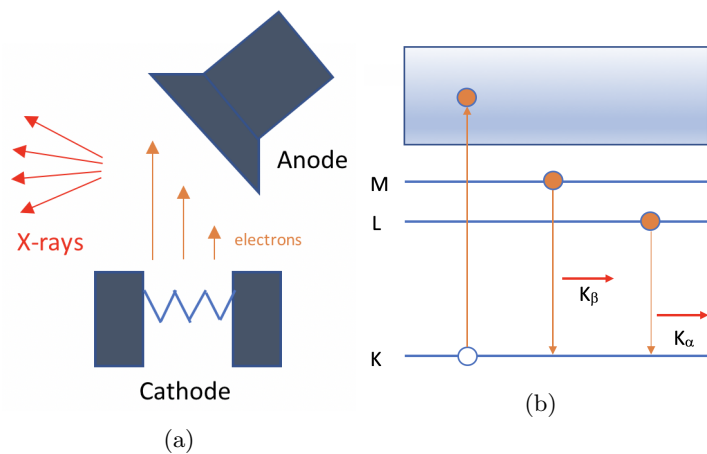
Figure 2.5: (a) Scheme of a x-ray tube. (b) K_α and K_β lines.
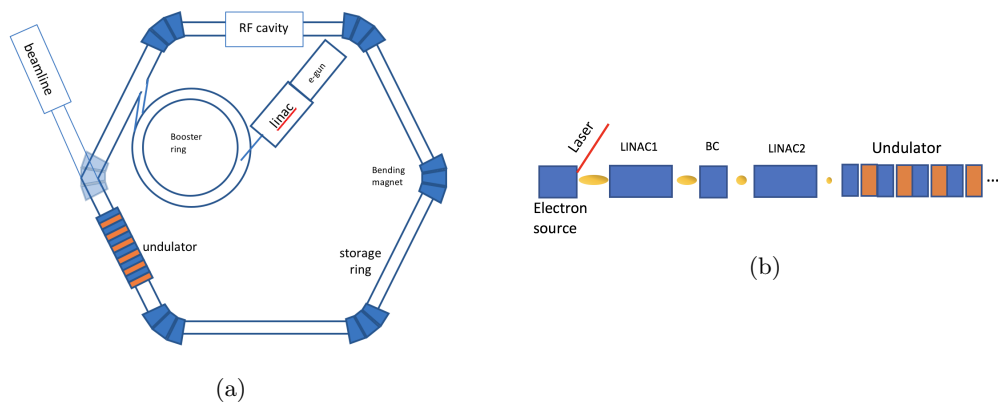
Figure 2.6: (a) Simplified scheme of a Synchrotron. (b) Working principle of a Free Electron Laser, BC for Bunch Compression.
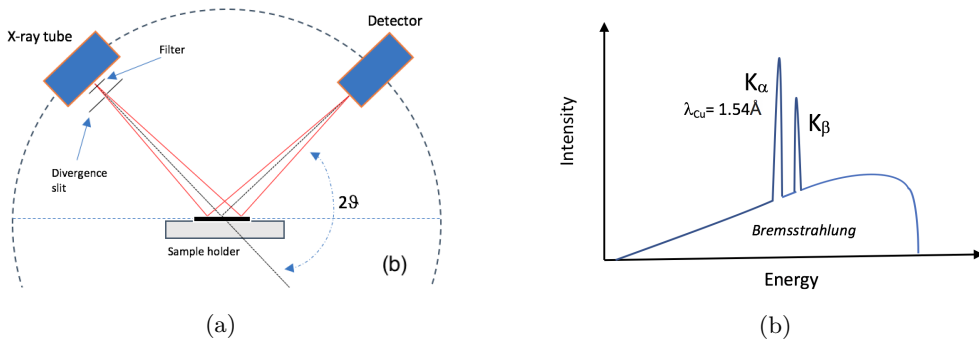
Figure 2.7: (a) Scheme of the Bragg-Brentano geometry. (b) Radiation spectrum from a copper anode.

2.6.3 X-ray diffraction

X-ray diffraction is a non-destructive technique used to solve crystal structures. Interacting elastically with the electrons through the Thomson effect, the X-rays are subject to interferences reflecting the density of electrons inside the crystal. The experimental principle is then very similar to the diffraction of neutrons described earlier (2.5.3). The penetration of the X-rays in the samples is limited (on the order of several tens of micrometers) as it is strongly subject to absorption. It is often complementary with neutron diffraction as X-rays benefit from intense flux, high resolution and a wide range of wavelength. The scattering cross section is in this case related to the number of electrons held by the scatterer, providing a different elemental contrast than neutrons. In addition, the incident energy can be tuned to correspond to the absorption edge of some scatterer contained in the sample under investigation (more on that in the next section), allowing to modify the 'contrast' between the different elements.

2.6.4 X-ray absorption spectroscopy

X-ray absorption spectroscopy or XAS relies on the drop of the x-ray beam intensity as it is passing through a medium. As the simplest case, this can be assimilated with the Lambert-Beer law :

$$I(d) = I_0 e^{-\mu d} \qquad (2.25)$$

where I_0 is the intensity of the incoming radiation prior to entering the medium, d the depth in the medium and μ the absorption of the medium. This μ is actually the quantity withholding valuable information about the system. It approximatively varies like the inverse of the incident radiation's energy to the power three. This dependence is interrupted by step-like features when the energy matches that of an ionization potential of the target medium. Such feature is call an *absorption edge* and is element and/or material specific (see example for cerium in section 2.8). Studying the position and structure of the absorption spectrum around these absorption edges (called XANES or NEXAFS) provides valuable insight into the system such as the oxidation state of the present elements, the orientation of their electronic orbitals, their electronic environment (as the crystal-electric field) or their surrounding (uncovering local structural disorder using the EXAFS signal for instance).

In addition to the absorption spectrum, other related events such as fluorescence or photoemission also contain information about the sample. For example, photoemission
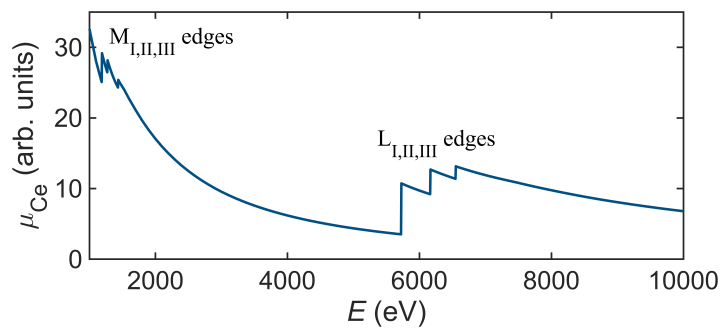
Figure 2.8: X-ray absorption spectrum of cerium.

spectroscopy allows one to resolve the electronic band structure of a material, which is very useful in many areas of material science.

Chapter 3

Cerium based Spin Liquids

Preamble

$\mathcal{W}$HILE multipoles have been proposed as a source of transverse terms in models dominated by couplings among magnetic dipoles [19], correlated phases of higher-rank multipoles have also been conjectured for pyrochlores where the trivalent rare earth has a dipole-octupole ground-state doublet [50, 51]. Such single-ion ground states are notably possible in pyrochlore materials based on cerium, samarium or neodymuim [50, 51, 128]. As we shall see, cerium based pyrochlores seem to readily stabilize a dipole-octupole ground-state doublet, owing to their crystal-electric field environment. Interestingly, these compounds are thought to form a peculiar $U(1)$ quantum spin liquid state where couplings between the octupolar components of the pseudo-spins dominate, while couplings between the dipole components play the role of transverse terms, resulting in a QSI based on a manifold of octupole ice configurations [50, 51]. In this chapter, we will present results on two of these compounds, namely $Ce_2Sn_2O_7$ and $Ce_2Hf_2O_7$, starting by discussing their synthesis as well as their structural properties. We will then show that, despite small structural differences, both systems display similar single-ion properties. Finally, we will explore their low temperature magnetic correlations, demonstrating the presence of similar magnetic ground states, although governed by different energy scales.

3.1   Synthesis and structural properties

Large amounts of $Ce_2Sn_2O_7$ can be obtained in powder form making use of the solid state oxido-reductive reaction between CeO_2 and SnO_2, allowing to produce a high quality sample where all cerium are trivalent to a good approximation. This was confirmed by diffraction and thermogravimetric analysis [129, 130] (Fig. 3.1). Unfortunately, the high vapor pressure of Sn makes it difficult to prepare large single crystal of $Ce_2Sn_2O_7$, limiting the present study to powder samples. X-ray and neutron powder diffraction (HRPT, SINQ) as well as pair distribution function (GEM, ISIS) experiments confirm a well ordered pyrochlore structure (space group Fd$\bar{3}$m), with a lattice parameter of 10.6517 Å at room temperature and no sign of structural disorder [130] (Fig. 3.1).

Polycrystalline samples of $Ce_2Hf_2O_7$ were prepared via solid-state synthesis, using stoichiometric amounts of pre-annealed CeO_2 and HfO_2. The mixture was thoroughly ground and subject to several cycles of sintering and grinding, until the observation

(a)

(b)

(c)
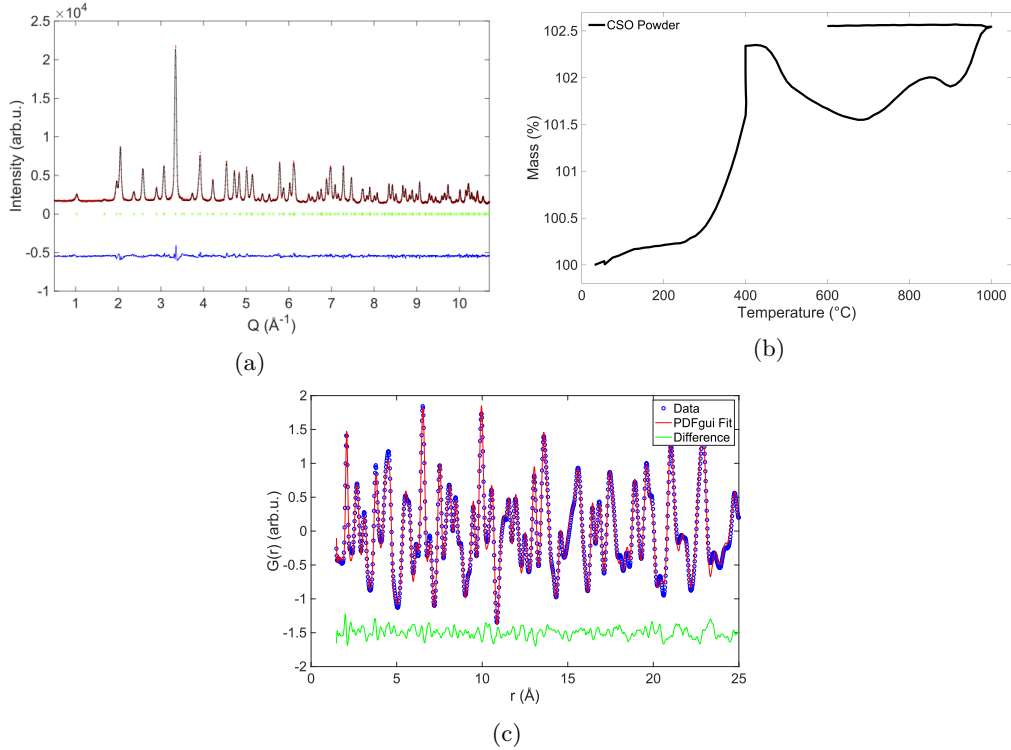
Figure 3.1: (**a**) Rietveld refinement of neutron diffraction patterns of $Ce_2Sn_2O_7$ measured on the constant-wavelength diffractometer HRPT at 300 K. Data (red points), calculated pattern (black line), Bragg positions (green markers) and difference pattern (blue line) are shown.(**b**)Thermogravimetric measurement of our $Ce_2Hf_2O_7$ samples. The obtained mass gain is used to estimate the exact oxygen content according to the reaction $Ce_2Sn_2O_{7+\delta} + (1 - \delta)/2 \ O_2 \rightarrow 2 \ CeO_2 + 2 \ SnO_2$. X-ray diffraction of the product of the reaction corroborates the above chemical equation. (**c**) Experimental Pair Distribution Function (PDF) of $Ce_2Sn_2O_7$ (blue open circles) obtained from all detector banks on GEM. The red line is a fit of the PDF using the PDFGui program, and the green line shows the difference between the data and the calculation for a perfect pyrochlore structure.

of a single pyrochlore phase in x-ray diffraction patterns. Sintering was carried out at 1600 ℃ in a reductive atmosphere (He/H$_2$, 10% H$_2$) for 150 hours at each cycle. A special alumina furnace was used to carry out these sinterings, allowing to reach 1800 ℃ in clean atmospheric conditions. Part of the $Ce_2Hf_2O_7$ powder was subsequently used as starting material for single-crystal growth using the optical floating zone technique. The growth was performed using a high pressure, high temperature optical-image travelling solvent floating zone furnace. The crystallinity and the phase purity of the as-grown single-crystal (Fig 3.2) were checked using both x-ray Laue camera (Fig 3.2) and x-ray diffraction on a powdered fragment.

X-ray powder diffraction, on the starting $Ce_2Hf_2O_7$ powder, reflected a well ordered $Fd\bar{3}m$ pyrochlore phase with a lattice parameter of 10.71680(7) Å at room temperature. This value is slightly smaller than expected, based on the relationship between the lattice parameter of rare-earth pyrohafnates [131] and the ionic radii of trivalent rare-earth ions [132] (see Fig. 3.3). A deviation can be explained by the presence of non-

(a)

(b)

(c)
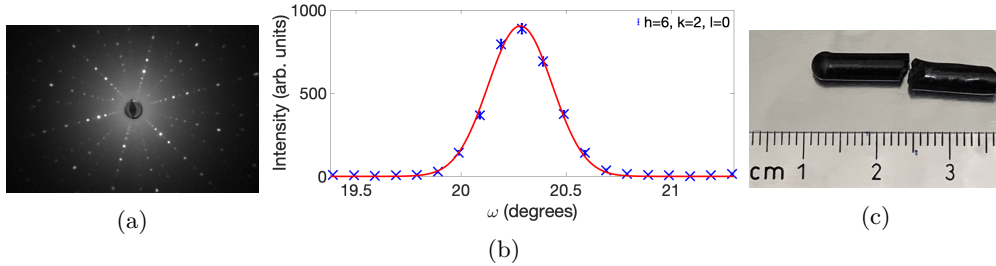
Figure 3.2: (**a**) X-ray Laue pattern from our $Ce_2Hf_2O_7$ single-crystal. (**b**) Rocking curve over the (620) reflection measured using the single-crystal neutron diffractometer Zebra. (**c**) Single-crystal of $Ce_2Hf_2O_7$ used for bulk and neutron diffraction experiments.

magnetic Ce^{4+} ions, which have a smaller ionic radius compared to Ce^{3+}. A ground fragment of single-crystal was subject to the same analysis, yielding a further reduced lattice parameter of 10.69875(3) Å, suggesting a higher concentration of defects. In both cases, laboratory x-ray diffraction could not resolve the excess of oxygen, thus motivating the use of other techniques, as described hereafter. Rietveld refinement of the $Ce_2Hf_2O_7$ neutron powder diffraction pattern, collected on HRPT (SINQ)) at 1.5 K (Fig. 3.3), yielded a typical pyrochlore structure [18, 99] with the introduction of an additional small amount of oxygen atoms on the normally empty (8a) crystallographic site (Appendix, Table 4). The presence of such defects confirms the deviation from the nominal oxygen stoichiometry and implies that some cerium ions are indeed in a nonmagnetic tetravalent state. From Rietveld refinement, the amount of Ce^{4+} defects is estimated to be around 6±1%. Other techniques were employed to improve our estimate of the defect density.
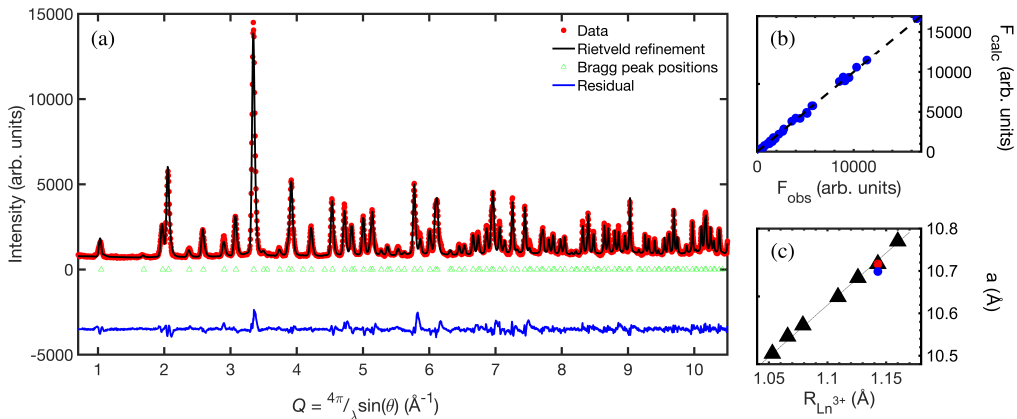
Figure 3.3: (**a**) Rietveld refinement of high-resolution neutron diffraction pattern collected on the starting powder at 1.5 K. The model used corresponds to a perfect pyrochlore structure with additional oxygen ions located at the 8a crystallographic site (Table 4). (**b**) Nuclear refinement of our single-crystal neutron diffraction data using a similar model (Table 5). (**c**) Relationship between the lattice parameter of rare-earth pyrohafnates and the ionic radii of trivalent rare-earth ions. Our values of the lattice parameter for the single-crystal and the starting powder are highlighted in red and blue, respectively. Only the compounds crystallizing in a pyrochlore structure were included.

The raw $Ce_2Hf_2O_7$ powder was subject to thermogravimetry analysis following a similar procedure as for $Ce_2Sn_2O_7$ in [133]. The variation of sample weight is directly related to changes in oxygen stoichiometry, thus providing a robust estimate of the tetravalent cerium concentration. In our powder sample, the oxygen stoichiometry was found to be 7.027 ± 0.007 (see Fig. 3.4a), which translates into 2.7 ± 0.7 % of Ce^{4+} defects.
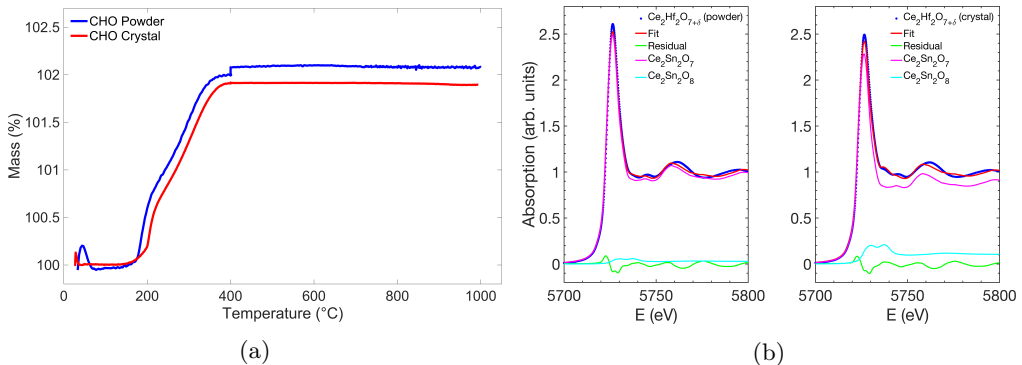
Figure 3.4: (**a**) Thermogravimetric measurement of our $Ce_2Hf_2O_7$ samples. The obtained mass gain is used to estimate the exact oxygen content according to the reaction $Ce_2Hf_2O_{7+\delta} + (1 - \delta)/2\ O_2 \rightarrow 2\ CeO_2 + 2\ HfO_2$. X-ray diffraction of the product of the reaction corroborates the above chemical equation. (**b**) X-ray absorption spectra of $Ce_2Hf_2O_7$ at the Ce L3-edge measured on samples of starting powder (**a**) and powdered crystal (**b**). The signal was fitted using a linear combination of $Ce_2Sn_2O_7$ (in pink) and $Ce_2Sn_2O_8$ (in cyan) spectra measured in identical conditions. The difference in height of the absorption edge is presumably coming from grain size effects.

Finally, we have directly confirmed the deviation in cerium oxidation state using XAS. To provide a meaningful analysis using this technique, we first measured samples that can be used as references. The isostructural $Ce_2Sn_2O_7$ was obviously an appropriate choice to evaluate the amount of trivalent cerium ions. On the other hand, we use $Ce_2Sn_2O_8$, where the cerium are all tetravalent and experience a cubic O_h point group symmetry, as a reference to evaluate the amount of Ce^{4+}. The $Ce_2Hf_2O_7$ x-ray absorption spectrum is well reproduced using a linear combination of the $Ce_2Sn_2O_7$ and $Ce_2Sn_2O_8$ spectra (Fig. 3.4b). The best fit for our $Ce_2Hf_2O_7$ powders is reached with a 3 ± 0.3 % contribution of $Ce_2Sn_2O_8$, which is in good agreement with our quantification of the defects obtained from thermogravimetry. We note that measurements performed on samples stored in helium and in air lead to very similar results, indicating that the compound is stable in air, at least on the scale of several months. The latter significantly differs from observations made on $Ce_2Zr_2O_7$, by other groups [134] as well as by us, that the lattice constant and colour of cerium zirconate show substantial variations after exposure to air of only a few days. This may indicate important differences in the reactivity of the Ce^{3+} zirconates and hafnates, which is not anticipated since tetravalent Hf and Zr are in principle very similar, both sterically and chemically.

We now turn to estimates of the stoichiometry in single-crystals. Using single-crystal neutron diffraction data, refinements yielded an anticipated higher amount of defects (7 ± 2%, Appendix 6.4, Table 5), most probably stabilized during the high-temperature growth. The thermogravimetric analysis was also performed on a ground piece of the $Ce_2Hf_2O_7$ crystal. In this case, 10.54 ± 1% of the cerium cations appear to be in a

tetravalent oxidation state. XAS measurements also corroborate this result with an estimated $11 \pm 0.3\%$ of Ce^{4+} defects. A summary of the results obtained using different techniques can be found in Table 3.1.

	Starting powder	Single-crystal
Neutron diffraction	$6 \pm 1\%$	$7 \pm 2\%$
Thermogravimetry	$2.7 \pm 0.7\%$	$10.5 \pm 1\%$
XAS	$3 \pm 0.3\%$	$11 \pm 0.3\%$

Table 3.1: Estimated amount of oxygen defects obtained from different methods on both powder and single-crystal samples of $Ce_2Hf_2O_7$.

3.2 Single-ion properties

In the investigated compounds, the magnetism is produced by Ce^{3+}, which possesses a single $4f$ electron. This single electron can thus be described using the quantum numbers S = 1/2, L = 3 which, based on Hund's rules, lead to a six times degenerated $^2F_{5/2}$ ground state and an eight time degenerated $^2F_{7/2}$ excited state (using the spectroscopic notation $^{2S+1}L_J$). The trigonal (D_{3d}) crystal-electric field experienced by the cerium in the pyrochlore structure is then responsible for the splitting of the ground multiplet into three doublets and of the excited multiplet into 4 doublets (see 1.1.2 and Fig. 1.2). The degeneracy of these seven energy levels is protected due to the Kramers nature of Ce^{3+} and thus no further degeneracy lifting can happen in absence of magnetic field. As mentioned in 1.1.2, INS can be and was used to measure these energy levels and determine the single ion ground state wavefunction, as described hereafter.

3.2.1 Crystal-electric field in $Ce_2Hf_2O_7$

We start with INS data measured on MAPS (ISIS) probing the crystal-electric field splitting of Ce^{3+} in powders of $Ce_2Hf_2O_7$ at $T = 7$ K (Fig. 3.5a-b). Phonon contributions were removed by subtraction of $La_2Hf_2O_7$ data collected in an identical configuration. The resulting data were corrected considering the Ce^{3+} magnetic form factor so as to evaluate the intensity at $\mathbf{Q} = 0$. Using an incident energy of 200 meV, five CEF excited states could be observed, as can be seen on Fig. 3.5c. The two main peaks, located at 56 meV and 110 meV, are representative of the transitions from the ground-state doublet to the two excited Kramers doublets of the $J = 5/2$ multiplet. A third excitation visible around 100 meV is reminiscent of the additional CEF excitation observed in $Ce_2Zr_2O_7$ [134] and is likely to stem from hybridization of the CEF with a phonon. Hybridized excitations of mixed magnetic and phononic character were observed in other pyrochlore magnets, such as in $Pr_2Zr_2O_7$ [135], $Tb_2Ti_2O_7$ [48] as well as other Ce^{3+}-based compounds [136, 137, 138]. From their weaker spectral weight, the two remaining excitations (around 47 meV and 90 meV) are most likely due to a second CEF environment related to interstitial oxygen atoms (O"($8a$)) and tetravalent cerium ions. The estimated 3 % of defects translates into 18 % of the cerium sites experiencing a disturbed crystallographic environment. This effectively lowers the symmetry with respect to the usual D_{3d} point group symmetry at the pyrochlore's A site, down to the C_1 point group symmetry where all CEF parameters are allowed. However, a symmetry lowering does not lift any degeneracy as the three doublet of the $J = 5/2$ multiplet of this Kramers ion are already maximally separated. Another measurement with incident energy of 500 meV allowed the observation of an additional excitation

located at 264 meV (Fig. 3.5d)), explained by a transition from the ground state to the first level of the $J = 7/2$ multiplet.
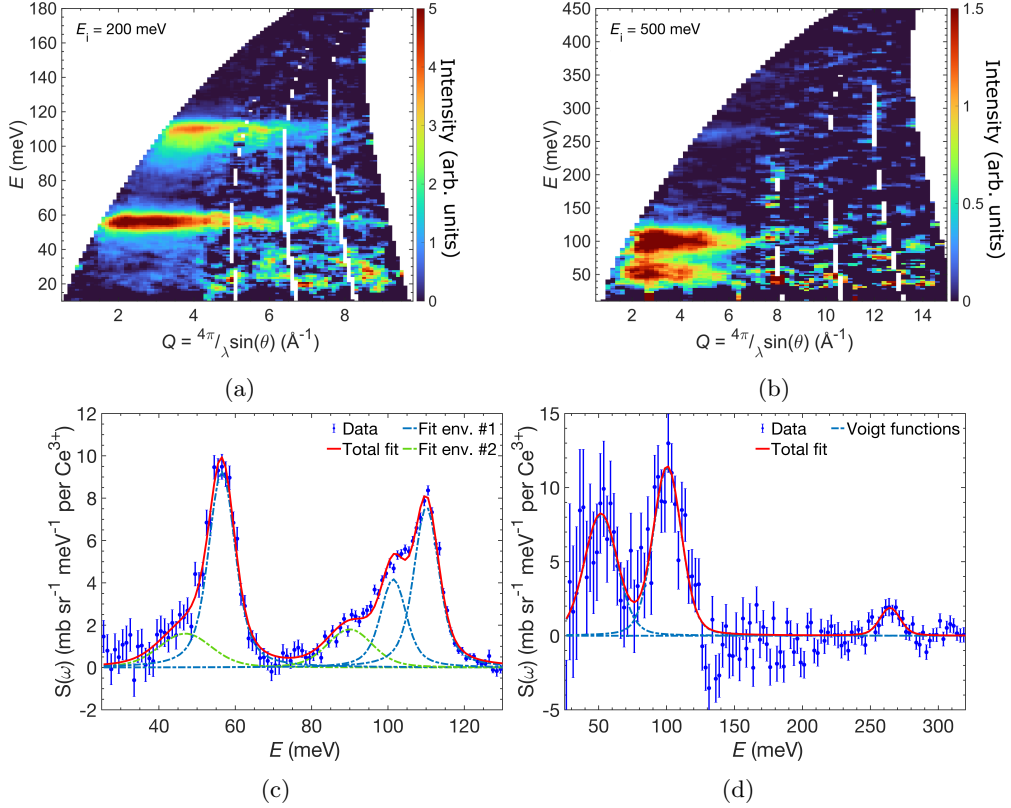
Figure 3.5: (**a,b**) Inelastic scattering neutron spectra measured using incident energies of 200 meV and 500 meV, respectively. Phonon contributions were accounted for by subtraction of the spectrum measured on the isostructural $La_2Hf_2O_7$ compound. (**c,d**) Constant-Q cut in the INS data above, corrected for magnetic form factor and integrated between 3.2 Å^{-1} and 4.5 Å^{-1} ($E_i = 200$ meV) and 3.45 Å^{-1} and 7.4 Å^{-1} ($E_i = 500$ meV). Voigt functions were used to fit the observed excitations, as described in the text. Only one set of excitations could be identified in the high energy data due to the coarser resolution.

The three major CEF excitations were fitted using Voigt functions, restricting their gaussian widths to the instrumental resolution (Fig. 3.5c). The two weaker excitations, stemming from the presence of impurities, could be fitted using the same function but with larger widths (Fig. 3.5d). This can be justified by a probable distribution of defective environments. The measured spectrum was then deconvoluted into two artificial spectra (Fig. 3.6a-b), corresponding to the perfect and defective CEF environments, respectively. The first one contains the two main peaks at 56 and 110 meV. The fitted Voigt of the extra peak at 100 meV was also added on top of the excitation around 110 meV to account for the observed splitting. However, its width was changed to match the experimental resolution at the corresponding energy. The second spectrum solely contains the weaker excitations attributed to cerium ions experiencing a defective environment. The two decomposed spectra were subsequently used to fit the crystal field

parameters using the PyCrystalField [139] package. To do so, we defined a model with two crystal field Hamiltonians, both using the whole set of 14 intermediate-coupling basis states of the $J = 5/2$ and $7/2$ multiplets [38]. This is particularly important for light rare-earth elements where the strength of the spin-orbit coupling competes with the crystal field. The first Hamiltonian is representative of Ce^{3+} in a perfect D_{3d} symmetry, thus incorporating only six non-zero CEF parameters (B_2^0, B_4^0, B_4^3, B_6^0, B_6^3 and B_6^6). The second one includes Ce^{4+} defects in the second coordination sphere of the Ce^{3+} ions as well as interstitial oxygens ($8a$), allowing all CEF parameters to be non-zero. We began by fitting the CEF parameters to the observed transition energies in order to get reasonable starting values for the subsequent steps. We then included the intensities of these excitations as displayed in Fig. 3.6a. At this stage, the excitation observed at around 260 meV was not used in the fitting routine as it is not possible to separate the contributions from either the perfect or defective CEF environments. Nonetheless, both the positions and the intensities of the observed transitions are well accounted for by our model (Table 3.2 and Fig. 3.6a-b).
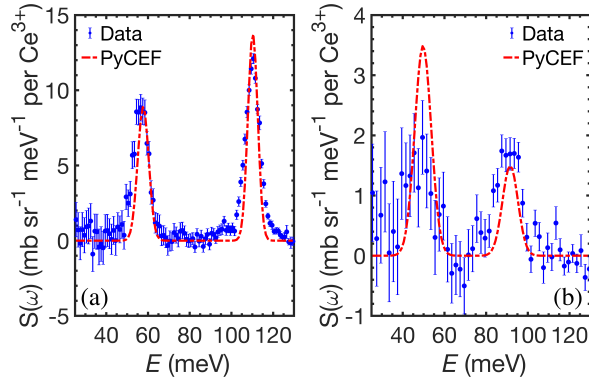
Figure 3.6: Decomposed spectra with the CEF excitations coming from Ce^{3+} experiencing a perfect D_{3d} (**a**) and defective (**b**) environment, using an incident energy of 200 meV. The red lines represent the fits obtained with PyCrystalField using two different CEF Hamiltonians.

Taking our analysis a step further, we integrated the magnetic susceptibility measured on the powder sample to the fitting routine. The contributions from each environment were weighted based on the estimated amount of defects (3 % of Ce^{4+}). The result of the fit is shown on Fig. 3.7a-b. From the entire CEF analysis, it follows that the wavefunction of the ground state doublet is a dominated by a linear combination of the $|m_{J_z} = \pm 3/2\rangle$ states. As exemplified in section 1.9, and demonstrated in [51], applying a pseudo-spin $1/2$ formalism on this wavefunction yields a pseudo-spin where σ_x and σ_z transform like the z-component of a magnetic dipole under the symmetries of the underlying $F_{d\bar{3}m}$ lattice, whereas σ_y transforms like a magnetic octupole. It also implies a strong Ising anisotropy. Interestingly, the ground-state wavefunction includes a non negligible contribution from the $7/2$ multiplet (Table 3.2). This admixture of J states implies a magnetic moment having a less Ising character than in the case of a single $J = 5/2$ state and also implies the existence of non-zero higher order multipole couplings [39, 56].

We note that the number of allowed parameters of the second CEF environment compared to the number of observables does not enable to provide a reliable analysis. This limitation explains the rather poor fit of the defective CEF presented in Fig. 3.6b, and is expected to contribute to the small deviation between the measured magnetic
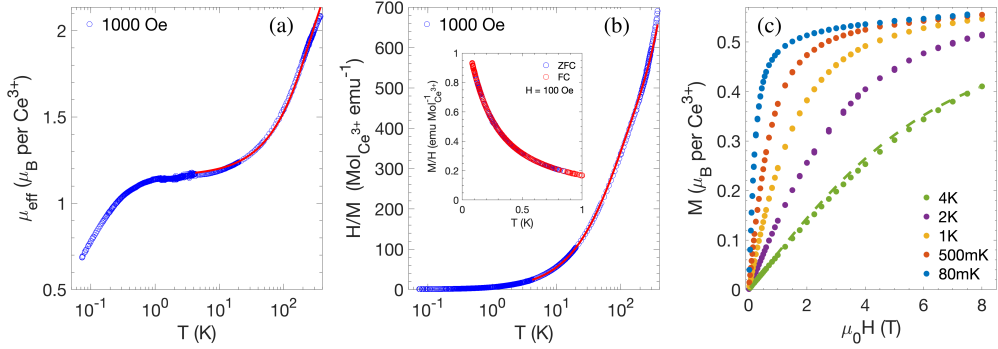
Figure 3.7: (**a**) Effective magnetic moment obtained from the experimental magnetic susceptibility data (in blue) and CEF model (red line). (**b**) Inverse magnetic susceptibility of the same sample measured with 1000 Oe. The red line corresponds to our CEF model, based on both susceptibility and INS data. The inset shows the magnetic susceptibility obtained under field-cooled (FC) and zero-field cooled (ZFC) conditions. (**c**) M vs H measured at different temperatures on a powder sample together with the computed magnetization at 4 K obtained from our CEF model.

susceptibility and the calculation (see Fig. 3.7a-b). The values of CEF coefficients for the defective environment can be found in Appendix 6.4. Although we cannot conclude on a precise composition of the wavefunction of the ground state doublet for the defective environment, the dipole-octupole nature of the latter appears to be robustly preserved as the $|m_{J_z} = \pm 3/2\rangle$ states remain largely predominant.

Degeneracy	E_{obs}	E_{calc}	I_{0bs}	I_{calc}	CEF env.#
2	0	0			1 - 2
2	46.9(1.2)	49.8	0.30(0.18)	0.45	2
2	56.5(0.3)	57.5	1.00	1.00	1
2	90.0(1.1)	91.7	0.29(0.10)	0.21	2
2	110.1(0.2)	110.3	1.26(0.08)	1.2	1
2	264.4(0.1)	280.6	0.14(0.03)	0.08	1

Table 3.2: Observed and calculated crystal-field transition energies of $Ce_2Hf_2O_7$ in the intermediate coupling scheme. The intensity of the transition located at 110 meV is actually the sum of the intensities located at 101 and 110 meV, taking into account the observed splitting. The values of Stevens operators obtained from the fit were $B_2^0 = -0.835$, $B_4^0 = 0.223$, $B_4^3 = 1.771$, $B_6^0 = -0.008$, $B_6^3 = 0.074$ and $B_6^6 = -0.075$ meV for the first defined environment. The obtained ground-state wavefunction is $|\pm\rangle = 0.977|^2F_{5/2},\pm 3/2\rangle \mp 0.152|^2F_{5/2},\mp 3/2\rangle - 0.106|^2F_{7/2},\mp 3/2\rangle \mp 0.102|^2F_{7/2},\pm 3/2\rangle$.

3.2.2 Crystal-electric field in $Ce_2Sn_2O_7$

We now turn to crystal-electric field data collected on our powder sample of $Ce_2Sn_2O_7$ at 6 K. These measurements were performed and analyzed before the beginning of this work but are nevertheless reported here as they plays an important role in the understanding of the magnetic ground state. The CEF spectra were also measured on MAPS (ISIS), at incident energies of 150, 450 and 700 meV (Fig. 3.8). In this case, $La_2Sn_2O_7$ was utilized to remove phononic contributions.
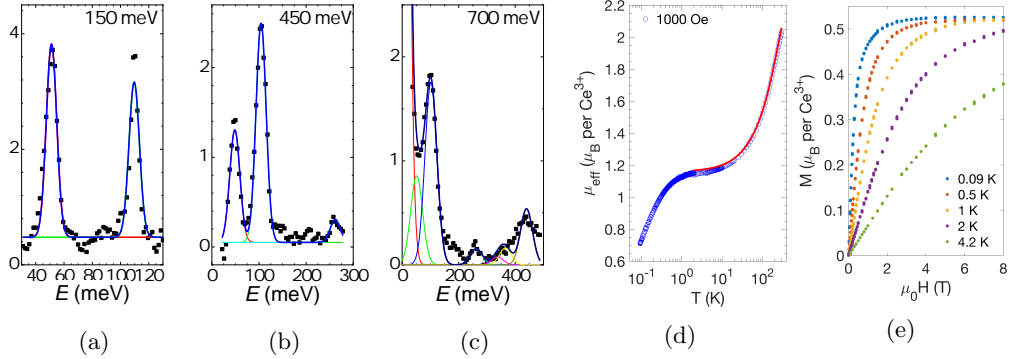
Figure 3.8: (**a-c**) Energy spectra measured on $Ce_2Sn_2O_7$ at 6 K and recorded using incident neutrons of different energies as specified on the top right-hand corner of each panel. The solid lines are fits of the experimental data (black squares) using Gaussian peaks (peaks within each spectrum are constrained to the same width). (**d**) Effective magnetic moment measured on $Ce_2Sn_2O_7$ (blue circles) together with the calculation from our CEF model using SPECTRE (red line). (**e**) M vs H measured at different temperatures on a powder sample.

Looking at the spectra collected with incident energy of 150 meV (Fig. 3.8a), the two transitions expected between the ground state and the excited states of the $J = 5/2$ mutliplet were identified, located at 51 and 110 meV. The transitions from the ground state to the levels of the $J = 7/2$ multiplet could also be observed in the spectra covering a larger energy range (Fig. 3.8b-c). Based on the six observed transitions, the SPEC-TRE [140] program was employed to fit the data using the whole set of 14 intermediate-coupling basis states (for the same reasons as of $Ce_2Hf_2O_7$). The results of the fit can be seen in Table 3.3. The obtained ground-state wavefunction was found to be a linear combination of $|m_{J_z} = \pm 3/2\rangle$ states and thus a dipole-octupole ground state.

Level degeneracy	E_{obs}	E_{calc}	I_{obs}	I_{calc}
2	0.0	0.0	-	-
2	51.16(16)	51.1	1.00	1.00
2	109.7(2)	109.4	0.58(15)	0.44
2	262(10)	275.6	2.1(5)	1.16
2	330(30)	337.6	3(3)*	5.8
2	375(30)	365.9	3(3)*	7.6
2	430(20)	442.1	3(3)*	5.6

Table 3.3: Observed and calculated crystal-field transition energies and intensities of $Ce_2Sn_2O_7$ obtained using the intermediate coupling scheme. The best crystal-field Wybourne parameters used for the calculations are $B_0^2 = 74.8$, $B_0^4 = 433.1$, $B_3^4 = 49.7$, $B_0^6 = 99.2$, $B_3^6 = -140.8$, $B_6^6 = 148.4$ meV. The obtained ground-state wavefunction is as follows: $|\pm\rangle = 0.87|^2F_{5/2}, \pm 3/2\rangle \pm 0.46|^2F_{5/2}, \mp 3/2\rangle \mp 0.15|^2F_{7/2}, \pm 3/2\rangle - 0.01|^2F_{7/2}, \mp 3/2\rangle$. The three higher-energy levels cannot be resolved from the experiment, therefore their parameters in the table are estimates, not fitted values, and their intensities* are given relative to the transition around 262 meV, which is well resolved in the same spectrum using $E_i = 700$ meV.

Using the CEF parameters of the best fit, the magnetic susceptibility from room

temperature down to about 1 K could be computed (see Fig. 3.8d). It is clearly in good agreement with the experimental data, strongly supporting the correctness of our CEF model. It is worth noting that, in the case of $Ce_2Sn_2O_7$, the ground-state wavefunction is largely dominated by the 5/2 multiplet (Table 3.3), implying a stronger Ising character than in $Ce_2Hf_2O_7$.

3.2.3   Magnetic behavior

Neither of the compounds display signs of long range order, which would show up in magnetic susceptibility measurements as well as in neutron diffraction patterns. As can be seen in figures 3.7a and 3.8d, the behavior of the effective moment (extracted from the susceptibility) in both compounds is very similar. The high temperature part is dictated by the population/depopulation of the CEF states until it reaches a plateau at about 10 K. At this temperature only the ground state contributes to the magnetization. In both cases, the effective moment of the ground state doublet is about 1.18 μ_B, in good agreement with what is calculated from the crystal field models ($\mu_{eff}^{CEF} = 1.18\ \mu_B$). The magnetization curves measured on the powder samples up to 8 T (Fig. 3.7c and Fig. 3.8e) saturate at roughly half the effective magnetic moment, which is expected for Ising moments on a pyrochlore lattice due to the important non-collinear local anisotropy [141]. This strong local anisotropy is also consistent with the large energy gaps to the first excited state observed in both INS data sets. Upon further cooling, one can observe a substantial loss of the effective moment. In absence of long range order, as it is the case here, this behavior is likely to be a manifestation of the progressive stabilization of a correlated state.

3.3   Low-temperature correlated state

3.3.1   Bulk measurements

Magnetic susceptibility measured on polycrystalline samples of $Ce_2Hf_2O_7$ did not display any sign of long-range order down to 0.08 K, nor any zero-field-cooled/field-cooled effects (see inset of Fig. 3.7b). Furthermore, ac-susceptibility data do not exhibit any sizeable χ'' response at frequencies ranging from 0.11 Hz up to 211 Hz (as can be seen with the flat signal at zero in Fig. 3.9). This behavior is identical to what was reported in $Ce_2Sn_2O_7$ [129] and indicates that spins evade freezing down to the lowest temperatures achieved here. However, we do observe the rise of magnetic correlations through the appearance of a broad peak in specific heat measurements (Fig. 3.9b).

Lattice contributions were subtracted from the measured specific heat of $Ce_2Hf_2O_7$ using identical measurements carried out on non-magnetic isostructural compounds. The onset of correlations appears as a strong increase of C_{mag} when the temperature decreases below 2 K. In order to compare the magnetic contributions to the heat capacity with other Ce^{3+} pyrochlores, we also reproduce in Fig. 3.9 literature data for crystals of $Ce_2Sn_2O_7$ [130, 142] and of $Ce_2Zr_2O_7$ [143]. Remarkably, the results obtained for $Ce_2Hf_2O_7$ and $Ce_2Sn_2O_7$ are very similar down to 0.4 K, while $Ce_2Zr_2O_7$ [143] shows a significantly different behavior, with a rise of magnetic contribution appearing at higher temperatures and spread on a wider temperature range. However, $Ce_2Sn_2O_7$ and $Ce_2Hf_2O_7$ seem to deviate below 0.3 K, with $Ce_2Hf_2O_7$ saturating more quickly and behaving similarly to $Ce_2Zr_2O_7$.

In order to determine the exchange couplings associated with the magnetic correlations, we collaborated with Dr. Sylvain Petit (CEA, Saclay, France) to follow a mean
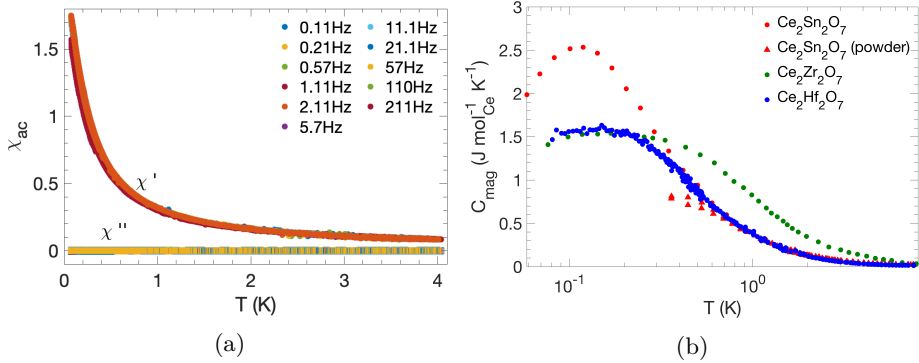
Figure 3.9: (**a**) *ac*-susceptibility measured on $Ce_2Hf_2O_7$ powder down to 0.08 K with frequencies ranging from 0.11 Hz to 211 Hz. The same measurements were performed on $Ce_2Sn_2O_7$, leading to practically identical results. (**b**) Magnetic contribution to the heat capacity measured on a piece of $Ce_2Hf_2O_7$ single-crystal and compared to similar data on other cerium pyrochlores. The magnetic contribution to the heat capacity of $Ce_2Hf_2O_7$ was obtained by subtracting lattice contributions using data for $La_2Hf_2O_7$ that were obtained in the same way. The experimental data for $Ce_2Sn_2O_7$ and $Ce_2Zr_2O_7$ are reproduced from references [142, 130] and [143], respectively. We note that the discrepancy observed between the magnetic contributions to the heat capacity of $Ce_2Sn_2O_7$ from references [130] and [142] only concerns few data points from [130] that were measured between 0.5 K and the lowest temperature achieved (0.36 K). This is unlikely to reflect different correlated ground states between $Ce_2Sn_2O_7$ samples used in [130] and [142] but rather results from difficulties in measuring heat capacity on powder samples below 0.5 K.

field approach of the problem. We attempted to reproduce the magnetization and specific data measured on $Ce_2Sn_2O_7$ [130]. To do so, a simplified exchange Hamiltonian for a rare-earth pyrochlore with a dipolar-octupole ground-state doublet with the addition of a Zeeman term was considered. We adopted the generic pseudo-spin approach [50, 51], where the x- and z-components transform like magnetic dipoles and the y-component like a magnetic octupole:

$$\mathcal{H}_{DO} = \sum_{ij} \mathcal{J}^{xx}\tau_i^x\tau_j^x + \mathcal{J}^{yy}\tau_i^y\tau_j^y + \mathcal{J}^{zz}\tau_i^z\tau_j^z + \mathcal{J}^{xz}(\tau_i^x\tau_j^z + \tau_i^z\tau_j^x) - \sum_i (\mathbf{h}\cdot\mathbf{z}_i)(\mathbf{g}\cdot\tau) \quad (3.1)$$

Here τ is the pseudo-spin, $\mathbf{h}$ is an applied magnetic field, $\mathbf{z}$ is the local quantification axis on site i and $\mathbf{g}$ is the g-tensor. The $\mathcal{J}^{xx}$ and $\mathcal{J}^{xz}$ exchange couplings are assumed to be null in order to reduce the number of variables but still capture the essential physics of the octupolar phase. One is then left with $\mathcal{J}^{zz}$ and $\mathcal{J}^{yy}$, coupling the z- and y-component of the pseudo-spin, respectively. The fit was performed on the magnetization versus magnetic field data shown in Fig. 3.10a. Assuming a g-factor of 2.18 for Ce^{3+}, the analysis yielded two possible sets of variables, depending on the sign of the starting values. The first set reaches $\mathcal{J}^{zz} = 0.03 \pm 0.01\ K$ and $\mathcal{J}^{yy} = -0.16 \pm 0.02\ K$, corresponding to an ordered 'all-in-all-out' octupolar phase. Such state would be accompanied by a phase transition, which was not observed in specific heat data nor neutron diffraction nor muons spin relaxation experiments [129, 130], allowing to rule out this solution. On the other hand, the second set, yielding $\mathcal{J}^{zz} = 0.03 \pm 0.01\ K$ and $\mathcal{J}^{yy} = 0.48 \pm 0.06\ K$, stabilizes a correlated phase where octupoles obey a '2-plus-2-
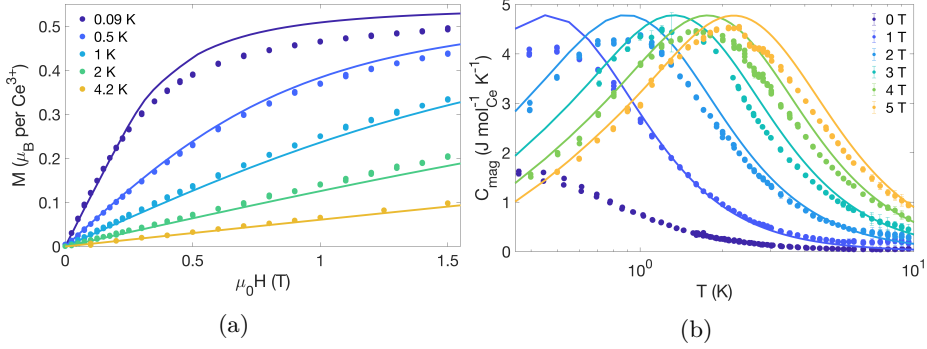
Figure 3.10: (**a**) Magnetization as a function of applied magnetic field and (**b**) temperature dependence of the specific heat under various applied magnetic fields. The continuous lines are the results of the mean field analysis.

minus' rule on each tetrahedron. This second set of parameters was also used to compute the magnetic contribution to the specific heat under the application of a magnetic field, showing a good agreement with the experimental data, as can be seen in Fig. 3.10b. Based on the obtained values and the theoretical phase digram [144], $Ce_2Sn_2O_7$ finds itself in the π-flux octupolar quantum spin ice regime. Indeed, the octupolar coupling, $\mathcal{J}^{yy}$, is largely dominant and enforces this '2-plus-2-minus' ice-rule, whereas the dipolar one, $\mathcal{J}^{zz}$, acts as a transverse term, allowing to tunnel between degenerate configurations. In addition, $\mathcal{J}^{yy}$ in $Ce_2Sn_2O_7$ appears to be strongly dominating, suggesting strong octupolar correlations.

Owing to the availability of single crystals, another approach could be taken to estimate the magnitude of the exchange couplings in $Ce_2Hf_2O_7$, using exact diagonalization methods. The magnetic contribution to the specific heat at various magnetic field for $Ce_2Hf_2O_7$ is displayed in Fig. 3.11. Upon application of a magnetic field along the [111] crystallographic direction, the signal shifts to higher temperatures and its maximum becomes readily visible at $\mu_0 H = 2$ T [Fig. 3.11d], as it was the case for $Ce_2Sn_2O_7$. This time, we collaborated with Dr. Anish Bhardwaj and Dr. Hitesh J. Changlani (Florida State University, USA) to use finite temperature Lanczos, a numerical method employing exact diagonalization, to reproduce the data at each field (blue points in Fig. 3.11) and extract the exchange couplings. The same Hamiltonian as in 3.1 was assumed, but this time only setting J^{xz} to be zero. This can be achieved by performing a rotation around the y-axis without modifying the physics of the Hamiltonian, although it implies new x and z directions. The components of the g-tensor were initially estimated from magnetization data as a function of magnetic field collected at 4 K, far from the correlated regime, yielding:

$$g = \begin{bmatrix} 0 & 0 & 0 \\ 0 & 0 & 0 \\ 0.8 & 0 & 2.187 \end{bmatrix} \tag{3.2}$$

which is in good agreement with expected values from $Ce_2Hf_2O_7$ crystal-electric field scheme ($g_{zx} = 0.95$ and $g_{zz} = 2.168$). These values were then fixed for the rest of the analysis while the exchange interactions are fitted to the data. The best fits (see red curves in Fig. 3.11) were obtained with the following exchange couplings: $\mathcal{J}^{xx} = 0.12$ K, $\mathcal{J}^{yy} = 0.51$ K and $\mathcal{J}^{zz} = 0.20$ K. Once again, these values confirm the hypothesis of dominant octupolar interactions while dipolar components play the role of transverse

terms in the spin-spin Hamiltonian [50, 51, 144, 145], but suggest less dominant octupolar correlations compared to $Ce_2Sn_2O_7$.
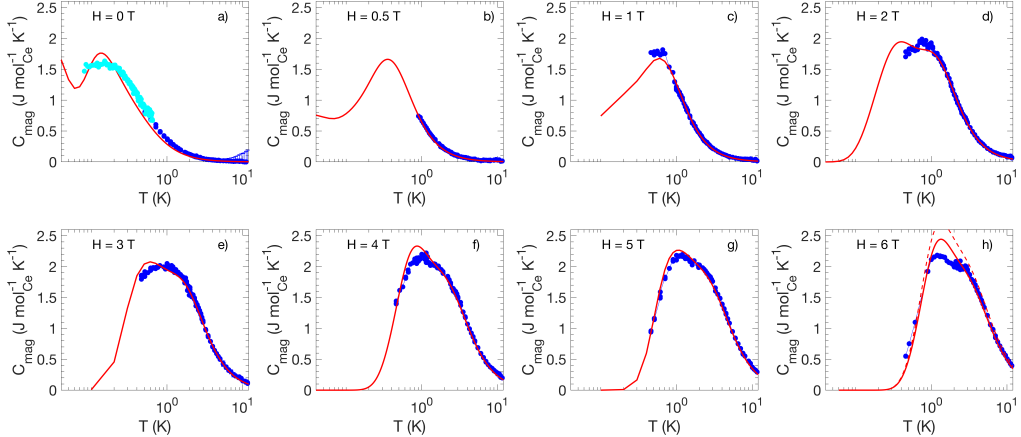
Figure 3.11: Magnetic contribution to the heat capacity with magnetic fields $\mu_0 H$ from 0 T to 6 T applied along [111]. The red curves are the results of the Lanczos analysis using a 16 sites system, scaled to take into account the presence of about 10% of non magnetic cerium ions. The dashed red lines in panel h) is displayed to show the unscaled result for $\mu_0 H = 6$ T.

Calculations from our $Ce_2Hf_2O_7$ model were also compared with magnetization curves measured at 0.08 K for magnetic fields aligned along the high symmetry directions [100], [1$\bar{1}$0] and [111], as displayed in Fig. 3.12. The magnetization at saturation is different in each direction, confirming the presence of a relatively strong anisotropy. At a magnetic field of $\mu_0 H = 8$ T, $M_{[100]} > M_{[111]} > M_{[1\bar{1}0]}$ as predicted for a system of Ising spins on the pyrochlore lattice [57]. This hierarchy is also found in the results from our model (lines in Fig. 3.12a) and in the investigation of the magnetic field induced magnetic order which we will describe hereafter (black symbols in Fig. 3.12a).

3.3.2 Magnetic field induced magnetic order

The induced magnetic structures with the field applied along the [110] and [111] directions, were investigated using the single crystal neutron diffractometer Zebra (SINQ). The same piece of $Ce_2Hf_2O_7$ single crystal was used for both field orientations. Experiments were conducted at 0.05 K in vertical magnetic fields up to 8 T. For both field orientations, the same procedure was followed.

Let us consider one configuration at a time, starting with the field applied along the [110] direction. First, many Bragg reflections were measured at several magnitude of magnetic field. Least-square fits were performed on the 0 T data sets in order to determine and fix some parameters such as the scale factor and atomic Debye-Waller coefficients. For each value of magnetic field, the magnetic Bragg peaks were extracted by subtracting the Bragg intensities measured in zero field. From the obtained sets of magnetic Bragg peaks, those having negative values or unreasonably large uncertainty were discarded. Such unwanted data points are typically present due to the small magnetic moment of Ce^{3+} (which makes for complicated fits as we shall see later on) as well as the uncertainty of the measurements themselves. Thus, they have to be disregarded as they are either unphysical (the negative ones) or would propagate too much error in the least-square fits. The same applies to the data collected in the other field configu-
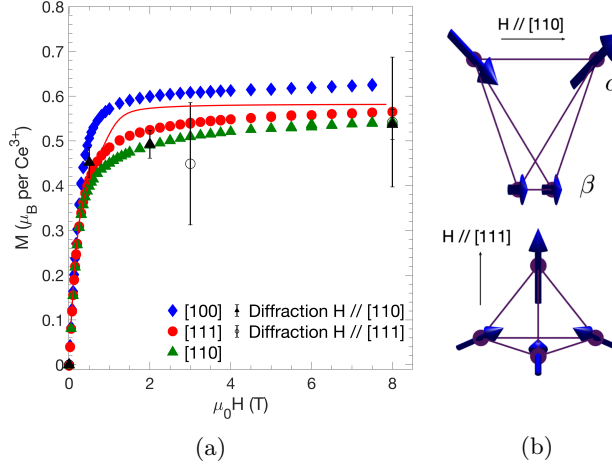
Figure 3.12: (**a**) Magnetization as a function of external magnetic field H at 0.08 K for field directions along [100] (blue diamonds), [111] (red dots) and [1$\bar{1}$0] (green triangles). The continuous lines are the associates simulation from our model. The empty and filled black squares correspond to the values of M obtained from fits of neutron diffraction data for fields applied along [111] and [1$\bar{1}$0] directions, respectively. (**b**) Sketch of the induced magnetic structures determined from neutron diffraction data and magnetization analysis.

ration.

The obtained magnetic Bragg intensities are then fitted assuming a model structure. Starting with the data collected with the field along the [111] direction, a first remark is the absence of magnetic peaks rising away from the peaks of the face-centered-cubic lattice, implying that the stabilized magnetic structure can be described by a $\mathbf{k} = (0,0,0)$ propagation vector. Based on this propagation vector, on the lattice symmetry, the direction of the field and on the Ising character of the magnetic moment, somewhat restrained to their local $< 111 >$ axis, either the '3-in-1-out' or the 'all-in-all-out' (AIAO) structures are typically formed. In both cases the site having its $< 111 >$ local axis parallel to the field has to be treated separately from the three others (see Fig. 3.12b bottom structure). A more rigorous argumentation will be provided in section 4.4.2, but the previous arguments will be considered as sufficient for the present analysis, as was argued in [27]. Unfortunately the weakness of the reflections and the rather large uncertainties did not lead to a clear distinction of the fits performed assuming the two mentioned structures. In order to distinguish between the two structures, we calculated the magnetization resulting of the fits. In this case the magnetization (per cerium atom) can be calculated by summing the magnetic moment of a single tetrahedron as vectors and taking the resulting component parallel to the applied magnetic field:

$$M_{111} = \frac{1}{4}\mathbf{z} \cdot \sum_i \mathbf{m}_i \qquad (3.3)$$

with $\mathbf{z}$ a unit vector giving the direction onto which the magnetic field is applied and $\mathbf{m}_i$ the magnetic moment of site i, running on the four sites a single tetrahedron [27]. Comparing the computed and experimental magnetizations show that the AIAO structure cannot account for the observed magnetization. We therefore conclude that the '3-in-1-out' is formed.

Now turning to the second field configuration (applied along the [110]), the field induced

magnetic reflections can be accounted for by a $\mathbf{k} = (0,0,0)$ propagation vector. In this configuration, and considering the same arguments as used in the previous paragraph, the magnetic moment typically split into two categories denoted as α and β (this is also more rigorously explained in section 4.4.2) [27]. The α sites have their local $< 111 >$ axis at a $35°$ from the field direction, whereas the β sites have their axis perpendicular to it. In this case, the α moments couple to the field while retaining their anisotropy. The β moment do not couple to the field and to a first approximation remain zero on average, still obeying the '2-in-2-out' rule. However small field misalignments and coupling between the α and β chains tend to lift the degeneracy of the β chain. In our case, the α moments appear to grow with the field whereas the β moments seem to weakly polarize with the field (see Fig. 3.12b, top). Although the size of the induced moments is again small and difficult to fit, the magnetization computed from obtained magnetic structures, using the same formula as 3.3, is in agreement with the experimentally measured magnetization. The fit results for both field configurations at 8 T are displayed in Fig. 3.13.

(a) (b)
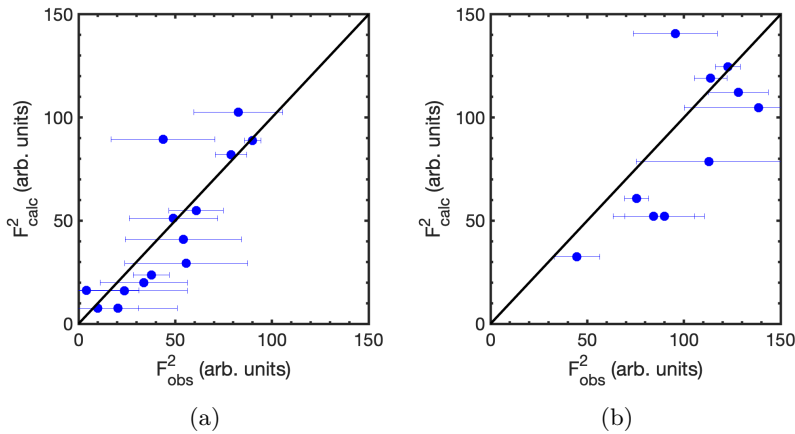
Figure 3.13: Observed versus calculated intensities for a magnetic field of 8 T applied along the (**a**) [110] and (**b**) [111] crystallographic direction, giving an agreement factor R_f of 17.0 and 25.0, respectively. In the case of the magnetic field applied along the [111], allowing a small polarization of the moments with the field proved to improve the fit.

3.3.3 Magnetic diffuse scattering

Owing to their short range correlations and, most importantly, local constraints on each tetrahedra, spin ices display a characteristic magnetic diffuse scattering at low temperatures. When entering the correlated phase, a structured signal appears, such as the one displayed in Fig. 1.7b, with its overall Q-dependence following that of a dipolar form factor (intense at low momentum transfer and decaying rather rapidly). Unexpectedly, no such signal could be identified in $Ce_2Sn_2O_7$ via diffraction experiments using cold neutrons. Instead, the magnetic diffuse scattering obtained via thermal neutron powder diffraction exhibits a broad liquid like signal located at high momentum transfer (shown in Fig. 3.14a). The momentum transfer dependence of the diffuse intensity is in stark contrast with the expected dipolar signal (green dots) in terms of shape and intensity, as can be seen in Fig. 3.14a (bottom panel). The observed signal is

rather reminiscent of the shape of the octupolar form factor [146, 147, 148, 149, 150, 151].

The collaboration with Dr. Sylvain Petit also tackled the understanding of this feature. He started by defining an effective Hamiltonian taking into account the CEF and a molecular field. Two cases were then considered, where this molecular field was assumed to reflect either a dipolar or octupolar spin-ice configuration. Employing a mean-field approach using this Hamiltonian onto a large pyrochlore lattice made up of several unit cells, we get the corresponding dipolar/octupolar spin ice states. The elastic neutron scattering intensity from the obtained system, $S(\mathbf{Q}, \omega = 0)$, was computed using the equation 2.14 and the magnetic interaction operators described in section 2.5.7. This was done for a few randomly generated starting pyrochlore configurations to take an average of the generated $S(\mathbf{Q}, \omega = 0)$. The resulting $S(\mathbf{Q}, \omega = 0)$ was subsequently integrated over all direction so as to obtain the scattering intensity as a function of momentum transfer $\|\mathbf{Q}\|$ and compare it with our powder data. In the case of dominant dipolar correlations (green points in Fig. 3.14a), the signal is peaked at small momentum transfer and is expected to be much more intense than the signal we observe. For octupolar correlations, the signal takes the shape of a large bump at high momentum transfer (red points in Fig. 3.14a). Once slightly scaled down (light red line), the prediction for an ice of octupoles is in very good agreement with the measured data. In addition, the growth of this octupolar signal is concomitant with the loss of effective magnetic moment (see Fig. 3.14c). We interpret this behavior as the evolution of the mixing of the two states of the single-ion doublet's wavefunctions under the effect of dominant octupolar correlations, resulting in a strengthening of the octupolar moment upon cooling, at the expense of the dipolar one.

Following an identical experimental procedure, a similar, although significantly weaker, signal was observed for $Ce_2Hf_2O_7$ (Fig. 3.14b). The weakness of the diffuse signal found in the hafnate compared to the stannate, measured in the same conditions is likely to be due, at least partially, to the non negligible amount of Ce^{4+} defects [152]. However, there most likely are additional energetic explanations. $Ce_2Hf_2O_7$ is apparently located in a region of the phase diagram that is less dominated by the octupole-octupole exchange, as concluded by our specific heat analysis. This was also recently proposed to be the case for $Ce_2Zr_2O_7$ [145]. Additionally, both heat capacity and the low-energy neutron spectroscopy (discussed in the next section) of cerium hafnate suggest a less dominant octupolar coupling term compare to the stannate and zirconate compounds. Thus, one would expect the correlations in $Ce_2Hf_2O_7$ to be less established at a given temperature. This last remark could also be argued from the faster loss of effective magnetic moment in $Ce_2Sn_2O_7$ (see Fig. 3.14c)

3.3.4 Continuum of excitations

In order to probe the low energy magnetic excitations, low-energy neutron time-of-flight spectrometry was performed on IN5 (ILL) on both $Ce_2Sn_2O_7$ and $Ce_2Hf_2O_7$ powder samples, following an identical procedure. An incident wavelength of 10 Å was selected to carry out the experiments, providing an energy resolution of about 0.011 meV at the elastic line. The cooling was monitored by following the evolution of the inelastic contribution to the signal. Once the base temperature was reached, the actual temperature of the samples was estimated by fitting the spectrum using a phenomenological background function, a gaussian centered at zero energy transfer and two gapped Lorentzian multiplied by $(1 - e^{-E/k_B T})$ to account for temperature effects. The same method was applied to estimate the other temperatures reached during the experiments. The datasets were recorded in such a way to obtain similar statistics at each temperature. In addition to corrections using calibration scans (vanadium and empty copper
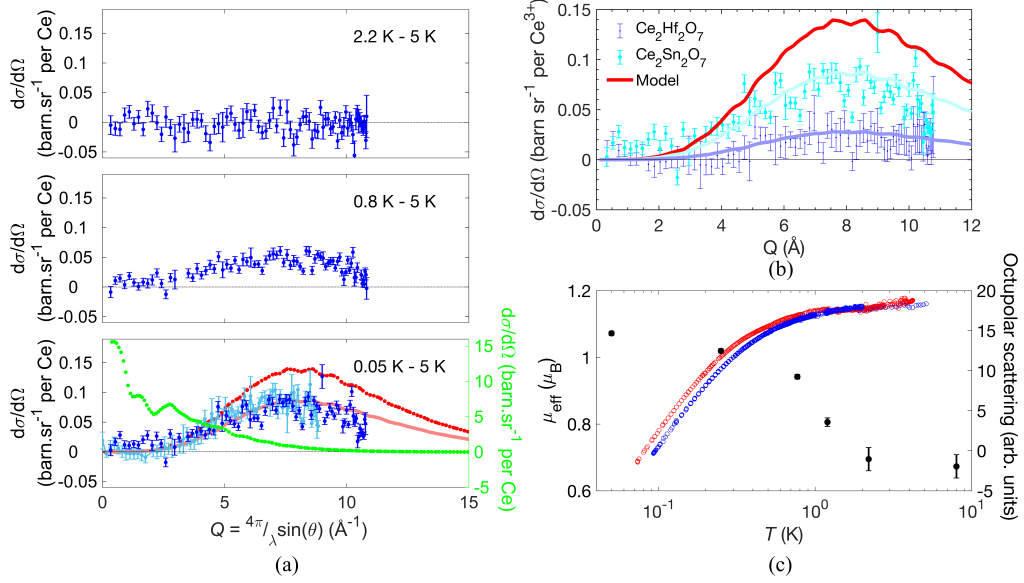
Figure 3.14: (**a**) Diffuse scattering obtained from the difference between neutron diffraction patterns measured on $Ce_2Sn_2O_7$ at 5 K and at a lower set-point temperature: 2.2 K, 0.8 K and 0.05 K. Data were measured on HRPT (SINQ, dark blue points) and D20 (ILL, light blue points). The red and green lines corresponds to the powder average of the diffuse scattering calculated for an octupolar and a dipolar spin ice states [130] at T = 0 K. (**b**) Diffuse scattering obtained from the difference between neutron diffraction patterns measured at set-point temperatures of 5 K and 0.05 K for $Ce_2Hf_2O_7$ (dark blue) and $Ce_2Sn_2O_7$ (light blue). The red line is the same as in (**a**) and both the dark and light blue lines were simply scaled down to overlap with the experimental data by factors of 0.2 and 0.625, respectively. The intensity of the signals was normalized using the refinements performed on the associated diffraction patterns. (**c**) Temperature dependence of the effective magnetic moment of $Ce_2Sn_2O_7$ and $Ce_2Hf_2O_7$ (blue and red circles, respectively) and integrated magnetic diffuse intensity (black points with error bars) measured on a powder sample of $Ce_2Sn_2O_7$.

can), a background subtraction was performed using the phenomenological function mentioned previously to produce the final datasets. The resulting spectra can be found in Fig. 3.15a-b. Furthermore, the imaginary part of the dynamic spin susceptibility, $\chi"(E)=(1 - e^{-E/k_B T})S(E)$, was calculated. Assuming the signal appearing upon cooling below 5 K to be purely magnetic, S(E) can be readily obtained by subtraction of the 5 K spectrum (far from the correlated regime) from the lower temperature ones (Fig. 3.15c-d).

As expected for quantum spin ices materials (see 1.2.3) [153, 15, 16], both samples display a continuum of excitations located at energy transfers close to the energy of their respective dominant exchange couplings (Fig. 3.15). A similar signal was also observed by two groups in $Ce_2Zr_2O_7$ [134, 143], using single crystals. We thus identify these continua as spinon excitations (1.2.3). The production of spinon involves creation and annihilation operators τ_{+-} associated with the transverse coupling J_{+-}. In the case of an oQSI, this operator is a combination the two dipolar pseudo-spin components τ_x and τ_z [51]. The spinon continuum is therefore expected to be neutron active and to follow a dipolar form factor. To the current knowledge, no significant difference is expected in the
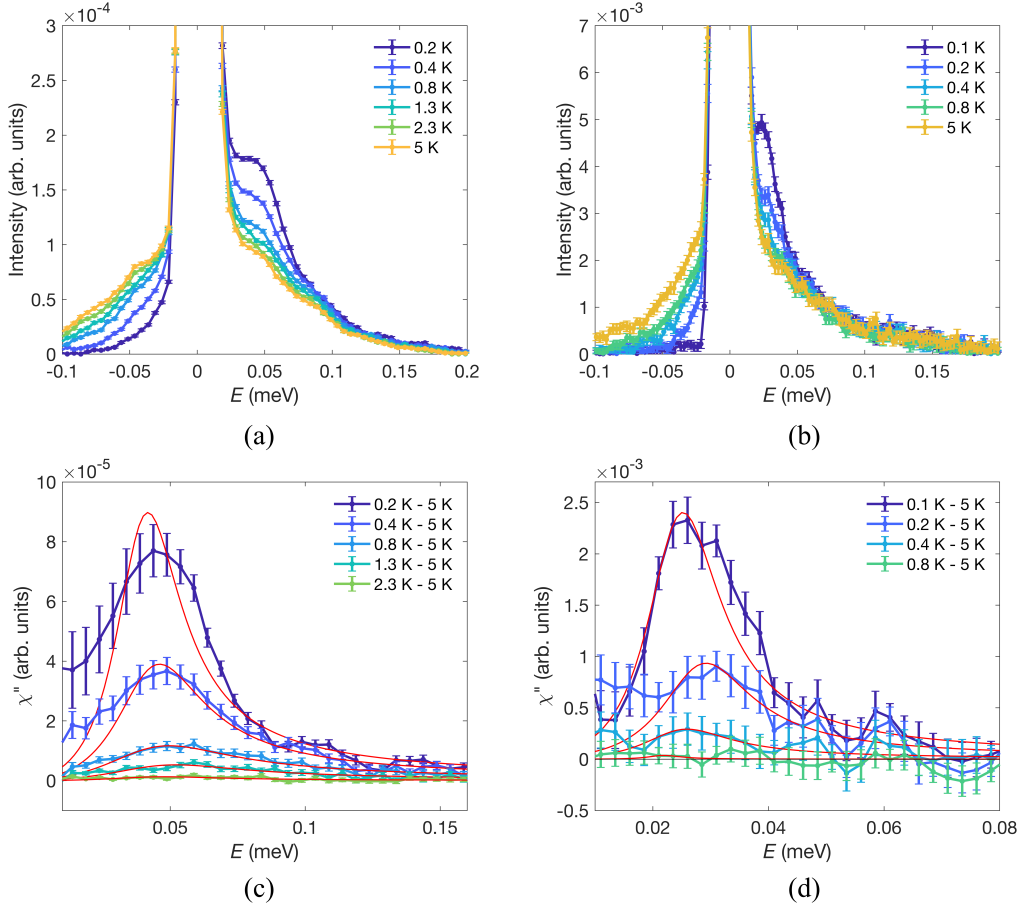
Figure 3.15: INS data collected on (**a**) $Ce_2Sn_2O_7$ and (**b**) $Ce_2Hf_2O_7$, respectively. The spectra were collected at various temperatures, as indicated in the plot, were corrected for instrumental background and integrated on the (Q)-ranges going from 0.3 Å^{-1} to 1.1 Å^{-1} and from 0.2 Å^{-1} to 1.0 Å^{-1}, respectively. The temperatures displayed here are the estimated temperatures. (**c-d**) χ''(E) curves extracted from the spectra in (**a-b**). The red lines are the fit to the data using a Lorentzian function defined as χ'' (E)=S$_f\Gamma$ E/((E-Δ)^2+Γ^2), where Δ defines the centering of the peak, Γ its damping and S$_f$ a global scale factor. Fitted parameters can be found in Fig. 3.16.

dynamical spin structure factor of spinons for a dipolar or octupolar quantum spin ice, as both magnetic ground states are described using the same gauge field formalism [15, 16, 17]. Additionally, the neutron spin being only sensitive to the $< S_z S_z >$ correlations, similar S_z correlations (same sign of exchange between the z pseudo-spin components) will produce similar neutron cross sections [154, 155]. Interestingly, recent work suggests different spectral signatures depending on the symmetry-enriched topological class of the QSI state [154, 155]. These topological classes refer to the magnetic fluxes going through hexagonal plaquettes - the shortest possible closed loops on the magnetic pyrochlore lattice. The 0- and π-flux states are indeed expected to lead to different enhancement of the dynamical spin structure factor in neutron experiments. Although the shape of the spinon continuum in both samples (and $Ce_2Zr_2O_7$) is very similar, it extends over rather different energies. On the one hand, the continuum of excitations in $Ce_2Sn_2O_7$ is

peaked around 0.04 meV and extends over a large range of 0.025 meV, surviving up to about 1.5 K. On the other hand, $Ce_2Hf_2O_7$ shows a sharper continuum (about 0.01 meV) sitting at lower energies (0.024 meV). In addition, the signal disappears more quickly in $Ce_2Hf_2O_7$, and is practically gone above 0.5 K. Interestingly, $Ce_2Zr_2O_7$ displays a signal located around 0.06 meV [143], suggesting yet another energy scale than in $Ce_2Sn_2O_7$ and $Ce_2Hf_2O_7$. It is also worth comparing the behavior of the effective magnetic moment [152] with the temperature evolution of the inelastic signal. One can notice a correlation between the progressive loss of the dipolar moment and the appearance and strengthening of the fractional excitations. This holds true for both compounds. Furthermore, the presence of fractional excitations in the $Ce_2Hf_2O_7$ spectra would confirm that the correlations are somewhat robust against small amounts of disorder (estimated to be around 3 % in this sample).
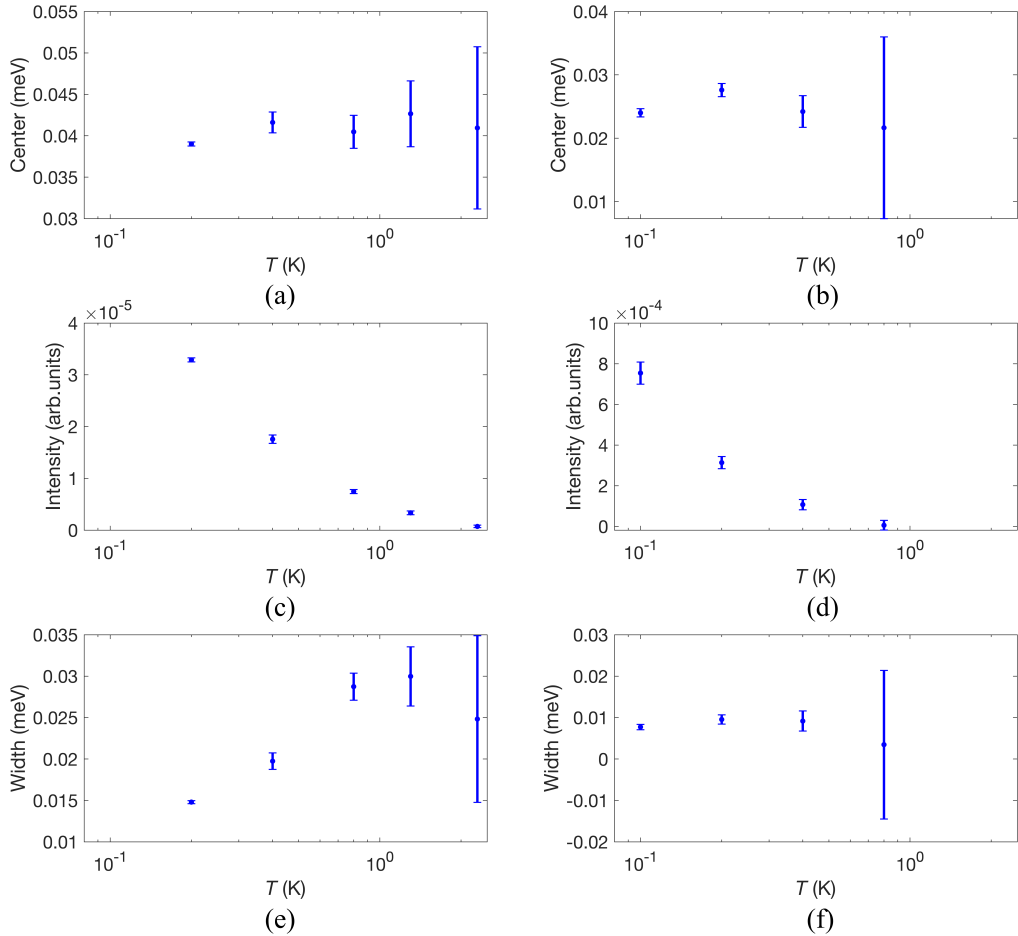
Figure 3.16: Temperature dependence of the center (**a-b**), Intensity (**c-d**) and width (**e-f**) of the continuum of excitations, obtained from fitting the $Ce_2Sn_2O_7$ (left panels) and $Ce_2Hf_2O_7$ (right panels) spectra.

Interestingly, in the case of $Ce_2Hf_2O_7$, a constant energy cut at the elastic line points to the presence of spin ice correlations following a dipolar form factor [Fig. 3.17a)] [156], with a Q-dependence differing from the gapped continuum of excitations [Fig. 3.17a]. This observation, in addition to the ones made from thermal neutron diffuse scattering,

suggest that two components of the pseudo-spin are subject to '2-in-2-out' correlations. The S_y-S_y octupolar correlations are responsible for the apparition of the diffuse scattering at high momentum transfer below 1 K. When cooling further, down to about 0.1 K, S_z-S_z appear to also correlate following an 'ice-rule', giving this weak diffuse scattering observed at low momentum transfer. This is most likely possible due to the relatively strong J_z exchange interaction compared to J_y in $Ce_2Hf_2O_7$. This effect is absent in $Ce_2Sn_2O_7$, despite our best effort hunting for this signal. Similar arguments could perhaps be used to explain the data measured on $Ce_2Zr_2O_7$ [134, 143, 145, 144]. However, at the moment it is not entirely clear whether this hypothetical behavior is backed up by theory.
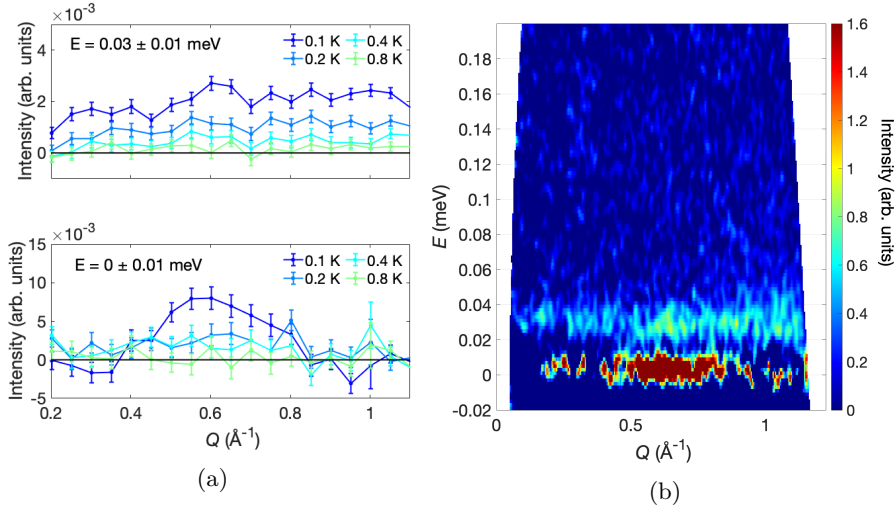
Figure 3.17: (**a**) Constant energy cuts in the elastic line (bottom panel) and in the spinon continuum (top panel). The cuts were performed on the difference maps where the 5 K data where subtracted. (**b**) Difference map between lowest and highest temperatures.

In a second time, INS experiments were carried out on IN16b (ILL), in order to better resolve the $Ce_2Sn_2O_7$ energy spectrum. IN16b is a neutron backscattering spectrometer, offering tremendous energy resolution as well as various instrumental set-ups depending on needs. The sample and sample preparation were identical to the IN5 experiment. In order to accommodate high resolution measurements at several temperatures, the BATS mode available at IN16b was selected [126]. This corresponds to a mode of the instrument where it operates in an inverted TOF configuration using analyzers in backscattering condition. This configuration has the advantage of covering a large and shiftable energy window at only a small resolution cost [157]. Two set-ups, denoted as lr4 and lr6 were used, providing a resolution of 4 μeV and 6 μeV respectively. The lr6 allowed to quickly measure at intermediate temperatures, benefiting from a more intense beam at the expense of a slightly coarser resolution with respect to lr4. The thermalization monitoring and data analysis were conducted following the same procedure as previously described (except for the background subtraction which was already accounted for by the data reduction routines). Data collected with lr6 are plotted in Fig. 3.18a. The imaginary part of the dynamical spin susceptibility was computed following the same method as for the IN5 data and the obtained curves were modeled using the previously introduced Lorentzian function (shown in Fig. 3.18b). The outcome of this analysis is very similar to the IN5 experiment (see Fig. 3.18c-e) but benefits from a better energy

resolution, uncovering a kind of shoulder on the low energy side of the continuum.
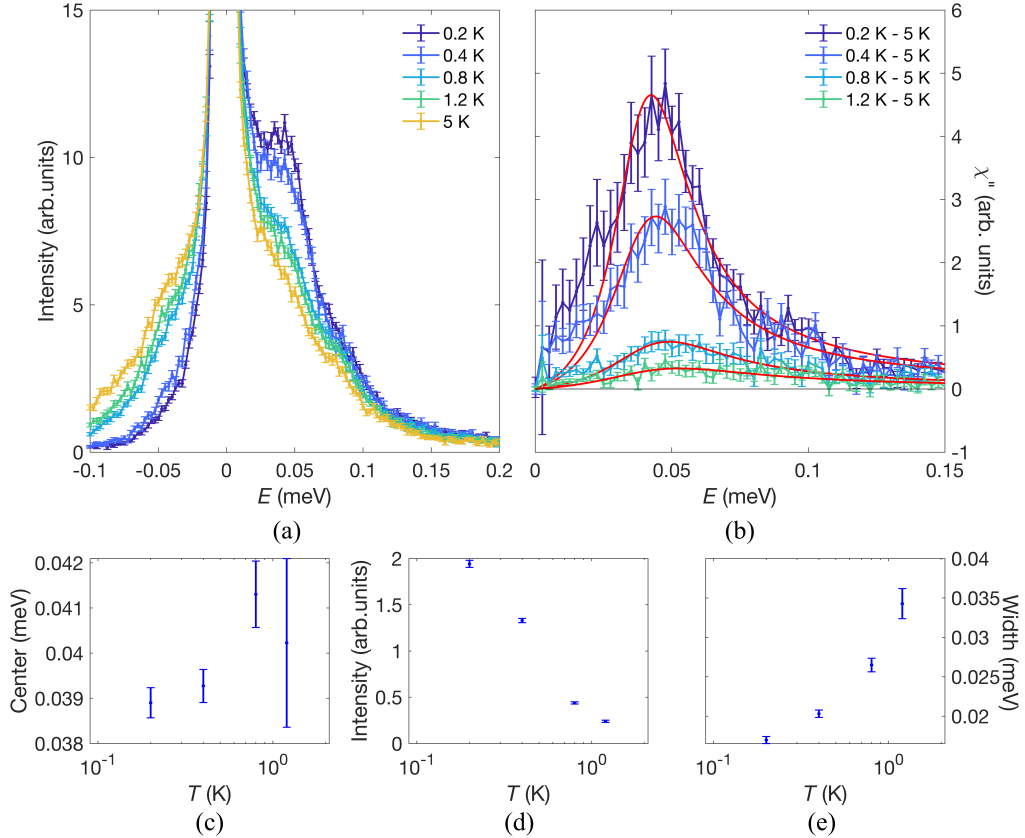
Figure 3.18: (**a**) Energy spectra at various temperatures collected on $Ce_2Sn_2O_7$, using the BATS mode of IN16b (lr6 set-up). Data are Q-integrated between 0.4 Å^{-1} to 1.7 Å^{-1}. (**b**) χ"(E) extracted from the energy spectra as described in the text. The red lines correspond to the Lorentzian fits of the signal. The temperature dependence of the fit parameters, center (**c**), intensity (**d**) and width (**e**), shows a similar behavior to what was observed in the IN5 experiment.

To better investigate the lower part of the energy spectrum, the high E-resolution mode of IN16b was used, having a resolution at the elastic line of about 0.7 μeV. The sample was this time loaded in a copper can with annular geometry of comparable volume. This allowed to maximize thermalization, but more crucially to reduce neutron absorption issues stemming from the geometry of the experiment. Data were recorded at three different temperatures, 0.2 K, 0.8 K and 5 K with similar statistics, allowing to track the signal's behavior and a direct comparison with previous experiments. To have a meaningful comparison of the BATS and high-resolution data, the spectra were integrated over a the same **Q** window ranging from 0.4 Å^{-1} to 1.7 Å^{-1} (see Fig. 3.19a). Additionally, the BATS lr4 datasets were subject to a minor rescaling, based on the relative intensities at the elastic line, thus compensating for any discrepancies between the two set-ups. The imaginary part of the dynamical spin susceptibility was once again computed following the same method as described previously and the superposition of the obtained signals for both set-ups can be seen in Fig. 3.19b.

Firstly, one can clearly see gapped nature of the excitation for the first time. The
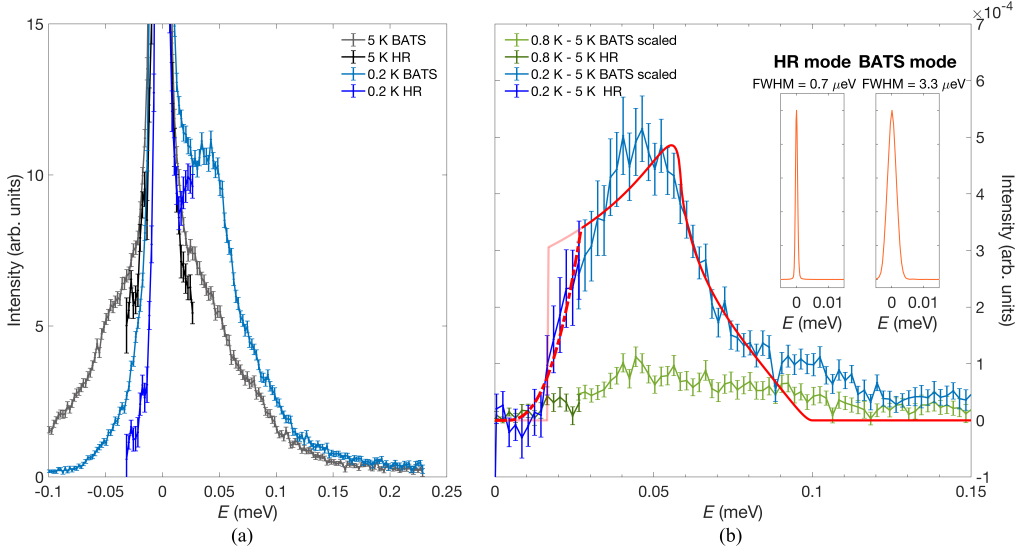
Figure 3.19: (**a**) Superposition of the $Ce_2Sn_2O_7$ spectra collected at 0.2 K and 5 K on IN16b in BATS and high resolution modes. The spectra were integrated on an identical Q-range and rescaled based on respective elastic line intensities, effectively correcting any discrepancies between the two set-ups. (**b**) Superposition of the imaginary part of the dynamical spin susceptibility extracted from both set-ups at 0.2 K and 0.8 K. The red continuous and dashed lines correspond to our spinon continuum model, as described in the text.

measurements obtained at the lowest temperature (≈ 0.2 K), reveals a threshold on the low-energy side of the gapped continuum. The threshold leads to a shoulder around 25 μeV, before the intensity rises further to a maximum located slightly below 50 μeV. Passed the maximum, the spectrum shows a rather steep decrease, which gradually slows down, giving the continuum its asymmetric and unusual shape. The same signal, measured at higher temperature (0.8 K), is found to be significantly weaker. This is in agreement with previous findings using TOF (see Fig. 3.15 and 3.16) and is explained by the proximity to the uncorrelated regime.

One way to strengthen our hypothesis on the origin of the excitation continuum is to compare it with theoretical predictions. Theory has recently focused on studying the density of states (DOS) of the spinon excitations, using analytical and numerical methods applied to the case of QSI [153, 15, 16]. Importantly, these predictions provide more specific features than just a continuum, highlighting the impact of the underlying field theory. In order to relate our results to the proposed theoretical models we worked in close collaboration with Dr. Han Yan and Dr. Andriy Nevidomskyy from Rice University.

Let us first address the asymmetry of the spinon spectrum. Considering a spin ice background at finite temperature, the propagation of spinons happens via the flipping of spins. The spinon hopping is therefore not free and is constrained by the surrounding flippable spins. For example, in a '3-in-1-out' configuration, the spinon is more likely to propagate by flipping one of the 3-in spins [158]. The constrain on the spinon propagation is the cause of the asymmetry of the wavevector-integrated spinon's density of states (DOS) [15]. Based on this consideration, the theoretical spinon DOS is remarkably similar to the continuum of excitations measured in $Ce_2Sn_2O_7$ (solid line in

Fig. 3.19b), in terms of both shape and position [15, 153]. For instance, the asymmetry and the sharp increase (threshold) on the low-energy side of the continuum predicted by theory [15] are also observed in our data. Both aspects are meaningful as they reflect the impact of the underlying spin ice state on the dynamics of the fractional quasiparticles.

The fitting the experimental spectrum with the analytical hopping model developed in [15] yields the exchange couplings $J_{//} = 48$ μeV and $J_{\pm} = 5.2$ μeV, where $J_{//}$ refers to a coupling between octupolar components of the pseudo-spins [100]. These values are in good agreement with previous estimates based on a mean-field analysis of bulk thermodynamic properties [130]. The fitted value of $J_{//}$ is also consistent with a recent measurement of the specific heat measured on a single crystal of $Ce_2Sn_2O_7$, showing evidence of a broad signal at T $\approx 0.2J_{//} = 0.12$ K [159, 142]. Comparing the temperature at which the experiment was carried out with these exchange couplings suggests that the measurements were performed in the intermediate temperature regime where part of the quantum coherence is destroyed by thermal fluctuations.

We will now discuss the low-energy 'threshold' of the spinon's DOS. Indeed, it appears to be softer in the experimental data than in the theoretical model. This is due to the actual coherent QSI background experienced by the spinon [16]. In this case, quantum electrodynamics (QED) effects have to be accounted for. In particular, in this emergent QED, spinons propagate faster than the emergent photons and therefore emit diffuse Cerenkov radiation [16]. As a result, the spinon threshold starts to broaden at 'large' momentum transfer, affecting the DOS accessed in our experiment. The corresponding analytical model applies in the long-wavelength limit and thus can only be compared with data at the onset of the spinon band, i.e. on the low-energy side of the continuum. Therefore, we fit the analytical QED model to our HR backscattering data, as shown with the dotted red line in Fig. 3.19b. To provide a meaningful analysis, we use the exchange parameters obtained considering a classical spin ice background (as discussed in the previous paragraph [15]) and convert them into the predefined parameters in the QED model [17] – namely the ring exchange, spinon mass and speed of light. The fine-structure constant of the emergent QED was fixed to $\alpha = 0.08$, based on numerical estimates for QSI [17]. After integrating the analytical model over the experimental window of momentum transfers, the calculated DOS matches the experiment remarkably well (Fig. 3.19b), only fitting the spinon gap $\Delta = 18$ μeV, and a scale factor.

The agreement between the experimental data collected on $Ce_2Sn_2O_7$ and the DOS expected for QSI is significant for several reasons. First, it constitutes a rare quantitative analysis of the excitations emerging from a QSI candidate. This is already remarkable given the notorious difficulties of experimentally assessing such defining characteristics of QSLs. In this case, the asymmetric shape of the spinon continuum observed in the data is a signature of the emergent gauge field. In particular, the low-energy threshold of the spinon continuum is captured on the basis of spinons experiencing a QSI background and interacting with the emergent photons through a fine-structure constant much higher than the $1/137$ value found in nature [16, 17]. Finally, we point out that exchange couplings could be estimated directly from the excitation spectrum within the spin liquid ground state, as opposed to conventional methods relying on the study of field-induced ordered phases.

3.4 Summary

The understanding of the correlated ground state in cerium-based pyrochlores has improved tremendously over the last few years. The DO ground state doublet, shared by

the three investigated systems [130, 143, 134], provides the key ingredients to stabilize the exotic octupolar QSI state anticipated by theory [50, 51]. None of the compounds show signs of long-range order, while strong evidence for low temperature magnetic correlations can be found through the observation of a gapped continuum of excitations in INS experiments, the rise of a broad magnetic signal in heat capacity data and spin ice like behavior in magnetometry measurements.

Despite chemical proximity and apparent magnetic similarities of the three reported cerium pyrochlores, their respective correlated states appear to cover different energy scales, having prominent consequences. In addition to sitting in slightly different regions of the QSI phase diagram (Fig. 3.20), the three compounds display contrasting experimental observations. Both $Ce_2Sn_2O_7$ and $Ce_2Hf_2O_7$ exchange Hamiltonians are thought to be dominated by the octupolar coupling, consistent with the observation of magnetic diffuse scattering at large momentum transfer in NPD experiments. This was not reported for $Ce_2Zr_2O_7$ so far, which could be explained by similar strengths of the estimated dipolar and octupolar couplings [144, 145]. A similar argument can be drawn looking at the onset of magnetic correlations in heat capacity data, where the stannate and hafnate data overlap while the zirconate signal starts to rise at higher temperature. Interestingly, cooling further down reveals a different behavior with $Ce_2Zr_2O_7$ and $Ce_2Hf_2O_7$ behaving similarly while $Ce_2Sn_2O_7$ drastically differs (Fig. 3.9b). In addition, the INS spectra collected on $Ce_2Hf_2O_7$ at the lowest accessible temperature suggest the concomitance of dipolar and octupolar ice-like correlations. This is consistent with the relatively stronger dipolar couplings assessed in cerium hafnate compared to cerium stannate.

So far, INS experiments on single crystals of $Ce_2Sn_2O_7$ and $Ce_2Hf_2O_7$ have unfortunately not been possible. Nevertheless, measurements on powder samples have already proven to contain a significant amount of information. Both quantum spin ice candidates showed continua of fractional excitations in their neutron spectra. The detailed analysis of the excitation spectra measured on QSL candidates is paramount to verify theory predictions and estimate crucial physical quantities, such as the emergent fine-structure constant in QSIs. Ultimately, single crystal samples and enhanced spectroscopic capabilities are most likely required to extend our understanding of the emergent QED in QSI materials such as $Ce_2Sn_2O_7$.
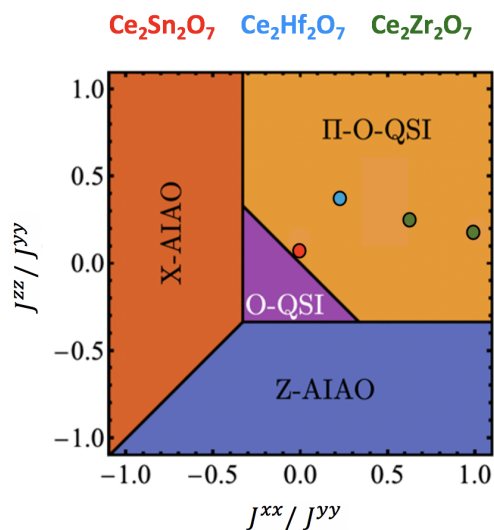
Figure 3.20: Spin ice phase diagram of cerium based pyrochlores. The colored dots represent the estimated position of the three cerium compounds as reported in this work and in the literature [130, 144, 145].

Chapter 4

Structural disorder and magnetic correlations in $Tb_2Hf_2O_7$

Preamble

*T*ERBIUM-based pyrochlores have caught a lot of attention owing to their low temperature magnetic properties. Particularly, $Tb_2Ti_2O_7$ has been the subject of many studies aimed at identifying its ground state as well as the mechanisms involved in its stabilization [156, 160]. At low temperatures (below about 20 K), $Tb_2Ti_2O_7$ develops a spin liquid state, stable down to the lowest temperature accessible, and this despite antiferromagnetic spin interactions estimated to -19 K, based on Curie-Weiss fit of the magnetic susceptibility [161]. Several mechanism have been proposed in order to explain the absence of long-range order in $Tb_2Ti_2O_7$, among which, quantum fluctuations via virtual crystal field excitations[20], structural distortions [162] (although not experimentally observed) or anisotropic exchange [163]. Ultimately, a magnetoelastic mode, emerging from the hybridization of the first low lying excited CEF level and transverse acoustic phonon, has been observed, supporting the idea of dynamical frustration from the strong coupling between spin and lattice degrees of freedom [48, 164].

$Tb_2Hf_2O_7$ is another terbium pyrochlore evading long-range magnetic order. Its magnetic diffuse scattering response in neutron experiments [25] is strikingly similar to $Tb_2Ti_2O_7$ [160]. However, its crystallographic properties display clear signs of strong structural disorder, which may be expected to threaten the stabilization of a spin liquid phase. Indeed, due to the non-Kramers nature of Tb^{3+}, its ground state degeneracy inferred by the D_{3d} symmetry of the CEF at the pyrochlore A site, is not protected. Its magnetic state is thus expected to be very sensitive to structural disorder and Jahn-Teller distortions [165]. Nonetheless, $Tb_2Hf_2O_7$ sports a strong correlated magnetic phase below about 50 K and manages to evade long-range order down to sub-Kelvin temperatures. We hereby present a detailed study of the structural disorder in terbium hafnate and attempt to relate our results to its single-ion properties and low temperature magnetic behavior.

4.1 Structural disorder

We begin our study of Tb$_2$Hf$_2$O$_7$ from its average nuclear structure as reported in [25]. The same samples (powder and single crystal) were used all along the present work. Joined x-ray and neutron diffraction showed that the average structure is best described as being midway between the pyrochlore and defective fluorite structures (see Fig. 4.1). Quantitatively, this equals to 8 % of the 48f oxygen site to be empty, compensated by an occupation of about 50 % of the 8a site, which are usually empty in the pyrochlore case. Such defects, denoted as Frenkel pair defects, have stark consequences as it means that around 50 % of the Tb^{3+} directly experience a defective CEF environment and also equates to 8 % of Tb-O-Tb exchange paths being missing. However, what the average structure determination does not capture is the local disorder engendered by the presence of this high density of defects. Indeed, every missing or additional oxygen ion causes a relaxation or stress of the structure around the associated site, once again affecting the CEF around the Tb^{3+} cations.

(a)   (b)   (c)
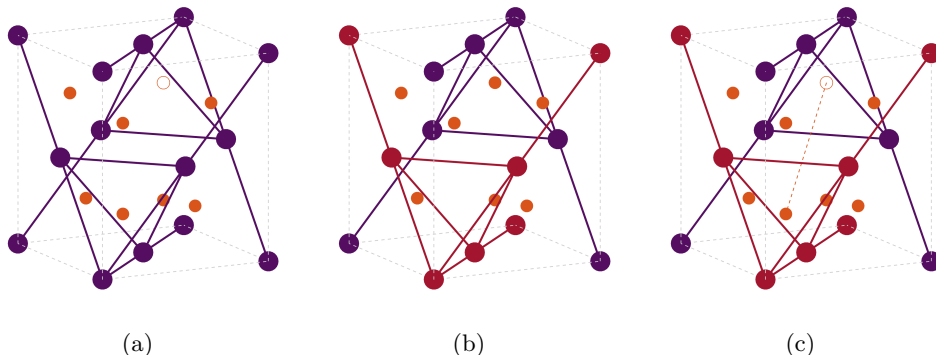
Figure 4.1: Crystallographic structures of (**a**) a defective fluorite, (**b**) a pyrochlore and (**c**) Tb$_2$Hf$_2$O$_7$. The orange circles represent the vacancies in both the defective fluorite and Tb$_2$Hf$_2$O$_7$. Terbium atoms are represented in violet, the hafnium in red and the oxygen in orange. The dotted orange line in (**c**) represents one Frenkel pair defect.

In order to collect more insights on the local disorder, we performed a neutron pair distribution function (PDF, 2.5.4) experiment at room temperature on GEM (ISIS). Reciprocal space data were collected using several detectors covering a large solid angle around the sample. The data were then corrected and normalized to account for background, absorption, multiple scattering and the energy distribution of the incident neutron beam. A sine Fourier transform was then applied to generate the final PDF data sets. We started by fitting the PDF signal using small box modeling ; the average structure determined from diffraction was implemented in PDFGui [117] and compared to experimental observations (see results on Fig. 4.2a). Clear discrepancies appear at several spots of the signal - a particularly strong one being emphasized in Fig. 4.2b. This is a clear demonstration that a single average structure is not able to account for every crystallographic configurations. In order to capture both the average structure as well as the local disorder, big box modeling was performed. The RMCProfile program [118] was chosen to perform this task, allowing to fit both real and reciprocal space data at the same time. The fitting was repeated independently for three different initial structures: one perfect pyrochlore, one fluorite and one having the average structure determined from diffraction. In each case a large box of 5 by 5 by 5 unit cells was created, containing 2000 terbium, 2000 hafnium, 7000 oxygen as well as 1000 vacancies.
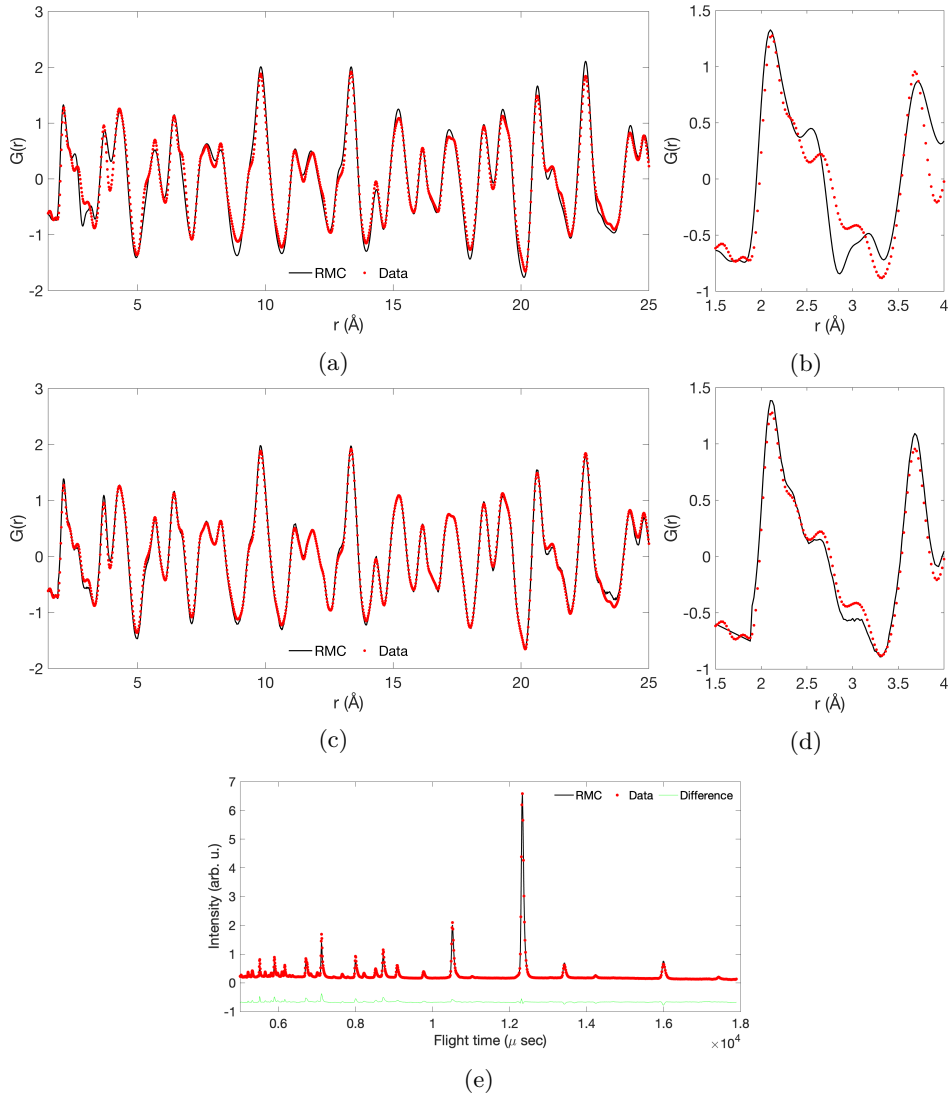
Figure 4.2: (**a-b**) Experimental Pair Distribution Function (PDF) of Tb$_2$Hf$_2$O$_7$ obtained from all detector banks on GEM (red points). The black line is a fit of the PDF using the PDFGui program. (**c-d**) The same experimental data, this time fitted using the RMCProfile program (black line). (**e**) Result of the RMC simulation for the Bragg data used to generate the PDF curves.

Based on these big boxes, Reverse Monte Carlo simulations were performed, fitting both reciprocal and real space data. In all simulations, all atoms were free to move around (within reasonable boundaries to avoid unphysical distances between atoms) and the oxygen and vacancies were allowed to swap their positions. This was repeated several times for each starting structure and the resulting distributions of bond distances and angles were averaged. The three starting structures resulted in very similar final structures, with close to identical distributions of bond angles and distances (the averaged results are displayed in Fig. 4.3a-b). The fits to the PDF data were also equally good, with a χ^2 of about 21 compare to 430 when using the average structure (an example

61

of PDF fit can be seen on Fig. 4.2c). The overall fit is significantly better than solely using the average structure.

Looking at Fig. 4.3a-b, it is clear that the sample contains a large distribution of angles and distances compared to the ideal cases, but that their average values are consistent with the average structure. In addition, the obtained atomic distribution confirms the creation of Frenkel pair defects as the vacant 48f and occupied 8a sites are almost always in close proximity. The spatial distribution of the Frenkel pair defects is illustrated in Fig. 4.3c. One can clearly see particular orientations of these defects as well as a correlation between the orientation and the 'length' of the Frenkel pair. This structural analysis was carried out in collaboration with Prof. Peter M. Derlet (PSI).
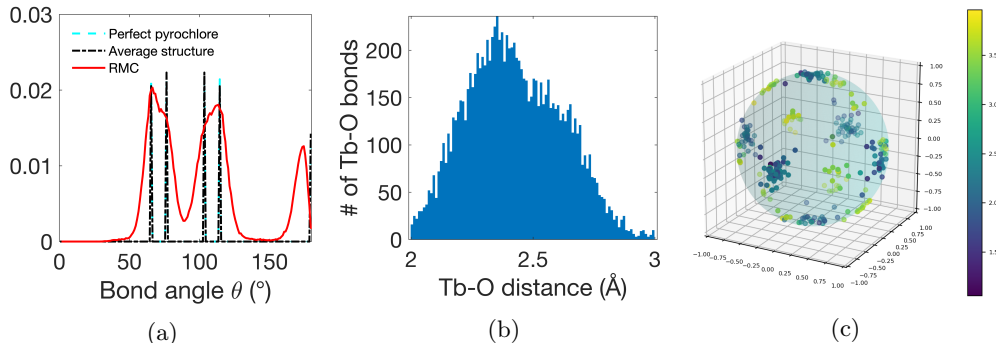
Figure 4.3: (**a**) Comparison between the distribution of O-Tb-O bond angles from the RMC simulation (red line) and the expectations from a perfect pyrochlore (dash cyan line) and from the average structure of Tb$_2$Hf$_2$O$_7$ (black dotted line). The y axis corresponds to the corresponding faction of O-Tb-O. The expectation curves were scaled down in allow for a direct comparison. (**b**) Distribution of Tb-O bond length obtained after the RMC simulation. The y axis gives the number of associated Tb-O bonds. (**c**) Spatial distribution of the created Frenkel pair defects. The position of a dot on the surface of the shaded sphere indicates the orientation of the created Frenkel pair (from the original position toward the new position of an oxygen). The color of the dot indicates the distance between the original and new positions.

One obvious question is whether this simulation of powder data is also able to replicate similar data obtained on a single crystal. An attempt at answering this question was made using the result of the previously described RMC simulation. The obtained list of atom was prepared to be read by the Scatty software [166]. Scatty performs fast Fourier transforms to calculate the diffuse scattering associated with an input list of atoms or spins. Using this program, we could compute neutron scattering maps in particular planes and compare the output against the scattering intensities in identical planes measured on a single crystal with the Laue diffractometer SXD (ISIS). This instrument uses a time-of-flight method to measure and reconstruct a large portion of reciprocal space from a white incident neutron beam [167]. An example of such maps is shown in Fig. 4.4.

Experimental data are quite difficult to interpret as the diffuse intensity coming from the sample is not separable from the noise or instrumental background in a straightforward way. The strong diffuse signal with triangular shape along the HH0 axis is an example of such instrumental signal. Diffuse features located at high momentum transfer, as well as some small 'satellite' reflections (around [118] for instance) are qualitatively replicated by the simulation. Ultimately, the data and the simulation are not
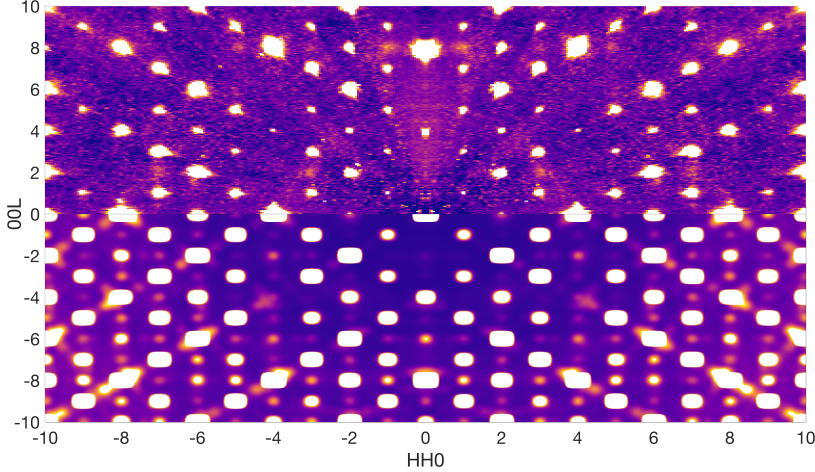
Figure 4.4: Top part: single crystal neutron diffuse scattering map in the HHL plane measured on SXD. Leftover circles of intensity are due to an imperfect subtraction of the Debye-Scherrer cones emanating from the aluminum pin on which the sample is mounted. Bottom part: simulated intensities in the same plane computed using Scatty from the output of the RMC simulation.

in perfect agreement but close enough to speculate that the local disorder uncovered in the powder sample is also present in the single crystal sample ; although further work is required to quantitatively replicate the SXD data, ideally applying MC or RMC methods to the full three dimensional SXD data set. In collaboration with Dr. Arkadiy Simonov and Dr. Nicola Casati, we performed a similar study using x-ray diffuse scattering. A small fragment of single crystal was measured on the MS Beamline of the Swiss Light Source (SLS, PSI). The reciprocal space maps were reconstructed based on the images acquired during a full rotation of the crystal around the vertical axis. The observed diffuse intensity would require a dedicated analysis, perhaps by looking at the associated PDF signal but at the moment we simply compare the measured reciprocal space maps with equivalent planes computed from our RMC simulation using Scatty. For instance, the maps showed in Fig. 4.5 display the same vertical and horizontal lines located in the same regions of reciprocal space.

4.2 Continuum of crystal-electric field states

As already mentioned, the crystal-electric scheme of Tb^{3+} is highly sensitive to disorder. Thus, it does not come as a surprise to see a very complicated CEF spectrum in Tb$_2$Hf$_2$O$_7$, knowing the amount of disorder present in the system. In fact, in this case, the disorder is so strong and spread that one cannot distinguish in between the many CEF transitions probed using INS. Using incident energies of 45 meV and 80 meV on the MAPS spectrometer (ISIS), a continuum of excitations was observed, testifying of the wide distribution of energy levels (Fig. 4.6). This is very different from observations made on Tb$_2$Ti$_2$O$_7$ or Tb$_2$Sn$_2$O$_7$, as reported in [168, 169, 170]. Phonon contributions to the spectrum were removed using a dataset measured in identical experimental conditions on La$_2$Hf$_2$O$_7$. Of course, this subtraction does not take into account the impact of the structural disorder on the phonon excitations but is nonetheless expected to subtract the strongest contributions due to their cooperative nature. Additionally, phonons
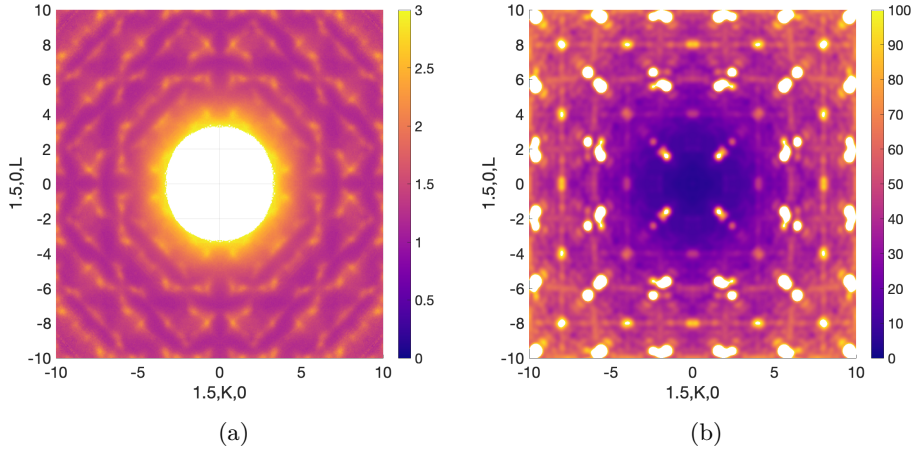
Figure 4.5: Experimental (**a**) and simulated (**b**) maps of the $(1.5, k, l)$ plane in reciprocal space. The simulated map was computed from the result of the Reverse Monte Carlo simulation using the program Scatty.

typically show up at relatively high momentum transfer in INS experiments, thus not expected to contribute strongly in the integrated momentum window.
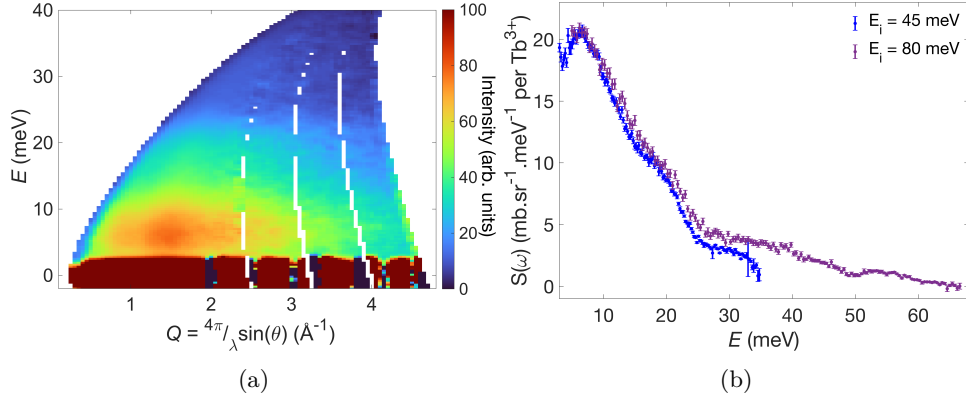
Figure 4.6: (**a**) INS map of Tb$_2$Hf$_2$O$_7$ measured on MAPS with incident energy of 45 meV. Phonon contributions are removed using a nonmagnetic analog (La$_2$Hf$_2$O$_7$). (**b**) Constant-Q cuts in the INS data in the E$_i$ = 45 meV and E$_i$ = 80 meV data, giving corresponding energy resolutions of approximately 1.5 meV and 2.6 meV. The data were integrated between 1.45 Å and 2.3 Å and between 2.3 Å and 3.6 Å, respectively.

Given the instrumental resolution at the employed incident energies, it is clear that a few sets of CEF energy levels would not be able to reproduce the experimental data. This is illustrated in Fig. 4.7a, where the spectrum recorded with E$_i$ = 45 meV is plotted together with point charge simulations of four possible oxygen environments around Tb^{3+} in Tb$_2$Hf$_2$O$_7$, all based on the determined average structure. The first one is a perfect CEF environment where the Tb^{3+} ion has the proper eight oxygen neighbors ; six of them occupying the 48f site and the two others the 8b site (see Fig. 4.7b). The second environment is missing a 48f oxygen whereas the third environment is missing a 48f oxygen but has an extra 8a oxygen. The last one has all its 48f oxygens as well as

an additional one on the 8*a*. Looking at Fig. 4.7a, one can easily conclude that many more CEF environments are necessary to explain the spectrum, as a simple broadening of the displayed excitations would still fall short of reproducing this large continuum.

(a)　　　　　　　　　　　　　　　(b)
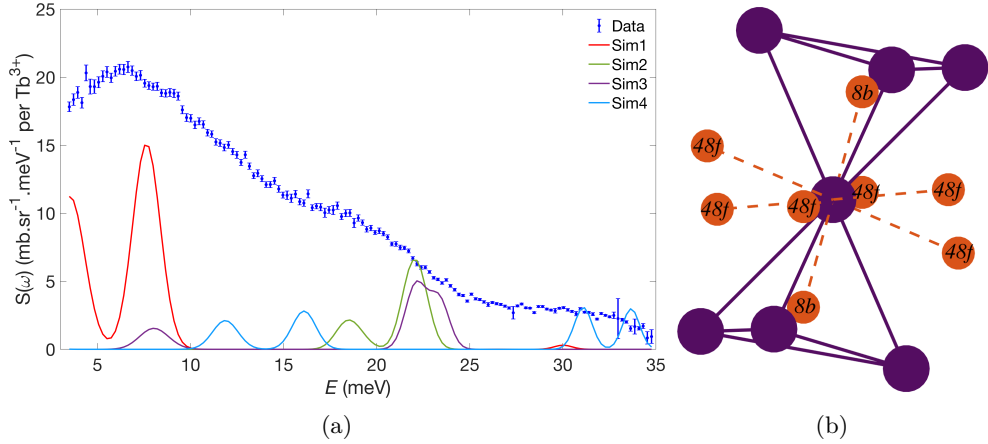
Figure 4.7: (**a**) Crystal-electric field spectrum of $Tb_2Hf_2O_7$ measured on MAPS with incident energy of 45 meV (blue points with error bars). The simulations plotted here are point charge calculations of the CEF schemes based on four different possible oxygen configurations around the Tb^{3+} ions using the PyCrystalField package [139]. (**b**) Disposition of the O^{-2} anions (orange spheres, containing the corresponding crystallographic site denomination) around the Tb^{3+} cations (violet spheres).

In order to better reflect the CEF spectrum, we used the point charge calculation (PCC) capabilities of PyCrystalField [139], but this time based on the 2000 Tb^{3+} ions and associated neighboring oxygens from the RMC simulation. The CEF scheme is calculated in the intermediate-coupling regime based on the remarks made in [170]. Using this approach, the only parameters are the charges attributed to the oxygen neighbors. One typically assumes a negative charge of two electrons for oxygen ligands and then fit the CEF transitions by varying the charges, discriminating between apical and basal oxygens. Unfortunately this is not a reasonable course of action in the present case due to the significant overlap of numerous CEF excitations. Furthermore, the majority of the oxygens are now slightly away from their ideal crystallographic sites, implying that almost all oxygens should be attributed a slightly different charge in order to account for the various bondings that the point charge calculation is trying to approximate. In order to reflect this effect, the Tb-O distances were slightly rescaled prior to the point charge calculations and the associated oxygen charges were renormalized based on these new distances, as proposed in [171]. In addition, a systematic search was performed to determine the best starting values for the apical and basal oxygen charges, based on the comparison between the experimental and simulated spectra. The simulated data were obtained by summing all the individual calculated CEF spectra, followed by a renormalization of the total signal (division by 2000 to get a signal per Tb^{3+}) as well as a global rescaling factor. The best fit can be seen in Fig. 4.8a.

One can notice an obvious discrepancy at low energy transfer, with the simulation clearly overestimating the signal but providing a good qualitative agreement above 7 meV. Probing the low energy part of the CEF spectrum using the Eiger triple-axis spectrometer (SINQ) further shows a CEF spectrum peaked around 10 meV, clearly decreasing in intensity at lower energies (see Fig. 4.8b). This suggests an inconsistency of the PCC with respect to the data and motivated an in-depth investigation of the

(a)   (b)
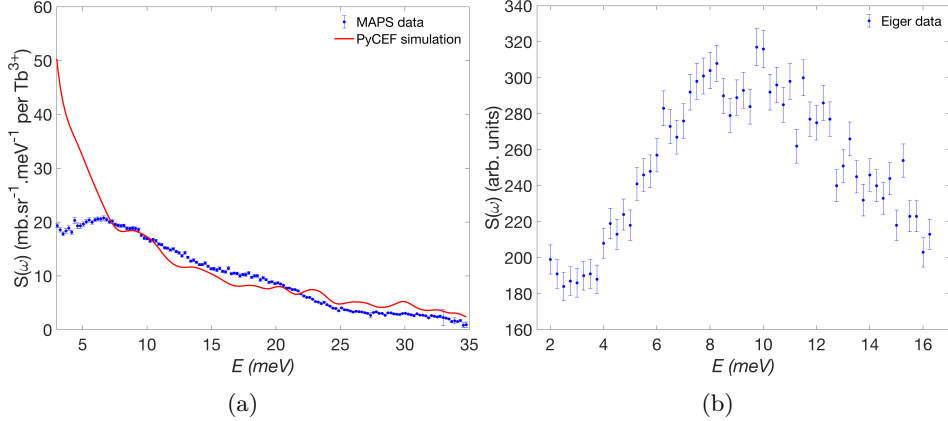
Figure 4.8: (**a**) Crystal-electric field spectrum of $Tb_2Hf_2O_7$ measured on MAPS with
incident energy of 45 meV (blue points with error bars). The red line is the full CEF
model as described in the main text. (**b**) Low energy CEF spectrum of $Tb_2Hf_2O_7$ mea-
sured using the triple axis spectrometer Eiger (SINQ) at 50 K.

simulated spectra. As it turned out, the strong signal at low energy transfer emanates
from overly split ground-state doublets. Indeed, the degeneracy of the ground-state,
expected in the ordered case, is actually lifted by the disorder, leading to split singlets.
Most of these splittings are quite small (about 60 % are below 0.1 meV, with a median
value of 0.096 meV) and are therefore englobed by the elastic line. But some splittings
are calculated as being as high as a few milli-electronvolts, effectively causing the calcu-
lated spectrum to differ at energies below 7 meV. The distribution of the ground-state
splittings can be found in Fig. 4.9b. Disregarding splittings above 1.3 meV (about 10 %
of the environments) reaches a rather satisfactory agreement with the experimental
data and is adopted as our CEF model (which can be seen in fig.4.9a). The justifi-
cation for disregarding these levels is simply that they are not observed in any of our
measurements, at least not with this intensity (cold INS seem to confirmed the absence
of CEF levels between our selected threshold value of 1.3 meV and the next excited
levels). There could be several reasons for their appearance in the calculation. RMC
simulations cannot directly account for systematic error in the data, for instance coming
from finite size effects. However such effect would typically produced minor errors. A
more plausible explanation is the overestimation of the defect population discussed here
(almost cubic CEF env.) due to the limited size of the big box used [172]. Finally, more
stringent constraints and/or other data sets (for instance using x-ray PDF or EXAFS)
could perhaps tell us more about the presence or not of such ionic configurations [118].
Finally, the PPC is know to be a crude approximation, giving starting values allowing to
then fit the experimental data [171]. This might enhance possible mistakes of the RMC
simulation. Unfortunately, in our case, we cannot perform a fit due to the continuous
nature of the signal and must discard these large splittings instead.

The first take home message, from the confrontation between our model and the INS
measurement, is that about 90 % of our simulated CEF environments are in reasonable
agreement with the data, providing a good qualitative approximation of the CEF spec-
trum. The second significant finding is that we are dealing with a broad distribution
of single ion states, as evidenced by the many different values of ground state splitting
(Fig. 4.9b). However, this lifting of the degeneracy does not mean that $Tb_2Hf_2O_7$ is not
a magnetic system. On the contrary, as we shall see later, $Tb_2Hf_2O_7$ shows a strong

magnetic signal. In fact, this precise type of disorder (non-magnetic disorder) has been proposed as a mechanism allowing to stabilize a quantum spin liquid in non-Kramers rare-earth pyrochlores [19, 21, 22]. In this instance, the splitting of the ground state doublets allows the coupling of transverse fields with the magnetization's quadrupolar degrees of freedom, introducing transverse terms in the spin ice Hamiltonian. We shall now attempt to connect our finding on the single ion properties to the low temperature magnetic behavior of Tb$_2$Hf$_2$O$_7$, where clear signs of correlations appear.
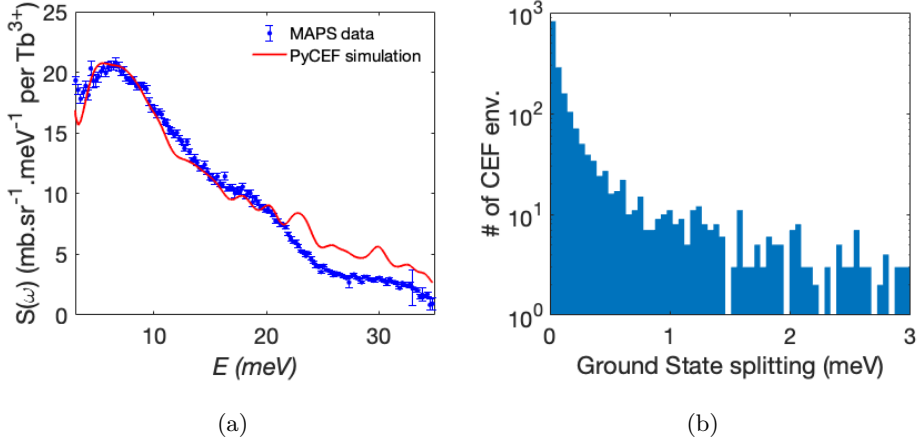
Figure 4.9: (**a**) Crystal-electric field spectrum of Tb$_2$Hf$_2$O$_7$ measured on MAPS with incident energy of 45 meV (blue points with error bars). The red line is the CEF model described in the text. (**b**) Energy splitting distribution of the ground-state doublet obtained from point charge calculation of the CEF based on the results of RMC simulations.

4.3 Signatures of correlated physics

4.3.1 Magnetic susceptibility

Let us first look at the magnetic susceptibility measured on a powder sample and showed in Fig. 4.10a. The red lines represent the expected magnetic susceptibility from our CEF model, which considers single ion physics only. The two curves agree above 100 K, but then start to deviate slightly, until the temperature reaches about 40 K, at which point there is clear difference between the two. Below 40 K, the experimental curve increases much slower than the calculated one, suggesting the presence of correlations.

The local magnetic susceptibility (Fig. 4.10b), was previously measured on the 5C1 diffractometer at the LLB (Saclay, France). This instrument could measure the flipping ratio of a previously polarized neutron beam after interaction with the sample (subject to a magnetic field), giving access to magnetic susceptibility tensor. The local susceptibility tensor was computed assuming a perfect F$d\bar{3}m$ space group symmetry. The parallel and perpendicular components of the local magnetic susceptibility clearly differ, with the former remaining close to zero, suggesting a strongly Ising character of the Tb^{3+} magnetic moments. Thus, the magnetic moments are expected to point in a direction close to their local (111) axis, despite the substantial disorder and distribution of single ion states evidenced in the previous section.
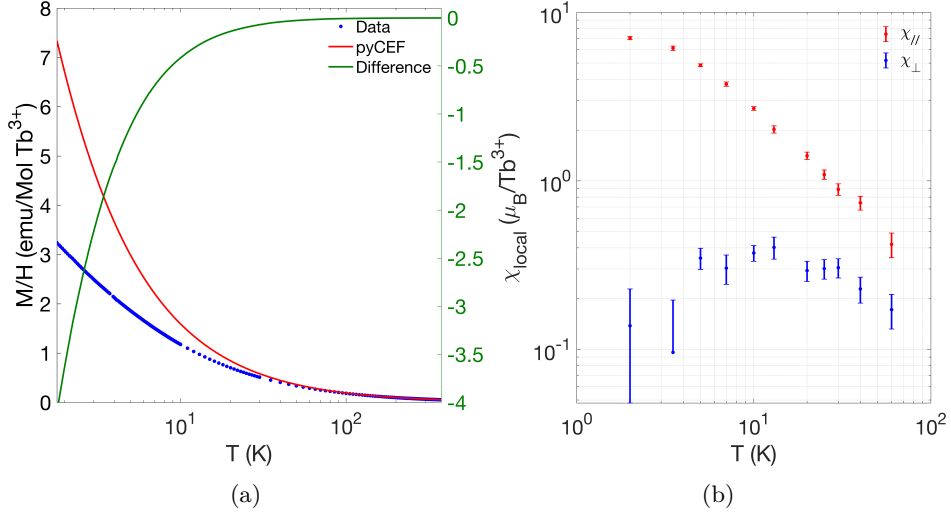
Figure 4.10: (**a**) Magnetic susceptibility as a function of temperature measured on a powder sample of Tb$_2$Hf$_2$O$_7$, under a magnetic field of 1000 Oe. The data are displayed by the blue points whereas the red line represents the expected susceptibility based on the CEF model. The green line is the difference between the two. (**b**) Local magnetic susceptibility measured on a single crystal of Tb$_2$Hf$_2$O$_7$, using neutron polarimetry.

4.3.2 Specific heat

The presence of correlations can also be spotted in the specific heat data. The raw data had to be corrected so as to isolate the contribution of the magnetic correlations. Lattice contributions were subtracted using measurements performed on La$_2$Hf$_2$O$_7$, whereas the CEF contributions were accounted for based on our CEF model (as described previously). A tail signal stemming from the hyperfine contribution was modeled and removed considering a Schottky-like function with an energy gap of about 0.24 meV, giving a peak with a maximum located at approximatively 0.1 K [173]. The obtained magnetic contribution to the specific heat is shown in Fig. 4.11, taking the shape of a Schottky-like signal peaked at 1 K. The recovered magnetic entropy S, obtained by integrating C_{mag}/T over the covered temperature range, is also plotted. The recovered value of magnetic entropy (dashed dark blue line) lies quite a bit below the expectation for a spin ice (dashed green line in the plot). The attempt to account for a contribution at temperatures lower than the accessed range using a straight line down to 0 K did not significantly raise the recovered entropy (dashed light blue line). This result is in stark contrast with observations made on Tb$_2$Ti$_2$O$_7$, where the recovered magnetic entropy was clearly higher than the expectation for a two-levels system [161]. In our case, the splitting of the ground state doublet, owing to the disorder as explained previously and displayed in Fig. 4.9b, is believed to introduce some magnetic defects. Indeed, some Tb ions, with large ground-state splitting are expected to behave as non-magnetic singlets. An attempt at estimating the amount of such defect was made, based on the theoretical predictions for a diluted spin ice derived in [174] (purple curve in Fig. 4.11). However, our curves intersect the theoretical one in a rather flat region, refraining us to make any reliable claims. Nevertheless, a possible evaluation of the fraction of nonmagnetic Tb ions is indicated in Fig. 4.11, translating into about 18 % of defects.

4.3.3 Inelastic neutron scattering

In a previous work [25], magnetic diffuse scattering was measured on a single crystal using the D7 (ILL) diffractometer. In this instance, the observed signal was reminiscent of a magnetic Coulomb phase. Using neutron TOF spectroscopy on FOCUS (SINQ), we could separate the quasi-elastic and inelastic contributions with a resolution of approximatively 0.05 meV in the temperature range going from 0.05 T to 300 K (see Fig. 4.12). Spectra representative of the different temperature regimes are shown in Fig. 4.13. The data were modeled using a Gaussian and Lorentzian functions to fit the quasi-elastic and inelastic contributions respectively. Upon cooling below 100 K, an increase of both the quasi-elastic and inelastic contribution is observed (Fig. 4.12a). The elastic signal then reaches a region of slower increase, between 1 K and 10 K. Passed 1 K, the inelastic contribution starts to decrease and appears as gapped (Fig. 4.12b). On the other hand, the elastic intensity resumes its growth, first sharply at 1 K, and then steadily down to the lowest measured temperature. This change of behavior around 1 K was already spotted in μSR data reported in [25] and corresponds to a partial freezing of the spin degrees of freedom. Such freezing could have a similar explanation as the missing recovered entropy in the specific heat data, or could alternatively come from the distribution of exchange paths originating from the structural disorder.
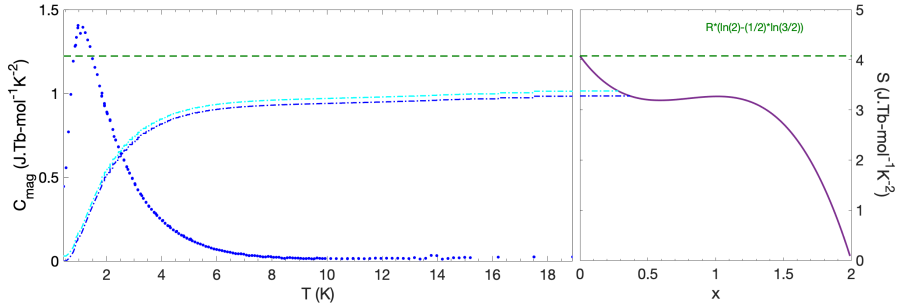
Figure 4.11: Left panel: Magnetic contribution to the specific heat (blue points peaking at low temperature) and recovered entropy (blue and cyan curves). The blue recovered entropy curve is obtained by integrating the experimental signal as a function of temperature. The cyan curve includes an estimation of the missing specific heat signal at temperatures lower than accessed here using a linear interpolation to 0 K. Right panel: Predicted recovered entropy as a function of nonmagnetic doping on the A site.

INS was also performed on a single crystal at IN5 (ILL), using a $\lambda = 5.5$ Å incident wavelength. Data were recorded at the lowest temperature accessible (about 0.04 K) as well as at higher temperature (100 K). This second data set is used to remove nuclear and background contributions from the low temperature data set. The obtained difference is displayed in Fig. 4.14a. The shape of the diffuse signal is identical to what was observed using the D7 diffractometer (summing both spin channels) [25], in the resolution of the experiment (0.06 meV at the elastic line). Looking at the inelastic response (Fig. 4.14b), one can clearly see a broad continuum of excitations peaked around 0.5 meV. The inelastic neutron spectra retains a weak structure in **Q** (Fig. 4.14c) and appears slightly dispersive (Fig. 4.14d). Its center appears to be higher in energy compared to the FOCUS data. Probable origins of this disagreement are the nature of the sample (powder on FOCUS and single crystal on IN5), a slightly higher base temperature for the FOCUS experiment, as well as the subtraction of the high temperature data done for the IN5 data. The exact subtraction cannot be rigorously carried out for
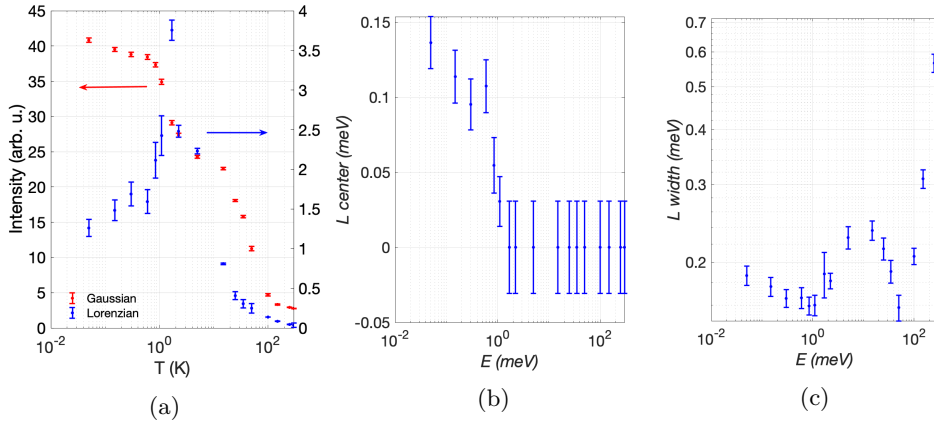
Figure 4.12: (**a**) Temperature dependence of the intensities from the elastic (red) and inelastic (blue) contributions. Temperature of the position (**b**) and width (**c**) of the lorentzian fit to the inelastic contribution.
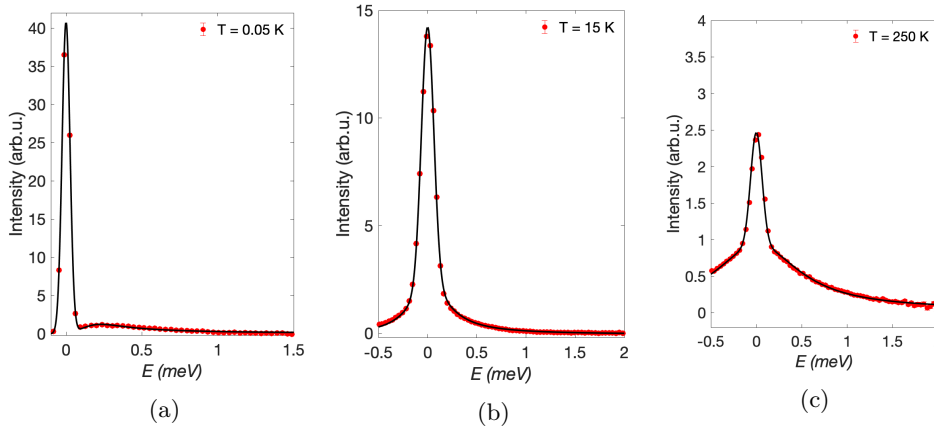
Figure 4.13: Inelastic neutron spectra of Tb$_2$Hf$_2$O$_7$ using the time-of-flight instrument FOCUS measured at 0.05 K (**a**), 15 K (**b**) and 250 K (**c**). The black lines represent the best fits obtained using a Gaussian function for the quasi-elastic signal and a Lorentzian function for the inelastic signal, taking into account the effect of temperature.

the FOCUS data, as the two data sets were collected during different experiments and using different sample environments. Nonetheless a quick attempt at subtracting both data sets does yield a spectrum similar to the IN5 one.

4.4 Magnetic field-induced behavior

4.4.1 Magnetization

In order to gain further insight into the low temperature magnetic properties of Tb$_2$Hf$_2$O$_7$, its magnetization as a function of applied magnetic field was measured at 0.5 K and up to 8 T. The field was applied along three high symmetry crystallographic
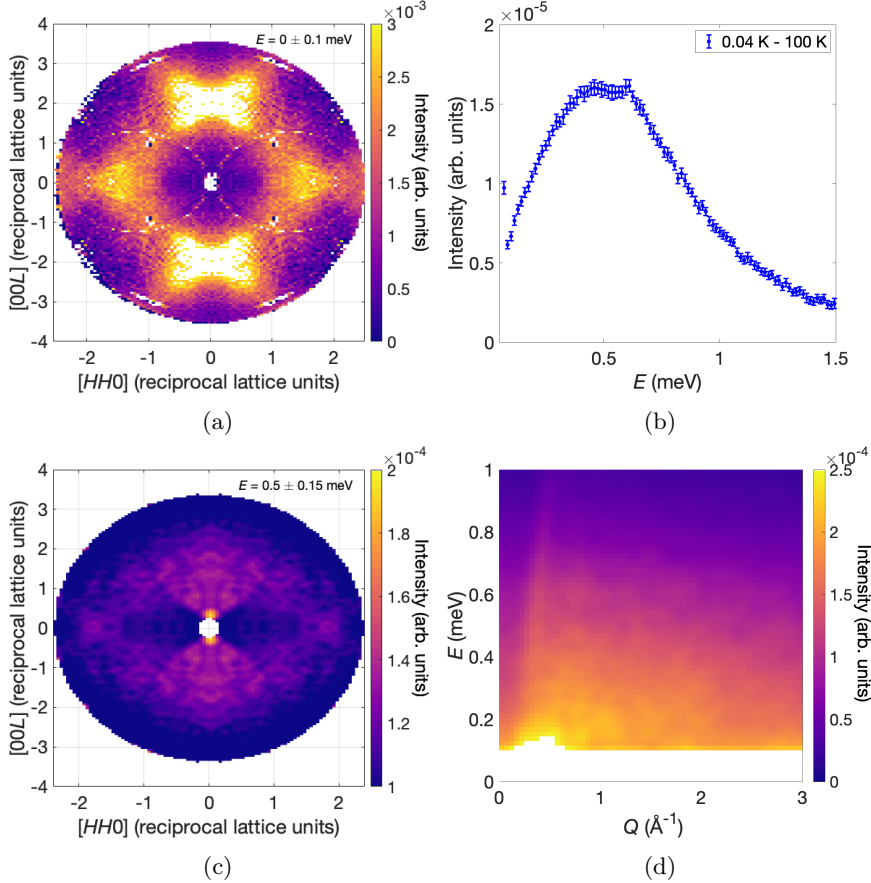
Figure 4.14: (**a**) Magnetic diffuse scattering obtained by subtracting high temperature data to the low temperature data. Both data set were integrated over $\pm$ 0.06 r.l.u. (reciprocal lattice units) in the direction perpendicular to the scattering plane. The obtained S(**Q**,E) was integrated over $\pm$ 0.1 meV in order to produce this map. (**b**) Energy dependence of the spin-spin correlation function obtained by integrating the low and high temperature datasets over all **Q** and subtracting the high temperature S(E) from the low temperature one, taking into account the Bose factor. (**c**) **Q** dependence of the continuum of excitation around its maximum in the non-subtracted low-temperature data. (**d**) Dynamical structure factor measured at low temperature integrated over all **Q** directions in the non-subtracted low-temperature data.

directions of the pyrochlore structure, namely the [001], [1$\bar{1}$0] and [111] directions (displayed in Fig. 4.15). At first glance, two observations can be made. First, the three signals do not show a clear saturation at high field, suggesting a significant degree of frustration. Second, the usual hierarchy of magnetization in a spin ice is not respected, where one would expect $M_{[001]} > M_{[111]} > M_{[1\bar{1}0]}$. The slow increase of the magnetization, not yet saturated under 8 T is reminiscent of observations made on its sister compound Tb$_2$Ti$_2$O$_7$ [175], implying a very anisotropic exchange interaction. The expected magnetization curves calculated from our CEF model are plotted in red. It is clear that the single ion physics is not able to reproduce the measured data on its own and that interactions between the magnetic moments have to be taken into account, even at high magnetic field values. In order to determine the magnitude and shape of

the exchange tensor, we looked at the magnetic structures induced by the application of an external magnetic field along particular crystallographic direction.
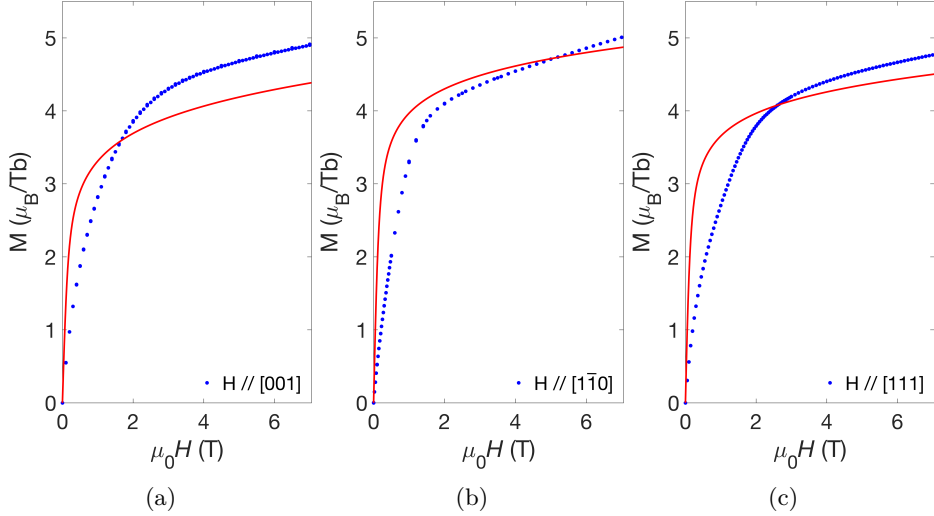
Figure 4.15: Magnetization versus magnetic field measured on a single crystal of Tb$_2$Hf$_2$O$_7$ at 0.5 K, with the field applied along the [001] (**a**), [1$\bar{1}$0] (**b**) and [111] (**c**) crystallographic directions. The data points are showed in blue while the red lines depict the corresponding expected curves calculated from our CEF model.

The determination of the induced magnetic structure will be treated in the next section but the main outcome is the similarity between the magnetic structures found in Tb$_2$Hf$_2$O$_7$ and its sister compound, the heavily studied Tb$_2$Ti$_2$O$_7$. Considering they also display similar magnetic diffuse scattering, it seemed reasonable to assume an exchange tensor for terbium hafnate similar to that of terbium titanate. We chose a tensor identical to what was proposed in [176, 177] as our stating point. The exchange Hamiltonian was added to the CEF, spin-orbit and Zeeman Hamiltonians in order to perform a mean-field analysis using again the 2000 terbium atoms of our RMC simulation. Following the same formalism as in [176]. Considering two spins located at R_i and R_j, we define the direction **c** as the direction linking the two spin (**c**= R_{ij}). The direction **a** is perpendicular to R_{ij} and contained in the planed defined by the *local* z-axis of site i and j (pointing toward the center of their tetrahedron). The last direction, b, is taken as the cross product of c and a. We define the interaction between the spins along these three directions as $\mathcal{J}_a$, $\mathcal{J}_b$ and $\mathcal{J}_c$. Once written in the global reference frame (corresponding to the main axis of the pyrochlore lattice), the shape of the tensor depends on the respective sites of the two interacting spins. For example, the spins located at $(1/4, 3/4, 0)$ and $(0, 1/2, 0)$ will interaction through the tensor:

$$\begin{bmatrix} \frac{(\mathcal{J}_c+\mathcal{J}_b)}{2} & \frac{(\mathcal{J}_c-\mathcal{J}_b)}{2} & 0 \\ \frac{(\mathcal{J}_c-\mathcal{J}_b)}{2} & \frac{(\mathcal{J}_c+\mathcal{J}_b)}{2} & 0 \\ 0 & 0 & \mathcal{J}_a \end{bmatrix} \quad (4.1)$$

so far neglecting the dipolar interaction. We start by setting $\mathcal{J}_a = 1.29$ K (dominant coupling estimated from the position of a kink in the derivative of the magnetization for a field applied along the [111], see Appendix 6.4), $\mathcal{J}_b = 0.196$ K and $\mathcal{J}_c = 0.091$ K.

The first step was to determine the zero-field spin configuration by running several iterations of the mean-field until convergence of the structure. This was done with different starting spin configurations to test the robustness of the simulation. The only way to check our results is to compare the measured magnetic diffuse scattering against the magnetic diffuse intensity computed from our mean-field model. Preliminary results can be seen in Fig. 4.16, showing a diffuse pattern somewhat similar to that of the neutron scattering maps. Some spots resembling magnetic Bragg peaks seem to appear and suggest that the magnitude of the exchange tensor components might not be completely accurate. To progress on the estimation of these exchanges, the mean-field is currently being expanded to the non-zero magnetic field and compared with the magnetization as a function of magnetic field reported earlier (Fig. 4.15).
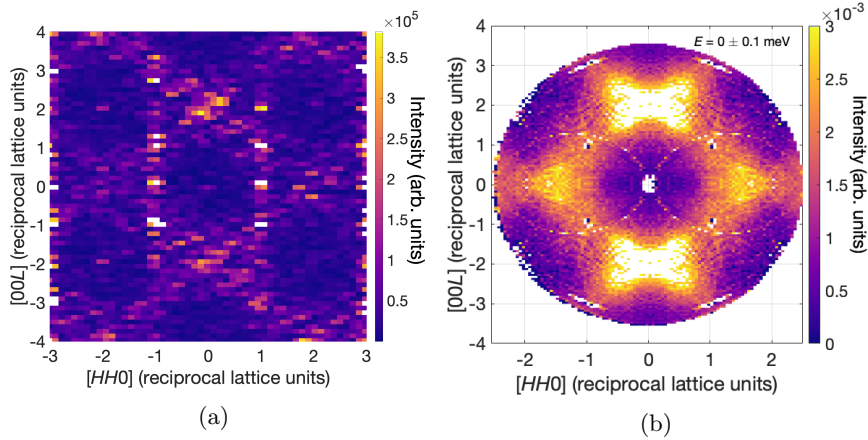
Figure 4.16: (**a**) Magnetic diffuse scattering in the [HHL] plane computed from our mean-field model in absence of magnetic field. (**b**) Measured magnetic diffuse scattering as described in the previous section.

4.4.2 Field-induced magnetic structures

The magnetic field induced magnetic structures were investigated at 0.05 K, using neutron scattering with fields applied along two crystallographic directions: the [1$\bar{1}$0] and [111]. Experiments were performed on two instruments: D23 (ILL) and Zebra (SINQ). In both cases, many Bragg reflections were measured in zero-field as well as at several magnetic field magnitudes. The magnetic field dependence of some Bragg peaks was also recorded (in both field directions).

Let us start with the [1$\bar{1}$0] field direction. The appearing peaks under the effect of the magnetic field could be indexed using a $\mathbf{k} = (0,0,0)$ propagation vector. The application of a field in that direction lowers the symmetry of the system, going from the F$d\bar{3}m$ pyrochlore space group to the I$4_1/amd$ one. This latter is the highest subgroup of F$d\bar{3}m$, consistent with $\mathbf{k} = \mathbf{0}$ and allowing a non-zero magnetization along the [1$\bar{1}$0] direction (corresponding to the [1,0,0] direction in the new I$4_1/amd$ space group). Carrying out the symmetry analysis in the new space group, the only irreproducible representation allowing for a net magnetization along the field is Γ_9, with two independent Tb sites often denoted as α (local anisotropy axis has a non-zero projection on the field direction) and β (local anisotropy axis perpendicular to the field direction). The magnetic structure is then described using six parameters (c1-c6), as was explained in details in the case of Tb$_2$Ti$_2$O$_7$ [178]. The fit to the data was performed on the

magnetic intensities collected at various fields (one fit per field value) using the Full-ProfSuite program [179]. The magnetic field dependence of some reflections (Fig. 4.17) was fitted together with the magnetization data collected with the same field orientation (Fig. 4.15c, magnetization was collected at 0.5 K but no big difference related to the magnetic structure is expected compared to data collected at lower temperatures), using a non-linear-least-square method. The result of this combined fit can be seen in Fig. 4.18.
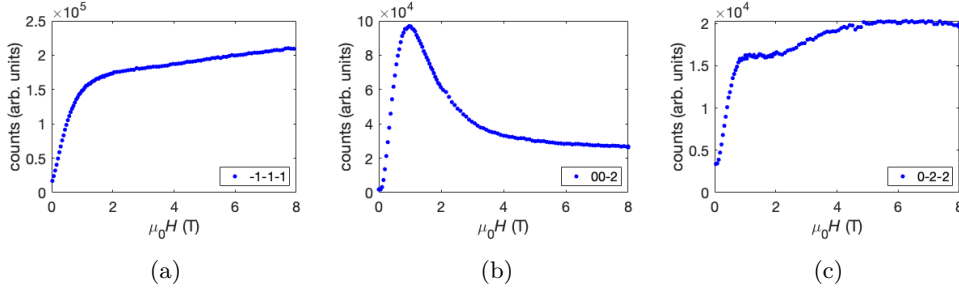
Figure 4.17: Magnetic field dependence of the (**a**) (-1,-1,-1), (**b**) (0,0,-2) and (**c**) (0,-2,-2) magnetic reflections induced for a field applied along the [1$\bar{1}$0] directions.

Both analysis proved to be more reliable and consistent if the c1 and c3 coefficients are restricted to be close to zero, thus suggesting a weak, if any, magnetization perpendicular to the field direction. The combined fit to the data describes a structure where the α spins lie along their local easy axis, pointing in such a way to have a positive projection with the field. As the field strengthens, the α-chain gradually polarizes, slowly leaving the easy axis to align more and more with the field direction (see Fig. 4.18). On the other hand, the spins on the β-chain initially grows pointing opposite to the field, for small field amplitude. The β moments flip to align with the field roughly between 1 T and 2 T, and steadily increase with the field (see Fig. 4.18). Note that some very weak forbidden reflections seem to appear at high field values, coherent with a possible **k** = (0,0,1) propagation. This observation was made in Tb$_2$Ti$_2$O$_7$ for magnetic fields misaligned from the crystallographic [1$\bar{1}$0] direction. In our case these reflections appear only at the high field and remain very weak which may relate to the relatively good orientation of the sample with respect to the magnetic field.

A similar analysis was performed for the [111] field direction. Once again, the rising magnetic reflections could be accounted for using a **k** = (0,0,0) propagation vector. This time, the space group R$\bar{3}$m is found to be the highest subgroup of F$d\bar{3}$m allowing a homogeneous and invariant net magnetization along the field direction. In this configuration, the Tb site splits into two inequivalent sites with different magnetic representations. As was demonstrated in the case of Tb$_2$Ti$_2$O$_7$ [180], Γ_3 is the appropriate irreproducible representation for both Tb sites, allowing to model the magnetic structure without further lowering of symmetry. In this case, the first Tb site (occupying the 3b site in this formalism, thus having its easy axis along the field) is described by a single mode, whereas the second one (9e site) has two possible modes, leading to a total of three parameters. Using this model to fit datasets of Bragg peaks obtained at various field amplitudes, it is difficult to discriminate between the '3-in-1-out' and 'all-in-all-out' structure types. In order to introduce more constrains to the model, a combined fit of a few magnetic peak field dependence (Fig. 4.19) and of the magnetization measured with this field direction (Fig. 4.15c, also measured at 0.5 K) was implemented using the same method as in the previous field direction. The result of the fit can be found in Fig. 4.20.
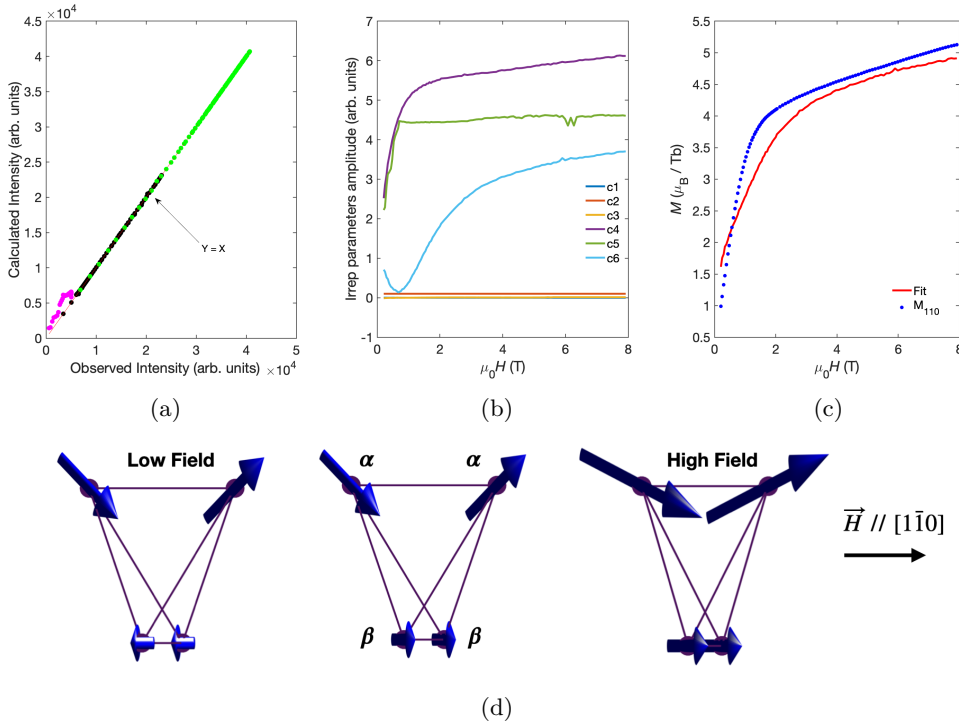
Figure 4.18: (**a**) Observed versus calculated magnetic Bragg intensities from the combined fit of the magnetic field dependence of magnetic Bragg peaks and magnetization for the [1$\bar{1}$0] direction. Each color corresponds to a given Bragg reflection. (**b**) Magnetic field dependence of the irreproducible representation's coefficients used to determine the magnetic structure. (**c**) Fit of the bulk magnetization using the combined fitting approach. (**d**) Sketch of the induced magnetic structure as a function of applied magnetic field in the [1$\bar{1}$0] crystallographic direction.

This approach favored the '3-in-1-out' structure and confirmed some observations made on the fits of the large datasets.

The induced magnetic structure appears to be '3-in-1-out' for all field values. However it undergoes some variations which can be described as follow: the only change for the Tb siting at the 3b site is the magnitude of its magnetic moment, which grows together with the field. Indeed the field is applied in the same direction as its easy axis. Things are a bit different for the three other Tb^{3+}. At low field values, the moments of the 9e site, which easy axes are at about 109.47° away from the field direction, gradually tilt towards the plane formed by the same three atoms. The trend then reverses and the moments realign with their respective easy axes. At higher field amplitude, the moment slowly polarize with the field, saturating when pointing directly to the 3b Tb atom. The evolution of the magnetic structure as a function of field magnitude is depicted in Fig. 4.20.

4.4.3 Inelastic neutron scattering under magnetic field

In addition to our study of the field induced magnetic structures, we used IN5 to look at the influence of a magnetic field applied along the [1$\bar{1}$0] direction on the diffuse scattering and excitations in Tb$_2$Hf$_2$O$_7$. The diffuse scattering at the elastic line is
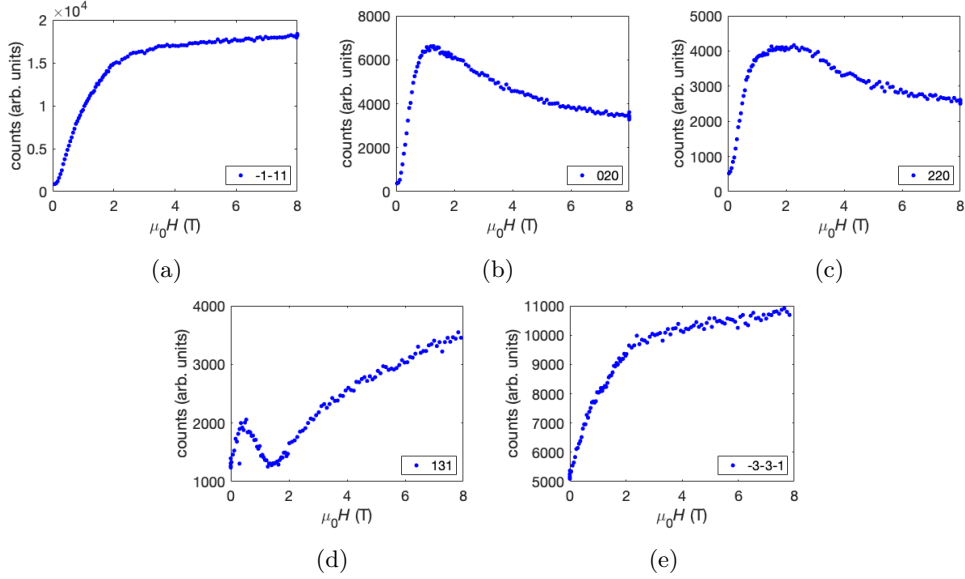
Figure 4.19: Magnetic field dependence of the (**a**) (-1,-1,1), (**b**) (0,2,0), (**c**) (2,2,0), (**d**) (1,3,1) and (**e**) (-3,-3,-1) magnetic reflections induced for a field applied along the [111] directions.

shown in Fig. 4.21a,b for magnetic field of 0.5 T and 2.5 T. The most notable feature is the apparition of a Bragg reflection at (00±2), which was a region of strong diffuse signal in zero field. The map at 0.5 T still displays some diffuse scattering with a similar Q-dependence compared to the zero field map. At 2.5 T, this broad diffuse scattering is almost gone. However we can observe some diffuse spots around the (112) points implying that some short-range correlations are still present. If the diffuse scattering around these points does end up forming Bragg peaks, their indexing would require the use of a magnetic propagation vector different than $\mathbf{k} = (0,0,0)$ as the mixed parity of the Miller indices corresponds to 'forbidden' momentum transfers in the F$d\bar{3}m$ space group. This was not observed in the diffraction data collected on D23 and Zebra, either because the intensities were too small or because of a field misalignment in the IN5 experiment. This misalignment effect was already spotted and studied in the case of Tb$_2$Ti$_2$O$_7$ [180].

In Fig. 4.21, we compare the Q-average spectra of the measurements collected with and without magnetic field. Interestingly, the broad continuum changes very little between 0 T and 0.5 T, indicating the survival of the collective excitations. The signal is then strongly reduced at 2.5 T. Looking at the Q-dependence of the scattering at 0.5 meV, around the maximum of the excitation, we see an almost unchanged signal at 0.5 T, whereas at 2.5 T the signal is almost isotropic in the [HHL] plane. Concerning the S($\mathbf{Q}$,E), the data collected at 0.5 T again appear unchanged compared to the zero field. At 2.5 T, the intensity of the signal is significantly suppressed and no dispersive mode is observed, suggesting the absence of well defined spin waves even at 2.5 T.

Plotting the intensity of the elastic and inelastic contributions to the spectra as a function of applied magnetic field (Fig. 4.23), we see that both signals have opposite behaviors. Interestingly, the increase of the elastic intensity is only partially compensated by the decrease of the inelastic contribution, meaning that intensity outside of the experimental window seems to move into the observed Bragg peaks upon application of
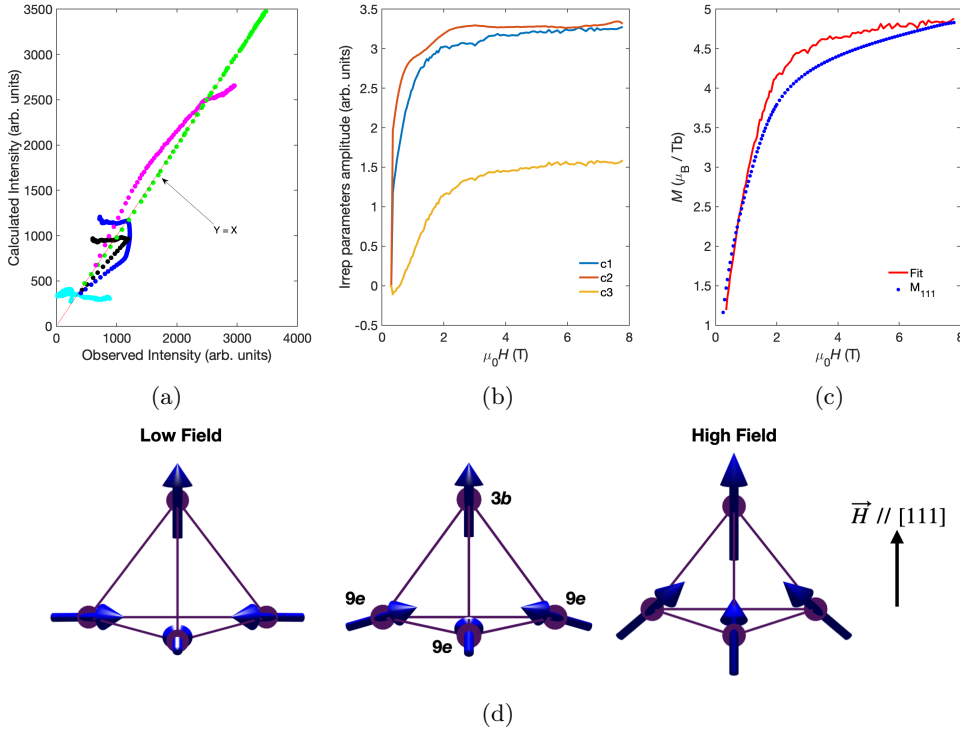
Figure 4.20: (**a**) Observed versus calculated magnetic Bragg intensities from the combined fit of the magnetic field dependence of magnetic Bragg peaks and magnetization for the [111] direction. Each color corresponds to a given Bragg reflection. (**b**) Magnetic field dependence of the irreproducible representation's coefficients used to determine the magnetic structure. (**c**) Fit of the bulk magnetization using the combined fitting approach. (**d**)Sketch of the induced magnetic structure as a function of applied magnetic field in the [111] crystallographic direction.

a magnetic field. Alternatively, the application of a magnetic field might cause of mix of CEF state, increasing the magnitude of the magnetic moments.

4.5 Relationship between disorder and correlated ground state in Tb$_2$Hf$_2$O$_7$

Despite having only a rough estimate of the magnetic exchange in the system, we can use it, together with the results of the CEF analysis, to see if the magnetic ground state of Tb$_2$Hf$_2$O$_7$ could be related to the disordered-induced QSL phase reported in [21, 22]. The proposal suggests the existence of a particular QSL phase (among other phases), which can be stabilized through non-magnetic disorder in non-Kramers spin ices. This disorder is expected to maintain the correct sample stoichiometry as well as the cation order but will split the ground-state doublet of the rare-earth ions and enhance quadrupolar degrees of freedom. The quadrupoles (rank 2 multipoles) can directly couple with the crystal-electric fields giving rise to the second term in the random transverse field Ising model 1.18 and promote a QSL, depending on the amount and strength of these transverse fields [21]. This was rationalized to the strength of the magnetic exchange
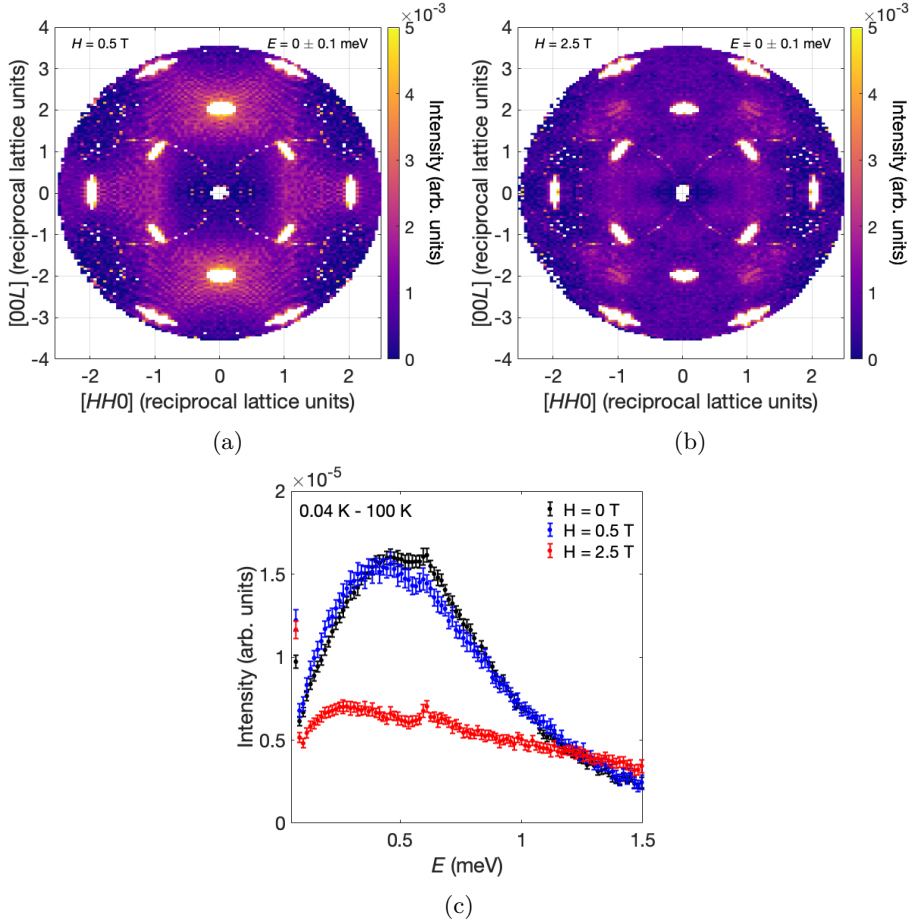
Figure 4.21: (**a**) and (**b**) are the same maps as in Fig. 4.14a but collected under a magnetic field of 0.5 T and 2.5 T, respectively. (**c**) shows the energy dependence of the Q-averaged spin-spin correlation function. The results obtained at each field are plotted together for comparison.

interaction in [22].

First, we can use our CEF analysis to quantify the transverse fields. From the point charge calculation we saw that almost all the Tb^{3+} have a singlet ground state with a very low lying excited singlet owing to the splitting induced by the disorder. In the dipole approximation, both singlets should be non-magnetic. However, experiments have shown that the majority of the terbium ions do carry a magnetic moment at low temperatures. One way to conciliate both statements is to invoke the formation of quasi-doublets made of a linear combination of the two singlet states [181, 182]. One can show that in that case, the distribution of ground state splitting can be directly linked to a distribution of transverse fields (see Appendix 6.4). We therefore have a direct access to the distribution of effective transverse fields (Fig. 4.9b) and we can now try to place Tb$_2$Hf$_2$O$_7$ in the phase diagram presented in [22] (see Fig. 4.25).

The present estimations place Tb$_2$Hf$_2$O$_7$ in the paramagnetic region of the phase diagram, although close to the boundary with the QSL phase. Nevertheless this does not rule out the magnetic ground state as being a QSL. Indeed, we know that the distribu-
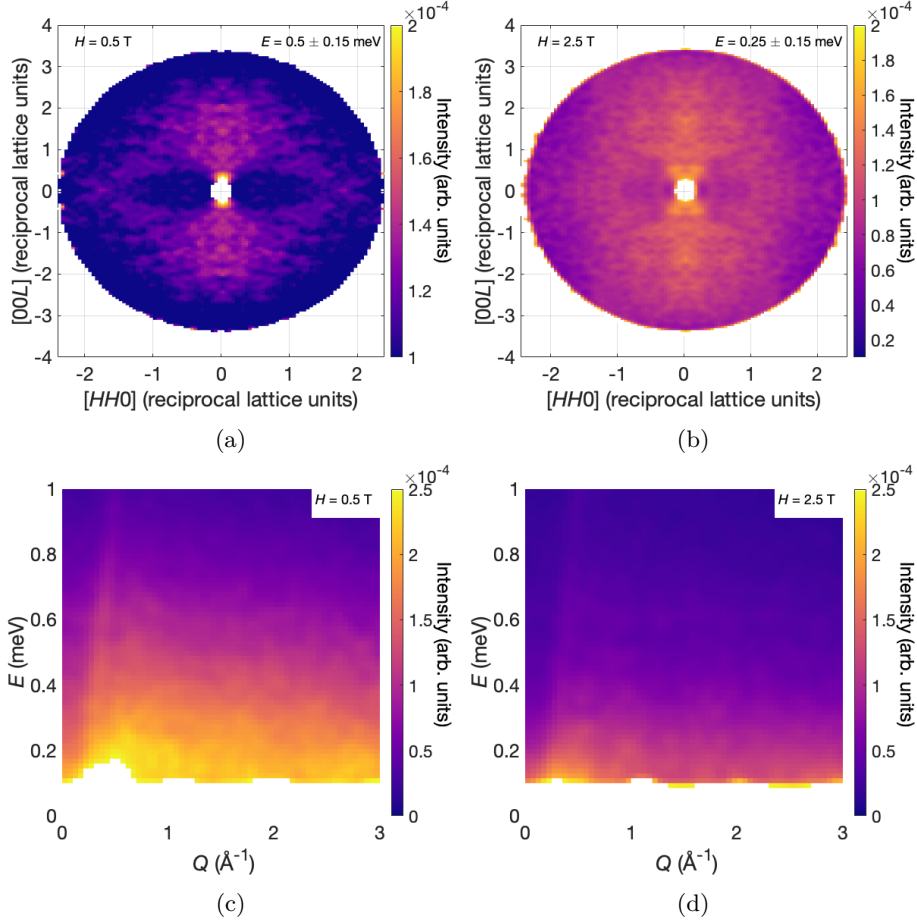
Figure 4.22: (**a**) and (**b**) are the Q-dependence of the magnetic excitation around their
maximum for data collected under 0.5 T and 2.5 T, respectively. (**c**) and (**d**) are the
Q-averaged S(Q,E) obtained from the spectra collected under both magnetic fields. In
all maps, the high temperature data were not subtracted.

tion of splitting is subject to errors due to the limited capabilities of the point charge
calculations. The attempted fits are also not able to accurately capture the width of
the distribution. Finally the estimation of the exchange is rather rough and would need
to be improved. We can nonetheless discuss our result while bearing in mind the ex-
perimental observations. The INS measurements are particularly relevant in this case.
The gapped continuum of excitations seen in the spectra (IN5 and FOCUS) suggest the
existence of correlations, although of unknown nature. On the one hand, It could corre-
spond to the fractional excitations of a QSL magnetic ground state, an hypothesis that
could also explain the strong quasi-elastic signal. One the other hand, a paramagnetic
state subject to quadrupolar correlations could also account for the inelastic signal, as
argued in the case of Pr$_2$Zr$_2$O$_7$ [27, 22]. Either ways, it is clear that the non-magnetic
disorder plays a significant role in the magnetic correlated ground state of Tb$_2$Hf$_2$O$_7$.

(a)

(b)
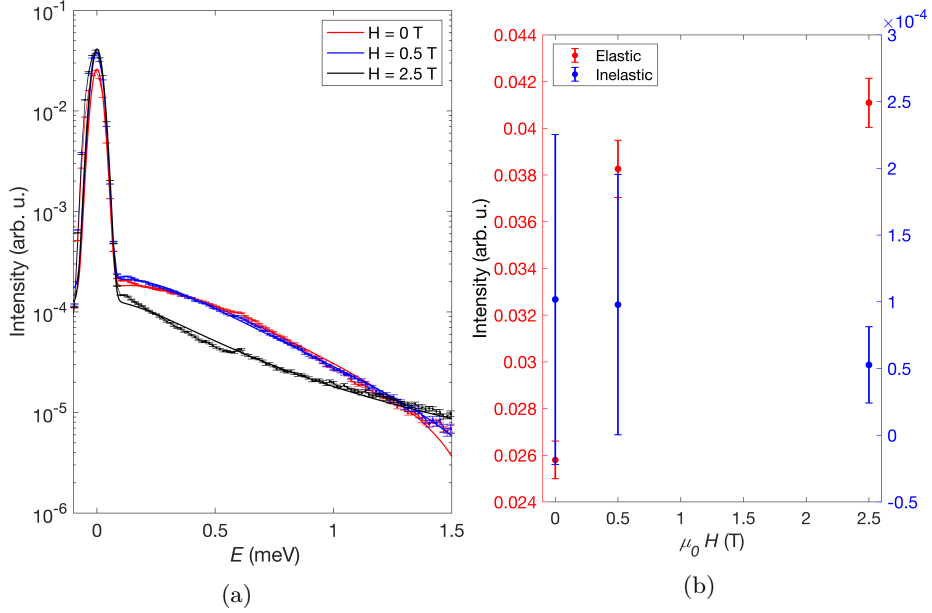
Figure 4.23: (**a**) Fit of the Q-integrated signal for the data collected at 0 T, 0.5 T and 2.5 T. (**b**) Magnetic field dependence of the elastic and quasi-elastic contributions to the Q-integrated signal.
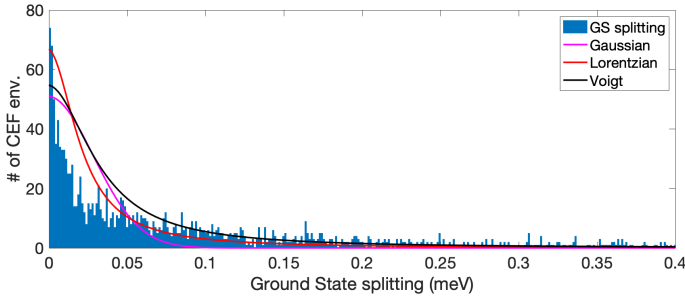
Figure 4.24: Distribution of ground state splitting and associated fits using various functions (Gaussian, Lorentzian and Voigt). The plotted range focuses on the splitting inferior to 0.4 meV, which represents more than 90 % of the Tb^{3+}. One can notice the change in the y-axis compared to the Fig. 4.9b. This is due to the smaller bin size used here, chosen to improve the visualization in the given energy window. A fit of the distribution using usual distribution functions (weibull, normal, Poisson, ...) was found inconclusive.

4.6 Summary

The crystallographic structure and correlated magnetic phases in pyrochlores are know to be very closely linked to one another (as discussed in 1.3), particularly when dealing with non-Kramers magnetic ions. Deviations from the ideal nuclear structure is usually associated with a destabilization of the sought after quantum spin ice state [27, 183, 96, 97]. Surprisingly, the strong structural disorder evidenced in Tb$_2$Hf$_2$O$_7$ is not inducing long-range magnetic order down to the lowest accessible tem-
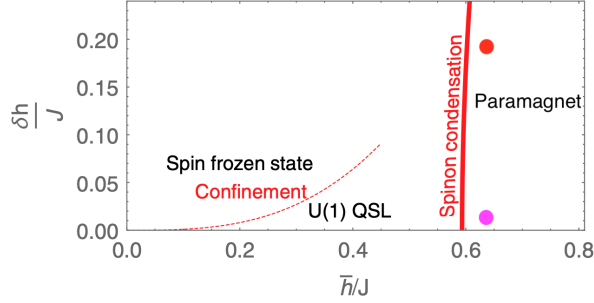
Figure 4.25: Estimated positions of Tb$_2$Hf$_2$O$_7$ in the phase diagram reported in [22]. J is an effective exchange interaction (estimated using the magnetization data (Appendix 6.4)), $\bar{h}$ and δh are the mean strength and FWHM of the distribution of transverse fields, respectively. The median value of the distribution (0.0728 meV) was used instead of the mean value (0.1895 meV), as the former seems overestimated and indeed places the points completely out of the phase diagram limits. Only the estimations from the Gaussian (magenta point) and Lorentzian (red point) are present on the plot as the one corresponding to the Voigt function lies above the limit of the diagram's y-axis.

peratures [25].

To understand this rather unusual behavior we undertook a detailed structural analysis. We showed that the structure of the investigated sample cannot be accurately described using an average structure with partial occupation of some oxygen sites. Using Reverse Monte Carlo simulation, we were able to better reproduce the neutron pair distribution function data and to some extend the structural diffuse scattering observed in single crystal data. Using the results of our RMC simulation, we could reproduce the continuum of crystal-electric field excitations evidenced in the neutron spectra.

One of the valuable piece of information coming from our analysis is the impressively large distribution of ground state doublet splittings caused by the structural disorder. Despite the complex distribution of wavefunctions describing the ground state and very close first excited states, the samples showed a remarkable Ising character. But this ground-state's splitting is not without consequences. For instance, looking at the magnetic contribution to the specific heat, we observe a lack of recovered entropy with respect to the spin ice case. This missing entropy could stem from the presence of non-magnetic Tb ions, those which ground-state's splitting is too large to form quasi-doublets after mixing under the effect of interactions. In the same spirit, the distribution of splitting and of disturbed exchange paths might explain the gradual freezing of the moments in the ac-susceptibility, μSR and INS experiments upon cooling.

Magnetic diffuse scattering observed in various neutron experiments strongly support the presence of a correlated magnetic ground state similar to the Coulomb spin liquid phase identified in the sister compound Tb$_2$Ti$_2$O$_7$. Polarized neutron diffraction, NPD and INS confirmed that both compounds have nearly the same anisotropic quasi-elastic diffuse signal, developing roughly on the same temperature behavior. However the dynamics of the systems are rather different as suggested by the respective ac-susceptibility measurements [25, 175].

In an attempt to determine the exchange tensor in Tb$_2$Hf$_2$O$_7$ we looked at its field-induced magnetic behavior. Comparing the magnetization as a function of applied magnetic field for both Tb compounds, Tb$_2$Hf$_2$O$_7$ shows a faster increase, but as for Tb$_2$Ti$_2$O$_7$, it does not saturate at fields of about 8 T either. The diffraction studies with magnetic fields applied along the [1$\bar{1}$0] and [111] crystallographic directions of terbium

hafnate yield almost identical magnetic structures as was found in the titanate, suggesting a similar structure of the exchange tensor. Although the field-induced magnetic structures of $Tb_2Hf_2O_7$ and $Tb_2Ti_2O_7$ are very similar, their inelastic neutron spectra are quite different. The excitations in terbium hafnate show very broad features, both in energy and momentum space. Furthermore, the application a moderate magnetic field was not successful in stabilizing clear spin waves despite the evident stabilization of long-range order. These observations make the precise identification of the magnetic ground state very difficult, most likely requiring the inclusion of the structural disorder, quadrupolar degrees of freedom and/or transverse fields within any model aiming at quantitatively reproduce the experimental observations. We hope that the ongoing mean-field analysis, which includes the results from our RMC simulation, will bring some answers.

Although the exact relationship between structural disorder and correlated ground state in $Tb_2Hf_2O_7$ is not entirely clear, the present analysis made a strong case in favor of a strong connection. As we shall see in the next chapters, such consideration could help explaining observations in other pyrochlore systems or motivate the exploration of new compounds with tunable structural disorder.

Chapter 5

Disorder and and correlated ground states in praseodymium-based pyrochlores

Preamble

$\mathscr{I}$ N this second part of our investigation of structural disorder in quantum spin liquid candidates, we perform a comparative study of the praseodymium pyrochlores $Pr_2Zr_2O_7$ and $Pr_2Hf_2O_7$, both of which have been thoroughly characterized in terms of their low temperature correlated states. We shall first sum up our current understanding of the magnetism displayed by both compounds before looking for structural discrepancies, which could possibly explain their magnetic disparities. The structural analysis maded use of several experimental probes in order to benefit from the best resolution and contrast possible.

5.1 Low temperature magnetic states of $Pr_2Zr_2O_7$ and $Pr_2Hf_2O_7$

We shall start by addressing the current understanding of $Pr_2Hf_2O_7$. Both powder and large single crystal of praseodymium hafnate have been successfully synthesized, enabling its characterization using several techniques, in particular INS. The quality of the samples is estimated to be very high based on x-ray and neutron diffraction experiments. Additionally, the aspect of the crystal (color, transparency, absence of cracks) further confirm this claim [184]. Crystal-electric field excitations are consistent with the expected splitting of the J = 4 state, considering an intermediate coupling treatment of a $4f^2$ ion in D_{3d} local symmetry [94].

In $Pr_2Hf_2O_7$, the CEF analysis supports a ground-state with a small magnetic moment ($\approx$ 2.43 μ_B) with strong Ising anisotropy, as well as significant admixture of $|M_J \neq J\rangle$ states. Due to the composition of the wavefunction, quadrupolar moments are non-zero and contribute to the Hamiltonian as transverse terms [28]. Magnetic susceptibility does not exhibit any sign of long-range order down to 70 mK, but does display

a deviation from the Curie-Weiss behavior below about 0.6 K, consistent with the rise of ferromagnetic correlations [94]. A Curie-Weiss fit above the correlated regime indicated dominant interactions of antiferromagnetic nature (0.40 ± 0.01 K). Magnetization measurements on single crystal with different magnetic field directions are consistent with the expected behavior of Ising moments (local [111] being the easy axis) on the pyrochlore lattice [94]. Additionally, an anomaly was observed in the magnetization curve for a field applied along the [111] crystallographic direction and is attributed to the transition between '2-in-2-out' and '3-in-1-out' states. Heat capacity revealed a broad bump centered around 2 K reflecting the build up of magnetic correlations [94].

All the previous observations hint toward the presence of a spin ice state in $Pr_2Hf_2O_7$. But the most interesting results come from INS data, which point to the stabilization of a QSI [28]. The typical spin ice pattern at the elastic line in the $[HHL]$ plane is indeed observed at low temperature. However the pinch points are found to be somehow suppressed compared to dipolar spin ice [81], a feature that is predicted by theory [10]. INS also reveals a broad continuum of excitations of magnetic origin [28], much weaker than the intensity of the (quasi-)elastic signal. The continuum is peaked at 0.2 meV, holding a starfish shape extending up to 0.3 meV where the intensity is then spread over momentum space. The exact nature of this excitation is not confirmed yet but could be spinon excitations accessible through the transverse terms mentioned in the CEF analysis, among other explanations [28, 13]. Nonetheless, both microscopic and macroscopic measurements make a strong case for $Pr_2Hf_2O_7$ being a promising QSI candidate.

Interestingly, $Pr_2Zr_2O_7$ shows both similarities and discrepancies with $Pr_2Hf_2O_7$. The praseodymium zirconate also exhibit antiferromagnetic exchange with a Curie-Weiss temperature of about -1 K (some variations are observed depending on the sample quality) [26, 27]. The determined CEF is very similar to $Pr_2Hf_2O_7$, with a similar ground-state wavefunction and effective magnetic moment at low temperature [96]. Magnetization curves also behave similarly, although no anomaly can be spotted when the field is applied in the [111] crystallographic direction [27]. The heat capacity displays an interesting behavior as a function of magnetic field, with the broad correlation bump first moving to lower temperature before going to higher temperature and broadening significantly at higher fields [27].

Some structural disorder was also experimentally observed in $Pr_2Zr_2O_7$, reporting either cation site mixing [26, 27] or strain around the Pr^{3+} site based on various diffraction (intensity at positions forbidden by the space group) and diffuse scattering (Huang scattering, electron imaging) studies [27, 26, 183, 97, 185]. Although not exactly characterized yet, this disorder is expected to have an impact on the ground-state, as we shall discuss hereafter.

The most discussed and puzzling observation of $Pr_2Zr_2O_7$ concerns its neutron scattering spectrum. Different experiments consistently show a spectrum where the magnetic intensity is mostly inelastic, with a structure in reciprocal space reminiscent of a spin ice [26, 27]. This is in opposition with the spectrum of $Pr_2Hf_2O_7$ where the signal is mostly in the (quasi-)elastic channels [28]. At first sight, the intensity distribution in the spectrum of $Pr_2Zr_2O_7$ is not consistent with spin ice physics solely considering the z-component of the pseudo-spin. However, due to the non-Kramers nature of Pr^{3+}, the ground-state is very sensitive to structural disorder. A tiny disturbance of the D_{3d} symmetry around the rare-earth site is enough to slightly split the ground-state doublet into singlets, at the same time strengthening the quadrupolar degrees of freedom [27, 183, 96, 97]. Models considering strong antiferro-quadrupolar correlations have shown to qualitatively reproduce the spectrum [27, 183, 96, 97], although no model could exactly reproduce all the data so far.

To summarize, although expected to display a similar magnetic ground state, $Pr_2Hf_2O_7$ and $Pr_2Zr_2O_7$ contain magnetic correlations leading to distinct inelastic neutron spectra. This discrepancy could be related to the weak diffuse signal spotted in $Pr_2Zr_2O_7$. As depicted earlier, the aim of this study is to hunt for signs of the structural disorder in order to better identify its nature. To do so, we used several probes on the same samples as used in [28] and [27], and present our results in this chapter.

5.2 Powder neutron pair distribution function on praseodymium compounds

We begin by looking at neutron pair distribution function data collected on powder samples at 5 K, using the GEM diffractometer (ISIS, UK). The obtained curves are displayed in Fig. 5.1a and Fig. 5.1b, for $Pr_2Hf_2O_7$ and $Pr_2Zr_2O_7$ respectively (blue circles).

(a)

(b)
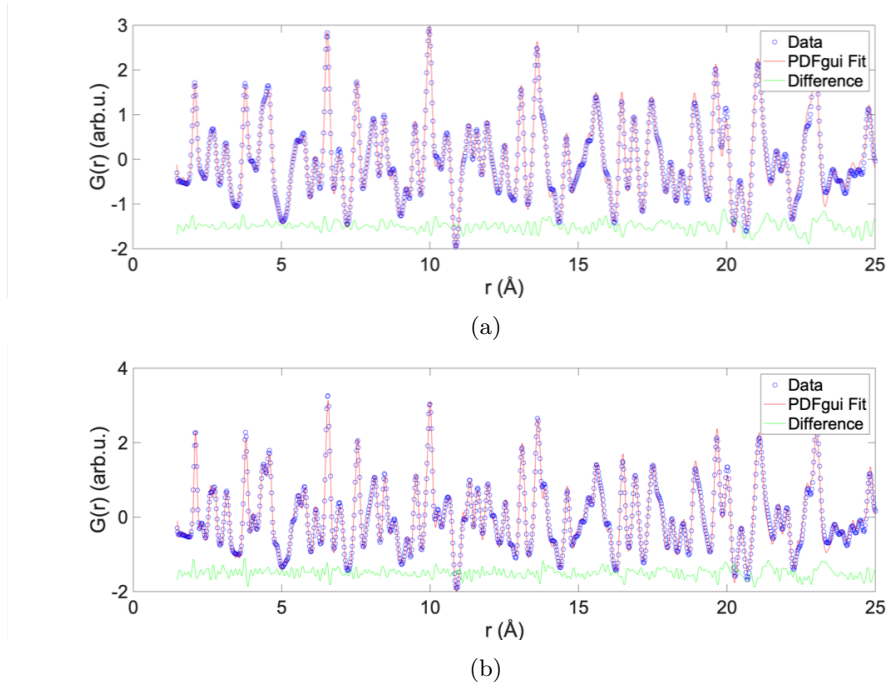
Figure 5.1: Neutron pair distribution function measured on $Pr_2Hf_2O_7$ (**a**) and $Pr_2Zr_2O_7$ (**b**) at room temperature on GEM (ISIS). The red lines correspond to the fit using the respective average structures (using the PDFGui software), whereas the green lines are the difference between the experimental and calculated curves.

The PDFGui software was used to reproduce the data using the typical $F d\bar{3}m$ pyrochlore structure. The x coordinate of the $48f$ oxygen as well as Deby-Waller factors were used as structural variables. The obtained fit (red lines) are superimposed with the experimental data and the residuals are shown below (green lines). No clear disagreement between the data and the fits are observed experimental resolution. More importantly, no discrepancy is spotted between the two compounds. Both data sets are fitted almost identically well by their respective average pyrochlore structures. The measured samples were both raw powder samples prepared in view of single crystal synthesis or

diverse bulk characterizations. One could thus argue that the structural defects do not
affect powder samples but actually occur during the single crystal growth. This could
also be argued from the absence of anomalies in powder diffraction patterns [94, 186].
We thus focused on single crystal samples for the remaining of the study.

5.3 Praseodymium zirconate and hafnate under electron microscopy

Our first measurements on single crystals were carried out at the Institut Jean Lamour (Nancy, France) with Dr. Jaafar Ghanbaja. A high resolution electron microscope
available at the institute was used to study $Pr_2Hf_2O_7$ and $Pr_2Zr_2O_7$ single crystals at
room temperature. Thin lamellae of each materials were carefully prepared in-house using a focused ion beam and a micro-manipulator. Two slices per samples were prepared
so as to measure both the surfaces of normal [111] and [110].

We first discuss the data collected for the [110] direction. Both electron diffraction
patterns and High-Angle Annular Dark-Field (HAADF) images can be found in Fig. 5.2.
Apart from the Bragg intensities and the expected instrumental artifacts (shadows due
to surface roughness and thickness effects, Kikuchi lines due to multiple scattering), no
distinction could be made between the electron diffraction patterns of the two samples.
The same goes for the HAADF images (see Fig. 5.2), showing the expected alternating
intensities of bright spots representing the different stacking of cations (oxygen atoms
are too light to be seen here). A more quantitative analysis of the spots intensity
modulation could be valuable to corroborate this claim, using for instance electron
energy loss spectroscopy.

We now look at the images taken for the normal to the [111] direction of $Pr_2Zr_2O_7$ and
$Pr_2Hf_2O_7$. In this instance one can identify a difference, in the shape of weak diffuse
lines perpendicular to the $< 110 >$ in the diffraction pattern of the zirconate, as seen
in Fig. 5.3a. This diffuse scattering forms concentric hexagons (highlighted with the
continuous blue lines in the plot) and was also spotted in another work [185]. This
feature appears to be absent or significantly weaker in the hafnate (Fig. 5.3b).
The corresponding HAADF images did not allow to draw further conclusions on the
possible disorder observed through the diffraction pattern. A much more detailed analysis of the images would be required in order to completement the diffraction results and
to compare with the observation made in [185]. Additionally, we expect a considerable
impact of the surface roughness, perhaps explaining the large and apparently random
modulation of intensity noticeable in the $Pr_2Zr_2O_7$ picture.

Although a weak diffuse signal could be observed in $Pr_2Zr_2O_7$, we could not extract
information about the disorder itself. Consequently, other methods were used in order
to identify and quantify the defects present in the system.

5.4 Neutron diffuse scattering from $Pr_2Zr_2O_7$ and $Pr_2Hf_2O_7$ single crystals

Our next investigation of the two praseodymium samples was performed using neutron single crystal diffuse scattering on the SXD instrument (ISIS, UK) [187]. For
both samples, we recorded scans using eleven area detectors and four sample angular
positions at a temperature of 40 K. Data were reduced for fits of the integrated peak
intensities and scattering planes were reconstructed using the SXD2001 software [188].
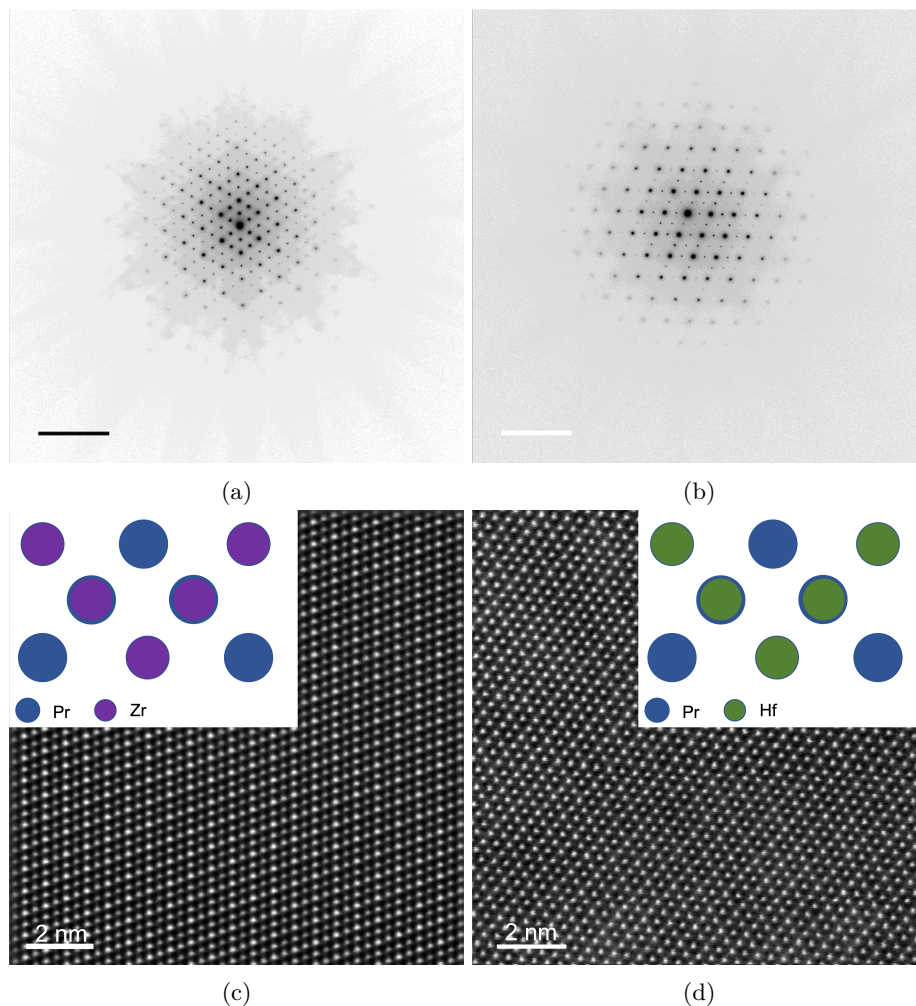
Figure 5.2: (**a**) and (**b**) are electron diffraction patterns perpendicular to the $[1\bar{1}0]$ crystallographic direction, collected using a TEM instrument on lamellae of $Pr_2Zr_2O_7$ and $Pr_2Hf_2O_7$, respectively. The images in (**c**) and (**d**) are the associated real space atomic distribution obtained using High-angle annular dark-field imaging (HAADF). In (c) and (d) is shown the stacking of the Zr/Hf and Pr atoms in the structure for this crystal orientation. Three different columns can be identified: one alternating the two elements and two containing either only Zr/Hf or only Pr. We thus expect three slightly different intensities

Both fits to the integrated intensities, using JANA2006 [189], reached very good results, suggesting no measurable deviation from the average structures in diffraction data.

Differences arise when looking at reciprocal space maps, particularly in the (HK) planes. A few of these planes are displayed for both compounds in Fig. 5.4. The color scales were adjusted in order to provide similar ratios between the incoherent background and the Bragg reflections, in order to compare the signals in both samples. A clear structured signal is observed at high momentum transfer in the case of $Pr_2Zr_2O_7$, which appears absent in $Pr_2Hf_2O_7$. Changing the color scale limits in the hafnate case only rises or lowers the overall background but cannot produce the appearance of such
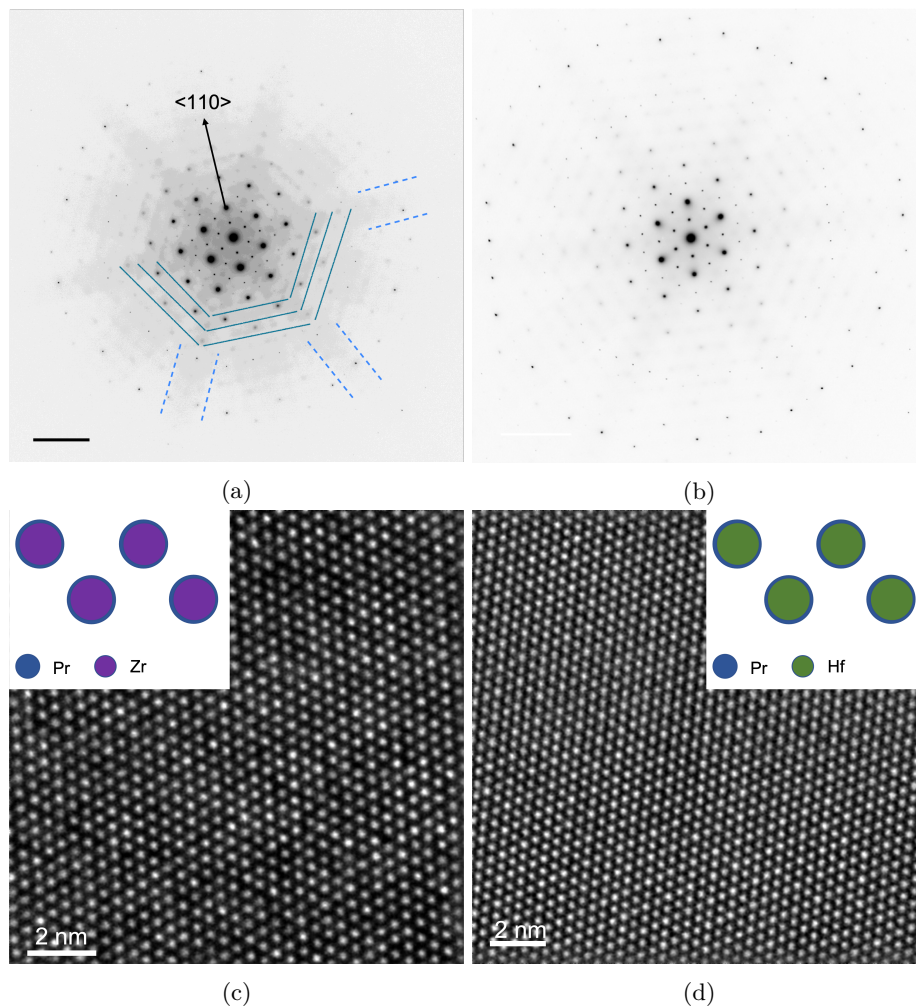
Figure 5.3: (**a**) and (**b**) are electron diffraction patterns perpendicular to the [111] crystallographic direction, collected using a TEM instrument on lamellae of $Pr_2Zr_2O_7$ and $Pr_2Hf_2O_7$, respectively. The continuous lines in (**a**) underline the shape of the diffuse signal, whereas the dashed lines show the instrumental artifacts known as Kikuchi lines.The images in (**c**) and (**d**) are the associated real space atomic distribution obtained using High-angle annular dark-field imaging (HAADF). In (c) and (d) is shown the stacking of the Zr/Hf and Pr atoms in the structure for this crystal orientation. All columns should be composed of an alternating stacking of Pr and Zr atoms, and thus should have identical intensities.

a clear structured diffuse intensity. If any diffuse scattering exists in $Pr_2Hf_2O_7$, it is considerably weaker than in its zirconate counterpart. The observation of such strong features with neutron but not with electrons suggests that the signal is mainly due to disorder of oxygen anions. As oxygen is a rather light element, electron diffraction is not so sensitive to it whereas its neutron cross section allows to resolve it more easily.

Performing a Reverse Monte Carlo simulation would be tempting, as was done in the previous chapter for $Tb_2Hf_2O_7$. However the tridimensionality of the data significantly complicates the procedure. Powder-averaging of the entire datasets could be lead

to false results, as the sine Fourier transform on these artificially symmetrized objects
would most probably generate some artifacts. Additionally, the necessary corrections to
obtain clean PDF data are not precisely defined for this instrument. We therefore opted
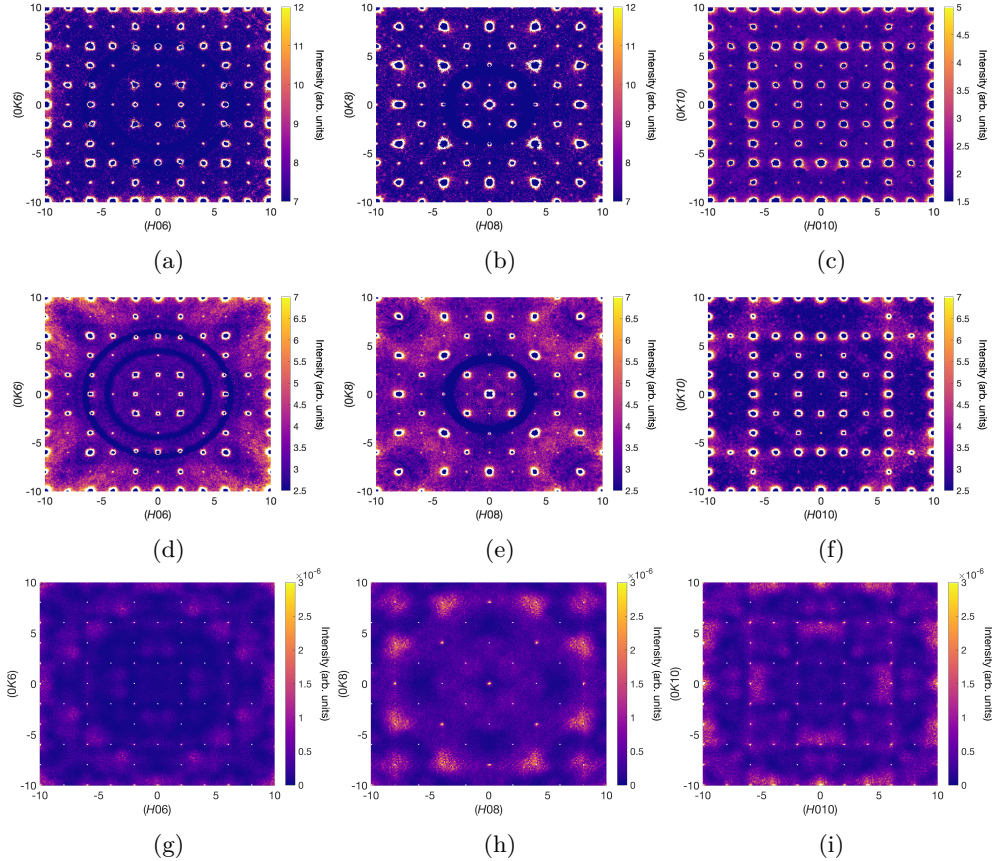
Figure 5.4: Reciprocal space maps in the HKL planes for L = 6, 8 ,10. The top (**a-c**) and
middle (**d-f**) rows correspond to data collected on $Pr_2Hf_2O_7$ and $Pr_2Zr_2O_7$, respectively.
The bottom row (**g-i**) corresponds to the result of our Monte Carlo calculation.

for another approach to reproduce the observed diffuse signal. The starting hypothesis
was the presence of a small amount of Frenkel pair defects, as observed in $Tb_2Hf_2O_7$,
but in a much smaller proportion (on the order of a couple percents). These Frenkel
pair defects involve the relocation of some $48f$ oxygen towards the usually empty $8a$
crystallographic site. This is found to be the most energetically favorable type of an-
ionic disorder in pyrochlore oxides [103, 101, 190]. In order to simulate the impact of
such defects on the diffuse scattering of neutrons, we collaborated with Prof. Peter.
M. Derlet (PSI). We used Density Functional Theory (DFT) calculations to estimate
the impact of oxygen interstitials, vacancies or Frenkel pair defects on the surrounding
atoms. The DFT calculations were performed using the Quantum Espresso DFT soft-
ware package [191, 192, 193] and considered four cases: the ideal $Pr_2Zr_2O_7$ lattice, a
configuration containing an oxygen interstitial, another one containing an oxygen va-
cancy at a $48f$ site and a last configuration corresponding to a Frenkel pair. For each
defect, the near-field displacements of the surrounding atoms were evaluated and the
associated elastic dipole tensors were computed.

In the case of an oxygen interstitial (i.e. at the $8a$ site), the four Zr of the surrounding tetrahedron move radially away from the interstitial by 0.163 Å whereas the four nearest oxygen move radially towards the interstitial by 0.283 Å. Overall, the displacement field around the interstitial is symmetric. When creating a vacancy at a $48f$ site, the implications are rather different. A picture of the displacements associated with a vacancy is shown in Fig. 5.5 and can be described as follows:

- The two neighboring Pr^{3+} cations (Pr1, Pr2) move radially towards the vacancy a distance of 0.154 Å.

- The two neighboring Zr atoms (Zr1, Zr2) move 'towards' the vacancy along the global z-axis (i.e. **c** crystallographic axis) a distance of 0.117 Å.

- The four nearest oxygen ions (O1a-O4a) on the plane perpendicular to the global z-axis move approximately radially away from the vacancy a distance of 0.178 Å.

- There is also a small component along the global z-axis which moves the O towards the two Zr.

- The next-nearest Zr (Zr3, Zr4) move radially outwards from their Zr-tetrahedron center (and away from the vacancy) a distance 0.183 Å.

- The four next nearest oxygen anions (O1b-4b), which are located on a plane perpendicular to the z-direction at the same height than the Zr tetrahedron center, move radially towards this centre.

As depicted here, an oxygen vacancy in the pyrochlore structure produces a non-trivial and asymmetric displacement field which would have been difficult to capture simply by using an elastic deformation theory.

In the case of a Frenkel pair defects, the atomic displacements roughly correspond to the sum of both defects, with a little tendency of the interstitial to move towards the vacancy site. The estimated energy per atom associated with each defects are $E_{vacancy}$ = -6.91910 eV, $E_{intersitial}$ = 6.91903 eV and E_{fp} = -0.00079 eV. The formation of an interstitial is thus energetically expensive whereas a vacancy has almost exactly the opposite energy. Interestingly, this is also reflected by the energy of the Frenkel pair defect being very close to the average of the two independent defects and thus almost zero. For the remaining of the discussion we restrict ourselves to Frenkel pair defects, although carrying out a more systematic study investigating the three types of defects would provide valuable information. Calculating the same quantities for $Pr_2Hf_2O_7$ would also be interesting as it might explain why defects appear to be absent in the hafnate.

In the next step, we created a large pyrochlore lattice (10 by 10 by 10 unit cells) containing praseodymium, zirconium and oxygen atoms siting at their ideal positions. A small amount of Frenkel pair defects was randomly created with a fraction of possible sites occupied by the defect of 0.01. The DFT results were then implemented to reproduce the atomic displacements around these defects. Elastic theory was subsequently applied using the computed elastic dipole tensors to estimate the far field effect of the defects. Reciprocal space maps were computed based on the final atomic configuration, focusing on the planes where the diffuse signal was experimentally the strongest. Such procedure was carried out for ten lattices with different starting defects in order to produce a meaningful average output.

The computed maps are shown in Fig. 5.4. A notable feature is the strength of the diffuse scattering at high momentum transfer, which dominates the rest of the maps. This is in agreement with the experimental data collected on $Pr_2Zr_2O_7$. Although the
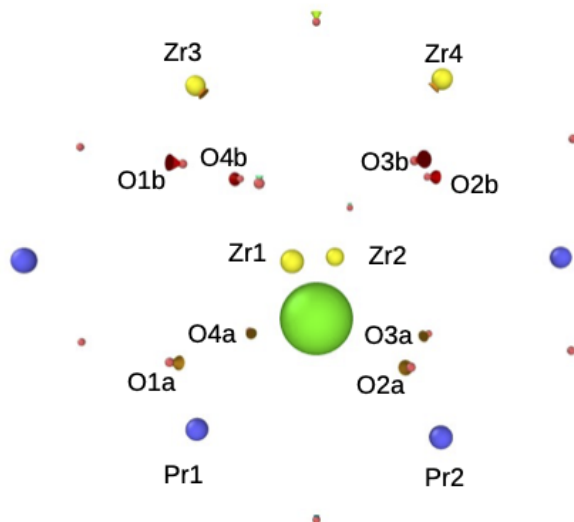
Figure 5.5: Sketch of the atomic displacements around a vacancy calculated from DFT calculations. The green sphere represents the vacancy and the arrows show the direction and amplitude of the displacement.

agreement is not perfect, as it often remains for such approach, the calculate scattering is located at the correct spots on the (HK) maps. So far we have not quantify the defects nor accounted for possible correlations between them, which would be the next steps of this analysis.

5.5 Summary

A first observation is that powder measurements did not evidence structural differences between the hafnate and zirconate compounds. It suggests that the structural defects observed on $Pr_2Zr_2O_7$ in single crystal experiments are either too small to be picked up in powder experiments or are created during single crystal growth. Electron diffraction performed on our single crystals corroborates the presence of some diffuse intensity in the zirconate compound, as observed in another work [185]. This is further confirmed by our single crystal diffuse scattering data, highlighting some difference between the two compounds in terms of diffuse scattering, $Pr_2Hf_2O_7$ showing little to no signal.

We then adopted a new approach to capture the diffuse features observed in praseodymium zirconate. Using DFT simulations we investigated the impact of three types of defects: interstitials, vacancies and Frenkel pair defects. It turns out that isolated interstitials are energetically unfavorable, compared to vacancies and Frenkel pairs. Introducing a little amount of Frenkel pair defects, simulating its effect on the crystallographic structure and computing the associated neutron scattering maps yields a qualitatively reasonable agreement with our experimental data. Although these results appear to confirm our initial hypothesis, more work is required to accurately determine the structural disorder in the structure, for instance whether the defects correlate in between themselves or if isolated interstitials/vacancies could also generate the same

signal.

It would be interesting to compute the electron diffraction pattern from our simulated lattices and compare it with our experimental data. Such a comparison could corroborate our findings or provide more information about the amount and possible correlations between Frenkel pair defects. This is being carried out for reciprocal space maps collected using x-rays. In this case, the probe is more sensitive to heavy elements and would provide more information about the diffuse scattering related to the cations of our systems. A last perspective of future work is the use of the DFT results of the near field atomic displacements to evaluate its impact on the Pr^{3+} crystal-electric field scheme in the slightly disordered $Pr_2Zr_2O_7$. It would constitute a way to evaluate the associated distribution of ground state splitting and compare it with the models brought forward to explain the presence of strong quadrupolar degrees of freedom in previous works [96, 97]. The disorder identified in $Pr_2Zr_2O_7$ appears to be minute but sufficient to favor antiferroquadrupolar correlations at the expense of the dipolar ones. Interestingly, the presumably same type of disorder is massively present in $Tb_2Hf_2O_7$ but does not have the same consequences on the INS spectrum, perhaps due to the robustness of the correlations between the large Tb moments.

Chapter 6

Tuning of quantum fluctuations via chemical substitution in $Ho_2Ti_2O_7$

Preamble

$\mathscr{I}$N this last part, we will demonstrate how the type of disorder evidenced in $Tb_2Hf_2O_7$ can be tuned and used in order to enhance fluctuations. This work is motivated by the theory proposed in [21], stating that non-magnetic disorder can be used to turn a classical spin ice, governed by entropy, into a quantum spin ice, controlled by entanglement. $Ho_2Ti_2O_7$ constitutes an obvious starting point in this quest, owing to its very well characterized classical spin ice state as well as the non-Kramers nature of Ho^{3+}. $Ho_2Ti_2O_7$ was one of the first spin ice materials to be experimentally discovered. Since then, it has been subject to many investigations using numerous techniques, among which neutron scattering [81, 194, 85], specific heat [195], AC-susceptibility [196] and neutron spin echo. It is now well establish that this compound exhibits a Coulomb phase, with large Ising moments following the local ice rule, as well as hosting monopole excitations interacting through a Coulomb-like dipolar interaction [82, 83, 84].

The impact of magnetic disorder has also been a topic of interest in the study of $Ho_2Ti_2O_7$. For instance, a small dilution of Ho, substituting it with non-magnetic Y, appears to have little to none effect on the dynamics of the system [197], whereas stuffing of Ho on some of the Ti sites increases the relaxation speed in the regime where relaxation happens via quantum fluctuations, in spite of introducing some kind of glassy behavior [198]. Both studies made use of AC-susceptibility and neutron spin echo in order to probe the relaxation time of the systems.

In our case, we will focus on a different type of disorder, one that leaves the magnetic sites unaffected. Previous experimental works showed that it was possible to control the creation of oxygen Frenkel pair defects, as found in $Tb_2Hf_2O_7$, by chemical substitution on the B site, while living the A site untouched [199, 200]. A structural study of a similar chemical substitution has already been done in $Ho_2Ti_2O_7$ using Zr. In this case, the Fd$\bar{3}$m structure survives up to about 50% substitution, without introducing A site disorder but still favoring the creation of oxygen defects [201]. Through the present work, we will gradually substitute the Ti^{4+} ions by Hf^{4+}, up to 40 % and carefully determine the impact on both the crystallographic structure, as well as on the magnetic

properties of the system.

6.1   Synthesis and structural analysis

Powder samples of $Ho_2(Ti_{1-x}Hf_x)_2O_7$ were prepared via solid state synthesis, for x taking the following nominal values: 0, 0.005, 0.02, 0.05, 0.1, 0.15, 0.2, 0.25, 0.3, 0.35, 0.4. Annealing was taking place in air, first at 1300 ℃ and then at 1500 ℃ for a couple more times. The evolution of the phase purity and crystallization was monitored by laboratory x-ray diffraction.

In order to precisely determine their crystallographic structures, all samples were subject to neutron powder diffraction on HRPT (SINQ) at room temperature and using a wavelength of 1.155 Å. Rietveld refinements were performed using the FullProf Suite software [179]. The result of the fits can be found in Appendix. The conclusions are as follow: all but the 40 % doped sample display a diffraction pattern verifying the $Fd\bar{3}m$ space group symmetry. The 40 % doped sample appears to be somewhat of a mix between the pyrochlore $Fd\bar{3}m$ and fluorite $Fm\bar{3}m$ structures. The refined lattice parameter follows a linear increase with the amount of Hf, going from 10.105 Å up to 10.235 Å. The refined occupations of Ti and Hf on the B site are very close to the nominal composition (typically within a percent). The low doping samples deviated the most but also suffered from more uncertainty due to the small impact on the diffraction pattern. Attempt at refining the presence of disorder on the Ho site led to zero occupation values within the error. Finally, the occupation of the oxygen sites ($48f$, $8a$ and $8b$) was refined. The inclusion of the $8b$ site occupation in the refinement led to unphysical results (negative occupation of the $8a$ site and over occupied $8b$ site) and was considered as fully occupied for the rest of the analysis. The results for the $48f$ and $8a$ can be found in Fig. 6.1a.

For the first two compositions, no evidence for the presence of Frenkel defects is found. Starting at 5 % substitution with see an increase of the $8a$ site occupation and decrease of the $48f$ one with increasing amount of Hf.
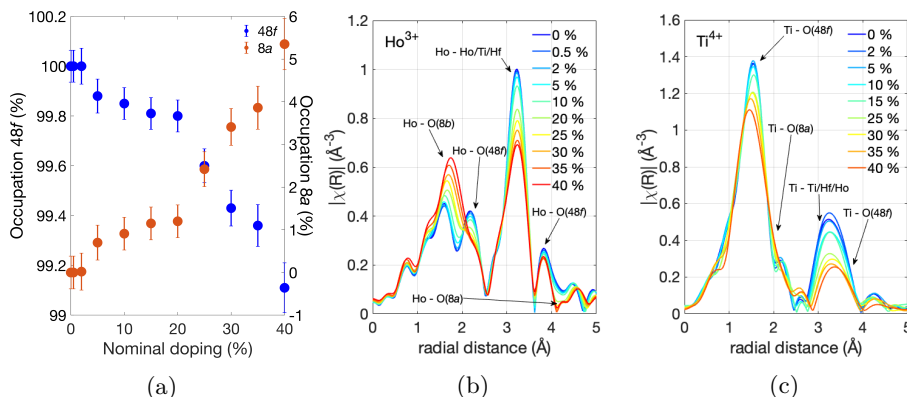
Figure 6.1: (**a**) Refined occupation (in %) of the oxygen $48f$ and $8a$ crystallographic sites as a function of nominal doping. (**b**) EXAFS signal recorded at the Ho L3-edge for most of the series (15 % is missing). (**c**) EXAFS signal recorded at the Ti K-edge for most of the series (0.5 % and 20 % are missing). In both (**b**) and (**c**), the arrows point to the approximate position of the peaks related to the associated atomic pairs. The EXAFS measurements were carried out at the SuperXAS beamline (SLS).

These conclusions are corroborated using EXAFS measurements at the Ho L3-edge

(Fig. 6.1b) and Ti K-edge (Fig. 6.1c), with a clear modification of the Ho and Ti
environments, explainable using the average structures determined via neutron powder
diffraction. Unfortunately the complexity of the signal did not allow to unveil the
local disorder created by the defects, as done for Tb$_2$Hf$_2$O$_7$. A finer analysis or the
use of neutron PDF might be able to solve this question and perhaps evidence some
correlations in the Hf and Ti distribution. The overall result is that, aside from the
40 % doped composition, all the synthesized samples displayed a nicely crystallized
pyrochlore structure, where the Ho ions do not exhibit any disorder. The distribution
of Hf ions on the B site is a priori random and leads to the anticipated oxygen defects,
which is tunable in some degree. Below 2 % of doping, a much finer technique should
be used to detect any oxygen disorder.

6.2 Magnetic properties

6.2.1 Magnetometry results

Now that we addressed the crystallographic structure of the Ho$_2$(Ti$_{1-x}$Hf$_x$)$_2$O$_7$ se-
ries, we shall explore their magnetic properties and how they compare to the ideal system
Ho$_2$Ti$_2$O$_7$. We first report magnetic susceptibility measurements performed down to
2 K under a magnetic field of 0.1 T (see Fig. 6.2a). One can clearly see that the mag-
netic susceptibility of the 40 % doped compound differs from the others over the entire
temperature range, which goes together with the observed mixed nuclear structure.
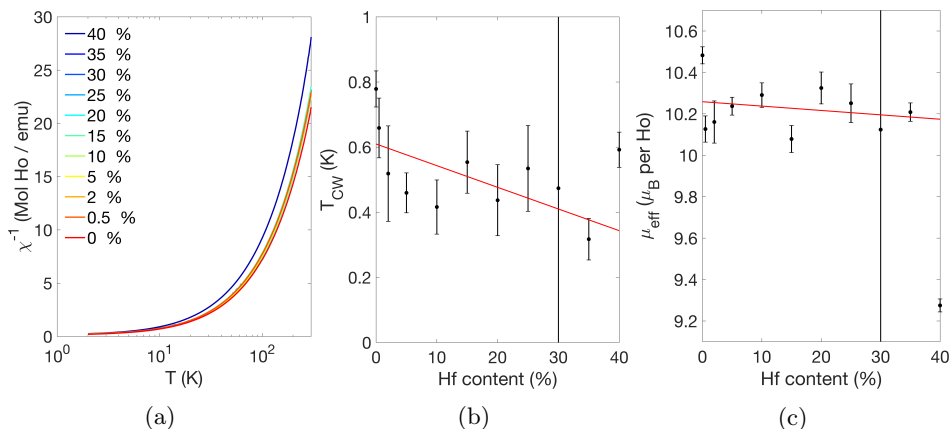
Figure 6.2: (**a**) Inverse magnetic susceptibility measured under a field of 0.1T, (**b**)
fitted Curie-Weiss temperatures and (**c**) extracted effective magnetic moments for all
synthesized samples, together with their respective fits using a linear function in red.

Fitting the inverse magnetic susceptibility curves using a Curie-Weiss law gives the
Curie-Weiss temperatures displayed in 6.2b. The Curie-Weiss temperature shows a
decreasing trend as a function of doping, which seems to also be the case for the effective
moment, although the trend is less clear (Fig. 6.2c). The ambiguous trend in both
plots is due to the difficulty to identify the temperature range onto which the fit has
to be carried out. One needs to be sure to choose a temperature window away from
the correlated regime and where only the CEF ground state level is populated. A
range from 20 K to 80 K was chosen although the CEF scheme of the doped samples
is currently unknown. Additionally, one has to bear in mind that demagnetization
effects are expected to be significant in these samples (about 1.4 K), as mentioned in

early works on Ho$_2$Ti$_2$O$_7$ [141, 202]. Nonetheless, the Curie-Weiss temperature and the
effective moment of the pure sample are slightly higher compared to the values reported
in [141].
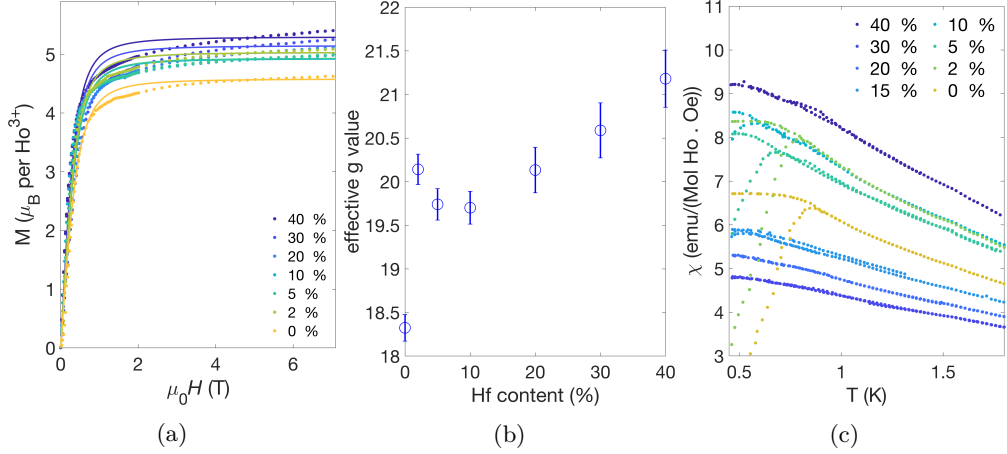
Figure 6.3: (**a**) Magnetization as a function of applied magnetic field measured at
0.6 K for different amounts of substitution. The fits (continuous lines) are obtained
using a modified Brillouin function [141] assuming an effective spin half and fitting the
associated effective g value. (**b**) Effective g values as a function of sample composition.
(**c**) ZFC-FC susceptibility curves as a function of temperature and composition, using
a field of 0.1 T.

The magnetization as a function of field (Fig. 6.3a) was measured at 0.6 K. Using the
same approach and approximations as in [141], we extracted effective g values ranging
from 18.3 (for the pure compound) to 21.18 (Fig. 6.3b). The value obtained for the pure
compound is slightly lower than previously reported [141] and lower than $g_{eff} = 20$,
expected for a pure m$_J = \pm 8$ ground-state doublet. In Ho$_2$Ti$_2$O$_7$, this is interpreted
as the sign of a ground-state dominated by m$_J = \pm 8$, together with some other small
contributions [141, 203]. The effective g values then suddenly increase together with
the amount of Hf, being around 20 for a Hf content between 2 % and 10 %, followed
by a linear increase for samples containing from 10 % up to 40 % of Hf. From these
observations, it appears clear that the samples also find themselves in a ground state
largely dominated by m$_J = \pm 8$, as was demonstrated for Ho$_2$Ti$_2$O$_7$. However we do
not expect an increase of the magnetic moment's magnitude when introducing disorder,
as it is already close to its maximum for a pure m$_J = \pm 8$ state. The increase of the
magnetization at saturation could therefore be attributed to a less Ising character of
the magnetic moments compared to the pure compound, making them more inclined to
polarize with the applied magnetic field. The effective g values demonstrate an overall
increase with the Hf content, suggesting an admixing of other m$_J$ states when introduc-
ing disorder as well as a weaker anisotropy, which is coherent with the hypothesis of a
diminished Ising character of the moments. A detailed crystal-electric field analysis of
the samples would be required to corroborate this interpretation.

No signs of long-range order could be evidenced down to 0.6 K looking at the mag-
netic susceptibility. However, Ho$_2$Ti$_2$O$_7$ is know to be subject to spin freezing when
cooled down below about 1 K [202]. Such behavior can be evidenced by performing
zero-field-cooled/field-cooled (ZFC/FC) measurements, in which the magnetic suscep-
tibility curves split at low temperature [204]. The deviation between the two curves is

due to the presence of magnetic monopoles having a slow relaxation rate at these temperatures, being effectively trapped when cooling under field. The freezing temperature is usually defined as the temperature of bifurcation between the ZFC and FC curves. Examining the evolution of the bifurcation as a function of sample composition, one can clearly identify a lowering of the freezing temperature with increasing Hf content (see Fig. 6.3c). This behavior is tractable up to about 15 % of doping, above which the bifurcation seems to be out of the covered temperature range. Naively, one would rather expect the opposite behavior with the freezing temperature increasing with increasing disorder in a system. In our case, the observed behavior suggests the increase of magnetic fluctuations with increasing amount of structural disorder, at least for the lower doping values.

6.2.2 Specific heat

Specific heat measurements were carried out on a few powder samples with and without application of a magnetic field (1 T, 2 T and 5 T). Phonon contributions were accounted for by fitting data points above 15 K with a Debye function. The hyperfine nuclear contribution at 0 T was subtracted assuming a Schottky-like signal centered at 0.3 K and of maximum intensity 0.9R, as previously done on Ho^{3+} pyrochlores [205, 195]. This contribution is not expected to change significantly under the application of 5 T, due to the size of the nuclear gyromagnetic ratio, and was thus kept constant for each field. Subtracting both the lattice and nuclear signal, one should now be left with the magnetic (electronic) contribution to the specific heat (see Fig. 6.4). No sharp signal, which would indicate a phase transition, was observed down to 1.8 K. One can nonetheless notice the onset of a broad signal at low temperature, attributed to the rise of magnetic correlations. In pure $Ho_2Ti_2O_7$ at zero magnetic field, this signal starts to rise around 11 K, and appears to almost reach its maximum at 1.9 K (the maximum is likely to be just outside of the covered temperature range, see yellow curve in Fig. 6.4). This is coherent with previous works [195], where an electronic magnetic peak centered at 1.9 K was evidenced. For 0.5 %, 2 % and 10 % of Hf, the signals appear to be almost identical to the pure compound. This is not the case for the other samples, with the maximum of the peak not following linearly the Hf content. In the assumption of a Schottky-like contribution to the specific heat, this would imply an energy gap between two levels which does not linearly depend on the Hf content. This is on the other hand the case for the onset of the signal (around 20 K), where the rise of the correlations appearing at higher temperatures for the samples containing more Hf. This hierarchy seems to hold true down to 5 K and suggests that the temperature at which correlations start to build up increases with the amount of structural disorder. Upon application of a magnetic field, one sees the typical shift of the correlation peak to higher temperatures due to the Zeeman effect, as seen in other spin ices [206, 130, 27]. All samples display a linear behavior of the peak position with respect to field, which would suggest a typical Zeeman splitting of a two levels system, although at a slightly different rate. At a field of 1 T, all signal seem to experience a similar shift to the right, with now all maxima within the measured range and following a similar hierarchy of intensities as in zero field. However the application of higher fields rearranges the curves, with all of them almost superimposed at 2 T and a complete change of hierarchy and intensity at 5 T.
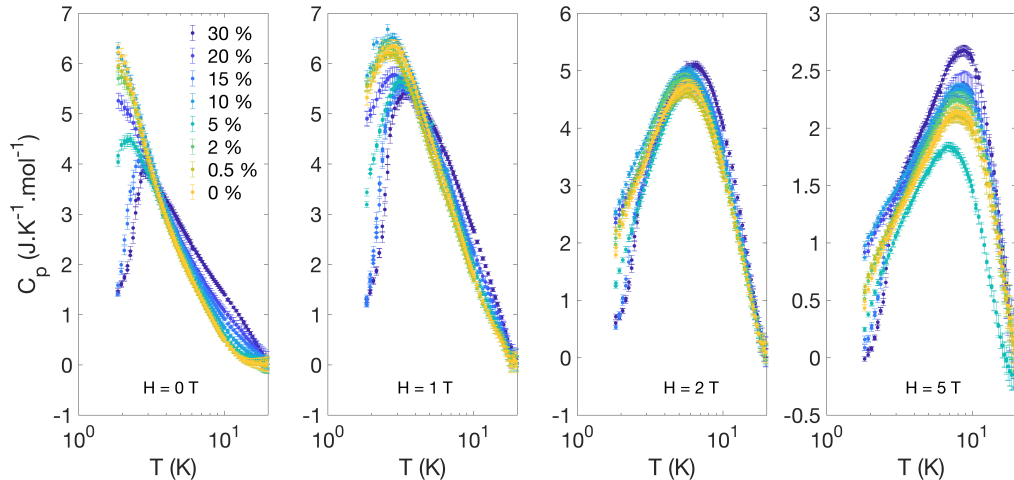
Figure 6.4: Temperature dependence of the magnetic contribution to the specific heat measured under several magnitudes of magnetic field and for various compositions.

6.2.3 Magnetic diffuse scattering

Signs of magnetic correlations can also be found in neutron diffraction data. Neutron diffraction patterns were measured on HRPT (SINQ) at 100 K and 1 K, on samples containing 40 %, 20 %, 5 % and 0 % of Hf. No additional Bragg peak (or Bragg intensity) appeared compared to the data collected at room temperature. The observed intensity corresponds to an energy integrated signal as the experiment was performed without analyzer. The high temperature data were subtracted from the low temperature one, removing the Bragg and background contributions from the low temperature patterns. We are then left with diffuse intensity showing a clear modulation as a function of momentum transfer in addition to a rapid convergence to zero (see Fig. 6.5a), which can readily be attributed to the effect of the magnetic form factor. Interestingly, the decreasing overall intensity as a function of composition. This suggests a progressive diminution of the effective magnetic moment when increasing the amount of Hf. This observation is consistent with the hypothesis of a mix of m_J states used to explain the magnetization data. As explained when describing the magnetic susceptibility data, the single-ion ground state of pure $Ho_2Ti_2O_7$ being a pure $m_J = \pm 8$ state [141], a mix of other m_J states will lead to a decreased effective moment, decreased overall magnetic signal and a reduced single-ion anisotropy. The modulation as a function of $\mathbf{Q}$ is clearly identical to what was observed in $Ho_2Ti_2O_7$, as well as other dipolar spin ice compounds [207], suggesting the presence of the same '2-in-2-out' correlations. The obtained diffuse intensities were used to perform a RMC simulation using the Spinvert program [208]. An example can be seen as the red line in Fig. 6.5a, corresponding to the fit of the 5 % doped sample. The obtained spin configurations were subsequently used to generate the expected diffuse scattering map in the typically probed HHL plane (see Fig. 6.5b showing the expected map for the 5 % doped sample). The shape of the diffuse signal is once again very similar to what has been measured on $Ho_2Ti_2O_7$ [81], strongly suggesting the presence of a similar magnetic ground state. Ultimately, single crystal experiments using polarized neutrons would be interesting in order to compare the pinch-point scattering with that of $Ho_2Ti_2O_7$.

(a)

(b)
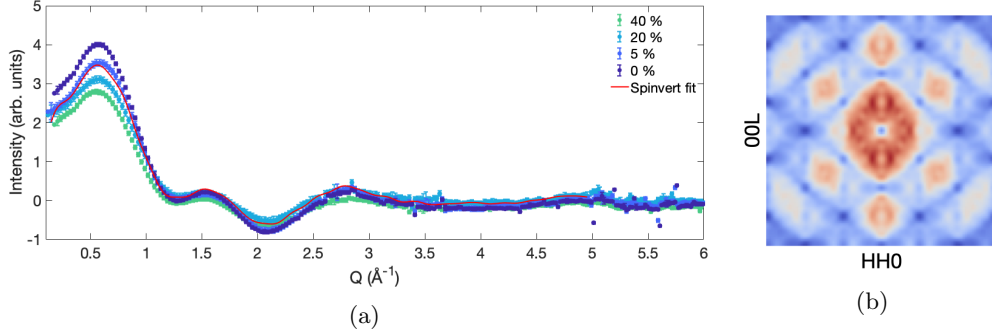
Figure 6.5: (**a**) Magnetic diffuse scattering obtained by subtracting data-sets recorded
at 100 K from 1 K data-sets. Patterns were collected using an incident wavelength of
1.886 Å. The red line represents the RMC fit to the data using Spinvert for the 5 %
doped system. (**b**) RMC simulation of the magnetic diffuse scattering in the HHL plane
for the 5 % doped compound computed using Spinvert.

6.3 Dynamics of the spin ice phase

6.3.1 ac-susceptibility

In order to gain further insight into the structural disorder's impact on the Coulomb
phase evidenced in $Ho_2Ti_2O_7$, we looked at the monopole relaxation in our sample con-
taining 10 % of Hf. The idea is that the non-magnetic disorder might enhance quantum
fluctuations, which in turn would accelerate the spin dynamics in the system and lead
to a decrease of the monopole relaxation times at low temperatures. To do so, we col-
laborated with Dr. Elsa Lhotel (Institut Néel, France) and performed AC-susceptibility
measurements on a powder sample of $Ho_2(Ti_{0.9}Hf_{0.1})_2O_7$. The obtained real and imag-
inary parts of the magnetic susceptibility is shown as a function of temperature and
frequency in Fig. 6.6. One can clearly see the frequency and temperature dependences,
with both signals moving to the right and decreasing in magnitude when increasing the
frequency or temperature.

Let us first look at the frequency dependence shown in Fig. 6.6a. The block-
ing/suppression of the in-phase susceptibility as a function of frequency suggests slow
relaxation, also corroborated by the broad shape of the χ''_{AC}. The maximum of the
imaginary part moves to smaller frequencies when the temperature is lowered, consis-
tent with a freezing of the magnetic moments. In addition, the asymmetry of the peak in
the χ''_{AC} curves implies that several processes with slightly different energy scales are in-
volved. Now turning to the temperature dependence of the ac-susceptibility (Fig. 6.6b),
we again see the typical signs of slow relaxation behavior with a peak in the imaginary
part with its maximum in the vicinity of the inflection point of the real part of the
signal, right before χ'_{AC} reaches its maximum and decreases. Again, the asymmetry of
the χ''_{AC} peak is very pronounced and cannot be captured using a single function.
The relaxation times were extracted using Debye functions and are displayed in Fig. 6.10.
Something to point out is the discrepancy at 'high' temperature between the relaxation
times extracted from $\chi''_{AC}(f)$ and $\chi''_{AC}(T)$. The exact reason for it is not certain but is
possibly due to instrumental effects or from corrections that should be applied, such as
demagnetization. Fitting both sets of relaxation times obtained from ac-susceptibility
together, using an Arrhenius law, yields a $\tau_0 = 7.4 \times 10^{-9}$ s (see continuous red line
in Fig. 6.10), which seems to be faster than previously observed in the pure compound
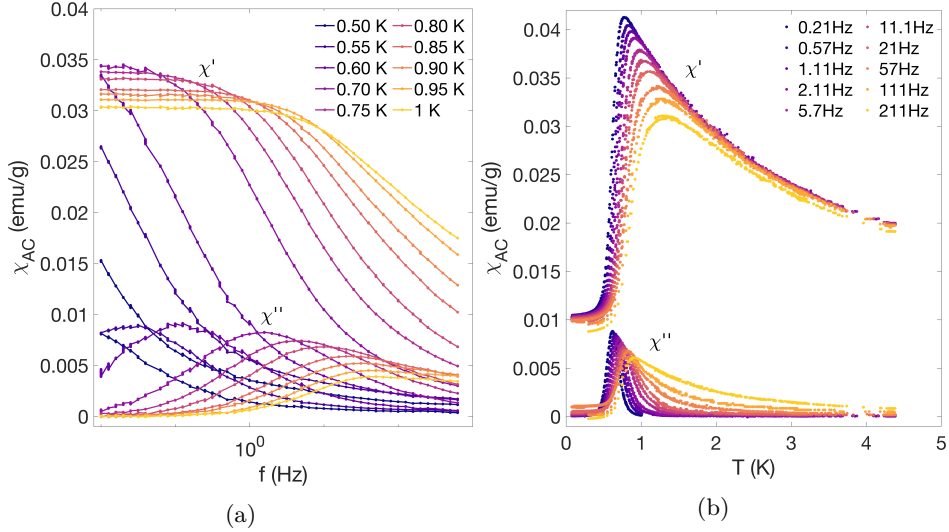
Figure 6.6: (**a**) Real and imaginary part of the ac-susceptibility measured on the 10 % doped sample as a function of frequency and at several temperatures. (**b**) Real and imaginary part of the ac-susceptibility measured on the 10 % doped sample as a function of temperature and at several frequencies. The real part was shifted up by 0.008 to improve visualization.

($\approx 10^{-6}$) [196] (see Table. 6.1). The fitted activation energy is $E_a = 11.2 \pm 0.9$ K, a bit higher than for Ho$_2$Ti$_2$O$_7$ (10.7 K) [196]. The difference could come from the same reasons enunciated for the deviation between τ extracted from $\chi''_{AC}(f)$ and $\chi''_{AC}(T)$, but more interestingly could be related to a distribution of effective exchange interaction between the magnetic moments [196]. A change of the effective exchange interaction would probably be linked to the disorder introduced in the system, affecting several parameters, such as the effective magnetic moment (through the CEF) or the exchange interaction due to a modified or a distribution of exchange paths.

In order to have a qualitative estimation of the distribution of activation energies, we look at the Cole-Cole plot of the ac-suscpetibility data collected as a function of frequency at various temperatures [209]. We therefore plot $\chi''_{AC}(f)$ as a function of $\chi'_{AC}(f)$ (see Fig. 6.7), restricting ourselves to data sets where the maximum of $\chi'_{AC}(f)$ is visible (T > 0.7 K). For a unique energy barrier, we expect to obtain a perfect semi-circle. This is clearly not the case here, indicating a distribution of energy barriers. To get an estimation of this distribution we can fit the data using a generalized Debye model [209]:

$$\chi'' = \left(\frac{\chi_T - \chi_S}{2} \tan \frac{\pi\alpha}{2} \right) + \sqrt{(\chi' - \chi_S)(\chi_T - \chi') + \left(\frac{\chi_T - \chi_S}{2} \tan \frac{\pi\alpha}{2} \right)^2} \qquad (6.1)$$

where χ_T and χ_S are the isothermal and adiabatic susceptibilities, respectively [209]. α is the fitted parameter, containing information about the distribution of relaxation processes, varying between 0 and 1 (0 being the case of a single relaxation process or single energy barrier). From the α values, obtained at different temperatures, we can now have a rough estimate of the distribution of energy barriers $g(E)$ [210] by calculating:

$$g(E) = \frac{1}{2\pi}\left(\frac{\sin\alpha\pi}{\cosh\left[(1-\alpha)\frac{E-E_m}{k_B T}\right] - \cos\alpha\pi}\right) \tag{6.2}$$

As shown in Fig. 6.7, the largest distribution is obtained at a temperature of 1 K and has a full width at half maximum $\Delta E_{FWHM} = 0.3\ K$, which is actually smaller than the estimated error on the fitted energy barrier E_a.
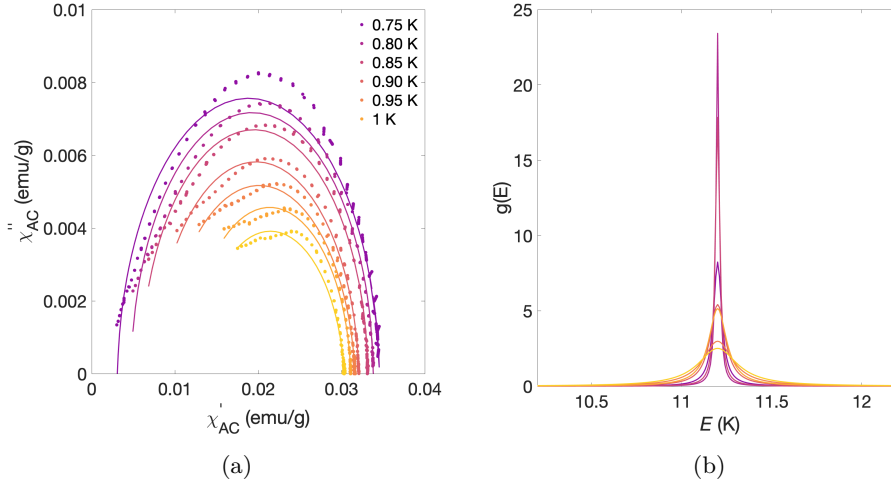
Figure 6.7: (**a**) Cole-Cole plot of the ac-suscpetibility data at various temperatures. The lines corresponds to the fit of the data using Eq. 6.1. (**b**) Distribution of energy barriers centered around the fitted mean energy of activation (11.2 K) obtained using Eq. 6.2.

6.3.2 Neutron spin echo

In order to extend our analysis and access faster relaxation times, we performed neutron spin echo spectroscopy on the same powder sample at the WASP spectrometer (ILL). We carried out measurements at several temperatures between 200 K and 0.08 K, providing a large coverage of the relaxation behavior as a function of temperature. Data measured at 0.08 K turned out to be essentially flat. This signal was thus considered as the static response of the sample (S(**Q**,0)) and used to normalize the rest of the data to get the 'echo' (S(**Q**,t)/S(**Q**,0)). The echo signals can be seen in Fig. 6.8, together with the fits using a stretched exponential (continuous lines).

Initial fits were carried out leaving all parameters free (scaling factor, relaxation time and stretching parameter). However, very good fits and a less erratic behavior of the relaxation time and scaling factor was obtained by fixing the stretching parameter to 2/3. Such behavior was also found in stuffed Ho₂Ti₂O₇ [198], for which this fixed stretching parameter was associated with two possible explanations: hierarchical cascades of relaxing clusters, or to the fact that the magnetic ions experience different magnetic environments. The second possibility could be related to the non-magnetic disorder induced in our sample, but as in the mentioned study, no Q-dependence of the signal could be identified, preventing us from ruling out any of the two hypotheses.

As can been seen in Fig. 6.9a, the fitted relaxation time seems to show a plateau at temperature below 1 K and relaxation times of about 400 ns. However, such relaxation
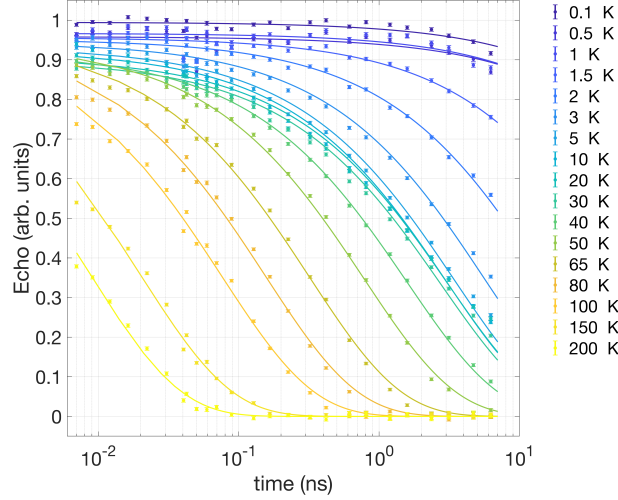
Figure 6.8: Spin Echo signal as a function of time collected at several temperatures and
fitted using a stretched exponential.
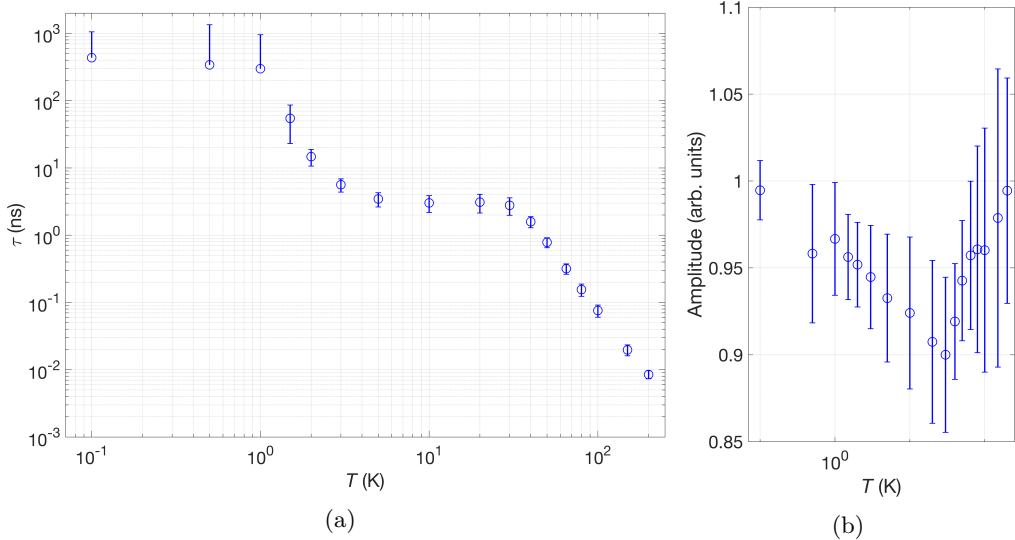
Figure 6.9: Extracted relaxation times (**a**) and fitted scaling factor (**b**) as a function of
temperature. The points obtained at the three lowest temperatures should be discarded
as they correspond to relaxation times too long to be accessible using neutron spin echo.

time is too long for the present neutron experiment, which is not expected to be sen-
sitive above a few tens of nanoseconds. Thus, the three points obtained at the lowest
temperatures should be neglected.

Plotting the relaxation times $\tau(T)$ obtained from ac-suscpetibility and NSE together,
as in Fig. 6.10, we get an overall view of the monopole dynamics in the compound.
On can clearly identify three regions: T < 5 K, 5 K < T < 30 K and T > 30 K.
The same behavior was observed in other Ho^{3+} pyrochlores [85, 197, 198, 196]. Upon
cooling from room temperature, we observe very fast relaxation times ($\tau < 10^{-10}s$),
gradually slowing down until the temperature reaches approximatively 40 K. In this

region, the monopole relaxation relies on the transition to excited CEF levels through
thermal fluctuations, which decreases together with the temperature, explaining the
slower dynamics at low temperatures. An attempt to fit $\tau(T)$ in this region using an
Arrhenius law gives a $\tau_0 \approx 5 \times 10^{-12}$ s and an activation energy $E_a = 237 \pm 50$ K
(see dashed red line in Fig. 6.10). This activation barrier is found to be lower than
in pure Ho$_2$Ti$_2$O$_7$ [85, 196] and is also lower than the magnetically disordered related
compounds [197, 198] (see Table. 6.1), which could mean that the CEF levels are shifted
to low energy by substitution of Ti by Hf. Once again this would need to be confirmed
with a detailed CEF analysis using Raman or INS. The moderate quality of the fit is also
pointing towards the presence of a distribution of CEF levels, certainly stemming from
the structural disorder. Below 30-40 K, we enter a plateau region. Previously [85, 197,
198, 196], this was interpreted as the region where the relaxation mechanism is largely
dominated by quantum tunneling processes. The tunneling rate depends on several
variables: the CEF, defining the energy barrier the moments have to tunnel through [86]
; the exchange and dipolar interactions, which will mix some CEF levels [211] ; and to
some extent the hyperfine interaction [211]. The height of the plateau lies around 3 ns,
which is faster than what is observed in Ho$_2$Ti$_2$O$_7$ ($\approx$ 10 ns) [198] (see Table. 6.1),
suggesting a more efficient tunneling. This is the result we hoped for if transverse fields
act as a source of quantum dynamics.
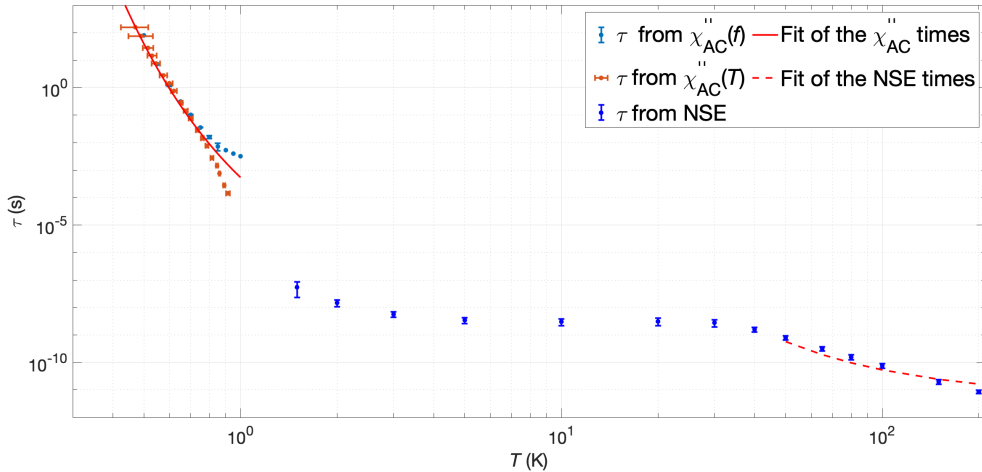
Figure 6.10: Superposition of the relaxation times extracted from ac-susceptibility mea-
sured as a function of frequency and temperature (points below 1 K) and extracted from
Neutron Spin Echo measurement (points above 1 K). The continuous red line represents
the combined fit of the relaxation times extracted from the χ_{AC} measurements using
an Arrhenius law, yielding an activation energy of 11.2 ± 0.9 K and $\tau_0 = 7.4 \times 10^{-9}$ s.
The dashed red line represent the Arrhenius fit of the high temperature data measured
using neutron spin echo, giving an activation energy of 237 ± 50 K and a τ_0 of about
5×10^{-12}.

On further cooling, below about 5 K, one observes a new increase of the relaxation
time. This region is best captured through the ac-suscpetibility data (see section 6.3.1)
due to neutron spin echo not being sensitive to such long times. At these temperatures,
the system is entering a frozen state, gradually condensing into a disordered ice-like
configuration. In this regime, the monopole density is very low, which considerably
slows down the relaxation of the system [85, 197, 198, 196, 158].

	$\tau_0^{lowT}(s)$	$E_a^{lowT}(K)$	$\tau_{Plateau}(s)$	$\tau_0^{highT}(s)$	$E_a^{highT}(K)$
Ho$_2$Ti$_2$O$_7$ [85, 196]	1.7422×10^{-6}	10.7	$\approx 10^{-8}$	9.09×10^{-12}	293
Ho$_{2+x}$Ti$_{2-x}$O$_{7-\delta}$ [198]	-	-	$3 \times 10^{-10} - 10^{-9}$	-	290
Ho$_{2-x}$Y$_x$Ti$_2$O$_7$ [197]	-	-	$1 - 3 \times 10^{-11}$	7.3×10^{-12}	270
Ho$_2$Ti$_{1.8}$Hf$_{0.2}$O$_7$	7.4×10^{-9}	11.2	$\approx 3 \times 10^{-9}$	5×10^{-12}	237

Table 6.1: Table summarizing the ac-susceptibility and neutron spin echo results on various holmium pyrochlores [85, 197, 198, 196]. The lowT exponent relates to the parameters of the Arrhenius fit to the low temperature ($<$ 1 K) relaxation time obtained via ac-susceptibility, whereas the exponent highT refers to the that of the high temperature ($>$ 40 K) relaxation times extracted from NSE. The $\tau_{Plateau}$ gives the approximative relaxation time of the system in the region where it is approximatively temperature independent. Other values were reported for Ho$_2$Ti$_2$O$_7$ in [212] but were collected on a single crystal.

6.4   Summary

Following up a theoretical proposal where non-magnetic structural disorder allows the stabilization of a quantum spin liquid state [21], we exploited the flexibility of the pyrochlore structure and the different chemical bonding properties of Ti^{4+} and Hf^{4+} to tune the oxygen disorder via progressive elemental substitution on the B site. We then studied the behavior of the static and dynamic magnetic properties of the samples as a function of the disorder and compared our results to the canonical spin ice system Ho$_2$Ti$_2$O$_7$.

First, we demonstrated the control of the oxygen disorder in the samples by progressively substituting the Ti atoms by Hf ones, while the Ho lattice remains ordered. The magnetic susceptibility data show very little changes in terms of the extracted Curie-Weiss temperature and effective magnetic moment. However the magnetization data display a clear trend as a function of substitution, with an interesting behavior of the g-factor motivating a more detail analysis of the crystal-electric field. The deviation between the zero-field-cooled and field-cooled susceptibility curves moves towards lower temperatures when the disorder is increased, suggesting an enhancing of the spin dynamics, as we hope for transverse field assisted dynamics.

The magnetic correlations also appear to be influenced by the disorder as evidenced in the specific heat measurements. In this instance, the magnetic contribution to the specific heat does not appear to follow a uniform behavior as a function of substitution. Interestingly, the application of a magnetic field of about 2 T seems to wash out these discrepancies. A more tractable influence of the disorder on the correlation can be found in the neutron magnetic diffusion signal, where the typical diffuse pattern expected for a spin ice decreases in magnitude with increasing substitution, suggesting less dominant ice-like correlations due to a reduced Ising character of the magnetic moments, which would be in agreement with the magnetization data. A development of the quadrupolar moments could also cause a reduction of the dipolar moments and would beg the question of whether spin ice and quadrupolar correlations are in competition or coexist.

Finally, focusing on one composition, we used ac-susceptibility and neutron spin echo spectroscopy to assess the dynamics of the system and compare it with the thoroughly studied Ho$_2$Ti$_2$O$_7$. Judging by the observed temperature and frequency behavior of the sample, it seems that the introduction of a small amount of structural disorder succeeded in enhancing the spin fluctuations leading to faster dynamics and monopole relaxation. Although our results are encouraging, experiments on a single crystal would be extremely valuable to confirm the kind of magnetic correlation by studying the anisotropy

of the magnetic diffuse scattering, to look for possible neutron active excitations using
INS and determine the spin anisotropy by application of a magnetic field in a specific
direction.

Conclusion and outlook

$\mathcal{F}$RUSTRATED magnets have been an important field for both chemists and physicists due to their unusual and sometimes exotic behaviors, as well as by their often challenging synthesis. The holy grails of frustrated systems are the highly anticipated quantum spin liquid states ; disordered yet highly correlated states of matter evading long-range magnetic order and freezing down to absolute zero temperature. The quantum spin ice is a three dimensional example of such state. In this case, ferromagnetically interacting magnetic moments, sitting on the nodes of a network of corner sharing tetrahedra are subject to geometrical frustration, enforcing a so-called 'two-in-two-out' local constrain on each tetrahedron.

The family of the magnetic pyrochlore oxides attracted a lot of attention owing to its predisposition to spin ice physics induced by their crystallographic structure. So far, the two most studied compounds are $Ho_2Ti_2O_7$ and $Dy_2Ti_2O_7$. Although all the questions around their dynamics are not yet answered, the understanding of these two classical spin ice systems has gone a long way. However, their quantum analogs, the quantum spin ice materials, are more elusive and at the moment remain to be unambiguously evidenced. The absence of smoking-gun experiment severely impairs the identification of this state, requiring a large variety of experimental techniques to investigate these highly frustrated and entangled systems.

Cerium-based pyrochlores surfaced as very promising quantum spin ice candidates owing to the single $4f$ electron of Ce^{3+}. Part of this work focused on two of these compounds, namely $Ce_2Sn_2O_7$ and $Ce_2Hf_2O_7$. After a fine determination of our samples's crystallographic structure, we performed detailed magnetometry measurements, suggesting that both systems display an Ising anisotropy, with magnetizations as saturation coherent with spin ice physics. However, some experimental observations are not in agreement with the conventional behavior of a quantum spin ice. Indeed, the magnetic correlations evidenced through specific heat are not observed in neutron diffuse scattering experiments in the same way as in other spin ices. Instead of following a dipolar form factor, the magnetic diffuse scattering appears as a broad liquid-like bump at high momentum transfer. In addition, the magnetic susceptibility data at very low temperature show a progressive loss of the effective magnetic moment concomitant with the rise of the magnetic correlations. Performing an exhaustive experimental and theoretical study, we could model the magnetic ground state of both materials. We showed that the correlated 'ice' state is formed by octupolar degrees of freedom, which are significant due to the crystal-electric field scheme of Ce^{3+} in the pyrochlore structure, leading to a ground state composed by a mixture of $|\pm 3/2\rangle$ states. We then performed multiple inelastic neutron scattering experiments, showing the existence of a continuum of excitations in both samples. Resolving the continuum of excitations in $Ce_2Sn_2O_7$ to high accuracy demonstrated its gapped nature and confirmed its asymmetric shape as a function of energy. The comparison of this continuum with predictions on the spinon

spectrum emerging from the QED of a quantum spin ice shows a remarkable agreement. Clear evidence of fractionalized excitations are rare and restricted to one dimensional magnetic systems so far, with higher dimensional systems only providing qualitative arguments. To our knowledge, this work presents the first quantitative comparison between experimentally observed continua of excitations in a quantum spin liquid candidate and theoretical models of spinon excitations. In order to gain further insight into this peculiar magnetic ground state, additional inelastic neutron scattering experiments on large single crystals are highly anticipated, allowing to look at the momentum dependence of the observed excitations and perhaps revealing the presence of pinch-points located at high momentum transfer.

Another very good candidate quantum spin liquid is the highly disordered $Tb_2Hf_2O_7$. This system displays a correlated phase in many aspects reminiscent of its sister compounds $Tb_2Ti_2O_7$, despite its very strong structural disorder that usually jeopardize spin liquid states. This disorder has in fact a dramatic impact on the crystal-electric field spectrum of Tb^{3+} in terbium hafnate, taking the shape of a continuum of excited states instead of discrete energy levels. This significantly complicates the determination of the single-ion ground and excited states, even without considering a coupling with phonon modes as observed in $Tb_2Ti_2O_7$. Performing a very detailed analysis using neutron pair distribution function, reverse Monte Carlo method and point charge calculations, we could qualitatively capture the crystal-electric field spectrum of $Tb_2Hf_2O_7$. We then used this analysis to compute experimental observables and compared them with measurements of magnetic susceptibility, magnetization, specific heat and neutron scattering. We showed that the structural disorder does not destroy the spin liquid state evidenced in terbium hafnate, although it might be responsible for the presence of some non-magnetic impurities as well as the partial freezing of the magnetic moments at very low temperature. Our results are to some extend able to account for the observed diffuse magnetic scattering and field induced behavior of $Tb_2Hf_2O_7$, but requires further work in order to determine the exact exchange tensor through which the magnetic moments interact as well as the importance of the quadrupolar degrees of freedom induced by the disorder.

Subsequently, we showed that a very small concentration of the same defects as found in $Tb_2Hf_2O_7$ could also be present and play a significant role in other pyrochlore quantum spin liquids. $Pr_2Zr_2O_7$ is a material presenting a magnetic ground state that has been thoroughly studied over the last ten years. It can be understood as stabilizing antiferro-quadrupolar correlations from which emerges spin-ice like excitations. The quadrupolar degrees of freedom could stem from very small structural distortions affecting the crystal-electric scheme of the non-Kramers praseodymium ions. This contrasts with its sister compound $Pr_2Hf_2O_7$, which shows signatures consistent with realization of a dipolar quantum spin ice. We therefore undertook a comparative structural study of the same samples previously used in inelastic neutron experiments. Performing electron microscopy and neutron scattering, we evidence a structural diffuse signal in the zirconate, which is hardly observable in the hafnate compound, corroborating the claims made on the role of structural disorder in these materials. Adopting a rational approached we computed the diffuse intensity expected from the presence of a small amount of Frenkel pair defects. Our results are in good agreement with the signal spotted in neutron single crystal diffuse scattering and seem to go in the same direction as the hypothesis introduced to justify the ground state of $Pr_2Zr_2O_7$. To take this analysis one step further, one would need to investigate the existence of possible correlations between the Frenkel pair defects, as well as the associated consequence of the crystal-electric field ground state.

In the last part of this work, we investigate the impact of non-magnetic disorder on

the magnetic dynamics of Ho$_2$Ti$_2$O$_7$. It was in fact theoretically proposed as a possible route to turn a classical spin liquid into a disorder induced quantum spin liquid, given an amount and strength of non-magnetic disorder within some boundaries. To explore this idea, we controlled the quantity of Frenkel pair defects in samples of holmium titanate where we gradually replace the titanium ions by hafnium ones. We then carefully investigated the impact of these increasing amounts of defects on the structure and on the magnetic properties through magnetometry and specific heat measurements. The global outcome is that the small amounts of disorder introduced seem to enhance spin fluctuations, consistent with a scenario of transverse field-induced quantum fluctuations. Focusing on one composition, we performed a detailed study of the dynamical properties using ac-susceptibility and neutron spin echo measurements in view of comparing our results with the results obtained on other holmium titanates samples. Although single crystal data would greatly benefit our work, powder data already suggest a magnetic ground state similar to the pure Ho$_2$Ti$_2$O$_7$, with improved monopole dynamics. Magnetic diffuse scattering using polarized neutrons on single crystal samples as well as inelastic neutron scattering would be of great interest in order to hunt for possible signatures of quantum spin ice, such as the broadening of the pinch-points.

Overall, we explored the great flexibility and complexity of the rare earth pyrochlore oxides. We showed the stark connection between the crystallographic structure, the single ion properties and the low temperature correlated states emerging in these compounds. Furthermore, we highlighted the importance of multipoles in such systems, playing either a dominant role, forming a 'hidden' ice state, or acting as transverse terms arising from diverse degrees of disorder. Finally, theoretical models and experimental results are becoming ever more reliable and comparable, perhaps paving the way to the discovery of a smoking-gun experiment allowing one to unequivocally identify a quantum spin ice state.

Appendices

Results of structural refinements for $Ce_2Sn_2O_7$

The crystallographic parameters resulting from the Rietveld refinement of the neutron powder diffraction data and neutron pair distribution function data are given in Table 2 and Table 3, respectively.

lattice parameter (Å):	10.6517(1)			Space Group	Fd-$3m$				
Atoms	x	y	z	u_{11}	u_{22}	u_{33}	u_{12}	u_{13}	u_{23}
Sn (16c)	0	0	0	0.0012(1)	0.0012(1)	0.0012(1)	-0.0001(1)	-0.0001(1)	-0.0001(1)
Ce (16d)	0.5	0.5	0.5	0.0018(1)	0.0018(1)	0.0018(1)	-0.0002(1)	-0.0002(1)	-0.0002(1)
O (8b)	0.375	0.375	0.375	0.0018(1)	0.0018(1)	0.0018(1)	0	0	0
O (48f)	0.3308(1)	0.125	0.125	0.0021(1)	0.0017(1)	0.0017(1)	0	0	0.0004(1)
Lambda (Å)	1.155		χ^2	3.32					
Number of parameters	31		R_f	1.87	Number of independent reflections	186			
(intensity dependent)	(12)		R_{Bragg}	2.91					

Table 2: Refined parameters for $Ce_2Sn_2O_7$ at 300 K from constant-wavelength neutron diffraction data recorded on HRPT.

lattice parameter (Å):	10.6509(62)			Space Group	Fd-$3m$				
Atoms	x	y	z	u_{11}	u_{22}	u_{33}	u_{12}	u_{13}	u_{23}
Sn (16c)	0	0	0	0.0047(34)	0.0047(34)	0.0047(34)	0.0006(26)	0.0006(26)	0.0006(26)
Ce (16d)	0.5	0.5	0.5	0.0075(56)	0.0075(56)	0.0075(56)	0.0007(8)	0.0007(8)	0.0007(8)
O (8b)	0.375	0.375	0.375	0.0085(71)	0.0085(71)	0.0085(71)	0	0	0
O (48f)	0.3308(13)	0.125	0.125	0.0094(68)	0.0072(51)	0.0072(51)	0	0	0.0014(38)
Number of parameters	15		$\chi^2_{Reduced}$	0.005308					
(intensity dependent)	(14)		R_w	0.123026					

Table 3: Refined parameters obtained from the Pair Distribution Function analysis of $Ce_2Sn_2O_7$ at 300 K.

Results of structural refinements for $Ce_2Hf_2O_7$

The crystallographic parameters resulting from the Rietveld refinement of the neutron powder diffraction data and least-square refinement of the single-crystal neutron diffraction data are given in Table 4 and Table 5, respectively.

a = 10.6938(6)Å	$T = 1.5$ K		x		y		z	occ
Ce (16d)			0.5		0.5		0.5	1
Hf (16c)			0		0		0	1
O (48f)			0.375		0.375		0.375	1
O' (8b)			0.333(2)		0.125		0.125	1
O" (8a)			0.125		0.125		0.125	0.06(1)
ADPs in Å^2	U_{11}	U_{22}	U_{33}	U_{12}	U_{13}	U_{23}		
Ce (16d)	0.00116	0.00116	0.00116	0.00047	0.00047	0.00047		
Hf (16c)	0.00075	0.00075	0.00075	-0.00009	-0.00009	-0.00009		
O (48f)	0.00167	0.00125	0.00125	0	0	0.00000		
O' (8b)	0.00166	0.00126	0.00126	0	0	0.00040		
O" (8a)	0.00465	0.00465	0.00465	0	0	0		

Table 4: Structural parameters obtained from Rietveld refinement of our starting polycrystalline sample of $Ce_2Hf_2O_7$ measured at 1.5 K (space group $Fd\bar{3}m$, origin choice 2): $R_{Bragg} = 6.68$; $R_F = 4.49$. The lattice parameters, the x coordinate of the oxygen (48f), the occupation of the oxygen (8a) as well as all the anisotropic temperature factors were refined.

a = 10.6988(1)Å T = 297 K	x	y	z	U_{iso}	occ
Ce ($16d$)	0.5	0.5	0.5	0.51287	1
Hf ($16c$)	0	0	0	0.20366	1
O ($48f$)	0.375	0.375	0.375	0.69443	1
O' ($8b$)	0.331(3)	0.125	0.125	0.61752	1
O" ($8a$)	0.125	0.125	0.125	0.83292	0.07(2)

Table 5: Structural parameters obtained from least-square refinement of neutron diffraction on our crystal of $Ce_2Hf_2O_7$ measured at room temperature using a Eulerian cradle (space group $Fd\bar{3}m$, origin choice 2): $R_F = 4.04$. The x coordinate of the oxygen ($48f$), the occupation of the oxygen ($8a$) as well as all the anisotropic temperature factors were refined. The value of the lattice parameter was obtained via X-ray diffraction, at room temperature, on a ground fragment of crystal.

Defective crystal electric field environment

As mentioned in the main text, the number of allowed parameters of the second CEF environment, the defective one, is too large compared to the number of observable CEF transitions. This part of the fit is thus underconstrained and the obtained fitting parameters are not very reliable. In the Stevens formalism, these CEF parameters are $B_2^0 = 2.638$, $B_2^1 = -0.152$, $B_2^2 = -0.029$, $B_4^0 = 0.160$, $B_4^1 = 0.001$, $B_4^2 = 0.001$, $B_4^3 = 0.182$, $B_4^4 = 8.749e - 05$, $B_6^0 = -0.007$, $B_6^1 = 3.02e - 06$, $B_6^2 = -1.470e - 05$, $B_6^3 = 0.038$, $B_6^4 = -1.016e - 05$, $B_6^5 = -1.663e - 05$ and $B_6^6 = -0.025$ meV. The corresponding ground-state wavefunction can be found in table 6.

Crystal-electric field calculation using SPECTRE

The flexibility of the PyCrystalField package was extremely important in our detailed analysis of the CEF data. Nevertheless, its approach is different from more classical ones based on Stevens and Wybourne formalism. SPECTRE, for instance, assumes a basis containing n electrons to be distributed within the $4f$ shell. The LS coupling along with electric repulsion between electrons allows to work in the term basis, formed by the collection of $|J,m_j\rangle$, J being not unique. Noteworthy, the Stevens formalism restricts to the J subset of lowest energy. This results in specific correspondence between Wybourne and Stevens coefficients. PyCEF uses the L and S values of the ground state to create the basis, which gives new and specific coefficients. It is thus worth benchmarking our results with another widely used software, like SPECTRE. Using the set of CEF parameters obtained with PyCrystalField and converting it to the Wybourne formalism using internal routines, we computed the expected neutron cross section and ground-state wavefunction using SPECTRE. The wavefunction computed by SPECTRE is very similar to the one mentioned in the main text: $|\pm\rangle = 0.992|^2F_{5/2},\pm3/2\rangle \mp 0.119|^2F_{7/2},\pm3/2\rangle \mp 0.029|^2F_{5/2},\mp3/2\rangle + 0.009|^2F_{7/2},\mp3/2\rangle$.

Both expected neutron cross sections as well as the measured data are plotted in Fig. 11. The small difference observed between both calculated CEF schemes potentially stems from rounding errors, different diagonalization routines and/or from the choice of formalism of each program. In addition, the simulated cross section from SPECTRE was plotted with a constant peak width whereas the PyCrystalField one uses a phenomenological energy dependence of the peak widths based on the predicted instrumental resolution and experimental data.

Uncertainty on the crystal-electric field parameters

Errors on the crystal-electric field parameters in table 3.2 were estimated using an incremental search over the variables used in the fit, following a similar method as in [213]. Due to the limited amount of observables compared to the number of CEF parameters, the fit was carried out by varying the charges used in the point charge calculations and not directly on the CEF parameters. The same applies for the incremental search which thus involves the two charges used in the point charge model (different charges for basal and apical oxygens) as well as a global scaling factor. The errors obtained on the variables were then used to determine the errors on the CEF parameters.
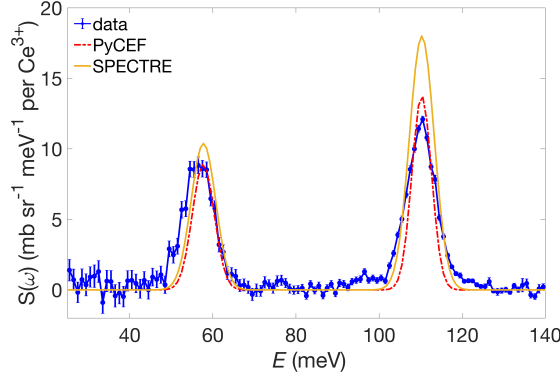
Figure 11: Comparison between measured CEF excitations and calculated neutron cross section from both PyCrystalField and SPECTRE, using phenomenological energy transfer dependent peak width or constant peak width, respectively.

$|^2F_{5/2},\mp5/2\rangle$	$|^2F_{5/2},\mp3/2\rangle$	$|^2F_{5/2},\mp1/2\rangle$	$|^2F_{5/2},\pm1/2\rangle$	$|^2F_{5/2},\pm3/2\rangle$	$|^2F_{5/2}, \pm5/2\rangle$
±0.001	-0.238	∓0.001	0.006	±0.833	+0.004
$|^2F_{7/2},\mp5/2\rangle$	$|^2F_{7/2},\mp3/2\rangle$	$|^2F_{7/2},\mp1/2\rangle$	$|^2F_{7/2},\pm1/2\rangle$	$|^2F_{7/2},\pm3/2\rangle$	$|^2F_{7/2},\pm5/2\rangle$
∓0.001	+0.155	±0.001	-0.004	∓0.475	-0.002

Table 6: List of contributions from the different states to the ground state wavefunction of the defective model. Note that the $|^2F_{7/2},\pm7/2\rangle$ state is not listed here as its contribution is calculated as null.

Estimation of the main exchange coupling in Tb$_2$Hf$_2$O$_7$

Taking the derivative of the magnetization as a function of applied magnetic field for a field applied in the [111] crystallographic direction, a kink at low field values can be observed (see Fig. 12). This was also spotted in other spin ice compounds and is associated with a metamagnetic transition from a 'two-in-two-out' to a 'one-in-three-out'/'three-in-one-out' structure [94].
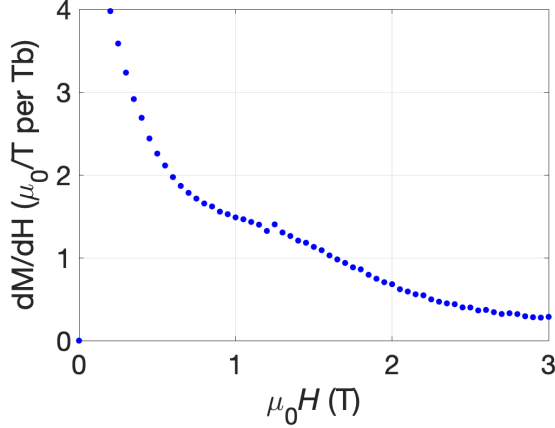
Figure 12: Derivative of the magnetization curve for a magnetic field applied along the [111] direction.

Taking a critical field value of 1.2 T and applying the same equation as in [94] $E_{eff} = \frac{1}{3}\mu_0\mu_{eff}H_c/k_B$, we estimate the effective exchange to be about 1.29 K.

Link between the distribution of ground state splitting and the random transverse field Ising model

We consider two singlets of given site i, $|E_{i,1}\rangle$ and $|E_{i,2}\rangle$, of respective energies E_2 and E_1. In the basis formed by these two singlets, the pseudo-spin-1/2 magnetic moment tensor, defined as $m_{i,j}^\alpha = \mu_B g_J \langle E_i|J_\alpha|E_j\rangle$, writes:

$$m^x = m^y = \begin{bmatrix} 0 & 0 \\ 0 & 0 \end{bmatrix} ; m^z = \begin{bmatrix} 0 & G \\ G^* & 0 \end{bmatrix} \tag{3}$$

with $|G| = g_{//}$. Thus, the eigenstates of this operator are $|\sigma = \pm\rangle = \frac{1}{\sqrt{2}}[(G/|G|)|E_{i,1}\rangle \pm |E_{i,2}\rangle]$. We can see that both $|E_{i,1}\rangle$ and $|E_{i,2}\rangle$ are non-magnetic states, whereas their linear combination $|\sigma = \pm\rangle$ has a magnetic moment $m^z = \pm\mu_B g_{//}/2$. We can now re-writte the two singlets in terms of $|\sigma = \pm\rangle$:

$$\begin{aligned} |E_{i,1}\rangle &= \frac{1}{\sqrt{2}}\frac{|G|}{G}(|\sigma = +\rangle + |\sigma = -\rangle) \\ |E_{i,2}\rangle &= \frac{1}{\sqrt{2}}(|\sigma = +\rangle - |\sigma = -\rangle) \end{aligned} \tag{4}$$

By resetting $\frac{E_1+E_2}{2} = 0$ K, one can show that we introduce a single-ion CEF term in the effective spin-1/2 (spin ice) Hamiltonian, of the form:

$$H_{single-ion} = \sum_n E_n |E_{i,n}\rangle\langle E_{i,n}| = \frac{(E_2 - E_1)}{2}(|E_{i,2}\rangle\langle E_{i,2}| - |E_{i,1}\rangle\langle E_{i,1}|)$$

$$= -(E_2 - E_1)\mathcal{S}_i^x = -\Delta_i \mathcal{S}_i^x$$

(5)

where $\mathcal{S}_i^x$ is the x-component of the pseudo-spin $\mathcal{S}$ at the site i. Comparing this single-ion Hamiltonian to the random transverse field Ising model 1.18 shows that this $\Delta_i \mathcal{S}_i^x$ constitutes an effective transverse field term $-h_i \mathcal{S}_i^x$ of a random transverse field Ising model (1.2.3).

Results of structural refinements for $Ho_2(Ti_{1-x}Hf_x)_2O_7$

The crystallographic parameters resulting from the Rietveld refinement of the neutron powder diffraction data collected at room temperature for each $Ho_2(Ti_{1-x}Hf_x)_2O_7$ sample.

a = 10.105284(35)Å	T = 300 K	x	y	z	occ
Ho ($16d$)		0.5	0.5	0.5	1
Ti ($16c$)		0	0	0	1
O ($48f$)		0.375	0.375	0.375	1.00(1)
O' ($8b$)		0.32921(9)	0.125	0.125	1
O" ($8a$)		0.125	0.125	0.125	0.00(1)
ADPs in Å^2	U_{11}	U_{22}	U_{33}	U_{12}	U_{13}	U_{23}
Ho ($16d$)	0.00130(2)	0.00130(2)	0.00130(2)	-0.00050(2)	-0.00050(2)	-0.00050(2)
Ti ($16c$)	0.001200(36)	0.001200(36)	0.001200(36)	0.000117(52)	0.000117(52)	0.000117(52)
O ($48f$)	0.000941(30)	0.000941(30)	0.000941(30)	0	0	0
O' ($8b$)	0.001581(39)	0.001134(22)	0.001134(22)	0	0	0.000296(34)
O" ($8a$)	0.00000	0.00000	0.00000	0	0	0

Table 7: Structural parameters obtained from Rietveld refinement of our starting polycrystalline sample of $Ho_2Ti_2O_7$ at 300 K (space group $Fd\bar{3}m$, origin choice 2): R_{Bragg} = 2.45; R_F = 1.55. The lattice parameters, the x coordinate of the oxygen ($48f$), the occupation of the oxygen ($8a$) as well as all the anisotropic temperature factors were refined.

a = 10.106559(35)Å	T = 300 K	x	y	z	occ
Ho ($16d$)		0.5	0.5	0.5	1
Ti ($16c$)		0	0	0	0.98(1)
Hf ($16c$)		0	0	0	0.02(1)
O ($48f$)		0.375	0.375	0.375	1.00(1)
O' ($8b$)		0.32923(5)	0.125	0.125	1
O" ($8a$)		0.125	0.125	0.125	0.00(1)
ADPs in Å^2	U_{11}	U_{22}	U_{33}	U_{12}	U_{13}	U_{23}
Ho ($16d$)	0.001332(21)	0.001332(21)	0.001332(21)	-0.000492(20)	-0.000492(20)	-0.000492(20)
Ti ($16c$)	0.001055(50)	0.001055(50)	0.001055(50)	0.000107(51)	0.000107(51)	0.000107(51)
Hf ($16c$)	0.00134(55)	0.00134(55)	0.00134(55)	0.00029(59)	0.00029(59)	0.00029(59)
O ($48f$)	0.000993(90)	0.000993(90)	0.000993(90)	0	0	0
O' ($8b$)	0.001597(39)	0.001188(22)	0.001188(22)	0	0	0.000330(33)
O" ($8a$)	0.00000	0.00000	0.00000	0	0	0

Table 8: Structural parameters obtained from Rietveld refinement of our starting polycrystalline sample of $Ho_2(Ti_{0.995}Hf_{0.005})_2O_7$ at 300 K (space group $Fd\bar{3}m$, origin choice 2): R_{Bragg} = 2.18; R_F = 1.24. The lattice parameters, the x coordinate of the oxygen ($48f$), the occupation of the oxygen ($8a$) as well as all the anisotropic temperature factors were refined.

a = 10.111819(34)Å	$T = 300$ K	x	y	z	occ
Ho (16d)		0.5	0.5	0.5	1
Ti (16c)		0	0	0	0.97(1)
Hf (16c)		0	0	0	0.03(1)
O (48f)		0.375	0.375	0.375	1.00(1)
O' (8b)		0.32937(5)	0.125	0.125	1
O" (8a)		0.125	0.125	0.125	0.01(2)

ADPs in Å^2	U_{11}	U_{22}	U_{33}	U_{12}	U_{13}	U_{23}
Ho (16d)	0.001349(19)	0.001349(19)	0.001349(19)	-0.000515(19)	-0.000515(19)	-0.000515(19)
Ti (16c)	0.001059(47)	0.001059(47)	0.001059(47)	0.000048(48)	0.000048(48)	0.000048(48)
Hf (16c)	0.00151(70)	0.00151(70)	0.00151(70)	0.00035(13)	0.00035(13)	0.00035(13)
O (48f)	0.001003(28)	0.001003(28)	0.001003(28)	0	0	0
O' (8b)	0.001645(36)	0.001232(21)	0.001232(21)	0	0	0.000317(32)
O" (8a)	0.00152(40)	0.00152(40)	0.00152(40)	0	0	0

Table 9: Structural parameters obtained from Rietveld refinement of our starting polycrystalline sample of Ho$_2$(Ti$_{0.98}$Hf$_{0.02}$)$_2$O$_7$ at 300 K (space group $Fd\bar{3}m$, origin choice 2): R$_{Bragg}$ = 2.23; R$_F$ = 1.37. The lattice parameters, the x coordinate of the oxygen (48f), the occupation of the oxygen (8a) as well as all the anisotropic temperature factors were refined.

a = 10.122550(35)Å	$T = 300$ K	x	y	z	occ
Ho (16d)		0.5	0.5	0.5	1
Ti (16c)		0	0	0	0.94(1)
Hf (16c)		0	0	0	0.06(1)
O (48f)		0.375	0.375	0.375	0.998(1)
O' (8b)		0.32956(5)	0.125	0.125	1
O" (8a)		0.125	0.125	0.125	0.007(4)

ADPs in Å^2	U_{11}	U_{22}	U_{33}	U_{12}	U_{13}	U_{23}
Ho (16d)	0.001399(18)	0.001399(18)	0.001399(18)	-0.000541(18)	-0.000541(18)	-0.000541(18)
Ti (16c)	0.001126(45)	0.001126(45)	0.001126(45)	0.000100(48)	0.000100(48)	0.000100(48)
Hf (16c)	0.00132(49)	0.00132(49)	0.00132(49)	0.00030(24)	0.00030(24)	0.00030(24)
O (48f)	0.001042(27)	0.001042(27)	0.001042(27)	0	0	0
O' (8b)	0.001829(35)	0.001336(20)	0.001336(20)	0	0	0.000343(31)
O" (8a)	0.00131(54)	0.00131(54)	0.00131(54)	0	0	0

Table 10: Structural parameters obtained from Rietveld refinement of our starting polycrystalline sample of Ho$_2$(Ti$_{0.95}$Hf$_{0.05}$)$_2$O$_7$ at 300 K (space group $Fd\bar{3}m$, origin choice 2): R$_{Bragg}$ = 2.07; R$_F$ = 1.19. The lattice parameters, the x coordinate of the oxygen (48f), the occupation of the oxygen (8a) as well as all the anisotropic temperature factors were refined.

a = 10.136129(41)Å	$T = 300$ K	x	y	z	occ
Ho (16d)		0.5	0.5	0.5	1
Ti (16c)		0	0	0	0.90(1)
Hf (16c)		0	0	0	0.10(1)
O (48f)		0.375	0.375	0.375	0.998(1)
O' (8b)		0.32996(5)	0.125	0.125	1
O" (8a)		0.125	0.125	0.125	0.009(4)

ADPs in Å^2	U_{11}	U_{22}	U_{33}	U_{12}	U_{13}	U_{23}
Ho (16d)	0.001560(18)	0.001560(18)	0.001560(18)	-0.000582(19)	-0.000582(19)	-0.000582(19)
Ti (16c)	0.000890(44)	0.000890(44)	0.000890(44)	-0.000039(46)	-0.000039(46)	-0.000039(46)
Hf (16c)	0.00082(32)	0.00082(32)	0.00082(32)	0.00009(12)	0.00009(12)	0.00009(12)
O (48f)	0.001170(27)	0.001170(27)	0.001170(27)	0	0	0
O' (8b)	0.002168(35)	0.001522(21)	0.001522(21)	0	0	0.000350(31)
O" (8a)	0.00133(49)	0.00133(49)	0.00133(49)	0	0	0

Table 11: Structural parameters obtained from Rietveld refinement of our starting polycrystalline sample of Ho$_2$(Ti$_{0.9}$Hf$_{0.1}$)$_2$O$_7$ at 300 K (space group $Fd\bar{3}m$, origin choice 2): R$_{Bragg}$ = 2.27; R$_F$ = 1.40. The lattice parameters, the x coordinate of the oxygen (48f), the occupation of the oxygen (8a) as well as all the anisotropic temperature factors were refined.

a = 10.149142(53)Å	$T = 300$ K	x	y	z	occ
Ho (16d)		0.5	0.5	0.5	1
Ti (16c)		0	0	0	0.85(1)
Hf (16c)		0	0	0	0.15(1)
O (48f)		0.375	0.375	0.375	0.998(1)
O' (8b)		0.32996(5)	0.125	0.125	1
O" (8a)		0.125	0.125	0.125	0.011(4)

ADPs in Å^2	U_{11}	U_{22}	U_{33}	U_{12}	U_{13}	U_{23}
Ho (16d)	0.001758(19)	0.001758(19)	0.001758(19)	-0.000642(20)	-0.000642(20)	-0.000642(20)
Ti (16c)	0.000982(46)	0.000982(46)	0.000982(46)	-0.000069(51)	-0.000069(51)	-0.000069(51)
Hf (16c)	0.00151(39)	0.00151(39)	0.00151(39)	0.00039(17)	0.00039(17)	0.00039(17)
O (48f)	0.001272(29)	0.001272(29)	0.001272(29)	0	0	0
O' (8b)	0.002594(37)	0.001767(22)	0.001767(22)	0	0	0.000352(34)
O" (8a)	0.00131(57)	0.00131(57)	0.00131(57)	0	0	0

Table 12: Structural parameters obtained from Rietveld refinement of our starting polycrystalline sample of $Ho_2(Ti_{0.85}Hf_{0.15})_2O_7$ at 300 K (space group $Fd\bar{3}m$, origin choice 2): $R_{Bragg} = 2.18$; $R_F = 1.46$. The lattice parameters, the x coordinate of the oxygen (48f), the occupation of the oxygen (8a) as well as all the anisotropic temperature factors were refined.

a = 10.169876(51)Å	$T = 300$ K	x	y	z	occ
Ho (16d)		0.5	0.5	0.5	1
Ti (16c)		0	0	0	0.79(1)
Hf (16c)		0	0	0	0.21(1)
O (48f)		0.375	0.375	0.375	0.998(1)
O' (8b)		0.33092(5)	0.125	0.125	1
O" (8a)		0.125	0.125	0.125	0.012(4)

ADPs in Å^2	U_{11}	U_{22}	U_{33}	U_{12}	U_{13}	U_{23}
Ho (16d)	0.001826(19)	0.001826(19)	0.001826(19)	-0.000749(20)	-0.000749(20)	-0.000749(20)
Ti (16c)	0.000910(47)	0.000910(47)	0.000910(47)	-0.000330(53)	-0.000330(53)	-0.000330(53)
Hf (16c)	0.00143(36)	0.00143(36)	0.00143(36)	0.00017(21)	0.00017(21)	0.00017(21)
O (48f)	0.001378(29)	0.001378(29)	0.001378(29)	0	0	0
O' (8b)	0.003003(37)	0.001952(22)	0.001952(22)	0	0	0.000397(34)
O" (8a)	0.00131(55)	0.00131(55)	0.00131(55)	0	0	0

Table 13: Structural parameters obtained from Rietveld refinement of our starting polycrystalline sample of $Ho_2(Ti_{0.8}Hf_{0.2})_2O_7$ at 300 K (space group $Fd\bar{3}m$, origin choice 2): $R_{Bragg} = 2.27$; $R_F = 1.46$. The lattice parameters, the x coordinate of the oxygen (48f), the occupation of the oxygen (8a) as well as all the anisotropic temperature factors were refined.

a = 10.186256(64)Å	$T = 300$ K	x	y	z	occ
Ho (16d)		0.5	0.5	0.5	1
Ti (16c)		0	0	0	0.74(1)
Hf (16c)		0	0	0	0.26(1)
O (48f)		0.375	0.375	0.375	0.996(1)
O' (8b)		0.33160(6)	0.125	0.125	1
O" (8a)		0.125	0.125	0.125	0.024(4)

ADPs in Å^2	U_{11}	U_{22}	U_{33}	U_{12}	U_{13}	U_{23}
Ho (16d)	0.002004(21)	0.002004(21)	0.002004(21)	-0.000785(23)	-0.000785(23)	-0.000785(23)
Ti (16c)	0.000959(52)	0.000959(52)	0.000959(52)	-0.000139(64)	-0.000139(64)	-0.000139(64)
Hf (16c)	0.00206(45)	0.00206(45)	0.00206(45)	0.00082(24)	0.00082(24)	0.00082(24)
O (48f)	0.001484(34)	0.001484(34)	0.001484(34)	0	0	0
O' (8b)	0.003484(43)	0.002185(26)	0.002185(26)	0	0	0.000397(34)
O" (8a)	0.00131(57)	0.00131(57)	0.00131(57)	0	0	0

Table 14: Structural parameters obtained from Rietveld refinement of our starting polycrystalline sample of $Ho_2(Ti_{0.75}Hf_{0.25})_2O_7$ at 300 K (space group $Fd\bar{3}m$, origin choice 2): $R_{Bragg} = 2.52$; $R_F = 1.67$. The lattice parameters, the x coordinate of the oxygen (48f), the occupation of the oxygen (8a) as well as all the anisotropic temperature factors were refined.

a = 10.203392(69)Å	T = 300 K	x	y	z	occ
Ho (16d)		0.5	0.5	0.5	1
Ti (16c)		0	0	0	0.69(1)
Hf (16c)		0	0	0	0.31(1)
O (48f)		0.375	0.375	0.375	0.994(1)
O' (8b)		0.33240(6)	0.125	0.125	1
O" (8a)		0.125	0.125	0.125	0.034(4)
ADPs in Å^2	U_{11}	U_{22}	U_{33}	U_{12}	U_{13}	U_{23}
Ho (16d)	0.002102(23)	0.002102(23)	0.002102(23)	-0.000846(25)	-0.000846(25)	-0.000846(25)
Ti (16c)	0.000768(56)	0.000768(56)	0.000768(56)	-0.000161(71)	-0.000161(71)	-0.000161(71)
Hf (16c)	0.00207(60)	0.00207(60)	0.00207(60)	0.00079(43)	0.00079(43)	0.00079(43)
O (48f)	0.001643(37)	0.001643(37)	0.001643(37)	0	0	0
O' (8b)	0.004055(49)	0.002353(28)	0.002353(28)	0	0	0.000451(42)
O" (8a)	0.00131(57)	0.00131(57)	0.00131(57)	0	0	0

Table 15: Structural parameters obtained from Rietveld refinement of our starting polycrystalline sample of Ho$_2$(Ti$_{0.7}$Hf$_{0.3}$)$_2$O$_7$ at 300 K (space group $Fd\bar{3}m$, origin choice 2): R$_{Bragg}$ = 2.92; R$_F$ = 1.91. The lattice parameters, the x coordinate of the oxygen (48f), the occupation of the oxygen (8a) as well as all the anisotropic temperature factors were refined.

a = 10.218227(97)Å	T = 300 K	x	y	z	occ
Ho (16d)		0.5	0.5	0.5	1
Ti (16c)		0	0	0	0.64(1)
Hf (16c)		0	0	0	0.36(1)
O (48f)		0.375	0.375	0.375	0.994(1)
O' (8b)		0.33324(7)	0.125	0.125	1
O" (8a)		0.125	0.125	0.125	0.038(5)
ADPs in Å^2	U_{11}	U_{22}	U_{33}	U_{12}	U_{13}	U_{23}
Ho (16d)	0.002312(28)	0.002312(28)	0.002312(28)	-0.000924(30)	-0.000924(30)	-0.000924(30)
Ti (16c)	0.000337(65)	0.000337(65)	0.000337(65)	-0.000223(83)	-0.000223(83)	-0.000223(83)
Hf (16c)	0.00205(60)	0.00205(60)	0.00205(60)	0.00077(43)	0.00077(43)	0.00077(43)
O (48f)	0.001732(47)	0.001732(47)	0.001732(47)	0	0	0
O' (8b)	0.004589(61)	0.002572(35)	0.002572(35)	0	0	0.000449(51)
O" (8a)	0.00131(57)	0.00131(57)	0.00131(57)	0	0	0

Table 16: Structural parameters obtained from Rietveld refinement of our starting polycrystalline sample of Ho$_2$(Ti$_{0.65}$Hf$_{0.35}$)$_2$O$_7$ at 300 K (space group $Fd\bar{3}m$, origin choice 2): R$_{Bragg}$ = 3.20; R$_F$ = 2.14. The lattice parameters, the x coordinate of the oxygen (48f), the occupation of the oxygen (8a) as well as all the anisotropic temperature factors were refined.

a = 10.234823(139)Å	T = 300 K	x	y	z	occ
Ho (16d)		0.5	0.5	0.5	1
Ti (16c)		0	0	0	0.58(1)
Hf (16c)		0	0	0	0.42(1)
O (48f)		0.375	0.375	0.375	0.991(1)
O' (8b)		0.33416(9)	0.125	0.125	1
O" (8a)		0.125	0.125	0.125	0.054(6)
ADPs in Å^2	U_{11}	U_{22}	U_{33}	U_{12}	U_{13}	U_{23}
Ho (16d)	0.002418(35)	0.002418(35)	0.002418(35)	-0.000991(37)	-0.000991(37)	-0.000991(37)
Ti (16c)	0.000017(13)	0.000017(13)	0.000017(13)	-0.000063(105)	-0.000063(105)	-0.000063(105)
Hf (16c)	0.00215(66)	0.00215(66)	0.00215(66)	0.00091(33)	0.00091(33)	0.00091(33)
O (48f)	0.002048(61)	0.002048(61)	0.002048(61)	0	0	0
O' (8b)	0.005054(78)	0.002865(45)	0.002865(45)	0	0	0.000650(65)
O" (8a)	0.00131(57)	0.00131(57)	0.00131(57)	0	0	0

Table 17: Structural parameters obtained from Rietveld refinement of our starting polycrystalline sample of Ho$_2$(Ti$_{0.6}$Hf$_{0.4}$)$_2$O$_7$ at 300 K (space group $Fd\bar{3}m$, origin choice 2): R$_{Bragg}$ = 3.59; R$_F$ = 2.59 The lattice parameters, the x coordinate of the oxygen (48f), the occupation of the oxygen (8a) as well as all the anisotropic temperature factors were refined.

List of Figures

List of Tables

Bibliography

[1] L.J. Henderson. *The Fitness of the Environment: An Inquiry Into the Biological Significance of the Properties of Matter.* Lowell Institute lectures. Macmillan, 1913.

[2] R. H. Dicke. Dirac's Cosmology and Mach's Principle. *Nature*, 192(4801):440–441, November 1961.

[3] Paul Dirac. A new basis for cosmology. *Proceedings of the Royal Society of London. Series A. Mathematical and Physical Sciences*, 165(921):199–208, 1938.

[4] Paul Dirac. The evolution of the physicist's picture of nature. `http://web.archive.org/web/20080207010024/http://www.808multimedia.com/winnt/kernel.htm`.

[5] R.B. Laughlin. *A Different Universe: Reinventing Physics from the Bottom Down.* Basic Books, 2005.

[6] Alan Guth. Inflation and the new era of high-precision cosmology. `https://physics.mit.edu/wp-content/uploads/2021/01/physicsatmit_02_cosmology.pdf`.

[7] Arnold Sommerfeld. Zur quantentheorie der spektrallinien. `https://uni-tuebingen.de/fileadmin/Uni_Tuebingen/Fakultaeten/MathePhysik/Institute/IAP/Forschung/MOettel/Geburt_QM/sommerfeld_AnnPhys_356_125_1916.pdf`.

[8] R.P. Feynman and A. Zee. *QED: The Strange Theory of Light and Matter.* Princeton Science Library. Princeton University Press, 2014.

[9] The standard model. `https://home.web.cern.ch/science/physics/standard-model`.

[10] Owen Benton, Olga Sikora, and Nic Shannon. Seeing the light: Experimental signatures of emergent electromagnetism in a quantum spin ice. *Phys. Rev. B*, 86(7):075154, 2012.

[11] Attila Szabó and Claudio Castelnovo. Seeing beyond the light: Vison and photon electrodynamics in quantum spin ice. *Phys. Rev. B*, 100:014417, Jul 2019.

[12] M Hermele, M P A Fisher, and L Balents. Pyrochlore photons: The U(1) spin liquid in a S=1/2 three-dimensional frustrated magnet. *Phys. Rev. B*, 69(6):064404, 2004.

[13] Gang Chen. Dirac's "magnetic monopoles" in pyrochlore ice $U(1)$ spin liquids: Spectrum and classification. *Phys. Rev. B*, 96:195127, Nov 2017.

[14] M J P Gingras and P A McClarty. Quantum spin ice: a search for gapless quantum spin liquids in pyrochlore magnets. *Rep. Prog. Phys.*, 77(5):056501, May 2014.

[15] Masafumi Udagawa and Roderich Moessner. Spectrum of itinerant fractional excitations in quantum spin ice. *Phys. Rev. Lett.*, 122:117201, Mar 2019.

[16] Siddhardh C. Morampudi, Frank Wilczek, and Chris R. Laumann. Spectroscopy of spinons in coulomb quantum spin liquids. *Phys. Rev. Lett.*, 124:097204, Mar 2020.

[17] Salvatore D. Pace, Siddhardh C. Morampudi, Roderich Moessner, and Chris R. Laumann. Emergent fine structure constant of quantum spin ice is large. *Phys. Rev. Lett.*, 127:117205, Sep 2021.

[18] Jason S. Gardner, Michel J. P. Gingras, and John E. Greedan. Magnetic pyrochlore oxides. *Rev. Mod. Phys.*, 82:53–107, Jan 2010.

[19] Shigeki Onoda and Yoichi Tanaka. Quantum melting of spin ice: emergent cooperative quadrupole and chirality. *Phys. Rev. Lett.*, 105:047201, Jul 2010.

[20] Hamid R. Molavian, Michel J. P. Gingras, and Benjamin Canals. Dynamically induced frustration as a route to a quantum spin ice state in $Tb_2Ti_2O_7$ via virtual crystal field excitations and quantum many-body effects. *Phys. Rev. Lett.*, 98:157204, Apr 2007.

[21] Lucile Savary and Leon Balents. Disorder-induced quantum spin liquid in spin ice pyrochlores. *Phys. Rev. Lett.*, 118:087203, Feb 2017.

[22] Owen Benton. Instabilities of a U(1) quantum spin liquid in disordered non-kramers pyrochlores. *Phys. Rev. Lett.*, 121:037203, Jul 2018.

[23] A.Yu. Kitaev. Fault-tolerant quantum computation by anyons. *Annals of Physics*, 303(1):2–30, 2003.

[24] Maissam Barkeshli, Erez Berg, and Steven Kivelson. Coherent transmutation of electrons into fractionalized anyons. *Science*, 346(6210):722–725, 2014.

[25] Romain Sibille, Elsa Lhotel, Monica Hatnean Ciomaga Hatnean, Gøran J. Nilsen, Georg Ehlers, Antonio Cervellino, Eric Ressouche, Matthias Frontzek, Oksana Zaharko, Vladimir Pomjakushin, Uwe Stuhr, Helen C. Walker, Devashibhai T. Adroja, Hubertus Luetkens, Chris Baines, Alex Amato, Geetha Balakrishnan, Tom Fennell, and Michel Kenzelmann. Coulomb spin liquid in anion-disordered pyrochlore $Tb_2Hf_2O_7$. *Nature Communications*, 8:892, December 2017.

[26] K Kimura, S Nakatsuji, J-J Wen, C Broholm, M B Stone, E Nishibori, and H Sawa. Quantum fluctuations in spin-ice-like $Pr_2Zr_2O_7$. *Nat. Commun.*, 4:1934, 2013.

[27] S. Petit, E. Lhotel, S. Guitteny, O. Florea, J. Robert, P. Bonville, I. Mirebeau, J. Ollivier, H. Mutka, E. Ressouche, C. Decorse, M. Ciomaga Hatnean, and G. Balakrishnan. Antiferroquadrupolar correlations in the quantum spin ice candidate $Pr_2Zr_2O_7$. *Phys. Rev. B*, 94:165153, Oct 2016.

[28] Romain Sibille, Nicolas Gauthier, Han Yan, Monica Ciomaga Hatnean, Jacques Ollivier, Barry Winn, Uwe Filges, Geetha Balakrishnan, Michel Kenzelmann, Nic Shannon, and Tom Fennell. Experimental signatures of emergent quantum electrodynamics in $Pr_2Hf_2O_7$. *Nature Physics*, 14(7):711–715, 2018.

[29] J. M. D. Coey. *Magnetism and Magnetic Materials*. Cambridge University Press, 2010.

[30] S. Blundell. *Magnetism in Condensed Matter*. Oxford Master Series in Condensed Matter Physics. OUP Oxford, 2001.

[31] A. Mirmelstein. *Crystal-Field Phenomena in Rare-Earth Compounds*, pages 206–218. worldscientific, 2000.

[32] F Albert Cotton. I-ligand field theory. *Journal of Chemical Education*, 41(9):466, 1964.

[33] H Schilder and H Lueken. Computerized magnetic studies on *d*, *f*, *d-d*, *f-f*, and *d-s*, *f-s* systems under varying ligand and magnetic fields. *J. Magn. Magn. Mater.*, 281(1):17–26, 2004.

[34] M.S. Dresselhaus, G. Dresselhaus, and A. Jorio. *Group Theory: Application to the Physics of Condensed Matter*. Springer Berlin Heidelberg, 2007.

[35] H. A. Kramers. Théorie générale de la rotation paramagnétique dans les cristaux. *Proceedings of the Royal Netherlands Academy of Arts and Sciences*, 33(6-10):959–972, 1930.

[36] J CAJKO. WYBOURNE,BG - SPECTROSCOPIC PROPERTIES OF RARE EARTHS. *CESKOSLOVENSKY CASOPIS PRO FYSIKU SEKCE A*, 16(6):566–&, 1966.

[37] K. W. Stevens. *Magnetic Ions in Crystals*. Princeton University Press, 2014.

[38] A. T. Boothroyd, S. M. Doyle, D. MK. Paul, and R. Osborn. Crystal-field excitations in Nd_2CuO_4, Pr_2CuO_4, and related n -type superconductors. *Phys. Rev. B*, 45:10075–10086, May 1992.

[39] Paolo Santini, Stefano Carretta, Giuseppe Amoretti, Roberto Caciuffo, Nicola Magnani, and Gerard H. Lander. Multipolar interactions in f-electron systems: The paradigm of actinide dioxides. *Rev. Mod. Phys.*, 81:807–863, Jun 2009.

[40] A. R. Edmonds. *Angular Momentum in Quantum Mechanics*. Investigations in Physics. Princeton University Press,, Princeton, NJ, 2nd ed. edition, 2016.

[41] Ryousuke Shiina, Osamu Sakai, Hiroyuki Shiba, and Peter Thalmeier. Interplay of field-induced multipoles in CeB_6. *Journal of the Physical Society of Japan*, 67(3):941–949, 1998.

[42] Roberto Caciuffo and Gerard H. Lander. X-ray synchrotron radiation studies of actinide materials. *Journal of Synchrotron Radiation*, 28(6):1692–1708, Nov 2021.

[43] Andrea Amorese, Martin Sundermann, Brett Leedahl, Andrea Marino, Daisuke Takegami, Hlynur Gretarsson, Andrei Gloskovskii, Christoph Schlueter, Maurits W. Haverkort, Yingkai Huang, Maria Szlawska, Dariusz Kaczorowski, Sheng Ran, M. Brian Maple, Eric D. Bauer, Andreas Leithe-Jasper, Philipp Hansmann, Peter Thalmeier, Liu Hao Tjeng, and Andrea Severing. From antiferromagnetic and hidden order to pauli paramagnetism in UM_2Si_2 compounds with $5f$ electron duality. *Proceedings of the National Academy of Sciences*, 117(48):30220–30227, 2020.

[44] P. Santini, S. Carretta, N. Magnani, G. Amoretti, and R. Caciuffo. Hidden order and low-energy excitations in NpO_2. *Phys. Rev. Lett.*, 97:207203, Nov 2006.

[45] Peter Thalmeier and Alireza Akbari. *Resonant Spin Excitations in Unconventional Heavy Fermion Superconductors and Kondo Lattice Compounds*, pages 44–77. worldscientific, 2015.

[46] A J Princep, A M Mulders, U Staub, V Scagnoli, T Nakamura, A Kikkawa, S W Lovesey, and E Balcar. Triakontadipole and high-order dysprosium multipoles in the antiferromagnetic phase of DyB_2C_2. *Journal of Physics: Condensed Matter*, 23(26):266002, jun 2011.

[47] M.-T. Suzuki, T. Koretsune, M. Ochi, and R. Arita. Cluster multipole theory for anomalous hall effect in antiferromagnets. *Phys. Rev. B*, 95:094406, Mar 2017.

[48] T. Fennell, M. Kenzelmann, B. Roessli, H. Mutka, J. Ollivier, M. Ruminy, U. Stuhr, O. Zaharko, L. Bovo, A. Cervellino, M. K. Haas, and R. J. Cava. Magnetoelastic excitations in the pyrochlore spin liquid $Tb_2Ti_2O_7$. *Phys. Rev. Lett.*, 112:017203, Jan 2014.

[49] A. A. Turrini, M Ruminy, F. Bourdarot, U. Stuhr, J. S. White, G. Tucker, M. Skoulatos, M. Núñez Valdez, and T. Fennell. Magnetic-field control of magnetoelastic coupling in the rare-earth pyrochlore $Tb_2Ti_2O_7$. *Phys. Rev. B*, 104:224403, Dec 2021.

[50] Yi-Ping Huang, Gang Chen, and Michael Hermele. Quantum spin ices and topological phases from dipolar-octupolar doublets on the pyrochlore lattice. *Phys. Rev. Lett.*, 112:167203, Apr 2014.

[51] Yao-Dong Li and Gang Chen. Symmetry enriched U(1) topological orders for dipole-octupole doublets on a pyrochlore lattice. *Phys. Rev. B*, 95:041106, Jan 2017.

[52] H.A Kramers. L'interaction entre les atomes magnétogènes dans un cristal paramagnétique. *Physica*, 1(1):182–192, 1934.

[53] P. W. Anderson. Antiferromagnetism. theory of superexchange interaction. *Phys. Rev.*, 79:350–356, Jul 1950.

[54] Junjiro Kanamori. Superexchange interaction and symmetry properties of electron orbitals. *Journal of Physics and Chemistry of Solids*, 10(2):87–98, 1959.

[55] I. Dzyaloshinsky. A thermodynamic theory of "weak" ferromagnetism of antiferromagnetics. *Journal of Physics and Chemistry of Solids*, 4(4):241–255, 1958.

[56] J M Baker. Interactions between ions with orbital angular momentum in insulators. *Reports on Progress in Physics*, 34(1):109–173, jan 1971.

[57] S T Bramwell and M J Harris. Frustration in Ising-type spin models on the pyrochlore lattice. *J. Phys. Condens. Matter*, 10(14):L215, 1998.

[58] Jacques Villain. Insulating spin glasses. *Zeitschrift für Physik B Condensed Matter*, 33(1):31–42, 1979.

[59] G. H. Wannier. Antiferromagnetism. the triangular ising net. *Phys. Rev.*, 79:357–364, Jul 1950.

[60] Leon Balents. Spin liquids in frustrated magnets. *Nature*, 464(7286):199, March 2010.

[61] P. W. Anderson. The resonating valence bond state in La_2CuO_4 and superconductivity. *Science*, 235(4793):1196–1198, 1987.

[62] P.W. Anderson. Resonating valence bonds: A new kind of insulator? *Materials Research Bulletin*, 8(2):153–160, 1973.

[63] D. A. Tennant, T. G. Perring, R. A. Cowley, and S. E. Nagler. Unbound spinons in the s=1/2 antiferromagnetic chain $KCuF_3$. *Phys. Rev. Lett.*, 70:4003–4006, Jun 1993.

[64] Bella Lake, D. Alan Tennant, Chris D. Frost, and Stephen E. Nagler. Quantum criticality and universal scaling of a quantum antiferromagnet. *Nature Materials*, 4(4):329–334, 2005.

[65] Martin Mourigal, Mechthild Enderle, Axel Klöpperpieper, Jean-Sébastien Caux, Anne Stunault, and Henrik M. Rønnow. Fractional spinon excitations in the quantum heisenberg antiferromagnetic chain. *Nature Physics*, 9(7):435–441, 2013.

[66] F. D. M. Haldane. Spontaneous dimerization in the $s = \frac{1}{2}$ heisenberg antiferromagnetic chain with competing interactions. *Phys. Rev. B*, 25:4925–4928, Apr 1982.

[67] W. J. L Buyers, R. M. Morra, R. L. Armstrong, M. J. Hogan, P. Gerlach, and K. Hirakawa. Experimental evidence for the haldane gap in a spin-1 nearly isotropic, antiferromagnetic chain. *Phys. Rev. Lett.*, 56:371–374, Jan 1986.

[68] M. Kenzelmann, R. A. Cowley, W. J. L. Buyers, Z. Tun, R. Coldea, and M. Enderle. Properties of haldane excitations and multiparticle states in the antiferromagnetic spin-1 chain compound $CsNiCl_3$. *Phys. Rev. B*, 66:024407, Jun 2002.

[69] Yao Shen, Yao-Dong Li, Hongliang Wo, Yuesheng Li, Shoudong Shen, Bingying Pan, Qisi Wang, H. C. Walker, P. Steffens, M. Boehm, Yiqing Hao, D. L. Quintero-Castro, L. W. Harriger, M. D. Frontzek, Lijie Hao, Siqin Meng, Qingming Zhang, Gang Chen, and Jun Zhao. Evidence for a spinon fermi surface in a triangular-lattice quantum-spin-liquid candidate. *Nature*, 540(7634):559–562, 2016.

[70] M. R. Norman. Colloquium: Herbertsmithite and the search for the quantum spin liquid. *Rev. Mod. Phys.*, 88:041002, Dec 2016.

[71] Alexei Kitaev. Anyons in an exactly solved model and beyond. *Annals of Physics*, 321(1):2–111, 2006. January Special Issue.

[72] Atsuo Shitade, Hosho Katsura, Jan Kuneš, Xiao-Liang Qi, Shou-Cheng Zhang, and Naoto Nagaosa. Quantum spin hall effect in a transition metal oxide Na_2IrO_3. *Phys. Rev. Lett.*, 102:256403, Jun 2009.

[73] K. Kitagawa, T. Takayama, Y. Matsumoto, A. Kato, R. Takano, Y. Kishimoto, S. Bette, R. Dinnebier, G. Jackeli, and H. Takagi. A spin–orbital-entangled quantum liquid on a honeycomb lattice. *Nature*, 554(7692):341–345, 2018.

[74] J. A. Sears, Y. Zhao, Z. Xu, J. W. Lynn, and Young-June Kim. Phase diagram of α-$RuCl_3$ in an in-plane magnetic field. *Phys. Rev. B*, 95:180411, May 2017.

[75] Simon Trebst and Ciarán Hickey. Kitaev materials. *Physics Reports*, 950:1–37, 2022. Kitaev materials.

[76] Tian-Heng Han, Joel S. Helton, Shaoyan Chu, Daniel G. Nocera, Jose A. Rodriguez-Rivera, Collin Broholm, and Young S. Lee. Fractionalized excitations in the spin-liquid state of a kagome-lattice antiferromagnet. *Nature*, 492(7429):406–410, 2012.

[77] Yukitoshi Motome, Ryoya Sano, Seonghoon Jang, Yusuke Sugita, and Yasuyuki Kato. Materials design of kitaev spin liquids beyond the Jackeli–Khaliullin mechanism. *Journal of Physics: Condensed Matter*, 32(40):404001, jun 2020.

[78] J. D. Bernal and R. H. Fowler. A theory of water and ionic solution, with particular reference to hydrogen and hydroxyl ions. *The Journal of Chemical Physics*, 1(8):515–548, 1933.

[79] Linus Pauling. The structure and entropy of ice and of other crystals with some randomness of atomic arrangement. *Journal of the American Chemical Society*, 57(12):2680–2684, 1935.

[80] A. P. Ramirez, A. Hayashi, R. J. Cava, R. Siddharthan, and B. S. Shastry. Zero-point entropy in 'spin ice'. *Nature*, 399(6734):333–335, May 1999.

[81] T. Fennell, P. P. Deen, A. R. Wildes, K. Schmalzl, D. Prabhakaran, A. T. Boothroyd, R. J. Aldus, D. F. McMorrow, and S. T. Bramwell. Magnetic Coulomb phase in the spin ice $Ho_2Ti_2O_7$. *Science*, 326(5951):415–417, 2009.

[82] C Castelnovo, R Moessner, and S L Sondhi. Magnetic monopoles in spin ice. *Nature*, 451(7174):42–45, 2008.

[83] C L Henley. The "Coulomb phase" in frustrated systems. *Annual Review of Condensed Matter Physics*, 1(1):179–210, 2010.

[84] C Castelnovo, R Moessner, and S L Sondhi. Spin ice, fractionalization, and topological order. *Annual Review of Condensed Matter Physics*, 3:35–55, 2012.

[85] G Ehlers, A L Cornelius, M Orendác, M Kajnaková, T Fennell, S T Bramwell, and J S Gardner. Dynamical crossover in 'hot' spin ice. *J. Phys. Condens. Matter*, 15(2):L9, 2003.

[86] J. Snyder, B. G. Ueland, J. S. Slusky, H. Karunadasa, R. J. Cava, and P. Schiffer. Low-temperature spin freezing in the $Dy_2Ti_2O_7$ spin ice. *Phys. Rev. B*, 69:064414, Feb 2004.

[87] L D C Jaubert and P C W Holdsworth. Magnetic monopole dynamics in spin ice. *Journal of Physics: Condensed Matter*, 23(16):164222, 2011.

[88] Bruno Tomasello, Claudio Castelnovo, Roderich Moessner, and Jorge Quintanilla. Correlated quantum tunneling of monopoles in spin ice. *Phys. Rev. Lett.*, 123:067204, Aug 2019.

[89] C. Paulsen, M. J. Jackson, E. Lhotel, B. Canals, D. Prabhakaran, K. Matsuhira, S. R. Giblin, and S. T. Bramwell. Far-from-equilibrium monopole dynamics in spin ice. *Nature Physics*, 10(2):135–139, 2014.

[90] Lucile Savary and Leon Balents. Coulombic Quantum Liquids in Spin-1/2 Pyrochlores. *Phys. Rev. Lett.*, 108:037202, 2012.

[91] Lucile Savary and Leon Balents. *Quantum Coherence: Quantum Spin Ice and Lattice Gauge Theory*, pages 239–271. Springer International Publishing, Cham, 2021.

[92] Lucile Savary, Kate A. Ross, Bruce D. Gaulin, Jacob P. C. Ruff, and Leon Balents. Order by quantum disorder in $Er_2Ti_2O_7$. *Phys. Rev. Lett.*, 109:167201, Oct 2012.

[93] Kate A. Ross, Lucile Savary, Bruce D. Gaulin, and Leon Balents. Quantum excitations in quantum spin ice. *Phys. Rev. X*, 1:021002, Oct 2011.

[94] Romain Sibille, Elsa Lhotel, Monica Ciomaga Hatnean, Geetha Balakrishnan, Björn Fåk, Nicolas Gauthier, Tom Fennell, and Michel Kenzelmann. Candidate quantum spin ice in the pyrochlore $Pr_2Hf_2O_7$. *Phys. Rev. B*, 94:024436, Jul 2016.

[95] M. Léger, E. Lhotel, M. Ciomaga Hatnean, J. Ollivier, A. R. Wildes, S. Raymond, E. Ressouche, G. Balakrishnan, and S. Petit. Spin dynamics and unconventional coulomb phase in $Nd_2Zr_2O_7$. *Phys. Rev. Lett.*, 126:247201, Jun 2021.

[96] P. Bonville, S. Guitteny, A. Gukasov, I. Mirebeau, S. Petit, C. Decorse, M. Ciomaga Hatnean, and G. Balakrishnan. Magnetic properties and crystal field in $Pr_2Zr_2O_7$. *Phys. Rev. B*, 94:134428, Oct 2016.

[97] N. Martin, P. Bonville, E. Lhotel, S. Guitteny, A. Wildes, C. Decorse, M. Ciomaga Hatnean, G. Balakrishnan, I. Mirebeau, and S. Petit. Disorder and quantum spin ice. *Phys. Rev. X*, 7:041028, Oct 2017.

[98] F Wöhler. Ueber den pyrochlor, eine neue mineralspecies. *Annalen der Physik*, 83(8):417–428, 1826.

[99] M.A. Subramanian, G. Aravamudan, and G.V. Subba Rao. Oxide pyrochlores — a review. *Progress in Solid State Chemistry*, 15(2):55–143, 1983.

[100] Jeffrey G. Rau and Michel J.P. Gingras. Frustrated quantum rare-earth pyrochlores. *Annual Review of Condensed Matter Physics*, 10(1):357–386, 2019.

[101] Mikhail V. Talanov and Valeriy M. Talanov. Structural diversity of ordered pyrochlores. *Chemistry of Materials*, 33(8):2706–2725, 04 2021.

[102] G.C. Lau, B.D. Muegge, T.M. McQueen, E.L. Duncan, and R.J. Cava. Stuffed rare earth pyrochlore solid solutions. *Journal of Solid State Chemistry*, 179(10):3126–3135, 2006.

[103] Juanli Zhao, Yuchen Liu, Yun Fan, Wei Zhang, Chengguan Zhang, Guang Yang, Hongfei Chen, and Bin Liu. Native point defects and oxygen migration of rare earth zirconate and stannate pyrochlores. *Journal of Materials Science & Technology*, 73:23–30, 2021.

[104] T. Fennell, M. J. Harris, S. Calder, M. Ruminy, M. Boehm, P. Steffens, M. H. Lemée-Cailleau, O. Zaharko, A. Cervellino, and S. T. Bramwell. Multiple coulomb phase in the fluoride pyrochlore $CsNiCrF_6$. *Nature Physics*, 15(1):60–66, 2019.

[105] Matthäus Rothensteiner, Alexander Bonk, Ulrich F. Vogt, Hermann Emerich, and Jeroen A. van Bokhoven. Structural changes in equimolar ceria–hafnia materials under solar thermochemical looping conditions: cation ordering, formation and stability of the pyrochlore structure. *RSC Adv.*, 7:53797–53809, 2017.

[106] Youssef Ben Smida, Riadh Marzouki, Sava Kaya, Sultan Erkan, Mohamed Faouzi Zid, and Ahmed Hichem Hamzaoui. Synthesis methods in solid-state chemistry. In Riadh Marzouki, editor, *Synthesis Methods and Crystallization*, chapter 2. IntechOpen, Rijeka, 2020.

[107] Hanna A. Dabkowska and Antoni B. Dabkowski. *Crystal Growth of Oxides by Optical Floating Zone Technique*, pages 367–391. Springer Berlin Heidelberg, Berlin, Heidelberg, 2010.

[108] A.N. Medina, A.M.F. Caldeira, A.C. Bento, M.L. Baesso, J.A. Sampaio, T. Catunda, and F.G. Gandra. Thermal relaxation method to determine the specific heat of optical glasses. *Journal of Non-Crystalline Solids*, 304(1):299–305, 2002.

[109] James Chadwick. The existence of a neutron. *Proceedings of the Royal Society of London A: Mathematical, Physical and Engineering Sciences*, 136(830):692–708, 1932.

[110] Louis De Broglie. Waves and quanta. *Nature*, 112(2815):540–540, 1923.

[111] G. L. Squires. *Introduction to the Theory of Thermal Neutron Scattering*. Cambridge University Press, 3 edition, 2012.

[112] S. W. Lovesey. *Theory of neutron scattering from condensed matter*. Clarendon Press, United Kingdom, 1984.

[113] H.M. Rietveld. A profile refinement method for nuclear and magnetic structures. *Journal of Applied Crystallography*, 2, 1969.

[114] David A. Keen. Total scattering and the pair distribution function in crystallography. *Crystallography Reviews*, 26(3):143–201, 2020.

[115] F. Zernike and J. A. Prins. Die beugung von röntgenstrahlen in flüssigkeiten als effekt der molekülanordnung. *Zeitschrift für Physik A Hadrons and nuclei*, 41(2):184–194, 1927.

[116] Peter F. Peterson, Emil S. Božin, Thomas Proffen, and Simon J. L. Billinge. Improved measures of quality for the atomic pair distribution function. *Journal of Applied Crystallography*, 36(1):53–64, Feb 2003.

[117] C L Farrow, P Juhas, J W Liu, D Bryndin, E S Božin, J Bloch, Th Proffen, and S J L Billinge. PDFfit2 and PDFgui: computer programs for studying nanostructure in crystals. *Journal of Physics: Condensed Matter*, 19(33):335219, jul 2007.

[118] Helen Y. Playford, Lewis R. Owen, Igor Levin, and Matt G. Tucker. New insights into complex materials using reverse monte carlo modeling. *Annual Review of Materials Research*, 44(1):429–449, 2014.

[119] Gen Shirane, Stephen M. Shapiro, and John M. Tranquada. *Neutron Scattering with a Triple-Axis Spectrometer: Basic Techniques*. Cambridge University Press, 2002.

[120] Jakob Lass, Dieter Graf, Felix Groitl, Christian Kägi, Raphael Müller, Roman Bürge, Marcel Schild, Manuel S. Lehmann, Alex Bollhalder, Peter Keller, Marek Bartkowiak, Uwe Filges, Frank Herzog, Urs Greuter, Gerd Theidel, Luc Testa,

Virgile Favre, Henrik M. Rønnow, and Christof Niedermayer. Design and performance of the multiplexing spectrometer camea, 2020.

[121] E. Mamontov and K. W. Herwig. A time-of-flight backscattering spectrometer at the spallation neutron source, basis. *Review of Scientific Instruments*, 82(8):085109, 2011.

[122] https://www.ill.eu/fr/users/instruments/instruments-list/in8/description/instrument-layout.

[123] https://www.ill.eu/users/instruments/instruments-list/in5/description/instrument-layout.

[124] Jason S. Gardner, Georg Ehlers, Antonio Faraone, and Victoria García Sakai. High-resolution neutron spectroscopy using backscattering and neutron spin-echo spectrometers in soft and hard condensed matter. *Nature Reviews Physics*, 2(2):103–116, 2020.

[125] Mezei Ferenc. Neutron spin-echo. Lecture Notes in Physics 128, Springer, Heidelberg, 1980.

[126] https://www.ill.eu/users/instruments/instruments-list/in16b/description/instrument-layout.

[127] Jason S. Gardner, Georg Ehlers, Antonio Faraone, and Victoria García Sakai. High-resolution neutron spectroscopy using backscattering and neutron spin-echo spectrometers in soft and hard condensed matter. *Nature Reviews Physics*, 2(2):103–116, 2020.

[128] Owen Benton. Ground-state phase diagram of dipolar-octupolar pyrochlores. *Phys. Rev. B*, 102:104408, Sep 2020.

[129] Romain Sibille, Elsa Lhotel, Vladimir Pomjakushin, Chris Baines, Tom Fennell, and Michel Kenzelmann. Candidate quantum spin liquid in the Ce^{3+} pyrochlore stannate $Ce_2Sn_2O_7$. *Phys. Rev. Lett.*, 115:097202, Aug 2015.

[130] Romain Sibille, Nicolas Gauthier, Elsa Lhotel, Victor Porée, Vladimir Pomjakushin, Russell A. Ewings, Toby G. Perring, Jacques Ollivier, Andrew Wildes, Clemens Ritter, Thomas C. Hansen, David A. Keen, Gøran J. Nilsen, Lukas Keller, Sylvain Petit, and Tom Fennell. A quantum liquid of magnetic octupoles on the pyrochlore lattice. *Nature Physics*, 16(5):546–552, 2020.

[131] Chinnathambi Karthik, Thomas J. Anderson, Delphine Gout, and Rick Ubic. Transmission electron microscopic study of pyrochlore to defect-fluorite transition in rare-earth pyrohafnates. *Journal of Solid State Chemistry*, 194:168–172, 2012.

[132] R. D. Shannon. Revised effective ionic radii and systematic studies of interatomic distances in halides and chalcogenides. *Acta Crystallographica Section A*, 32(5):751–767, Sep 1976.

[133] B Tolla, A Demourgues, M Pouchard, L Rabardel, L Fournes, and A Wattiaux. Oxygen exchange properties in the new pyrochlore solid solution $Ce_2Sn_2O_7$-$Ce_2Sn_2O_8$. *Comptes rendus de l'académie des sciences. Serie IIc, chimie*, 2(3):139–146, 1999.

[134] J. Gaudet, E. M. Smith, J. Dudemaine, J. Beare, C. R. C. Buhariwalla, N. P. Butch, M. B. Stone, A. I. Kolesnikov, Guangyong Xu, D. R. Yahne, K. A. Ross, C. A. Marjerrison, J. D. Garrett, G. M. Luke, A. D. Bianchi, and B. D. Gaulin. Quantum spin ice dynamics in the dipole-octupole pyrochlore magnet $Ce_2Zr_2O_7$. *Phys. Rev. Lett.*, 122:187201, May 2019.

[135] Yuanyuan Xu, Huiyuan Man, Nan Tang, Santu Baidya, Hongbin Zhang, Satoru Nakatsuji, David Vanderbilt, and Natalia Drichko. Importance of dynamic lattice effects for crystal field excitations in quantum spin ice candidate $Pr_2Zr_2O_7$, 2021.

[136] D. T. Adroja, A. del Moral, C. de la Fuente, A. Fraile, E. A. Goremychkin, J. W. Taylor, A. D. Hillier, and F. Fernandez-Alonso. Vibron quasibound state in the noncentrosymmetric tetragonal heavy-fermion compound $CeCuAl_3$. *Phys. Rev. Lett.*, 108:216402, May 2012.

[137] Petr Čermák, Astrid Schneidewind, Benqiong Liu, Michael Marek Koza, Christian Franz, Rudolf Schönmann, Oleg Sobolev, and Christian Pfleiderer. Magnetoelastic hybrid excitations in $CeAuAl_3$. *Proceedings of the National Academy of Sciences*, 116(14):6695–6700, 2019.

[138] V. K. Anand, A. Fraile, D. T. Adroja, Shivani Sharma, Rajesh Tripathi, C. Ritter, C. de la Fuente, P. K. Biswas, V. Garcia Sakai, A. del Moral, and et al. Crystal electric field and possible coupling with phonons in kondo lattice $CeCuGa_3$. *Physical Review B*, 104(17), Nov 2021.

[139] A. Scheie. *PyCrystalField*: software for calculation, analysis and fitting of crystal electric field Hamiltonians. *Journal of Applied Crystallography*, 54(1):356–362, Feb 2021.

[140] A. T. Boothroyd. SPECTRE. In *SPECTRE, a program for calculating spectroscopic properties of rare earth ions in crystals.* Boothroyd, A. T., 1990-2015.

[141] S T Bramwell, M N Field, M J Harris, and I P Parkin. Bulk magnetization of the heavy rare earth titanate pyrochlores-a series of model frustrated magnets. *J. Phys.: Cond. Matter*, 12:483, 2000.

[142] Matthew Powell, Liurukara D. Sanjeewa, Colin D. McMillen, Kate A. Ross, Colin L. Sarkis, and Joseph W. Kolis. Hydrothermal crystal growth of rare earth tin cubic pyrochlores, $RE_2Sn_2O_7$ (RE = La–Lu): Site ordered, low defect single crystals. *Crystal Growth & Design*, 19(9):4920–4926, 2019.

[143] Bin Gao, Tong Chen, David W. Tam, Chien-Lung Huang, Kalyan Sasmal, Devashibhai T. Adroja, Feng Ye, Huibo Cao, Gabriele Sala, Matthew B. Stone, Christopher Baines, Joel A. T. Verezhak, Haoyu Hu, Jae-Ho Chung, Xianghan Xu, Sang-Wook Cheong, Manivannan Nallaiyan, Stefano Spagna, M. Brian Maple, Andriy H. Nevidomskyy, Emilia Morosan, Gang Chen, and Pengcheng Dai. Experimental signatures of a three-dimensional quantum spin liquid in effective spin-1/2 $Ce_2Zr_2O_7$ pyrochlore. *Nature Physics*, 15(10):1052–1057, 2019.

[144] Anish Bhardwaj, Shu Zhang, Han Yan, Roderich Moessner, Andriy H. Nevidomskyy, and Hitesh J. Changlani. Sleuthing out exotic quantum spin liquidity in the pyrochlore magnet $Ce_2Zr_2O_7$. *npj Quantum Materials*, 7(1):51, 2022.

[145] E. M. Smith, O. Benton, D. R. Yahne, B. Placke, R. Schäfer, J. Gaudet, J. Dudemaine, A. Fitterman, J. Beare, A. R. Wildes, S. Bhattacharya, T. DeLazzer,

C. R. C. Buhariwalla, N. P. Butch, R. Movshovich, J. D. Garrett, C. A. Marjerrison, J. P. Clancy, E. Kermarrec, G. M. Luke, A. D. Bianchi, K. A. Ross, and B. D. Gaulin. Case for a $U(1)_\pi$ quantum spin liquid ground state in the dipole-octupole pyrochlore $Ce_2Zr_2O_7$. *Phys. Rev. X*, 12:021015, Apr 2022.

[146] P M Levy and G T Trammell. Magnetic octupole scattering of neutrons. *Journal of Physics C: Solid State Physics*, 10(8):1303–1310, apr 1977.

[147] M. J. Sablik. Magnetic octupole neutron scattering and quadrupolar excitations above and below the magnetic ordering temperature: Analysis using octupolar correlation functions. *Phys. Rev. B*, 32:5880–5891, Nov 1985.

[148] Ryousuke Shiina. Anisotropic form factors of neutron scattering by magnetic octupole in CeB_6. *Journal of Physics: Conference Series*, 391:012064, dec 2012.

[149] S W Lovesey. Theory of neutron scattering by electrons in magnetic materials. *Physica Scripta*, 90(10):108011, sep 2015.

[150] Keitaro Kuwahara, Kazuaki Iwasa, Masahumi Kohgi, Naofumi Aso, Masafumi Sera, and Fumitoshi Iga. Detection of neutron scattering from phase iv of $Ce_{0.7}La_{0.3}B_6$: A confirmation of the octupole order. *Journal of the Physical Society of Japan*, 76(9):093702, 2007.

[151] S. W. Lovesey and G. van der Laan. Magnetic multipoles and correlation shortage in the pyrochlore cerium stannate $Ce_2Sn_2O_7$. *Phys. Rev. B*, 101:144419, Apr 2020.

[152] Victor Porée, Elsa Lhotel, Sylvain Petit, Aleksandra Krajewska, Pascal Puphal, Adam H. Clark, Vladimir Pomjakushin, Helen C. Walker, Nicolas Gauthier, Dariusz J. Gawryluk, and Romain Sibille. Crystal-field states and defect levels in candidate quantum spin ice $Ce_2Hf_2O_7$. *Phys. Rev. Materials*, 6:044406, Apr 2022.

[153] Chun-Jiong Huang, Youjin Deng, Yuan Wan, and Zi Yang Meng. Dynamics of topological excitations in a model quantum spin ice. *Phys. Rev. Lett.*, 120:167202, Apr 2018.

[154] Félix Desrochers, Li Ern Chern, and Yong Baek Kim. Competing $U(1)$ and Z_2 dipolar-octupolar quantum spin liquids on the pyrochlore lattice: Application to $Ce_2Zr_2O_7$. *Phys. Rev. B*, 105:035149, Jan 2022.

[155] Félix Desrochers, Li Ern Chern, and Yong Baek Kim. Symmetry fractionalization in the gauge mean-field theory of quantum spin ice, 2022.

[156] J. S. Gardner, B. D. Gaulin, A. J. Berlinsky, P. Waldron, S. R. Dunsiger, N. P. Raju, and J. E. Greedan. Neutron scattering studies of the cooperative paramagnet pyrochlore $Tb_2Ti_2O_7$. *Phys. Rev. B*, 64:224416, Nov 2001.

[157] Markus Appel, Bernhard Frick, and Andreas Magerl. A flexible high speed pulse chopper system for an inverted neutron time-of-flight option on backscattering spectrometers. *Scientific Reports*, 8(1):13580, 2018.

[158] L. D. C. Jaubert and P. C. W. Holdsworth. Signature of magnetic monopole and dirac string dynamics in spin ice. *Nature Physics*, 5(4):258–261, 2009.

[159] Yasuyuki Kato and Shigeki Onoda. Numerical evidence of quantum melting of spin ice: Quantum-to-classical crossover. *Phys. Rev. Lett.*, 115:077202, Aug 2015.

[160] T. Fennell, M. Kenzelmann, B. Roessli, M. K. Haas, and R. J. Cava. Power-law spin correlations in the pyrochlore antiferromagnet $Tb_2Ti_2O_7$. *Phys. Rev. Lett.*, 109:017201, Jul 2012.

[161] M. J. P. Gingras, B. C. den Hertog, M. Faucher, J. S. Gardner, S. R. Dunsiger, L. J. Chang, B. D. Gaulin, N. P. Raju, and J. E. Greedan. Thermodynamic and single-ion properties of Tb^{3+} within the collective paramagnetic-spin liquid state of the frustrated pyrochlore antiferromagnet $Tb_2Ti_2O_7$. *Phys. Rev. B*, 62:6496–6511, Sep 2000.

[162] S H Curnoe. Structural distortion and the spin liquid state in $Tb_2Ti_2O_7$. *Phys. Rev. B*, 78:094418, 2008.

[163] S. H. Curnoe. Effective spin-1/2 exchange model for $Tb_2Ti_2O_7$. *Phys. Rev. B*, 88:014429, Jul 2013.

[164] Petit, Sylvain, Guitteny, Solène, Robert, Julien, Bonville, Pierre, Decorse, Claudia, Ollivier, Jacques, Mutka, Hannu, and Mirebeau, Isabelle. Spin dynamics in highly frustrated pyrochlore magnets. *EPJ Web of Conferences*, 83:03012, 2015.

[165] Sylvain Petit, F. Damay, Quentin Berrod, and J.-M. Zanotti. Spin and lattice dynamics in the two-singlet system $Tb_3Ga_5O_{12}$. *Physical Review Research*, 3(1), January 2021.

[166] Joseph A. M. Paddison. Ultrafast calculation of diffuse scattering from atomistic models. *Acta Crystallographica Section A*, 75(1):14–24, Jan 2019.

[167] https://www.isis.stfc.ac.uk/Pages/sxd.aspx.

[168] I. Mirebeau, P. Bonville, and M. Hennion. Magnetic excitations in $Tb_2Sn_2O_7$ and $Tb_2Ti_2O_7$ as measured by inelastic neutron scattering. *Phys. Rev. B*, 76:184436, Nov 2007.

[169] J. Zhang, K. Fritsch, Z. Hao, B. V. Bagheri, M. J. P. Gingras, G. E. Granroth, P. Jiramongkolchai, R. J. Cava, and B. D. Gaulin. Neutron spectroscopic study of crystal field excitations in $Tb_2Ti_2O_7$ and $Tb_2Sn_2O_7$. *Phys. Rev. B*, 89:134410, Apr 2014.

[170] A. J. Princep, H. C. Walker, D. T. Adroja, D. Prabhakaran, and A. T. Boothroyd. Crystal field states of Tb^{3+} in the pyrochlore spin liquid $Tb_2Ti_2O_7$ from neutron spectroscopy. *Phys. Rev. B*, 91:224430, Jun 2015.

[171] Zhiling Dun, Xiaojian Bai, Matthew B. Stone, Haidong Zhou, and Martin Mourigal. Effective point-charge analysis of crystal fields: Application to rare-earth pyrochlores and tripod kagome magnets $R_3Mg_2Sb_3O_{14}$. *Phys. Rev. Research*, 3:023012, Apr 2021.

[172] R.L McGreevy. RMC: progress, problems and prospects. *Nuclear Instruments and Methods in Physics Research Section A: Accelerators, Spectrometers, Detectors and Associated Equipment*, 354(1):1–16, 1995. Proceedings of the Third Workshop on Neutron Scattering Data Analysis.

[173] D. Neogy and A. Chatterji. Investigation of magnetic, thermal and hyperfine properties of tb3+ in tetragonal sites in SrF2. *Journal of Physics and Chemistry of Solids*, 40(12):1045–1049, 1979.

[174] T. Lin, X. Ke, M. Thesberg, P. Schiffer, R. G. Melko, and M. J. P. Gingras. Nonmonotonic residual entropy in diluted spin ice: A comparison between monte carlo simulations of diluted dipolar spin ice models and experimental results. *Phys. Rev. B*, 90:214433, Dec 2014.

[175] E. Lhotel, C. Paulsen, P. Dalmas de Réotier, A. Yaouanc, C. Marin, and S. Vanishri. Low-temperature magnetization in geometrically frustrated $Tb_2Ti_2O_7$. *Phys. Rev. B*, 86:020410, Jul 2012.

[176] Pierre Bonville, Isabelle Mirebeau, Arsène Gukasov, Sylvain Petit, and Julien Robert. Tetragonal distortion yielding a two-singlet spin liquid in pyrochlore $Tb_2Ti_2O_7$. *Phys. Rev. B*, 84:184409, Nov 2011.

[177] P. Bonville, A. Gukasov, I. Mirebeau, and S. Petit. Towards a model of a dynamical jahn-teller coupling at very low temperatures in $Tb_2Ti_2O_7$. *Phys. Rev. B*, 89:085115, Feb 2014.

[178] A. P. Sazonov, A. Gukasov, I. Mirebeau, H. Cao, P. Bonville, B. Grenier, and G. Dhalenne. Field-induced magnetic structures in $Tb_2Ti_2O_7$ at low temperatures: From spin-ice to spin-flip structures. *Phys. Rev. B*, 82:174406, Nov 2010.

[179] J. Rodríguez-Carvajal. *Physica B*, 192:55, 1993.

[180] A. P. Sazonov, A. Gukasov, H. B. Cao, P. Bonville, E. Ressouche, C. Decorse, and I. Mirebeau. Magnetic structure in the spin liquid $Tb_2Ti_2O_7$ induced by a [111] magnetic field: Search for a magnetization plateau. *Phys. Rev. B*, 88:184428, Nov 2013.

[181] Yuesheng Li, Sebastian Bachus, Hao Deng, Wolfgang Schmidt, Henrik Thoma, Vladimir Hutanu, Yoshifumi Tokiwa, Alexander A. Tsirlin, and Philipp Gegenwart. Partial up-up-down order with the continuously distributed order parameter in the triangular antiferromagnet $TmMgGaO_4$. *Phys. Rev. X*, 10:011007, Jan 2020.

[182] Yuesheng Li, Qiao-Yi Li, Wei Li, Tao Liu, David J. Voneshen, Pabitra K. Biswas, and Devashibhai Adroja. Spin dynamics and griffiths singularity in the random quantum ising magnet $PrTiNbO_6$. *npj Quantum Materials*, 6(1):34, 2021.

[183] J.-J. Wen, S. M. Koohpayeh, K. A. Ross, B. A. Trump, T. M. McQueen, K. Kimura, S. Nakatsuji, Y. Qiu, D. M. Pajerowski, J. R. D. Copley, and C. L. Broholm. Disordered route to the coulomb quantum spin liquid: Random transverse fields on spin ice in $Pr_2Zr_2O_7$. *Phys. Rev. Lett.*, 118:107206, Mar 2017.

[184] Monica Ciomaga Hatnean, Romain Sibille, Martin R Lees, Michel Kenzelmann, Voraksmy Ban, Vladimir Pomjakushin, and Geetha Balakrishnan. Single crystal growth, structure and magnetic properties of $Pr_2Hf_2O_7$ pyrochlore. *Journal of Physics: Condensed Matter*, 29(7):075902, dec 2016.

[185] B. A. Trump, S. M. Koohpayeh, K. J. T. Livi, J. J. Wen, K. E. Arpino, Q. M. Ramasse, R. Brydson, M. Feygenson, H. Takeda, M. Takigawa, K. Kimura, S. Nakatsuji, C. L. Broholm, and T. M. McQueen. Universal geometric frustration in pyrochlores. *Nature Communications*, 9(1):2619, 2018.

[186] S.M. Koohpayeh, J.-J. Wen, B.A. Trump, C.L. Broholm, and T.M. McQueen. Synthesis, floating zone crystal growth and characterization of the quantum spin ice pr2zr2o7 pyrochlore. *Journal of Crystal Growth*, 402:291–298, 2014.

[187] David A. Keen, Matthias J. Gutmann, and Chick C. Wilson. SXD – the single-crystal diffractometer at the ISIS spallation neutron source. *Journal of Applied Crystallography*, 39(5):714–722, Oct 2006.

[188] M. Gutmann. SXD2001 - a program for treating data from TOF neutron single-crystal diffraction. *Acta Crystallographica Section A*, 61(a1):c164, Aug 2005.

[189] Vaclav Petricek, Michal Dusek, and Lukas Palatinus. Crystallographic computing system jana2006: General features. *Zeitschrift fur Kristallographie - Crystalline Materials*, 229(5):345–352, 2014.

[190] Ghanshyam Pilania, Brian Puchala, and Blas P. Uberuaga. Distortion-stabilized ordered structures in $A_2BB'O_7$ mixed pyrochlores. *npj Computational Materials*, 5(1):7, 2019.

[191] Paolo Giannozzi, Stefano Baroni, Nicola Bonini, Matteo Calandra, Roberto Car, Carlo Cavazzoni, Davide Ceresoli, Guido L Chiarotti, Matteo Cococcioni, Ismaila Dabo, Andrea Dal Corso, Stefano de Gironcoli, Stefano Fabris, Guido Fratesi, Ralph Gebauer, Uwe Gerstmann, Christos Gougoussis, Anton Kokalj, Michele Lazzeri, Layla Martin-Samos, Nicola Marzari, Francesco Mauri, Riccardo Mazzarello, Stefano Paolini, Alfredo Pasquarello, Lorenzo Paulatto, Carlo Sbraccia, Sandro Scandolo, Gabriele Sclauzero, Ari P Seitsonen, Alexander Smogunov, Paolo Umari, and Renata M Wentzcovitch. QUANTUM ESPRESSO: a modular and open-source software project for quantum simulations of materials. *Journal of Physics: Condensed Matter*, 21(39):395502, sep 2009.

[192] P Giannozzi, O Andreussi, T Brumme, O Bunau, M Buongiorno Nardelli, M Calandra, R Car, C Cavazzoni, D Ceresoli, M Cococcioni, N Colonna, I Carnimeo, A Dal Corso, S de Gironcoli, P Delugas, R A DiStasio, A Ferretti, A Floris, G Fratesi, G Fugallo, R Gebauer, U Gerstmann, F Giustino, T Gorni, J Jia, M Kawamura, H-Y Ko, A Kokalj, E Küçükbenli, M Lazzeri, M Marsili, N Marzari, F Mauri, N L Nguyen, H-V Nguyen, A Otero de-la Roza, L Paulatto, S Poncé, D Rocca, R Sabatini, B Santra, M Schlipf, A P Seitsonen, A Smogunov, I Timrov, T Thonhauser, P Umari, N Vast, X Wu, and S Baroni. Advanced capabilities for materials modelling with quantum ESPRESSO. *Journal of Physics: Condensed Matter*, 29(46):465901, oct 2017.

[193] We used the pseudopotentials o.pbesol-n- kjpaw psl.0.1.upf, pr.gga-pbesol-paw.upf and zr pbesol v1.uspp.f.upf from http://www.quantum- espresso.org.

[194] T. Fennell, O. A. Petrenko, B. Fåk, J. S. Gardner, S. T. Bramwell, and B. Ouladdiaf. Neutron scattering studies of the spin ices $Ho_2Ti_2O_7$ and $Dy_2Ti_2O_7$ in applied magnetic field. *Phys. Rev. B*, 72:224411, Dec 2005.

[195] S. T. Bramwell, M. J. Harris, B. C. den Hertog, M. J. P. Gingras, J. S. Gardner, D. F. McMorrow, A. R. Wildes, A. L. Cornelius, J. D. M. Champion, R. G. Melko, and T. Fennell. Spin correlations in $Ho_2Ti_2O_7$: a dipolar spin ice system. *Phys. Rev. Lett.*, 87:047205, Jul 2001.

[196] J. A. Quilliam, L. R. Yaraskavitch, H. A. Dabkowska, B. D. Gaulin, and J. B. Kycia. Dynamics of the magnetic susceptibility deep in the coulomb phase of the dipolar spin ice material $Ho_2Ti_2O_7$. *Phys. Rev. B*, 83:094424, Mar 2011.

[197] G. Ehlers, J. S. Gardner, C. H. Booth, M. Daniel, K. C. Kam, A. K. Cheetham, D. Antonio, H. E. Brooks, A. L. Cornelius, S. T. Bramwell, J. Lago, W. Häussler, and N. Rosov. Dynamics of diluted Ho spin ice $Ho_{2-x}Y_xTi_2O_7$ studied by neutron spin echo spectroscopy and ac susceptibility. *Phys. Rev. B*, 73:174429, May 2006.

[198] G. Ehlers, J. S. Gardner, Y. Qiu, P. Fouquet, C. R. Wiebe, L. Balicas, and H. D. Zhou. Dynamic spin correlations in stuffed spin ice $Ho_{2+x}Ti_{2-x}O_{7-\delta}$. *Phys. Rev. B*, 77:052404, Feb 2008.

[199] Catherine Heremans, Bernhardt J. Wuensch, Judith K. Stalick, and Edward Prince. Fast-ion conducting $Y_2(Zr_yTi_{1-y})_2O_7$ pyrochlores: Neutron rietveld analysis of disorder induced by Zr substitution. *Journal of Solid State Chemistry*, 117(1):108–121, 1995.

[200] Bernhardt J. Wuensch and Kevin W. Eberman. Order-disorder phenomena in $A_2B_2O_7$ pyrochlore oxides. *JOM*, 52(7):19–21, 2000.

[201] Devon L. Drey, Eric C. O Quinn, Tamilarasan Subramani, Kristina Lilova, Gianguido Baldinozzi, Igor M. Gussev, Antonio F. Fuentes, Joerg C. Neuefeind, Michelle Everett, David Sprouster, Alexandra Navrotsky, Rodney C. Ewing, and Maik Lang. Disorder in $Ho_2Ti_{2-x}Zr_xo_7$: pyrochlore to defect fluorite solid solution series. *RSC Adv.*, 10:34632–34650, 2020.

[202] J. A. Quilliam, L. R. Yaraskavitch, H. A. Dabkowska, B. D. Gaulin, and J. B. Kycia. Dynamics of the magnetic susceptibility deep in the coulomb phase of the dipolar spin ice material $Ho_2Ti_2O_7$. *Phys. Rev. B*, 83:094424, Mar 2011.

[203] S. Rosenkranz, A. P. Ramirez, A. Hayashi, R. J. Cava, R. Siddharthan, and B. S. Shastry. Crystal-field interaction in the pyrochlore magnet $Ho_2Ti_2O_7$. *Journal of Applied Physics*, 87(9):5914–5916, 2000.

[204] J. Snyder, B. G. Ueland, J. S. Slusky, H. Karunadasa, R. J. Cava, and P. Schiffer. Low-temperature spin freezing in the $Dy_2Ti_2O_7$ spin ice. *Phys. Rev. B*, 69:064414, Feb 2004.

[205] H.W.J. Blöte, R.F. Wielinga, and W.J. Huiskamp. Heat-capacity measurements on rare-earth double oxides $R_2M_2O_7$. *Physica*, 43(4):549–568, 1969.

[206] Zenji Hiroi, Kazuyuki Matsuhira, Seishi Takagi, Takashi Tayama, and Toshio Sakakibara. Specific heat of kagomé ice in the pyrochlore oxide $Dy_2Ti_2O_7$. *Journal of the Physical Society of Japan*, 72(2):411–418, 2003.

[207] A. M. Hallas, J. A. M. Paddison, H. J. Silverstein, A. L. Goodwin, J. R. Stewart, A. R. Wildes, J. G. Cheng, J. S. Zhou, J. B. Goodenough, E. S. Choi, G. Ehlers, J. S. Gardner, C. R. Wiebe, and H. D. Zhou. Statics and dynamics of the highly correlated spin ice $Ho_2Ge_2O_7$. *Phys. Rev. B*, 86:134431, Oct 2012.

[208] Joseph A M Paddison, J Ross Stewart, and Andrew L Goodwin. spinvert: a program for refinement of paramagnetic diffuse scattering data. *Journal of Physics: Condensed Matter*, 25(45):454220, oct 2013.

[209] C V Topping and S J Blundell. A.c. susceptibility as a probe of low-frequency magnetic dynamics. *Journal of Physics: Condensed Matter*, 31(1):013001, nov 2018.

[210] D Huser, A J van Duyneveldt, G J Nieuwenhuys, and J A Mydosh. Phenomenological model for the frequency dependence of the susceptibility of spin glasses and related compounds. *Journal of Physics C: Solid State Physics*, 19(19):3697–3717, jul 1986.

[211] Moshe Schechter. $LiHo_xY_{1-x}F_4$ as a random-field ising ferromagnet. *Phys. Rev. B*, 77:020401, Jan 2008.

[212] Yishu Wang, T. Reeder, Y. Karaki, J. Kindervater, T. Halloran, N. Maliszewskyj, Yiming Qiu, J. A. Rodriguez, S. Gladchenko, S. M. Koohpayeh, S. Nakatsuji, and C. Broholm. Monopolar and dipolar relaxation in spin ice $Ho_2Ti_2O_7$. *Science Advances*, 7(25):eabg0908, 2021.

[213] Allen Scheie. Quantifying uncertainties in crystal electric field hamiltonian fits to neutron data, 2021.

Acknowledgements

I have been lucky to be surrounded by extremely nice and competent people during my stay at the Paul Scherrer Institut. Starting of course with my supervisor and friend, Dr. Romain Sibille. Romain, I cannot thank you enough for everything you did for me. You have been an amazing teacher and mentor, always available to answer my questions, to orient me in the right direction, to listen to my worries about work and life in general. Your unwavering good mood and humor, coupled with your knowledge and productivity kept my spirits and motivation high all along, making it a real pleasure to come to work. These four years simply flew behind and I am truly going to miss you. I would also like to thank my Doktorvater, Prof. Michel Kenzelmann, for his brilliant scientific insights and precious advice, showing me how to see the greater picture and how I should tackle my research by asking myself the important questions.

I also had the chance to have Dr. Oksana Zaharko and Dr. Jonathan White as line managers, who have always been very attentive to my development as a PhD student.

Many thanks to Dr. Ekaterina Pomjakushina and Dr. Dariusz Gawryluk. Katja and Darek, your generosity, time, help, advice and patience have been at the very root of this work. I started to miss bothering you with many questions towards the end and was always glad to occasionally walk across your corridor and have a quick chat with both of you. The help, efforts and great skills of Dr. Pascal Puphal have also been crucial in the obtention of the crystals studied in this work.

Sticking with the same building, I would like to thank Dr. Marisa Medarde. Marisa, thank you so much for welcoming me during my Master Thesis and for your kindness since then. I have learned so much during these few months, with many of the practical skills you taught me playing a major part of the success of my studies.

I of course benefited from the help of amazing collaborators. The impressive knowledge of Dr. Elsa Lhotel and her unique equipment have led to many of the low temperature measurements reported in this work. I deeply enjoyed talking, working and learning with Dr. Sylvain Petit. Thanks to Dr. Nicolas Gauthier for sharing many of his codes and to Dr. Vladimir Pomjakushin for many discussions about neutron scattering and group theory.

I have been fortunate to carry out experiments at many institutions and instruments with the help of a number of exceptionally competent beamline scientists, sample environments teams and technicians. The list would be too long to enumerate but I am grateful to have had the chance to interact with so many people of different origin, skills and goals.

All these data would have been extremely difficult to analyze without the softwares written by inspired scientists, a few of which I had to chance to meet and interact with, among whom Dr. Joe Paddison, Dr. Arkadiy Simonov, Dr. Allen Scheie and Dr. Matthias Gutmann. The understanding of our data was made possible with the great help of our theoretician friends Prof. Peter M. Derlet, Prof. Andriy Nevidomskyy, Dr. Han Yan, Dr. Anish Bhardwaj and Prof. Hitesh Changlani.

Curriculum vitea

Personal Information

Last name	Porée
First name	Victor
Date of birth	September 25th, 1995
Place of birth	Rennes, France
Nationality	French

Education

Ph.D. in Physics   10/2018-11/2022
Paul Scherrer Institut and University of Basel.
Laboratory for Neutron Scattering and Imaging.
Supervised by Dr. Romain Sibille and Prof. Michel Kenzelmann.

M.Sc. in Physics   09/2016-08/2018
Technische Universität of München and Università degli studi di Torino.
Master Thesis at the Paul Scherrer Institut, supervised by Dr. Marisa Medarde.

B.Sc. in Physics   09/2013-08/2016
Université de Rennes 1.
Bachelor Thesis at the Diamond Light Source, supervised by Dr. Alessandro Bombardi.

Baccalauréat - Scientific section   06/2013
L'Institution - La Providence, Saint Malo

Publications

A quantum liquid of magnetic octupoles on the pyrochlore lattice
R. Sibille, N. Gauthier, E. Lhotel, **V. Porée**, V. Pomjakushin, R. A. Ewings, T. G. Perring, J. Ollivier, A. Wildes, C. Ritter, T. C. Hansen, D. A. Keen, G. J. Nilsen, L. Keller, S. Petit, and T. Fennell, Nature Physics 16, 546 (2020) or in open source: arXiv:1912.00928.

Crystal-field states and defect levels in candidate quantum spin ice $Ce_2Hf_2O_7$
V. Porée, E. Lhotel, S. Petit, A. Krajewska, P. Puphal, A. H. Clark, V. Pomjakushin, H. C. Walker, N. Gauthier, D. J. Gawryluk, and R. Sibille, Phys. Rev. Materials 6, 044406 (2022) or in open source: arXiv:2203.16295.

Low-temperature magnetic crossover in the topological kagome magnet $TbMn_6Sn_6$
C. Mielke III, W. L. Ma, V. Pomjakushin, O. Zaharko, S. Sturniolo, X. Liu, V. Ukleev, J. S. White, J.-X. Yin, S. S. Tsirkin, C. B. Larsen, T. A. Cochran, M. Medarde, **V. Porée**, D. Das, R. Gupta, C. N. Wang, J. Chang, Z. Q. Wang, R. Khasanov, T. Neupert, A. Amato, L. Liborio, S. Jia, M. Z. Hasan, H. Luetkens and Z. Guguchia, Commun Phys 5, 107 (2022) or in open source: arXiv:2101.05763.

Unpublished work

Experimental spectrum of fractional excitations in a three-dimensional quantum spin liquid
V. Porée, H. Yan, S. Petit, E. Lhotel, M. Appel, J. Ollivier, T. Fennell, A. Nevidomskyy, R. Sibille, submitted to Science.

Dipolar-octupolar correlations and hierarchy of exchange parameters in $Ce_2Hf_2O_7$
V. Porée, A. Bhardwaj, N. Gauthier, E. Lhotel, S. Petit, H. Yan, V. Pomjakushin, J. Ollivier, M. Kofu, A. H. Nevidomskyy, H. J. Changlani, and R. Sibille, in preparation.

Structural disorder and magnetic correlations in non-Kramers $Tb_2Hf_2O_7$ pyrochlore
V. Porée, E. Lhotel, A. Krajewska, M. C. Hatnean, P. M. Derlet, D. A. Keen, M. Gutmann, H. C. Walker, A. Goukassov, J. Ollivier, E. Ressouche, S. Petit, T. Fennell, M. Kenzelmann and R. Sibille, in preparation.

$YBa_{1-x}Sr_xCuFeO_5$ layered perovskites: exploring the phase diagram beyond the collinear- spiral-paramagnetic triple point
V. Porée, T. Shang, E. Marelli, D.J. Gawryluk, J.A. Rodríguez-Velamazan, N. Casati, E. Pomjakushina, and M. Medarde, in preparation.

Investigation of high-temperature multiferroics
V. Porée, Master thesis

Contributions to conferences

Oral presentations

Disorder induced correlated phases in non-Kramers rare-earth pyrochlores
V. Porée, E. Lhotel, S. Petit, T. Mazet, & R. Sibille, International workshop on Correlated Disorder, February 2020, Herzberg, Switzerland. (Contributed)

Levels of defects in single crystals of praseodymium pyrochlores: from quantum spin ice $Pr_2Hf_2O_7$ to quadrupole-correlated $Pr_2Zr_2O_7$
V. Porée, S. Petit, M. C. Hatnean, E. Lhotel, D. A. Keen, M. J. Gutmann, J. Ghanbaja, G. Balakrishnan & R. Sibille, waiting for Highly Frustrated Magnetism, January 2021 (online, Dresden). (Contributed)

Octupolar correlations and spinon continuum in Ce^{3+} pyrochlores
V. Porée, S. Petit, E. Lhotel, T. Fennell, & R. Sibille, March Meeting 2022, Chicago, USA. (Contributed)

Structural disorder and magnetic correlations in non-Kramers $Tb_2Hf_2O_7$ pyrochlore
V. Porée, P. M. Derlet, M. Kenzelmann & R. Sibille, Tends In Quantum Magnetism, April 2022, Ascona, Switzerland. (Contributed)

Octupolar correlations in candidate quantum spin ice cerium hafnate
V. Porée, E. Lhotel, S. Petit, A. Bhardwaj, H. J. Changlani, H. Yan, A. Nevidomskyy & R. Sibille, European MicroKelvin Plateform User Meeting, May 2022 (online). (Invited)

Structural disorder and magnetic correlations in non-Kramers $Tb_2Hf_2O_7$ pyrochlore
V. Porée, P. M. Derlet, M. Kenzelmann & R. Sibille, SPS meeting, June 2022 Fribourg, Switzerland. (Contributed)

Poster presentations

A quantum liquid of magnetic octupoles on the pyrochlore lattice
V. Porée, N. Gauthier, E. Lhotel, S. Petit, V. Pomjakushin, J. Ollivier, R. A. Ewings, T. G. Perring, C. Ritter, T. C. Hansen, A. Wildes, D. A. Keen, G. J. Nilsen, L. Keller and T. Fennell & R. Sibille, Condensed Matter retreat, November 2019, Brugg, Switzerland.

Disorder-induced phases in non-Kramers rare-earth pyrochlores
V. Porée, E. Riordan, E. Lhotel, S. Petit, P. M. Derlet, M. Kenzelmann & R. Sibille,

March Meeting 2022, Chicago, USA.

$Ce_2Hf_2O_7$ - a 'dipole-octupole' cerium pyrochlore
V. Porée, E. Lhotel, S. Petit, A. Bhardwaj, H. J. Changlani, N. Gauthie, J. A. Quilliam, H. Yan, A. Nevidomskyy & R. Sibille, Highly Frustated Magnetism, June 2022, Paris, France.

$Ce_2Hf_2O_7$ - a 'dipole-octupole' cerium pyrochlore
V. Porée, Elsa Lhotel, Sylvain Petit, Anish Bhardwaj, Hitesh J. Changlani, Nicolas Gauthie, Jeffrey A. Quilliam, Han Yan, Andriy Nevidomskyy & Romain Sibille, 3rd PSI Condensed Matter Summer Camp, August 2022, Zuoz, Switzerland.